The Dissertation Committee for Xing-Xiang Liu certifies that this is the approved version of the following dissertation:

GENERALIZED HOMOGENIZATION THEORY AND INVERSE DESIGN OF PERIODIC ELECTROMAGNETIC METAMATERIALS

Committee:

Andrea Alù, Supervisor

Hao Ling

Gennady Shvets

Carlos Torres-Verdin

Zheng Wang

Ali Yilmaz

GENERALIZED HOMOGENIZATION THEORY AND INVERSE DESIGN OF PERIODIC ELECTROMAGNETIC METAMATERIALS

by

XING-XIANG LIU, B.S.; M.S.

Dissertation

Presented to the Faculty of the Graduate School of

The University of Texas at Austin

in Partial Fulfillment

of the Requirements

for the Degree of

DOCTOR OF PHILOSOPHY

The University of Texas at Austin

MAY 2013

GENERALIZED HOMOGENIZATION THEORY AND INVERSE DESIGN OF PERIODIC ELECTROMAGNETIC METAMATERIALS

Xing-Xiang Liu, Ph.D.

The University of Texas at Austin, 2013

Supervisor: Andrea Alù

Artificial metamaterials composed of specifically designed subwavelength unit cells can support an exotic material response and present a promising future for various microwave, terahertz and optical applications. Metamaterials essentially provide the concept to microscopically manipulate light through their subwavelength inclusions, and the overall structure can be macroscopically treated as homogeneous bulk material characterized by a simple set of constitutive parameters, such as permittivity and permeability. In this dissertation, we present a complete homogenization theory applicable to one-, two- and three-dimensional metamaterials composed of nonconnected subwavelength elements. The homogenization theory provides not only deep insights of electromagnetic wave propagation among metamaterials, but also gives useful analysis method for engineering metamaterials. We begin the work by proposing a general retrieval procedure to characterize arbitrary subwavelength elements in terms of a polarizability tensor. Based on this system, we may start the macroscopic analysis of metamaterials by analyzing the scattering properties of their microscopic building blocks. For one-dimensional linear arrays, we present the dispersion relations for single and

parallel linear chains and study their potential use as sub-diffractive waveguides and leaky-wave antennas. For two-dimensional arrays, we interpret the metasurfaces as homogeneous surfaces and characterize their properties by a complete six-by-six tensorial effective surface susceptibility. This model also offers the possibility to derive analytical transmission and reflection coefficients for metasurfaces composed of arbitrary nonconnected inclusions with TE and TM mutual coupling. For three-dimensional metamaterials, we present a generalized theory to homogenize arrays by effective tensorial permittivity, permeability and magneto-electric coupling coefficients. This model captures comprehensive anisotropic and bianisotropic properties of metamaterials. Based on this theory, we also modify the conventional retrieval method to extract physically meaningful effective parameters of given metamaterials and fundamentally explain the non-causal issue of parameter retrieval. Finally, we conceptually propose an inverse design procedure for three-dimensional metamaterials that can efficiently determine the geometry of the inclusions required to achieve the anomalus properties, such as double-negative response, in the desired frequency regime.

Table of Contents

List of Figures

Chapter 1 Introduction

Metamaterials are artificially structured media realized as periodic or aperiodic arrays with unit cells sufficiently smaller than wavelength of operation. These unit cells contain designed inclusions with specific geometry made of certain constituent materials. Conceptually, metamaterials may be macroscopically treated as homogeneous bulk media characterized by a set of effective parameters which are unavailable in natural materials. These bulk properties of homogenized metamaterials are directly related to the characteristics of each unit cells, such as polarization and resonance. Therefore, by engineering the unit cell and inclusions, the integrated complex structures may be built to present exotic material properties. Based on this concept, metamaterials have been extensively explored in the fields of electromagnetics [1-4], acoustics [6-9], seismic [10, 11] and matter waves [12, 13] to perform unconventional physics in the past decade. Particularly, in the field of electrodynamics, many interesting phenomena such as negative refractive index [14], artificial magnetism [15] and epsilon-near-zero materials [16], have been reported and these novel material properties have brought promising potentials for enhancing the performance of conventional optical or microwave devices.

1.1 History of Electromagnetic Metamaterials

The prehistory of artificial materials can be dated back to the stained glasses developed several centuries ago. Since the Middle Ages, artisans have managed to fabricate colorful stained glasses by adding a small amount of impurity into melted silica [17, 18]. By properly selecting the material of the particles and controlling the size of the impurities, they were able to manufacture glasses with a wide range of colors and transparency, as shown in Fig 1.1a. In the early twentieth century, scientists have started to be interested in even more anomalous response, such as strong optical activity or bianisotropic

properties, which may manipulate propagating waves and modify the polarization state. They found that the bianisotropic properties can be artificially enhanced by distributing small chiral objects, such as helix copper wires, in the substrate media [4] as shown in Fig 1.1b. When these composite materials are illuminated by a linearly polarized electromagnetic wave, rotation of the plane of polarization can be easily observed. As expected, the direction of rotation is consistent with the handedness of the embedded helices [19, 20].

Later, during World War II, the applications of microwave devices have received a great amount of attention and lens antennas became a topic of interest. In order to control the dielectric constant of lenses and manipulate wave propagation inside dielectric media, researchers proposed the design of convex lenses containing periodically arranged small metallic strips or baffle plates, as shown in Fig 1.1c. These artificial lenses present a high dielectric constant and enhanced bandwidth [21]. These classical artificial materials and manufacturing processes, proposed long time ago, have mostly focused on enhancing conventional material properties and they do not necessarily exhibit exotic features substantially different from their constituents or from other materials already available in nature.

The concept of modern artificial composite materials, or metamaterials, originated from the discussion of negative index of refraction to enhance optical image resolution. In 2000, a seminal work presented by John B. Pendry [24] claimed that a *superlens* made of materials with simultaneously negative values of permittivity and permeability may overcome the diffraction limit in optics and achieve perfect imaging. Although negative values of permeability are not readily available in nature (except for some special ferromagnetic alloys [25]), we are now able to engineer artificial subwavelength inclusions that can generate anti-magnetic effects at the microscopic level and achieve an

effective bulk negative permeability. Soon after, negative index of refraction was verified by experimental measurements at microwave frequencies based on split-ring resonator inclusions (SRRs) [26]. These pioneering works have injected a large amount of momentum to the research field of metamaterials and, more recently, several types of metamaterials have been presented to achieve promising applications at optical, terahertz and microwave frequencies. The interesting applications behind these works include high-resolution imaging [27-29], hyperlens [30-32], wave cloaking [33-35], high-impedance surfaces [36, 37] and novel antennas [38-40].

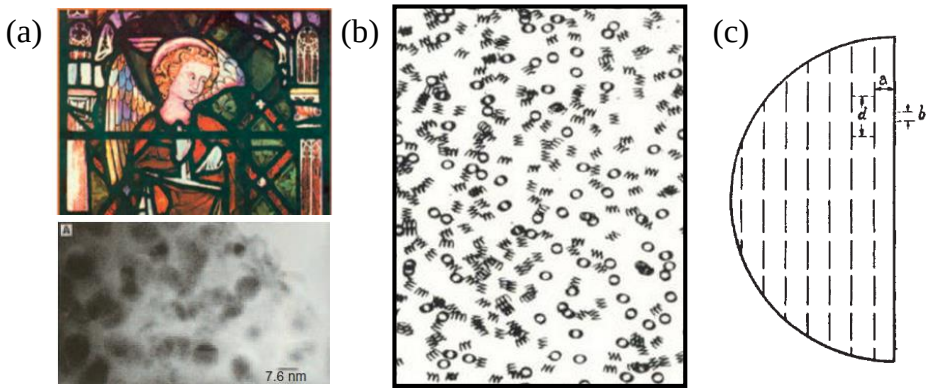

Figure 1.1 Examples of classic artificial materials (a) The colorful stained-glasses and SEM image of embedded nanoparticles [17], (b) artificial bianisotropic medium with helix wires [19, 22], (c) the convex lens containing small metallic strips [21].

1.2 CATEGORIES OF METAMATERIALS

Since the properties of metamaterials are dominated by the inclusion geometry and unit cell arrangements, different types of metamaterials may produce different bulk effects and the supported wave phenomena strongly depend on their microstructure features. In addition, different kinds of metamaterials may usually require different modeling techniques and fabrication technology in their design and manufacturing processes. Therefore, it is useful to properly categorize modern metamaterials and discuss their

electromagnetic properties and functions accordingly. Based on their structure features, metamaterials can be generally categorized by type of unit cells and dimension of arrays. Although some literature [41] suggests grouping metamaterials by the frequency regimes of operation, the modeling and analysis methods for characterizing these artificial media are usually not dependent of the frequency of interest. Therefore, in this section, we focus on the metamaterial categories in terms of inclusion geometry and array structures.

Generally, metamaterial inclusions can be divided into nonconnected and connected groups, based on their geometrical features. The former type is made of elements which are not in direct contact with each other across the unit cell. In other words, each unit cell is separate and the subwavelength inclusions can be treated as discrete elements, usually dominated by their dipolar response in the long-wavelength limit. As a consequence, the overall metamaterial structures can be simplified into electric/magnetic dipole arrays with same dimensions. Most common inclusions for this group of metamaterials include SRRs [26, 42-47], homogeneous and composite particles [48-54], rings [55-57] and rods [33, 58, 59].

The other type of metamaterials is composed of unit cells which connect across their boundaries, including structures like long-wire arrays [60, 61], metal-dielectric-metal (MDM) multilayered structures [30-32, 62] and fishnet structures [14, 63-66]. The unit cells and inclusions in this case are usually simpler than the nonconnected type, and they are also easier for fabrication at microwaves and optical regimes. Typically, these inclusions only meet the subwavelength condition in certain dimensions, and they extend in other directions over multiple wavelengths, creating more complications in their homogenization. For example, layers of MDM structures are much thinner than the operation wavelength in the longitudinal plane but they extend in the transverse direction over several wavelengths. Unlike the first group, the inclusions in these metamaterials

cannot to be described as discrete dipoles, and the characterization of this type of metamaterials highly depends on the nature of the continuous features in these structures. As a result, different theories should be carefully considered to correctly capture the special phenomena in these above metamaterials. For instance, although both wire arrays and fishnet metamaterials are characterized by strong spatial dispersion for oblique propagation, they require different theoretical approaches [67, 68] to accurately capture these phenomena.

It is also important to categorize metamaterials by their lattice dimension, and by the average distance among inclusions. This aspect may dominate the bulk response of metamaterials, and different array configurations may require different concepts for modeling and characterization. For example, two-dimensional (2-D) metamaterials are usually known as metasurfaces, and they are modeled using homogeneous surface susceptibility [69] in practical applications. It would make little sense to try to describe a 2-D surface in terms of permittivity and permeability (even if often times this was attempted, especially at optical frequencies) [70].

1.3 HOMOGENIZATION OF METAMATERIALS AND ITS CHALLENGES

From an engineering point of view, it is highly desirable to describe the complex metamaterials by a simple set of effective parameters, such as permittivity and permeability. In this way, we are able to describe metamaterials as conventional bulk materials in integrated devices and take advantage of their exotic properties in various applications. In general, there are two methods to describe and characterize electromagnetic metamaterials. The first approach is describing the metamaterial *a posteriori*, after the sample is designed and/or realized, usually based on the Nicolson-Ross-Weir (NRW) retrieval method [71, 72]. This approach assumes that the given

metamaterial may be treated as a uniform bulk (or surface) model which has certain effective constitutive parameters, such as permittivity and permeability. By sending certain excitation and probing the response of the sample, such as reflection and/or transmission coefficients, we are able to retrieve the effective constitutive parameters that match our measurements or simulations. The main advantage of this method is that the formulation is simple and it can be directly applied to conventional microwave and optical measurements. The drawbacks include the ambiguity in choosing the correct propagation constant [73, 74], which has a natural period of 2π in phase, and the incompleted set of constitutive parameters, which may erroneously interpret the given metamaterials [69]. In other words, before using this method to characterize metamaterials, we have to roughly understand the behaviors or properties of the given samples to assume the correct set of constitutive parameters.

On the other hand, we can take and analyze the given metamaterial geometry from the microscopic point of view, at the inclusion and lattice level, being able to relate the microscopic details to effective constitutive parameters. This approach is generally known as homogenization method. Many homogenization theories and medium mixing rules [67, 75-94] have been developed since the synthesis of compound materials became mature in modern material technology. Most of the theories developed before the advent of metamaterials are only applicable to composite media containing inclusions with feature sizes much smaller than the wavelength of interest, and with a density of inclusions dilute enough that the strong coupling and interaction between them can be ignored. Under these assumptions, homogenized parameters of the composite materials may be easily predicted by simply considering the volume fraction of a dopant in a background medium.

In metamaterials, however, these theories and mixing rules usually fail to extract reasonable effective bulk parameters, because the inclusion sizes are not sufficiently smaller than wavelength and the underlying exotic phenomena are inherently based on the anomalous responses of the inclusions and the strong coupling between them. As a consequence, in order to properly describe complex metamaterials, it is necessary to take into account the complex electromagnetic response at the unit cell level and the mutual coupling among inclusions in a much more careful way.

1.4 ROADMAP OF THIS DISSERTATION

In this dissertation, we present a rigorous homogenization theory for periodic metamaterials. In particular, we focus our analysis on nonconnected metamaterials and discuss proper homogenization models applied to one-, two- and three-dimensional metamaterials. The theory is analytically derived based on the fundamental assumption that the dipolar approximation is valid. Therefore, we focus on metamaterial structures that satisfy $k_0 d < 1.5$, with k_0 being the free-space wavelength and d being the unit cell size. In order to validate the derived homogenization theory, we employ numerical simulation tools, including Ansoft HFSS and CST Microwave Studio. For some simple cases, we also apply fundamental theories, such as Mie scattering theory, to examine the results for canonical shapes and structures.

The dissertation is organized as follows. Chapter 2 discusses a retrieval procedure for metamaterial inclusions to extract the complete polarizability tensor (with dimension of six-by-six) of arbitrary subwavelength nonconnected inclusions composed of arbitrary constituent materials. This method is based on a 2-D array configuration, which can be easily implemented in most commercial simulation software and be applied in realistic microwave or optical measurement systems. Furthermore, the proposed technique is

universally applicable for various frequency regimes as long as the subwavelength condition is satisfied. To verify the calculated polarizability, we report several examples including magnetodielectric particles, helix wires, conducting SRR pairs and plasmonic SRR U-shape inclusions. In each case, we extract the six-by-six polarizability tensor for subwavelength elements and validate the results with full-wave simulations.

Chapter 3 presents the analysis of 1-D linear particle arrays as metamaterial waveguides and antennas. In particular, we focus our interest on the optical regime in this chapter, so we can take advantage of the strong, localized resonances in plasmonic nanoparticles. Linear arrays composed of single or parallel chains with subwavelength elements are assumed to be infinitely extended in free-space. Analytical dispersion relations are derived and solved in the complex domain for both real and complex eigenvalues in lossy or lossless configuration. We focus in particular on leaky-wave propagation and radiation. We explain the phenomena of leaky (or so called improper) waves traveling along subwavelength particle arrays and employ numerical software to demonstrate this operation. We also discuss potential antenna applications.

Chapter 4 develops a homogenization model for 2-D metasurfaces composed of a single-layer of planar arrays with nonconnected subwavelength inclusions. We derive the tensorial surface susceptibility to describe the homogenized behavior of these metasurfaces. We rigorously formulate the surface susceptibility in terms of the polarizability tensor, Green's dyads and plane wave incident and polarization angles. We derive transmission and reflection coefficients for metasurfaces composed of arbitrary inclusions and constituent materials, taking into account coupling between TE and TM modes on a 2-D planar array. We also compare our analytical results to those obtained with numerical simulation tools and verify that the derived tensorial surface susceptibility

may comprehensively capture the scattering phenomena and homogenized properties of the considered metasurfaces.

Chapter 5 discusses a general homogenization theory and novel retrieval method for 3-D metamaterials composed of infinitely extended 3-D arrays with nonconnected elements. We derive the effective parameters of metamaterials based on the Tellegen form of constitutive relations, which consider the general interaction between electric and magnetic fields in the array. We apply this method to derive the set of effective parameters for symmetric and anti-symmetric SRR pairs. Based on this homogenization theory, we also modify the conventional NRW retrieval to develop a new method to extract local effective parameters of a given arbitrary metamaterial sample. This approach not only returns physically meaningful constitutive parameters, but also provides the polarizability of constituent subwavelength inclusions without knowing their detailed geometry and material parameters. Also in this case, in order to validate our theory and method, we apply numerical simulation tools to compare analytical and numerical results. Based on our full-wave simulations, we also provide several examples of metamaterials operating in double-positive and double-negative regimes that support interesting wave phenomena, such as backward-wave propagation, negative refraction and super-resolution. Due to our analytical efforts in the homogenization theory, this model can efficiently reduce the computational costs of full-wave simulations in 2-D and 3-D metamaterials. Finally, we discuss an inverse design technique to synthesize metamaterials with the desired properties, based on our homogenization theory. This design process relies on the analytical formulation and numerical optimization procedures to return detailed geometrical parameters of nonconnected inclusions that can provide certain effective parameters at the assigned frequency.

Finally, in Chapter 6, we conclude and summarize the main achievements of this dissertation and suggest future work and the potential associated challenges.

1.5 REFERENCES

1. N. Engheta and R. W. Ziolkowski, *Metamaterials: Physics and Engineering Explorations* (Wiley-IEEE Press, Denver, 2006).
2. W. Cai and V. Shalaev, *Optical Metamaterials: Fundamentals and Applications* (Springer, 2010).
3. M. A. Noginov and V. A. Podolskiy, *Tutorials in Metamaterials* (CRC Press, 2011).
4. R. Marqués, F. Martín, and M. Sorolla, *Metamaterials with Negative Parameters* (John Wiley & Son, Hoboken, 2008).
5. J. Yao, Z. Liu, Y. Liu, Y. Wang, C. Sun, G. Bartal, A. M. Stacy, and X. Zhang, "Optical Negative Refraction in Bulk Metamaterials of Nanowires," *Science* **321**, 930 (2008).
6. R. V. Craster and S. Guenneau, *Acoustic Metamaterials: Negative Refraction, Imaging, Lensing and Cloaking* (Springer, 2013).
7. S.-C. S. Lin, *Acoustic Metamaterials: Tunable Gradient-Index Phononic Crystals for Acoustic Wave Manipulation* (Academic Publishing, 2012).
8. N. Fang, D. Xi, J. Xu, M. Ambati, W. Srituravanich, C. Sun, and X. Zhang, "Ultrasonic metamaterials with negative modulus," *Nat. Mater.* **5**, 452-456 (2006).
9. J. Li, L. Fok, X. Yin, G. Bartal, and X. Zhang, "Experimental demonstration of an acoustic magnifying hyperlens," *Nat. Mater*. **8**, 931-934 (2009).
10. Y. Lai, Y. Wu, P. Sheng and Z.-Q. Zhang, "Hybrid elastic solids," *Nat. Mater*. **10**, 620-624 (2011).
11. S.-H Kim, "Seismic wave attenuator made of acoustic metamaterials," *J. Acoust. Soc. Am*. **131**, 3292-3292 (2012).
12. S. Zhang, D. A. Genov, C. Sun, and X. Zhang, "Cloaking of matter waves," *Phys. Rev. Lett*. **100**, 123002 (2008).
13. D.-H. Lin and P.G. Luan, "Cloaking of matter waves under the global Aharonov–Bohm effect," *Phys. Rev. A* **79**, 051605 (2009).
14. J. Valentine, S. Zhang, T. Zentgraf, E. Ulin-Avila, D. A. Genov, G. Bartal, and X. Zhang, "Three-dimensional optical metamaterial with a negative refractive index," *Nature* **455**, 376-379 (2008).
15. J. B. Pendry, A. J. Holden, D. J. Robbins, and W. J. Stewart, "Magnetism from conductors and enhanced nonlinear phenomena," *IEEE Trans. Microwave Theory Tech*. **47**, 2075-2084 (1999).
16. M. Silveirinha and N. Engheta, "Design of matched zero-index metamaterials using nonmagnetic inclusions in epsilon-near-zero media," *Phys. Rev. B* **75**, 075119 (2007).
17. J. Reithmaier, P. Petkov, W. Kulisch, and C. Popov, *Nanostructured Materials for*

Advanced Technological Applications (Springer, Bulgaria, 2008).
18. H. A. Atwater, "The Promise of Plasmonics," *Sci. Am*. **296**, 56-62 (2010).
19. I. V. Lindell, A. H. Sihvola, and J. Kurkijarvi, "Karl F. Lindman: The last Hertzian, and a harbinger of electromagnetic chirality," *IEEE Antennas Propag. Mag.* **34**, 24-30 (1992).
20. K. F. Lindmann, "Rotation polarisation of electromagnetic waves generated by the isotropic system of spiral resonators," *Annalen der Physik* **63**, 621-644 (1920).
21. W. E. Kock, "Path-length microwave lenses," *Proc. IRE* **37**, 852-855 (1948).
22. I. V. Lindell, *Electromagnetic waves in chiral and Bi-isotropic media* (Artech House, Boston 1994).
23. W. E. Kock, Metallic delay lenses, *Bell Syst. Tech. J*. **27**, 58-82 (1948).
24. J. P. Pendry, "Negative Refraction Makes a Perfect Lens," *Phys. Rev. Lett.* **85**, 3966-3969 (2000).
25. A. Pimenov, A. Loidl, K. Gehrke, V. Moshnyaga, and K. Samwer, "Negative Refraction Observed in a Metallic Ferromagnet in the Gigahertz Frequency Range," *Phys. Rev. Lett*. **98**, 197401 (2007).
26. R. A. Shelby, D. R. Smith, and S. Schultz, "Experimental Verification of a Negative Index of Refraction," *Science* **292**, 77-79 (2001).
27. B. D. F. Casse, W. T. Lu, Y. J. Huang, E. Gultepe, L. Menon, and S. Sridhar, "Super-resolution imaging using a three-dimensional metamaterials nanolens," *Appl. Phys. Lett*. **96**, 023114 (2010).
28. D. O. S. Melville and R. J. Blaikie, "Super-resolution imaging through a planar silver layer," *Opt. Express* **13**, 2127-2134 (2005).
29. X.-X. Liu and A. Alù, "Limitations and potentials of metamaterial lenses," *J. Nanophoton*. **5**, 053509 (2011).
30. Z. Liu, H. Lee, Y. Xiong, C. Sun, and X. Zhang, "Far-Field Optical Hyperlens Magnifying Sub-Diffraction-Limited Objects," *Science* **315**, 1686 (2007).
31. B Wood, J. B. Pendry, and D. P. Tsai, "Directed subwavelength imaging using a layered metal-dielectric system," *Phys. Rev. B* **74**, 115116 (2006).
32. A. Salandrino and N. Engheta, "Far-field subdiffraction optical microscopy using metamaterial crystals: Theory and simulations," *Phys. Rev. B* **74**, 075103 (2006).
33. W. Cai, U. K. Chettiar, A. V. Kildishev, and V. M. Shalaev, "Optical cloaking with metamaterials," *Nat. Photonics* **1**, 224-227 (2007).
34. D. Schurig, J. J. Mock, B. J. Justice, S. A. Cummer, J. B. Pendry, A. F. Starr, and D. R. Smith, "Metamaterial Electromagnetic Cloak at Microwave Frequencies," *Science* **314**, 977-980 (2006).
35. B. Edwards, A. Alù, M. G. Silveirinha, and N. Engheta, "Experimental verification of plasmonic cloaking at microwave frequencies with metamaterials," *Phys. Rev. Lett.* **103**, 153901 (2009).
36. L. Zhou and C. T. Chan, "High-impedance reflectivity and surface-wave band gaps in metamaterials," *Appl. Phys. Lett.* **84**, 1444-1446 (2004).
37. F. Yang and Y. Rahmat-Samii, "Reflection phase characterizations of the EBG ground plane for low profile wire antenna applications," *IEEE Antennas Propag.*

Mag. **51**, 2691 -2703 (2003).
38. C. Caloz and T. Itoh, "Metamaterial-based electronically controlled transmission-line structure as a novel leaky-wave antenna with tunable radiation angle and beamwidth," *IEEE Trans. Microwave Theory Tech*. **52**, 2678-2690 (2004).
39. M. A. Antoniades and G. V. Eleftheriades, "A compact and low-profile metamaterial ring antenna with vertical polarization," *IEEE Antennas Wirel. Propag. Lett.* **4**, 333-336 (2005).
40. B.-I. Wu, W. Wang, J. Pacheco, X. Chen, T. M. Grzegorczyk, and J. A. Kong, "a study of using metamaterials as antenna substrate to enhance gain," *Prog. Electromagn. Res.* **51**, 295-328 (2005).
41. N. I. Zheludev, "The Road Ahead for Metamaterials," *Science* **328**, 582-583 (2010).
42. R. Marqués, J. Martel, F. Mesa, and F. Medina, "Left-Handed-Media Simulation and Transmission of EM Waves in Subwavelength Split-Ring-Resonator-Loaded Metallic Waveguides," *Phys. Rev. Lett*. **89**, 183901 (2002).
43. S. Linden, C. Enkrich, M. Wegener, J. Zhou, T. Koschny, and C. M. Soukoulis, "Magnetic Response of Metamaterials at 100 Terahertz," *Science* **306**, 1351-1353 (2004).
44. D. R. Smith, J. B. Pendry, and M. C. K. Wiltshire, "Metamaterials and Negative Refractive Index," *Science* **305**, 788792 (2004).
45. N. Liu, H. Guo, L. Fu, S. Kaiser, H. Schweizer, and H. Giessen, "Three-dimensional photonic metamaterials at optical frequencies," *Nat. Mater*. **7**, 31-37 (2008).
46. R. W. Ziolkowski, "Design, fabrication, and testing of double negative metamaterials," *IEEE Trans. Antennas Propag*. **51**, 1516-1529 (2003).
47. E. Ozbay, K. Aydin, E. Cubukcu, and M. Bayindir, "Transmission and reflection properties of composite double negative metamaterials in free space," *IEEE Trans. Antennas Propag.* **51**, 2529-2595 (2003).
48. R. A. Shore and A.D. Yaghjian, "Travelling electromagnetic waves on linear periodic arrays of lossless spheres," *Electr. Lett*. **41**, 578 (2005).
49. A. Alù and N. Engheta, "Theory of linear chains of metamaterial/plasmonic particles as subdiffraction optical nanotransmission lines," *Phys. Rev. B* **74**, 205436 (2006).
50. J. A. Schuller, R. Zia, T. Taubner, and M. L. Brongersma, "Dielectric Metamaterials Based on Electric and Magnetic Resonances of Silicon Carbide Particles," *Phys. Rev. Lett*. **99**, 107401 (2007).
51. C. L. Holloway, E. F. Kuester, J. Baker-Jarvis, and P. Kabos, "A double negative (DNG) composite medium composed of magnetodielectric spherical particles embedded in a matrix," *IEEE Trans. Antennas Propag*. **51**, 2596-2603 (2003).
52. A. Alù and Nader Engheta, "Achieving transparency with plasmonic and metamaterial coatings," *Phys. Rev. E* **72**, 016623 (2005).
53. C. R. Simovski and S. A. Tretyakov, "Model of isotropic resonant magnetism in the visible range based on core-shell clusters," *Phys. Rev. B* **79**, 045111 (2009).

54. R. Paniagua-Domínguez, F. López-Tejeira, R. Marqués, and J. A. Sánchez-Gil, "Metallo-dielectric core–shell nanospheres as building blocks for optical three-dimensional isotropic negative-index metamaterials," *New J. Phys*. **13**, 123017 (2011).
55. S. F. Mahmoud, "A new miniaturized annular ring patch resonator partially loaded by a metamaterial ring with negative permeability and permittivity," *IEEE Antennas Wirel. Propag. Lett.* **3**, 19-22 (2004).
56. N. Papasimakis, Y. H. Fu, V. A. Fedotov, S. L. Prosvirnin, D. P. Tsai, and N. I. Zheludev, "Metamaterial with polarization and direction insensitive resonant transmission response mimicking electromagnetically induced transparency," *Appl. Phys. Lett.* **94**, 211902 (2009).
57. Z. G. Dong, M.-X. Xu, S.-Y. Lei, Shuang-Ying, H. Liu, T. Li, F.-W. Wang, and S.-N. Zhu, "Negative refraction with magnetic resonance in a metallic double-ring metamaterial," *Appl. Phys. Lett.* **92**, 064101 (2008).
58. Y. Zhao, M.A. Belkin, and A. Alù, "Twisted optical metamaterials for planarized ultrathin broadband circular polarizers," *Nat. Commun.* **3**, 870 (2012).
59. K. Vynck, D. Felbacq, E. Centeno, A. I. Căbuz, D. Cassagne, and B. Guizal, "All-Dielectric Rod-Type Metamaterials at Optical Frequencies," *Phys. Rev. Lett*. **102**, 133901 (2009).
60. P. A. Belov, R. Marqués, S. I. Maslovski, I. S. Nefedov, M. Silveirinha, C. R. Simovski, and S. A. Tretyakov, "Strong spatial dispersion in wire media in the very large wavelength limit," *Phys. Rev. B* **67**, 113103 (2003).
61. A. Fang, T. Koschny, and C. M. Soukoulis, "Optical anisotropic metamaterials: Negative refraction and focusing," *Phys. Rev. B* **79**, 245127 (2009).
62. E. Verhagen, R. de Waele, L. Kuipers, and A. Polman, "Three-Dimensional Negative Index of Refraction at Optical Frequencies by Coupling Plasmonic Waveguides," *Phys. Rev. Lett.* **105**, 223901 (2010).
63. M. Kafesaki, I. Tsiapa, N. Katsarakis, Th. Koschny, C. M. Soukoulis, and E. N. Economou, "Left-handed metamaterials: The fishnet structure and its variations," *Phys. Rev. B* **75**, 235114 (2007).
64. K. B. Alicia and E. Ozbay, "A planar metamaterial: Polarization independent fishnet structure," *Photonics Nanostruct. Fundam. Appl.* **6**, 102-107 (2008).
65. C. García-Meca, R. Ortuño, F. J. Rodríguez-Fortuño, J. Martí, and A. Martínez, "Double-negative polarization-independent fishnet metamaterial in the visible spectrum," *Opt. Lett*. **34**, 1603-1605 (2009).
66. C. Rockstuhl, C. Menzel, T. Paul, T. Pertsch, and F. Lederer, "Light propagation in a fishnet metamaterial," *Phys. Rev. B* **78**, 155102 (2008).
67. M. G. Silveirinha, "Nonlocal homogenization model for a periodic array of ϵ-negative rods," *Phys. Rev. E* **73**, 046612 (2006).
68. C. Menzel, T. Paul, C. Rockstuhl, T. Pertsch, S. Tretyakov, and F. Lederer, "Validity of effective material parameters for optical fishnet metamaterials," *Phys. Rev. B* **81**, 035320 (2010).

69. C. R. Simovski, "On electromagnetic characterization and homogenization of nanostructured metamaterials," *J. Opt*. **13**, 013001 (2011).
70. C. L. Holloway, M. A. Mohamed, E. F. Kuester, and A. Dienstfrey, "Reflection and Transmission Properties of a Metafilm: With an Application to a Controllable Surface Composed of Resonant Particles," *IEEE Trans. Electromag. Compat.* **47**, 853-865 (2005).
71. A. M. Nicolson and G. F. Ross, "Measurement of the intrinsic properties of materials by time-domain techniques," *IEEE Trans. Instrum. Meas.* **IM-19**, 377-382 (1970).
72. W. B. Weir, "Automatic measurement of complex dielectric constant and permeability at microwave frequencies," *Proc. IEEE* **62**, 33-36 (1974).
73. D. R. Smith, D. C. Vier, Th. Koschny, and C. M. Soukoulis, "Electromagnetic parameter retrieval from inhomogeneous metamaterials," *Phys. Rev. E* **71**, 036617 (2005).
74. X. Chen, T. M. Grzegorczyk, B.-I. Wu, J. Pacheco, Jr., and J. A. Kong, "Robust method to retrieve the constitutive effective parameters of metamaterials," *Phys. Rev. E* **70**, 016608 (2004).
75. C. R. Simovski, P. A. Belov, and S. He, "Backward wave region and negative material parameters of a structure formed by lattices of wires and split-ring resonators," *IEEE Trans. Antennas Propag*. **51**, 2582-2591 (2003).
76. P. A. Belov and C. R. Simovski, "Homogenization of electromagnetic crystals formed by uniaxial resonant scatterers," *Phys. Rev. E* **72**, 026615 (2005).
77. D. R. Smith and J. B. Pendry, "Homogenization of metamaterials by field averaging (invited paper)," *JOSA B* **23,** 391-403 (2006).
78. M. G. Silveirinha and C. A. Fernandes, "Homogenization of 3-D-connected and nonconnected wire metamaterials," *IEEE Trans. Microwave Theory Tech*. **53,** 1418-1430 (2005).
79. M. G. Silveirinha, "Metamaterial homogenization approach with application to the characterization of microstructured composites with negative parameters," *Phys. Rev. B* **75**, 115104 (2007).
80. J. D. Baena, L. Jelinek, R. Marqués, and M. Silveirinha, "Unified homogenization theory for magnetoinductive and electromagnetic waves in split-ring metamaterials," *Phys. Rev. A* **78**, 013842 (2008).
81. C. Fietz and G. Shvets, "Current-driven metamaterial homogenization," *Physica B* **405,** 2930-2934 (2010).
82. C. Fietz and G. Shvets, "Homogenization theory for simple metamaterials modeled as one-dimensional arrays of thin polarizable sheets," *Phys. Rev. B* **82**, 205128 (2011).
83. C. Fietz, Y. Urzhumov, and G. Shvets, "Complex k band diagrams of 3D metamaterial/photonic crystals," *Opt. Express* **19**, 19027-19041 (2011).
84. R. A. Shore and A. D. Yaghjian, "Traveling waves on two- and three-dimensional periodic arrays of lossless scatterers," *Radio Sci.* **42**, RS6S21 (2007).

85. R. A. Shore and A. D. Yaghjian, "Traveling Waves on Three-Dimensional Periodic Arrays of Two Different Alternating Magnetodielectric Spheres," *IEEE Trans. Antennas Propag.***57,** 3077-3091 (2009).
86. A. Pors, I. Tsukerman, and S. I. Bozhevolnyi, "Effective constitutive parameters of plasmonic metamaterials: Homogenization by dual field interpolation," *Phys. Rev. E* **84**, 016609 (2011).
87. I. Tsukerman, "Nonlocal homogenization of metamaterials by dual interpolation of field," *JOSA B* **28**, 2956-2965 (2011).
88. O. Ouchetto, C.-W. Qiu, S. Zouhdi, L.-W. Li, and A. Razek, "Homogenization of 3-D Periodic Bianisotropic Metamaterials," *IEEE Trans. Microwave Theory Tech.* **54**, 3893-3898 (2006).
89. J. Jin, S. Liu, Z. Lin, and S. T. Chui, "Effective-medium theory for anisotropic magnetic metamaterials," *Phys. Rev. B* **80**, 115101 (2009).
90. S. Zhou, W. Li, and Q. Li, "Design of 3-D Periodic Metamaterials for Electromagnetic Properties," *IEEE Trans. Microwave Theory Tech.* **58**, 910-916 (2010).
91. M. H. Belyamoun and S. Zouhdi, "On the modeling of effective constitutive parameters of bianisotropic media by a periodic unfolding method in time and frequency domains," *Appl. Phys. A* **103**, 881-887 (2011).
92. V. Boucher and D. Ménard, "Effective magnetic properties of arrays of interacting ferromagnetic wires exhibiting gyromagnetic anisotropy and retardation effects," *Phys. Rev. B* **81**, 174404 (2010).
93. S. B. Raghunathan and N. V. Budko, "Effective permittivity of finite inhomogeneous objects," *Phys. Rev. B* **81**, 054206 (2010).
94. A. Alù, "First-principles homogenization theory for periodic metamaterials," *Phys. Rev. B* **84**, 075153 (2011).

Chapter 2 Characterization of Metamaterial Inclusions

2.1 INTRODUCTION

Metamaterials are built by arrays of subwavelength inclusions engineered to support specific polarization properties. In order to achieve interesting phenomena, complicated inclusions, such as split-ring resonators (SRRs) [1-3], omega-shaped wires [4, 5] and helix wires [6], are usually considered, designed and fabricated as elements in metamaterial arrays, to support the required magneto-electric coupling effects at the inclusion and lattice levels. In the designer's point of view, a comprehensive understanding of the scattering properties of the complex inclusions is crucial to realize metamaterials with desired effective bulk material parameters. A classical and widely used approach to compactly describe the scattering of a given subwavelength inclusion is to model it as a point scatterer with induced dipole moments. Generally, the dipole moment supported by a simple scatterer is expressed as $\mathbf{p} = \alpha^{ee}\mathbf{E}_{loc}$, proportional to the local electric field $\mathbf{E}_{loc}$ at its phase center. The factor α^{ee}, or the electric polarizability, plays a crucial role to describe the polarization under external excitation. This model has been widely used to express the induced dipole moment of isotropic and electrically small scatterers in the quasi-static regime. In some circumstances, we also have to take into account the magnetic dipole moment $\mathbf{m} = \alpha^{mm}\mathbf{H}_{loc}$ to consider the magnetic polarization. Usually, for simple scatterers with some forms of symmetry with respect to the excitation, we can consider polarizabilities α^{ee} and α^{mm} in a scalar form.

This concept may be also extended to analyze the scattering of the complex inclusions typically used in metamaterials [3,7]. In this situation, and in the most general case, the polarizability coefficients have a tensorial form that allows to completely take into account the bianisotropic features of a complex subwavelength inclusion [7, 9-10]. These features are produced by the strong induced electric and magnetic effects in

complex-shaped structures, with current patterns that are directly influenced by the propagation direction and polarization of the impinging wave. It is in general a challenging task to accurately quantify all the entries of the polarizability tensor for arbitrary subwavelength inclusions.

In order to rigorously quantify them, measurements have been performed to observe the extinction cross sections of a single SRR and arrays of them for different incident polarizations [11, 14]. By probing the scattering quantities in the far-field, one can directly measure the bianisotropic effects or chirality generated by the building blocks. Regarding the issue of quantifying the dipolar response of complex inclusions, two approaches have been considered to determine the polarizabilities in previous relevant works. The first approach [3, 15-22] models the inclusions as effective circuit elements composed of inductive (L) and capacitive (C) lumped elements stemming from the flowing of conducting or displacement currents in and around the structures. For example, by using this model SRR inclusions can be effectively treated as parallel L-C circuit, when the applied electric and magnetic fields lay along the gap and normal to the ring, respectively [20, 22]. Generally, a correct layout of the equivalent circuit depends on the specific incident wave and polarization direction, because the metamaterial inclusions are usually strongly anisotropic. Moreover, determining the values of L and C can be very tricky. One should estimate the currents flowing around the structure [18, 19] or calculate the L and C components inspecting the resonance frequency and Q factor of an isolated inclusion [3]. Importantly, these approaches are theoretically valid only in the deeply subwavelength or quasi-static condition, because circuit theory based on lumped elements assumes no retardation effects.

The second approach uses electro- or magneto-static polarizabilities [16] as the basis and considers energy conservation to determine the effects of radiation damping

and retardation to correctly determine the dynamic polarizabilities [16, 23-28]. This approach is convenient but may be incorrect for some metamaterial inclusions, because the exotic wave phenomena usually happen at the border of the quasi-static limits. As a consequence, it may fail to predict the correct *dynamic* response of the inclusions, especially when the geometry is complicated and structures are made of dense dielectric or plasmonic materials. Moreover, the task of quantifying the static polarizabilities for arbitrary subwavelength elements is quite challenging, especially when anisotropic effects are to be considered.

Recently, some works based on retrieving the polarizability of inclusion arrays or rectangular waveguides filled with inclusions have been reported [9, 30, 31]. These methods use the known coupling effects in periodic structures or in waveguides to calculate the electromagnetic field coupling or dipole interaction at the inclusion level. In Ref. 9, the authors define a measurement procedure to evaluate the polarizabilities of artificial Tellegen particles based on the analytical derivation of the fundamental TE mode in a WR-90 waveguide. This method is however limited to simple inclusions, and was not extended to artificial complex inclusions with bianisotropic effects. Ref. 30 and 31 suggest a physically equivalent method to determine the polarizabilities of subwavelength inclusions based on 2-D arrays and PEC/PMC rectangular waveguides, respectively. Ref. 30 analytically considers the coupling coefficients to describe the interactions between electric and magnetic dipoles on the array. Ref. 31 takes into account the dipole scattering and coupling inside the waveguide and relates these field interactions to the scattering matrix. Both of them, however, still only deal with simple inclusions, and do not address the issue of anisotropic or bianisotropic effects in a general inclusion.

In this chapter, we propose and derive a general approach to extract the *complete* electrodynamic polarizability tensor for arbitrary subwavelength inclusions. We aim at precisely quantifying all the entries of the polarizability tensor, including anisotropic and bianisotropic terms, and validate the results by full-wave simulations. Instead of employing the parameters of the isolated element in the quasi-static regime, we take into account the full electrodynamic coupling within the inclusion and the array.

In our method, we use a similar approach as in [30, 31], placing the complex inclusion under analysis in a 2D array and considering the effects of magneto-electric dipole scattering in the periodic configuration to inversely retrieve the induced dipoles and polarizations on each element. This method requires a simple numerical solver to calculate the reflection and transmission coefficients from the planar array and we do not need to compute the detailed field distributions or current patterns on the inclusion, as in other procedures. Effectively, the computational cost is considerably less than the conventional numerical methods. Moreover, the accuracy of the results can be nicely preserved, even in the case of slightly larger inclusions, for which the dynamic effects are more important, as we discuss in the next sections.

In order to validate our proposed retrieval method, we present five examples of simple and complex inclusions, including spheres, spheroids, helices, conducting and plasmonic SRRs. In each example, we discuss the calculated tensors and the inherent physical properties of the geometry to validate the obtained polarizabilities. We demonstrate that this general approach provides the complete dyadic polarizability for subwavelength complex inclusions and these dyadic quantities accurately obey physical principles such as passivity, reciprocity and Onsager relations for dynamic dipole interaction.

2.2 ANALYTICAL FORMULATION

To determine the polarizability of subwavelength inclusions with arbitrary shape, we assume that their scattering response can be expressed by effective dipole moments. Generally, this assumption is well-accepted when $k_0 a < 1$, where k_0 is the background wavenumber of the impinging wave and a is the feature size of the inclusion. Here, we analytically ignore the higher-order scattering of inclusions, because their effects are usually much less important than dipole terms. Under this assumption, the electric and magnetic dipole moments of the subwavelength inclusion in free space can be related to the local fields at the phase center by

$$\begin{Bmatrix} \mathbf{p} \\ \mathbf{m} \end{Bmatrix} = \boldsymbol{\alpha} \begin{Bmatrix} \mathbf{E}^{loc} \\ \mathbf{H}^{loc} \end{Bmatrix} = \begin{bmatrix} \boldsymbol{\alpha}^{ee} & \boldsymbol{\alpha}^{em} \\ \boldsymbol{\alpha}^{me} & \boldsymbol{\alpha}^{mm} \end{bmatrix} \begin{Bmatrix} \mathbf{E}^{loc} \\ \mathbf{H}^{loc} \end{Bmatrix}, \tag{2.1}$$

in which the sub-tensors $\boldsymbol{\alpha}^{ee}$ and $\boldsymbol{\alpha}^{mm}$ (three-by-three matrices) govern the co-polarization of the inclusion and the off-diagonal terms $\boldsymbol{\alpha}^{me}$ and $\boldsymbol{\alpha}^{me}$ (three-by-three matrices) are responsible for magneto-electric cross-coupling effects of the polarized inclusions. To completely describe the effective dipole moments of an arbitrary subwavelength inclusion, we need an integrated six-by-six polarizability tensor $\boldsymbol{\alpha}$. In case of certain symmetries, this tensor may be simplified. For example, for a subwavelength homogeneous conducting sphere, the induced electric and magnetic dipole moments can be simply described by scalar α^{ee} and α^{mm}, and the cross-coupling terms α^{em} and α^{me} vanish.

In general it is challenging to determine the full tensor $\boldsymbol{\alpha}$ for complex scatterers in far-field measurements or simulations, because the radiated electromagnetic fields carry information on both co- and cross-coupling effects. As a consequence, it is not possible to probe and decompose these results and quantify all entries of the sub-tensors

in Eq. (2.1) with a single measurement. To overcome this challenge, we consider a 2-D array of identical subwavelength structures with period d satisfying the criterion $k_0 d < 1$. In this configuration, the reflection and transmission coefficients are the superposition of the incident fields and the scattered fields generated in the array, and we can capture how the induced current is distributed on the array plane by properly exciting the structure and monitoring the scattered fields.

In Fig. 2.1a, we schematically show the configuration of a 2-D array of complex subwavelength elements used in our proposed polarizability retrieval procedure. In this example, we use SRRs to illustrate the configuration, because this structure is one of the most popular inclusion geometry and supports strong magneto-electric coupling effects. In the examples presented in the following sections, we show that any subwavelength nonconnected inclusions can be considered in this configuration to extract the full polarizability tensor, after multiple measurements with proper rotations of the inclusions in the array.

We assume an excitation by plane wave with propagation direction normal to the array plane (*xy*-plane) and with polarization lying along the array axes. This arrangement can be also effectively seen as a squared waveguide with unit cell periodic boundaries (PBC1 and PBC2 in Fig. 2.1a) operated with its first TEM mode [31]. The pairs of periodic boundaries dominate the polarization direction excited in the array. For instance, the schematic plot in Fig. 2.1a illustrates that the waveguide is operated with a *y*-polarized plane wave.

It is important to notice that in Fig. 2.1a–d we define two different coordinate systems, i.e., the global waveguide coordinate (*xyz*-system) and the local inclusion coordinate (*XYZ*-system). These two systems are required to identify the coordinates of the impinging plane wave and the preferred reference axes of the inclusions. It is obvious

that the definition of local coordinates on the inclusion may directly affect the resulting polarizability tensor. Generally, we prefer to align the coordinates with the symmetry axes of the inclusions in order to effectively reduce the complexity of the polarizability tensor.

In this array-based configuration operating with the fundamental TEM mode, we can easily see that the induced dipole moment perpendicular to the array plane does not contribute to the reflection (S_{11} or S_{22}) and transmission (S_{21} or S_{12}) spectra measured at the ends of the waveguide. For example, in the configuration shown in Fig. 2.1a, the Z- and z-directions are parallel, and therefore we do not consider the entries in the polarizability tensor containing the Z-element. Based on the schematic plot in Fig. 2.1a and 2.1b, we can simplify Eq. (2.1) as

$$\begin{Bmatrix} p_X \\ p_Y \\ m_X \\ m_Y \end{Bmatrix} = \begin{bmatrix} \alpha_{XX}^{ee} & \alpha_{XY}^{ee} & \alpha_{XX}^{em} & \alpha_{XY}^{em} \\ \alpha_{YX}^{ee} & \alpha_{YY}^{ee} & \alpha_{YX}^{em} & \alpha_{YY}^{em} \\ \alpha_{XX}^{me} & \alpha_{XY}^{me} & \alpha_{XX}^{mm} & \alpha_{XY}^{mm} \\ \alpha_{YX}^{me} & \alpha_{YY}^{me} & \alpha_{YX}^{mm} & \alpha_{YY}^{mm} \end{bmatrix} \begin{Bmatrix} E_x^{loc} \\ E_y^{loc} \\ H_x^{loc} \\ H_y^{loc} \end{Bmatrix}, \tag{2.2}$$

where we ignore the dipole moments and cross-coupling in the *z*-direction, or the longitudinal direction of the waveguide. As expected, for this configuration we are not able to obtain the polarizability information of the inclusion along the Z-axis. However, we may rotate the inclusions in the array (see Fig. 2.1b-d) and perform additional measurements to find all the polarizability components and integrate them as a complete six-by-six tensor.

To determine the polarizability components, we need to introduce more relations between the plane wave incident fields and the induced dipole moments. Since we are treating the inclusions as effective dipole moments, we can easily define how these

induced dipole moments contribute to the incoming and outgoing waves at the waveguide ports, based on the relation

$$\begin{Bmatrix} E_{1x}^{-} \\ E_{1y}^{-} \\ E_{2x}^{-} \\ E_{2y}^{-} \end{Bmatrix} = \begin{bmatrix} 0 & 0 & 1 & 0 \\ 0 & 0 & 0 & 1 \\ 1 & 0 & 0 & 0 \\ 0 & 1 & 0 & 0 \end{bmatrix} \begin{Bmatrix} E_{1x}^{+} \\ E_{1y}^{+} \\ E_{2x}^{+} \\ E_{2y}^{+} \end{Bmatrix} + \begin{bmatrix} K_{xx}^{p} & 0 & 0 & -K_{xy}^{m} \\ 0 & K_{yy}^{p} & -K_{yx}^{m} & 0 \\ K_{xx}^{p} & 0 & 0 & K_{xy}^{m} \\ 0 & K_{yy}^{p} & K_{yx}^{m} & 0 \end{bmatrix} \begin{Bmatrix} p_x \\ p_y \\ m_x \\ m_y \end{Bmatrix}. \tag{2.3}$$

Here, we have introduced the matrix $\mathbf{K}$ (the second term in the right-hand side of this equation), composed of radiation coefficients K^p and K^m, which are responsible for the fields on the ports produced by the induced dipolar radiation from the inclusion (see Fig. 2.1e). Importantly, we are using the waveguide coordinates in this equation, because we are discussing how the effective dipoles influence wave transmission in the waveguide. It is interesting to notice that there are a few zero terms in the radiation tensor. This is due the nature of orthogonal dipole radiations. For instance, an electric dipole moment p_x does not contribute to the *y*-component of the electric fields at the ports. Similarly, m_x does not depend on the *x*-component of the electric fields.

On the other hand, from the planar array point of view (see Fig. 2.1f), we can relate the incident fields and dipole coupling to the local fields at the phase center of the inclusion, yielding

$$\begin{Bmatrix} E_x^{loc} \\ E_y^{loc} \\ H_x^{loc} \\ H_y^{loc} \end{Bmatrix} = \begin{bmatrix} 1 & 0 & 1 & 0 \\ 0 & 1 & 0 & 1 \\ 0 & -Y_0 & 0 & Y_0 \\ -Y_0 & 0 & Y_0 & 0 \end{bmatrix} \begin{Bmatrix} E_{1x}^{+} \\ E_{1y}^{+} \\ E_{2x}^{+} \\ E_{2y}^{+} \end{Bmatrix} + \begin{bmatrix} C_{xx}^{ee} & C_{xy}^{ee} & 0 & 0 \\ C_{yx}^{ee} & C_{yy}^{ee} & 0 & 0 \\ 0 & 0 & C_{xx}^{mm} & C_{xy}^{mm} \\ 0 & 0 & C_{yx}^{mm} & C_{yy}^{mm} \end{bmatrix} \begin{Bmatrix} p_x \\ p_y \\ m_x \\ m_y \end{Bmatrix}. \tag{2.4}$$

In the above equation, the parameter Y_0 is the background admittance, and the two groups of coupling coefficients C^{ee} and C^{mm} in the coupling matrix $\mathbf{C}$ govern

the electric and magnetic coupling produced by all the neighboring unit cells. These coupling coefficients are physically equivalent to the dyadic Green's functions for a 2-D dipole array [32]. Again, we are using the waveguide coordinates in this relation because we are focusing on the behavior of ideal dipole moments in the array regardless of how the effective dipoles are generated from the inclusions. In this equation, we show that the magnetic dipole moments m_x and m_y are independent of the local electric fields, and vice versa for p_x and p_y for magnetic fields. This can be easily verified by looking into the radiation patterns of electric and magnetic dipoles. The in-plane components of the local electric field are only affected by the in-plane electric dipole moments and out-of-plane magnetic dipole, and dual considerations apply for the in-plane local magnetic fields. Since we are not considering the out-of-plane dipoles in the 2-D array excited by normal plane wave incidence or the longitudinal dipoles in the waveguide operating in the fundamental TEM, we can ignore their contributions in this configuration.

Moreover, we have another fundamental relationship provided by the scattering matrix, relating the fields of the incoming and outgoing ports for any waveguide, which is written as

$$\begin{Bmatrix} E_{1x}^{-} \\ E_{1y}^{-} \\ E_{2x}^{-} \\ E_{2y}^{-} \end{Bmatrix} = \begin{bmatrix} S_{11}^{xx} & S_{11}^{xy} & S_{12}^{xx} & S_{12}^{xy} \\ S_{11}^{yx} & S_{11}^{yy} & S_{12}^{yx} & S_{12}^{yy} \\ S_{21}^{xx} & S_{21}^{xy} & S_{22}^{xx} & S_{22}^{xy} \\ S_{21}^{yx} & S_{21}^{yy} & S_{22}^{yx} & S_{22}^{yy} \end{bmatrix} \begin{Bmatrix} E_{1x}^{+} \\ E_{1y}^{+} \\ E_{2x}^{+} \\ E_{2y}^{+} \end{Bmatrix}, \tag{2.5}$$

where we generally consider the relation between the two in-plane components in the waveguide and take into account their cross-coupling effects. These S-parameters are influenced by the scattering and coupling fields on the inclusions and in the array, and one may easily monitor the change of variation in the induced dipole moments by measuring these parameters.

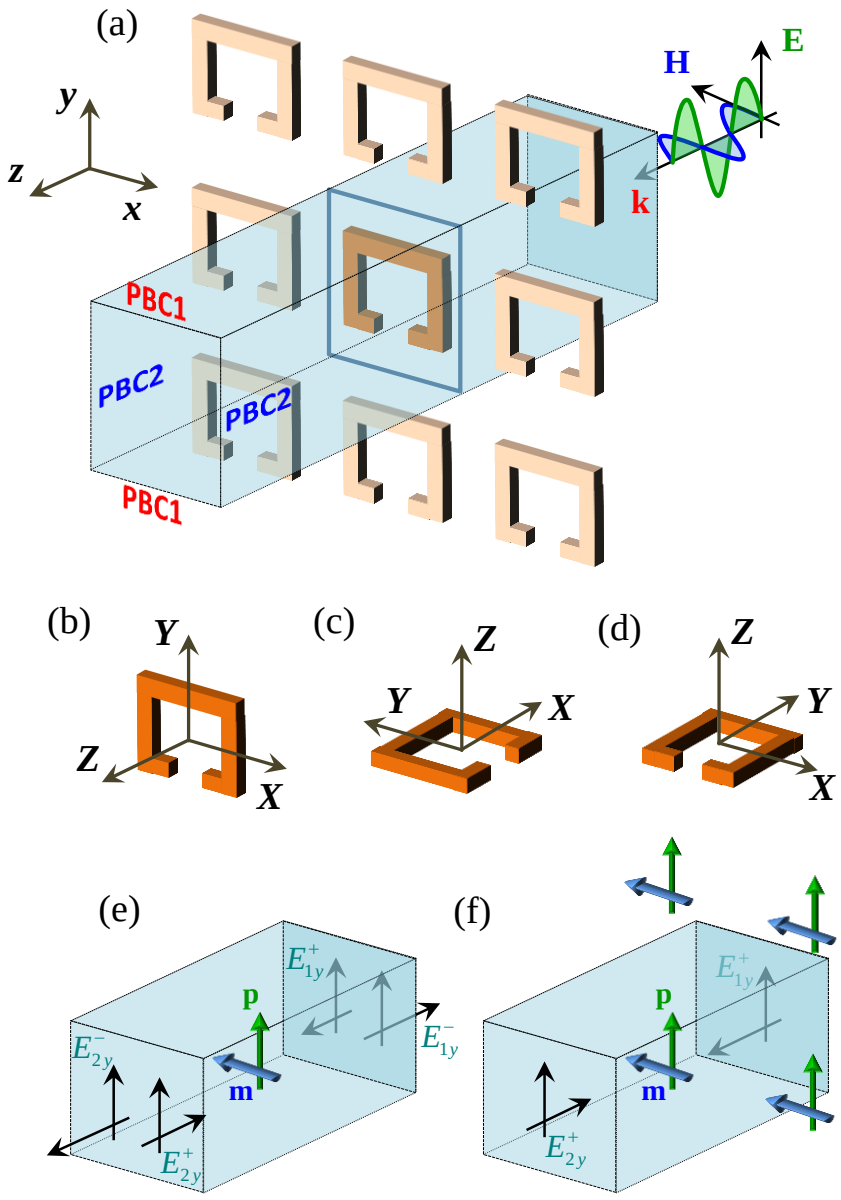

Figure 2.1 (a) The 2-D array configuration and the effective waveguide considered in the proposed polarizability retrieval method. (b)-(d) The local coordinate system defined on a complex inclusion. (e) Schematic plot for Eq. (2.3), to illustrate the relation between port fields and induced dipole moments. (f) Schematic plot for Eq. (2.4), to illustrate the relation between port fields and dipolar coupling within the array.

By considering the configuration in which the array and inclusion coordinates are consistent (see Fig. 2.1a and b) and combining Eqs. (2.2)-(2.5), we can obtain the equation

$$\begin{bmatrix} \alpha_{XX}^{ee} & \alpha_{XY}^{ee} & \alpha_{XX}^{em} & \alpha_{XY}^{em} \\ \alpha_{YX}^{ee} & \alpha_{YY}^{ee} & \alpha_{YX}^{em} & \alpha_{YY}^{em} \\ \alpha_{XX}^{me} & \alpha_{XY}^{me} & \alpha_{XX}^{mm} & \alpha_{XY}^{mm} \\ \alpha_{YX}^{me} & \alpha_{YY}^{me} & \alpha_{YX}^{mm} & \alpha_{YY}^{mm} \end{bmatrix}^{-1} = \begin{bmatrix} C_{xx}^{ee} & C_{xy}^{ee} & 0 & 0 \\ C_{yx}^{ee} & C_{yy}^{ee} & 0 & 0 \\ 0 & 0 & C_{xx}^{mm} & C_{xy}^{mm} \\ 0 & 0 & C_{yx}^{mm} & C_{yy}^{mm} \end{bmatrix}$$

$$+ \begin{bmatrix} 1 & 0 & 1 & 0 \\ 0 & 1 & 0 & 1 \\ 0 & Y_0 & 0 & -Y_0 \\ Y_0 & 0 & -Y_0 & 0 \end{bmatrix} \left\{ \begin{bmatrix} S_{11}^{xx} & S_{11}^{xy} & S_{12}^{xx} & S_{12}^{xy} \\ S_{11}^{yx} & S_{11}^{yy} & S_{12}^{yx} & S_{12}^{yy} \\ S_{21}^{xx} & S_{21}^{xy} & S_{22}^{xx} & S_{22}^{xy} \\ S_{21}^{yx} & S_{21}^{yy} & S_{22}^{yx} & S_{22}^{yy} \end{bmatrix} - \begin{bmatrix} 0 & 0 & 1 & 0 \\ 0 & 0 & 0 & 1 \\ 1 & 0 & 0 & 0 \\ 0 & 1 & 0 & 0 \end{bmatrix} \right\}^{-1} \begin{bmatrix} K_{xx}^{p} & 0 & 0 & -K_{xy}^{m} \\ 0 & K_{yy}^{p} & -K_{yx}^{m} & 0 \\ K_{xx}^{p} & 0 & 0 & K_{xy}^{m} \\ 0 & K_{yy}^{p} & K_{yx}^{m} & 0 \end{bmatrix}. \quad (2.6)$$

These equations contain 48 unknowns, including all the polarizability components and coefficients. Among these variables, the most interesting terms to us are the entries in the polarizability tensor. Ideally, only these quantities depend on the inclusions, and the other coupling coefficients are dominated by the waveguide configurations and excitation. In order to obtain these parameters, we have to collect enough equations to solve for the unknowns.

If we consider a fixed 2-D array (or a waveguide with periodic boundaries), we can see that the coefficients C^{ee}, C^{mm}, K^{p} and K^{m} are all fixed since they depend on the array (or waveguide) geometry. Therefore, we can retrieve these coefficients by calibrating our measurement with inclusions with known polarizabilities. For example, we can use dielectric and perfect electric conducting (PEC) spheres embedded in the same array configuration, and independently measure or calculate the scattering matrix to solve for all the coefficients in $\mathbf{K}$ and $\mathbf{C}$. Based on the coupling coefficients of the

waveguide system tested with these simple samples, we can place an arbitrary subwavelength inclusion inside the waveguide to determine its polarizability tensor.

In this work, we use two PEC spheres with different sizes to calibrate the radiation and coupling coefficients in Eq. (2.6) for the waveguide, and we use the fundamental mode of the ports to excite TEM waves. We take advantage of CST Microwave Studio to compute the complete scattering matrix in Eq. (2.5). We consider a square waveguide with 25mm in width and 120mm in length and place PEC spheres with 10 mm and 8 mm in radius to compute the corresponding scattering matrices (four-by-four) with a frequency-domain solver. Based on Mie theory, we are able to write the diagonal terms of the polarizability tensor for the conducting spheres, as

$$\alpha^{ee} = \frac{6\pi i \varepsilon_0}{k_0^3} c_1^{TM} \tag{2.7}$$

$$\alpha^{mm} = \frac{6\pi i \mu_0}{k_0^3} c_1^{TE} \tag{2.8}$$

where c_1^{TM} and c_1^{TE} are the first-order Mie coefficients [33]. Because of symmetric geometry and material, we may choose $\alpha^{em} = \alpha^{me} = 0$. Here, we are interested in the frequency band from 0.1 to 3 GHz, or equivalently $k_0 d = 0.052$ to $k_0 d = 1.571$, which covers the subwavelength regime of interest in most metamaterial applications.

In Figure 2.2, we show the relevant coefficients of $\mathbf{K}$ and $\mathbf{C}$ obtained from this calibration procedure based on PEC spheres. All the coefficient curves have the same decaying trend versus $k_0 d$, but in different scales. As expected, we have the relations $\left|K_{xx}^{p}\right| = \left|K_{yy}^{p}\right|$, $\left|K_{xx}^{m}\right| = \left|K_{yy}^{m}\right|$, $\left|C_{xx}^{EE}\right| = \left|C_{yy}^{EE}\right|$ and $\left|C_{xx}^{MM}\right| = \left|C_{yy}^{MM}\right|$, due to duality between electric and magnetic fields. It is important to notice that the accuracy of these coupling coefficients can be largely affected by the numerical accuracy of the computed scattering matrices. Therefore, scattering parameters with very small values should be avoided, in

order to get rid of potentially significant numerical noise from the solver. In this way, inclusions that provide moderately large values of scattering coefficients should be considered. We have found that PEC or dense dielectric and magnetic materials may be good candidates for this purpose, because they are able to largely interact with the incident wave, with both electric and magnetic effects. PEC is particularly useful in this context, for its wideband response and the limited computational costs.

2.3 RETRIEVAL OF POLARIZABILITY TENSORS

In this section, we apply the proposed retrieval method to determine polarizability tensors of various sample inclusions, including magnetodielectric spheres, magnetodielectric spheroids, PEC helices, PEC SRRs and Silver U-shape SRRs, as illustrated in Fig. 2.3. In order to validate the retrieved polarizabilities, we use the Mie coefficients and the free space point-dipole radiation to compare the results of sphere and spheroid scatterers. Since the scatterers considered here are moderately smaller than the wavelength, it is sufficient to take into account only the first-order Mie coefficients to describe the scattered fields. In addition, we also employ a straightforward method based on point-dipole radiation in free space to extract the polarizabilities of inclusions with simple geometry. We organize the basic formulation and details of this method in Appendix A, and explain its limitations for calculating polarizabilities of arbitrary inclusions. For complex inclusions, we use some fundamental physical principles, such as passivity, coordinate symmetry and Onsager relations, to validate the calculated polarizability tensors.

In the following examples, we use the identical waveguide system and coupling coefficients determined from the calibration setup in the previous section (Fig. 2.2). Although these examples are performed in the microwave regime, one can apply these

principles to terahertz or optical frequencies. To this end, we apply proper normalizations to all the presented polarizability values, in order to make them independent of the frequency. The normalization factors for the entries in $\boldsymbol{\alpha}^{ee}$, $\boldsymbol{\alpha}^{mm}$, $\boldsymbol{\alpha}^{em}$ and $\boldsymbol{\alpha}^{me}$ are $ik_0^3/6\pi\varepsilon_0$, $ik_0^3/6\pi\mu_0$, η_0^{-1} and η_0, respectively.

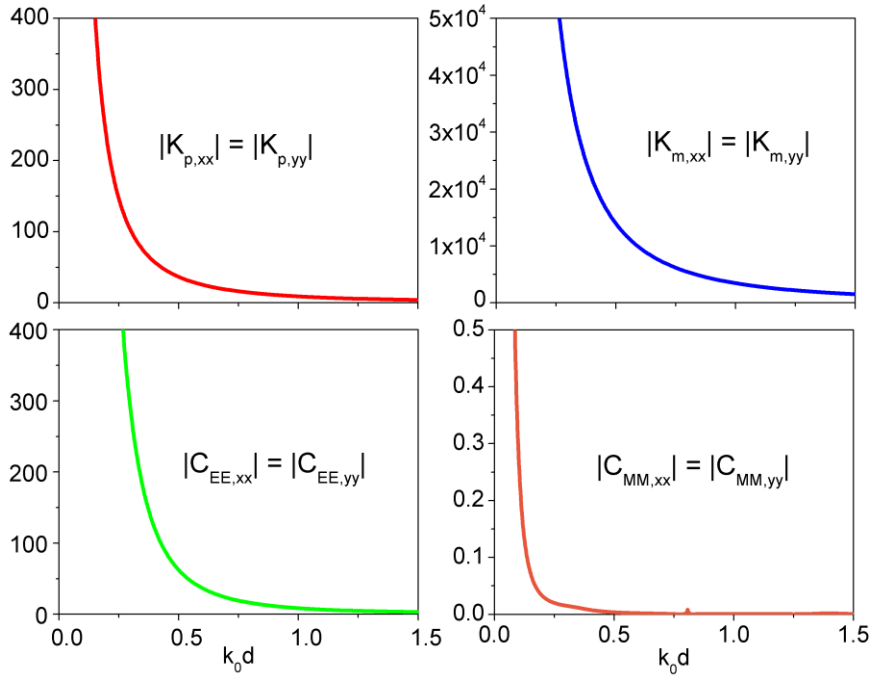

Figure 2.2 Amplitudes of the coefficients of $\mathbf{K}$ and $\mathbf{C}$ obtained in the calibration procedure based on PEC spheres.

2.3.1 Magnetodielectric sphere

As a first case, we consider the simple scenario of a sphere composed of homogeneous magnetodielectric materials with $\varepsilon_r = 13.8$ and $\mu_r = 11.0$, and with 10 mm in radius. This is a good test case, since we know the polarizability in closed analytical form. Due to symmetry considerations, we can consider α^{ee} and α^{mm} in scalar forms and also let $\alpha^{em} = \alpha^{me} = 0$. Figure 2.4 shows the magnitude and phase of the normalized electric and magnetic polarizabilities obtained from our retrieval method (indicated with Ret in the

legend), the exact first-order Mie coefficients (Mie) according to Eqs. (2.7) and (2.8), and the polarizability extracted by comparing the scattering from an isolated inclusion with the free-space dipole radiations (FS, see Appendix A for a detailed formulation of this third approach). It is evident that all the results nicely match, especially when the frequency satisfies $k_0 d < 1$. These results prove that our proposed retrieval method, with coupling coefficients calibrated by the PEC inclusions, may precisely return the polarizabilities for general magnetodielectric spheres. It is also worth noticing that the system correctly predicts the resonant nature of the magnetodielectric sphere around $k_0 d = 0.83$ even when the PEC spheres used in the calibration do not experience resonant phenomena in the frequency range of interest. This implies that this retrieval method can capture and is robust to resonances of the inclusions, regardless the objects we used for calibration procedures.

In addition, we find that the retrieved results correctly obey the expected passivity relationships for lossless subwavelength scatterers. At resonance, the normalized peak magnitudes exactly hit 1 because the scatterer is experiencing strongest scattering and all the energy losses are attributed to dipolar radiation. On the other hand, it can be seen that the phase experiences rapid jumps from 0 to $-\pi$ around the peak frequencies, which are also typical features of a dipole resonance. For frequency $k_0 d > 1$, we obtain some extra sharp peaks around $k_0 d = 1.1$ and $k_0 d = 1.35$, which are not predicted by the first-order Mie coefficients. These minor discrepancies are associated with higher-order resonant harmonics that affect the scattering among the array. These additional features are actually quite useful as we consider the arrays of metamaterials. In this example, our model can capture the correct polarizabilities up to $k_0 d = 1.5$, which corresponds to the range of interest for metamaterial inclusions.

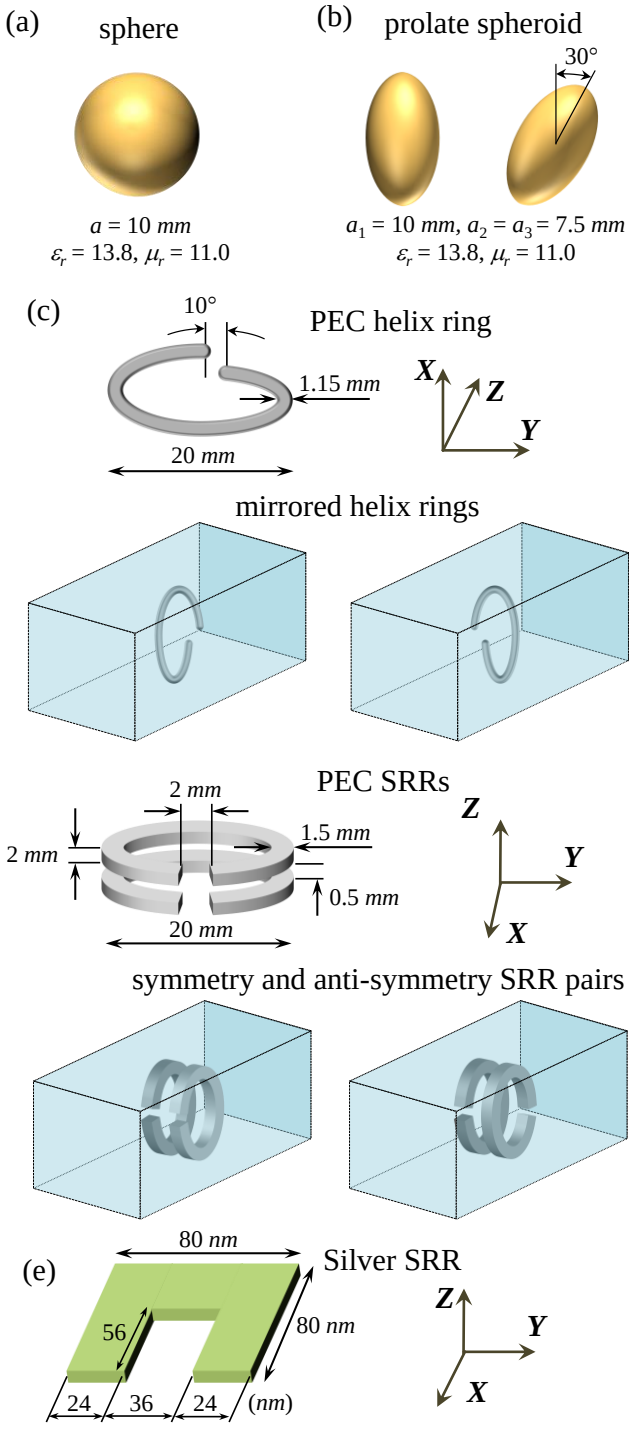

Figure 2.3 Considered inclusions and their local coordinate system used in the polarizability retrieval

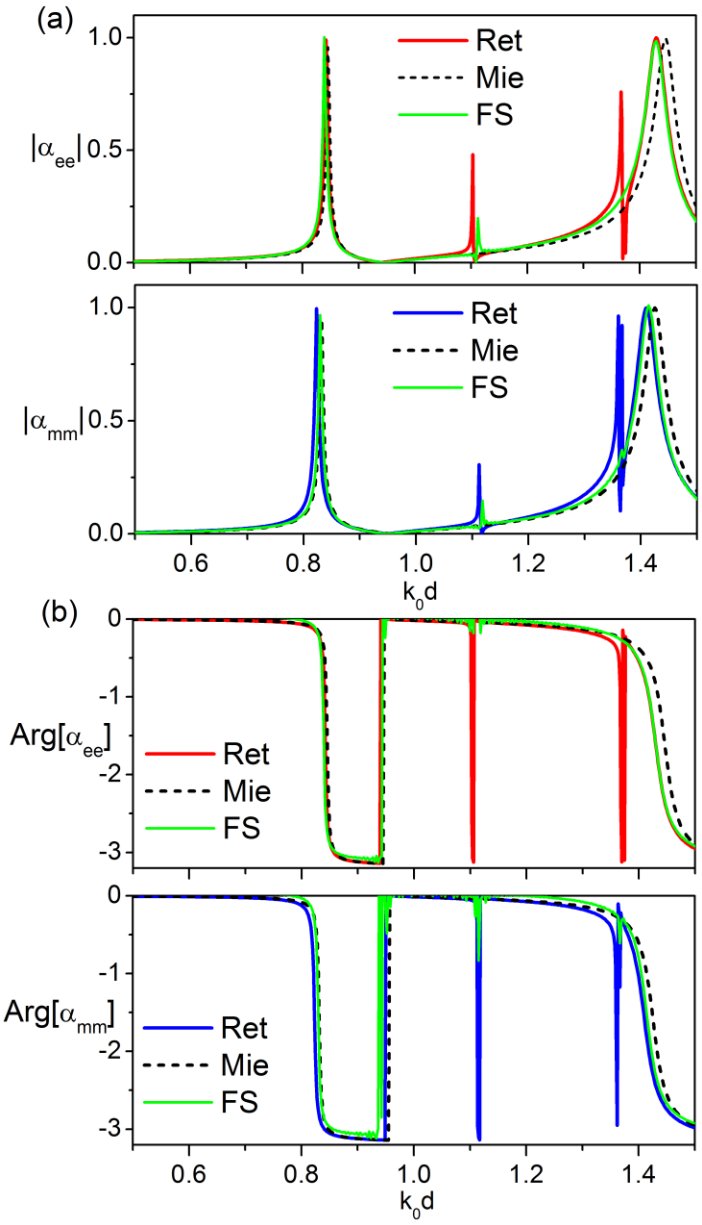

Figure 2.4 Magnitude and phase of the normalized electric and magnetic polarizabilities of a magnetodielectric sphere with parameters shown in Fig. 2.3a. We present three sets of results, obtained from our retrieval method (Ret), Mie scattering coefficients (Mie) and from the free-space dipole radiation (FS), respectively.

2.3.2 Magnetodielectric spheroids

After having tested our method for the case of an isotropic magnetodielectric sphere, we apply it to determine the polarizabilities of an anisotropic inclusion. Here, we consider a magnetodielectric prolate spheroid with the same material parameters as in the previous case and with major radius $a_1 = 10mm$ and minor radii $a_2 = a_3 = 7.5mm$, as shown in Fig. 2.3b. Due to anisotropy, the calculated electric and magnetic polarizabilities depend on the excitation, and we still consider $\boldsymbol{\alpha}^{em} = \boldsymbol{\alpha}^{me} = \mathbf{0}$ due to symmetries.

In this example, we apply the polarizability retrieval method twice, to the normal and to tilted arrangement of this inclusion (see Fig. 2.3b). We consider in both cases the same waveguide and coupling coefficients used in the previous case. Generally, the induced dipole moments of an anisotropic inclusion depend on the configurations of impinging waves and arrangement of the inclusion. However, the polarizability, or the capability of being polarized, is an intrinsic property of a given object, and the results on an identical inclusion obtained from two different excitation configurations should be consistent after proper coordinate transformation. For instance, by knowing the polarizabilities of a spheroid along the major and minor axes, we should be able to predict the polarizability tensor when the same object is oriented in an arbitrary direction with respect to the impinging field. In other words, by properly transforming the polarizability tensor of the vertical spheroid, we should be able to match the results obtained in the tilted case.

In the first part of this example, we compare the retrieved electric and magnetic polarizabilities of a vertical spheroid to the results obtained from the free-space point-dipole radiation formulation introduced in Appendix A and the previous section. Figure 2.5 shows the polarizabilities along the major and minor axes calculated with these two different methods. The results nicely match each other, and they clearly show that

different axis lengths support resonances at different frequencies. Generally, the longer axis gives a lower resonance frequency than the shorter one, as expected.

After obtaining the polarizabilities along the major and minor axes, we are able to transform these results to the tilted case. The coordinate transformation are written as

$$\begin{aligned}
\alpha_{xx}^{ee} &= \tilde{\alpha}_{xx}^{ee}\cos^2\theta + \tilde{\alpha}_{yy}^{ee}\sin^2\theta, \\
\alpha_{yy}^{ee} &= \tilde{\alpha}_{xx}^{ee}\sin^2\theta + \tilde{\alpha}_{yy}^{ee}\cos^2\theta, \\
\alpha_{xy}^{ee} &= \tilde{\alpha}_{xx}^{ee}\cos^2\theta + \tilde{\alpha}_{yy}^{ee}\sin^2\theta, \\
\alpha_{yx}^{ee} &= \tilde{\alpha}_{xx}^{ee}\sin^2\theta + \tilde{\alpha}_{yy}^{ee}\cos^2\theta,
\end{aligned} \tag{2.9}$$

in which θ is the tilted angle and the polarizability terms in left- and right-hand sides represent the tilted and normal cases, respectively. One can use similar relations to determine the magnetic terms.

Figure 2.6 shows the polarizability results of the tilted magnetodielectric spheroid directly obtained from the retrieval procedures (solid lines) and indirectly transformed from the normal cases (dots).These direct and indirect results match nicely to each other and that implies the proposed retrieval method can accurately capture the co-coupling effects of polarizability on the inclusion.

The amplitudes of the peaks in the tilted case do not reach unity because the energy is radiated in both diagonal and off-diagonal terms. It is worth noticing that the amplitudes of the two off-diagonal terms in the tilted case are exactly the same, due to reciprocity. We can observe that the results start to show some deviations as $k_0 d > 1.4$, and the off-diagonal terms show more obvious differences than the diagonal ones. Compared to the case of an isotropic sphere, the spheroid appears more sensitive to larger $k_0 d$.

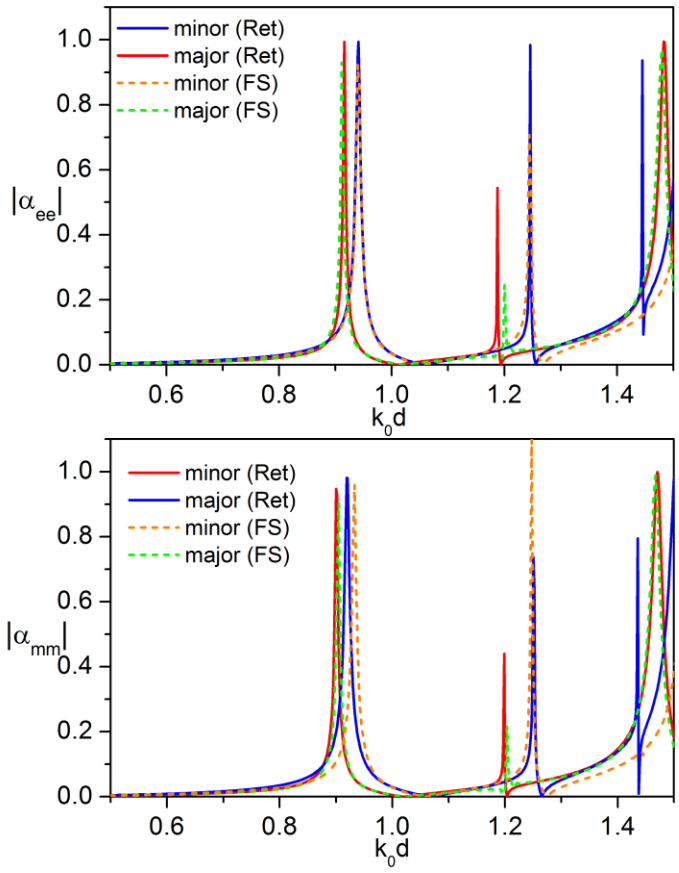

Figure 2.5 Normalized electric and magnetic polarizabilities of the vertical magnetodielectric spheroid obtained using the proposed polarizability retrieval method (Ret) and the free-space radiation method (FS). The major and minor labels in the legend denote the polarizabilities with respect to the major and minor axes, respectively.

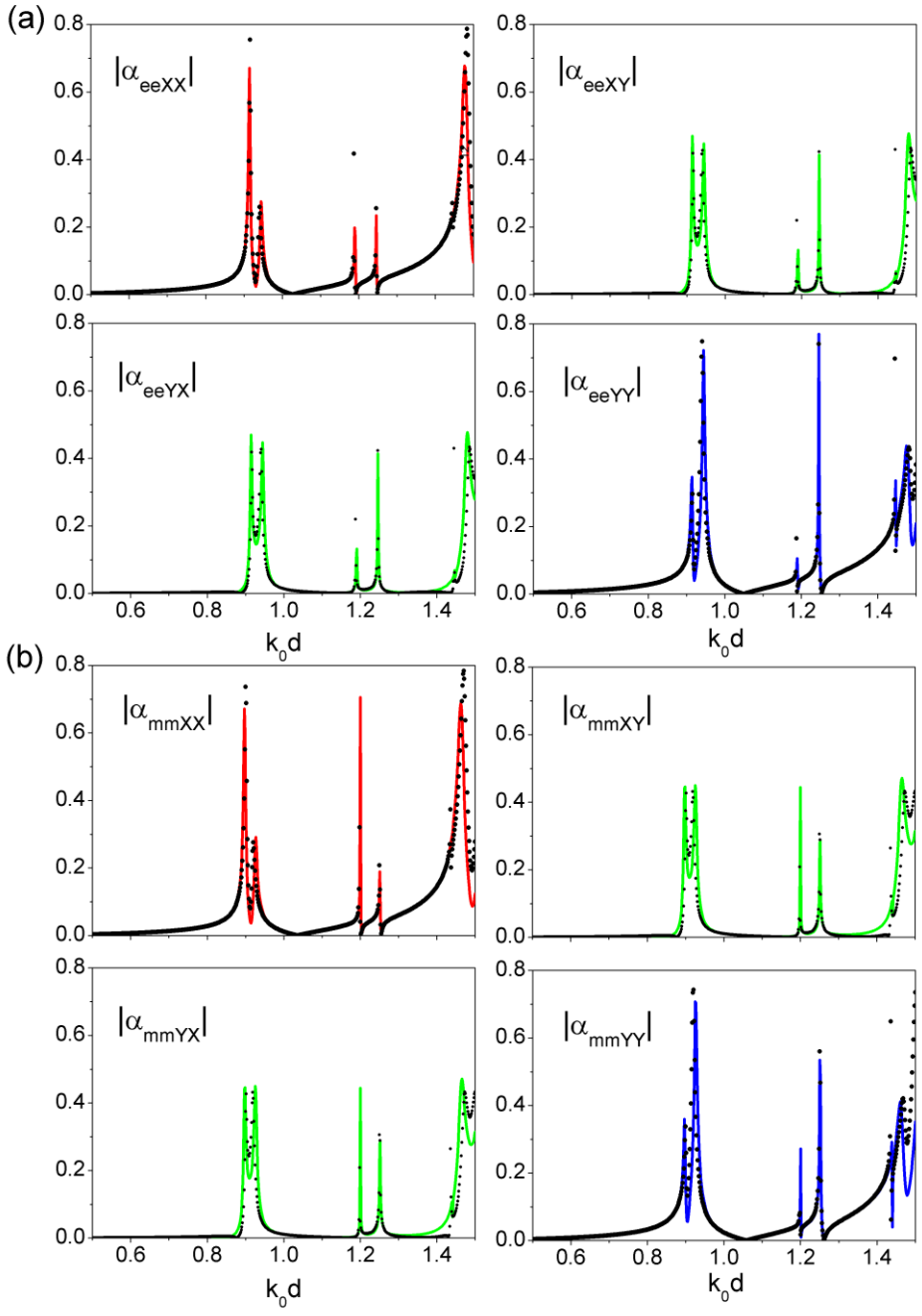

Figure 2.6 Electric (a) and magnetic (b) polarizability tensors of the tilted spheroid shown in Fig 3(b). We compare the results directly retrieved from the proposed method (solid lines) and indirectly transformed from the vertical case (dots).

2.3.3 Conducting helices

In this example, we consider helical inclusions to demonstrate that the bianisotropic terms in the polarizability tensor can also be accurately extracted by our retrieval method. We focus on a pair of single-round helices (see Fig. 2.3c for detailed dimensions) composed of PEC wires with left- and right-handed (LH and RH) winding. We arrange the inclusions in the same 2-D array such that the axis of spirals is aligned with the x-axis of the waveguide. In this way, the normal incident fields may experience different magneto-electric coupling for LH and RH helices. Here, we only present the interesting components of the polarizability tensor, i.e., the X- and Y-components. These extracted components are sufficient to reveal the symmetric and bianisotropic effects induced on the pair of helices. Instead of showing magnitudes and phases, we only present the real parts of the complex polarizabilities in this example to show the identical or inverse properties for the two objects. We find that some curves closely overlap, as expected due to symmetry.

In Fig. 2.7, we show that the diagonal terms in $\boldsymbol{\alpha}^{ee}$ and $\boldsymbol{\alpha}^{mm}$ for LH and RH helices. Our results show that in the arrangements shown in Fig. 2.3c the diagonal co-coupling effects on the two mirror-symmetric inclusions are the same. It is worth noticing that the helix structures are very anisotropic, since the values of α_{XX}^{ee} and α_{YY}^{ee} (or α_{XX}^{mm} and α_{YY}^{mm}) are significantly different. Indeed, the terms α_{XX}^{ee} and α_{YY}^{ee} mainly depend on the diameter of the rings and the pitch size of the spiral, respectively. Since the magnetic properties on the helix is largely dominated by the direction of the spiral axis, the effects of α_{XX}^{mm} are much stronger than α_{YY}^{mm} when the magnetic field aligns with the axis.

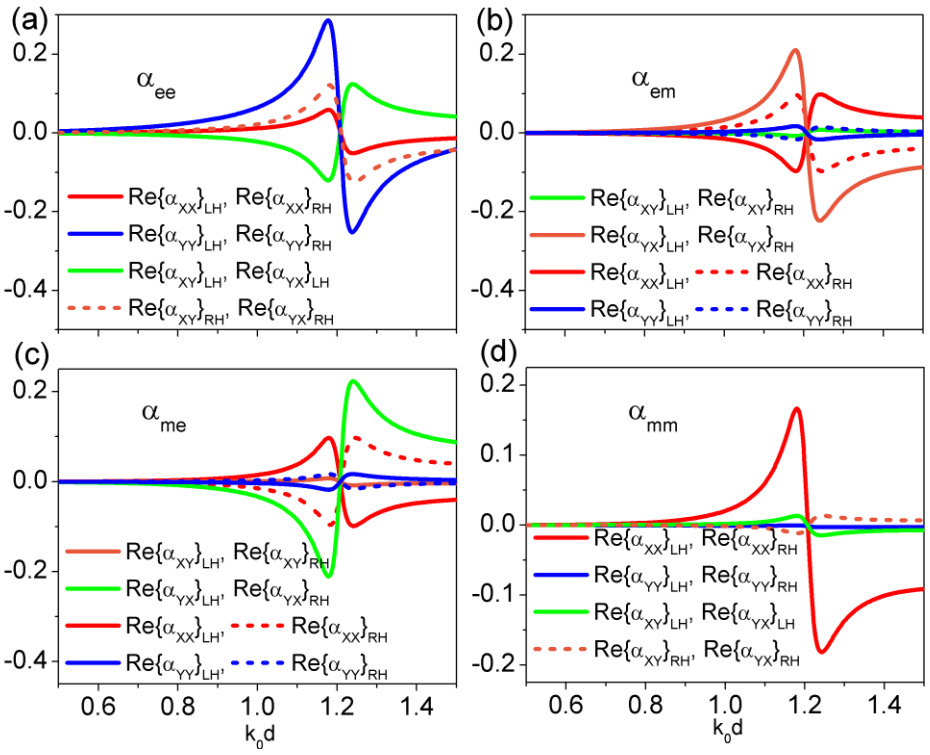

Figure 2.7 Real parts of $\boldsymbol{\alpha}^{ee}$, $\boldsymbol{\alpha}^{em}$, $\boldsymbol{\alpha}^{me}$ and $\boldsymbol{\alpha}^{mm}$ in the X- and Y-directions for LH and RH helices.

On the other hand, the results for the off-diagonal terms in $\boldsymbol{\alpha}^{ee}$ and $\boldsymbol{\alpha}^{mm}$ (see Fig. 2.7a and 2.7d) of the two mirrored helices have opposite signs. This is due to the symmetry and the definition of the local coordinates used in the inclusions. Interestingly, all the curves show Lorentzian or anti-Lorentzian shapes, which implies that the inclusions experience a natural resonance around $k_0 d = 1.2$.

Figure 2.7b and 2.7c show the cross-coupling or bianisotropic components $\boldsymbol{\alpha}^{em}$ and $\boldsymbol{\alpha}^{me}$ of the retrieved polarizability tensor. These terms of the polarizability tensor for helix inclusions are the most interesting because the magneto-electric coupling is generally challenging to quantify in the electrodynamic regime. The PEC spheres used to determine the coupling coefficients in the testing procedures do not support any form of

magneto-electric interaction in the 2-D array. However, when we deal with the helix, the retrieval system still returns physically reasonable results. As shown in Fig. 2.7b and 2.7c, the variations of all entries in the subtensors $\boldsymbol{\alpha}^{em}$ and $\boldsymbol{\alpha}^{me}$ also follow a Lorentzian dispersion, as expected. The diagonal terms in $\boldsymbol{\alpha}^{em}$ and $\boldsymbol{\alpha}^{me}$ for two mirror-symmetric inclusions are opposite in sign. However, the off-diagonal elements in $\boldsymbol{\alpha}^{em}$ and $\boldsymbol{\alpha}^{me}$ have the same sign. All these findings, which come directly from our retrieval procedure, are perfectly consistent with the Onsager relations for the polarizability tensor, which require for any reciprocal inclusion [19]:

$$\begin{aligned} \boldsymbol{\alpha}^{ee} &= \left[\boldsymbol{\alpha}^{ee}\right]^{T}, \\ \boldsymbol{\alpha}^{mm} &= \left[\boldsymbol{\alpha}^{mm}\right]^{T}, \\ \boldsymbol{\alpha}^{em} &= -\left[\boldsymbol{\alpha}^{me}\right]^{T}. \end{aligned} \tag{2.10}$$

It is important to note that the proposed retrieval method appears to correctly capture the physical response of magneto-electric polarization induced in chiral structures. We can precisely quantify the *dynamic* polarizability tensor without using approximated *LC* circuit models or considering static parameters based on the local current distribution in the inclusion.

2.3.4 Conducting SRRs

Next, we consider one of the most popular metamaterial inclusions, the SRRs, used to realize strong artificial magnetism. In order to analyze the bianisotropic nature of SRRs, we focus on two structures, which are built by pairing two SRRs in symmetric and anti-symmetric configurations. The building blocks are made of PEC and the detail geometry parameters are shown in Fig. 2.3d.

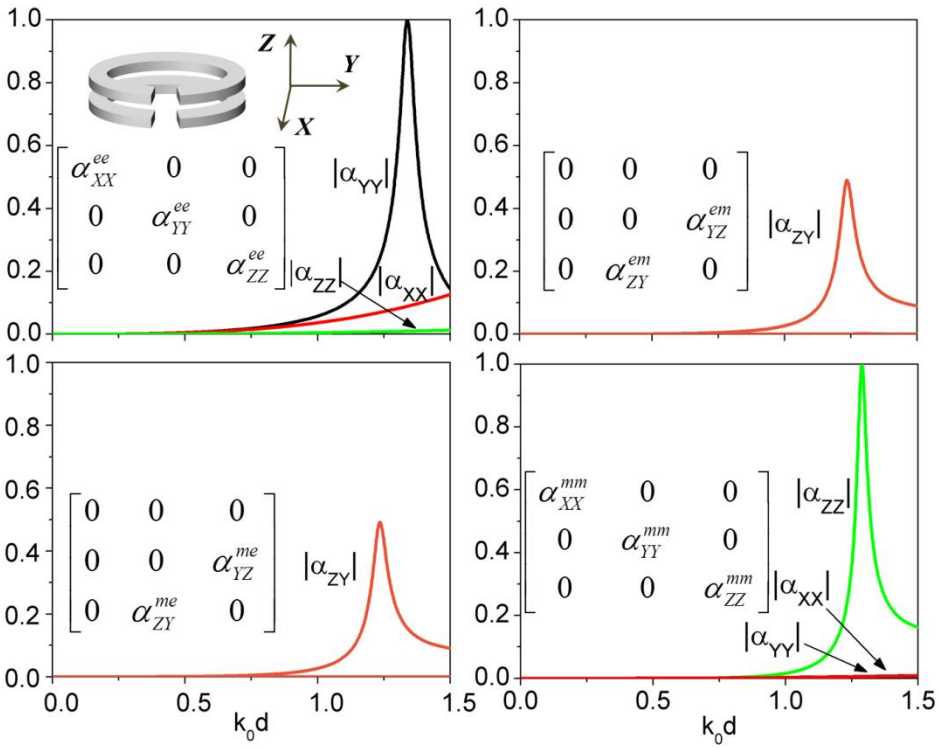

Figure 2.8 Full polarizability tensor of the symmetric SRR pair

For this example, we show the full polarizability tensor for the symmetric and anti-symmetric SRR pairs, respectively. Each case corresponds to 36 elements. For each pair of SRRs, we need three independent measurements with different inclusion orientation to capture all the polarization properties. Again, we check that the tensor satisfies the Onsager relations (2.10) and we make sure that the extracted properties satisfy fundamental physical principles. In Fig. 2.8, we see that all the subtensors have resonance features between $k_0 d = 1.0$ to 1.5. The peak of α_{YY}^{ee} mainly results from the strong electric interaction at the SRR gaps. The curves α_{XX}^{ee} and α_{ZZ}^{ee} do not experience peaks because the geometry in the X- and Z-direction does not excite strong scattering in the frequency regime of interest. Similarly, the most fundamental magnetic resonance can be excited in the Z-direction of the inclusions and, therefore, only α_{ZZ}^{mm}

shows a peak in the magnetic term. Overall, the SRR pair is highly symmetric and the anisotropy off-diagonal terms in $\boldsymbol{\alpha}^{ee}$ and $\boldsymbol{\alpha}^{mm}$ are very weak compared to the diagonal terms.

On the other hand, the peaks in α_{ZY}^{em} and α_{ZY}^{me} reveal the level of magneto-electric coupling induced on the symmetric SRR pair. These major terms in the cross-coupling tensors also imply that a Y-polarized plane wave may generate strong magnetic dipole moments in the Z-direction or, by reciprocity, that a Z-polarized magnetic field can produce electric polarization in the Y-direction. The nonzero terms in $\boldsymbol{\alpha}^{em}$ and $\boldsymbol{\alpha}^{me}$ indeed reveal bianisotropic effects on the SRR structure. Based on these quantified retrieval results, designers may have more precise access to the full electromagnetic response of SRR inclusions, in order to engineer the desired metamaterial properties. To the best of our knowledge, this is the first reported retrieval of the full dynamic polarizability tensor for SRR inclusions. Because of the chosen configuration, the calculated polarizabilities may contain some minor effects arising from higher-order interactions in the lattice. These embedded higher-order effects, may turn out to be useful, since these same effects arise in dense metamaterial arrays.

In Fig. 2.9, we apply the retrieval method to the anti-symmetric SRR pair and compare the bianisotropic effects to the previous symmetric structure. Interestingly, in the subtensor $\boldsymbol{\alpha}^{ee}$, we find no peak even if we have the same gaps in the Y-direction. This is because the electric polarization in this direction depends on the charge accumulation across the opening ends, and the types of accumulated charges are determined by the conductive currents circulating on the rings. For the fundamental mode, the currents are circulating in the same directions on the two rings, and this pattern may result in opposite charge distributions at the two gaps of the anti-symmetric pair. As a consequence, the dipole moments induced across the gaps are cancelled and the

resonance in the Y-direction cannot be radiating (also known as a *dark* mode [34]). On the contrary, we find that a magnetic resonance still exists, but shifts to lower frequency and becomes correspondingly narrower.

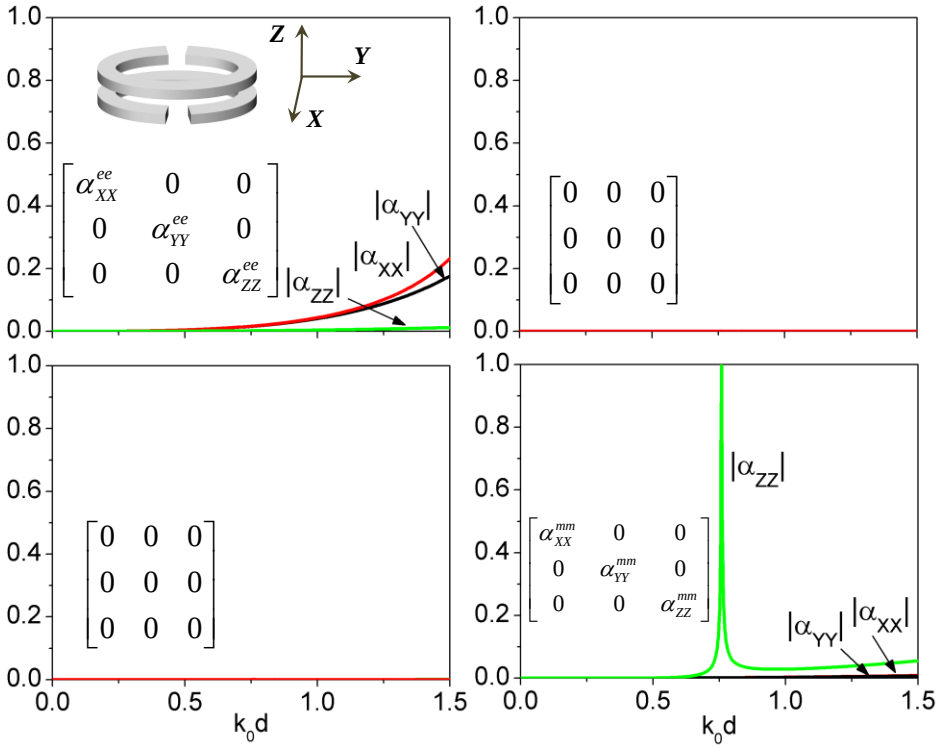

Figure 2.9 Full polarizability tensor for the anti-symmetric SRR pair

Most importantly, based on the retrieval results, we find that $\boldsymbol{\alpha}^{em}, \boldsymbol{\alpha}^{me} \approx \mathbf{0}$ and this anti-symmetric SRR pair does not show bianisotropic effects. This conclusion is consistent with the analysis in Ref. [3], in which the authors qualitatively predict that magneto-electric effects can be largely suppressed by considering anti-symmetric SRR pairs.

2.3.5 Plasmonic SRRs

For metamaterial applications in the optical regime, noble metals such as silver and gold are popular materials for subwavelength inclusions [35-36]. These metals may sustain surface plasmon effects with strong field enhancement at the interface under proper excitation. Therefore, metamaterials composed of plasmonic-based inclusions may exhibit significant energy localization [37]. Inevitable material losses due to electron collision and retardation are the major drawbacks of plasmonic materials at optical frequencies.

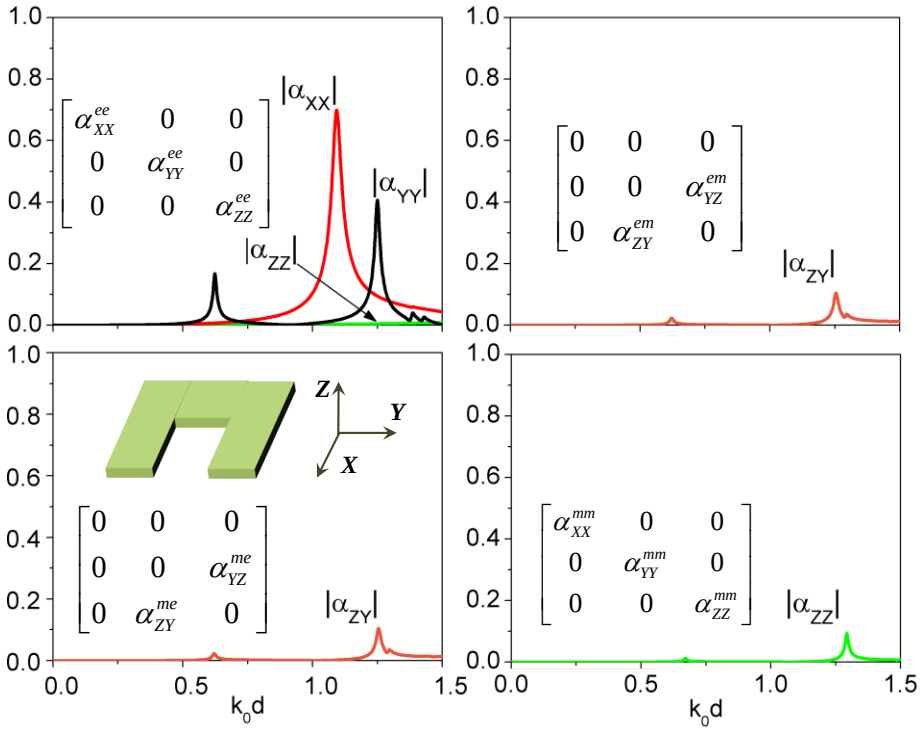

Figure 2.10 Full polarizability tensor retrieved for a silver SRR

Generally, the strong material dispersion may result in higher numerical instabilities when determining the scattering quantities of the subwavelength inclusions. The numerical solvers (e.g., eigen-solvers) in Ansoft HFSS and CST Microwave Studio

do not support lossy and dispersive media. Here, we apply the retrieval system to extract the polarizability tensors of a thin SRR inclusion made of silver, as shown in Fig. 2.3a. In order to use the coefficients applied in the previous examples, the square waveguide is scaled to 125nm in width and 600nm in length, and the valid frequency regime ranges up to 600 THz ($k_0 d = 1.5$ or 500 nm in wavelength.) The permittivity of silver is formulated using a Drude model fitted from the empirical measurement data [38] (see Appendix B).

Figure 2.10 shows the polarizability results, in which all the normalized peaks do not reach 1 due to material loss. Based on the same line of reasoning, the effect of magneto-electric terms are much weaker than in the PEC SRRs discussed in the previous example. The retrieval of this polarizability tensor is crucial for optical metamaterial design, because it provides comprehensive information on the dipolar scattering for such inclusion, which may induce some non-negligible magnetic response in the visible. For this geometry, as seen in Fig. 2.10, the induced artificial magnetism is quite limited, but improved geometries may be considered if larger effects are required.

2.4 CONCLUSIONS

In this chapter, we have proposed a general retrieval method to quantify the full polarizability tensor of arbitrary subwavelength inclusions. Instead of analyzing the scattering properties of an isolated inclusion, we employ a 2-D array configuration to take into account co- and cross-coupling effects induced on the inclusions. We have reported the detailed formulation for this method, which can be applied to optical, microwave and terahertz frequencies. We have examined and discussed the retrieval results for five different examples, from simple to complex inclusions. For simple particles, we have used Mie theory and point-dipole radiation to validate our results. The proposed method may precisely capture the resonance features of an electrically small sphere and the

anisotropic components of the full polarizability tensor of a tilted spheroid. For complex inclusions, we have verified that our retrieved tensors satisfy the dynamic Onsager relations, passivity and reciprocity conditions. We have also demonstrated that strong chirality can be obtained by considering two mirror-symmetric helices. Finally, we have presented the full polarizability tensor of symmetric and anti-symmetric SRR pairs, which are proving that the symmetric pair may sustain more versatile electric and magnetic resonances in the inclusions, while the anti-symmetric pair may suppress unwanted bianisotropic effects.

2.5 REFERENCES

1. J. B. Pendry, A. J. Holden, D. J. Robbins, and W. J. Stewart, "Magnetism from conductors and enhanced nonlinear phenomena," *IEEE Trans. Microwave Theory Tech*. **47**, 2075-2084 (1999).
2. R. A. Shelby, D. R. Smith, and S. Schultz, "Experimental Verification of a Negative Index of Refraction," *Science* **292**, 77-79 (2001).
3. R. Marqués, F. Medina, and R. Rafii-El-Idrissi, "Role of bianisotropy in negative permeability and left-handed metamaterials," *Phys. Rev. B* **65**, 144440 (2002).
4. C. R. Simovski and S. He, "Frequency range and explicit expressions for negative permittivity and permeability for an isotropic medium formed by a lattice of perfectly Ω conducting particles," *Phys. Lett. A* **311**, 254 (2003).
5. K. Aydin, Z. Li, M. Hudlicka, S. A. Tretyakov, and E. Ozbay, "Transmission characteristics of bianisotropic metamaterials based on omega shaped metallic inclusions," *New J. Phys.* **9,** 326 (2007).
6. J. K. Gansel, M. Thiel, M. S. Rill, M. Decker, K. Bade, V. Saile, G. von Freymann, S. Linden, and M. Wegener, "Gold Helix Photonic Metamaterial as Broadband Circular Polarizer," *Science* **325**, 1513-1515 (2009).
7. Bohren, C. F. and D. R. Huffman, *Absorption and Scattering of Light by Small Particles* (Wiley, New-York, 1983).
8. S. A. Tretyakov, A. H. Sihvola, A. A. Sochava, and C. R. Simovski, "Magneto-electric Interactions in Bi-Anisotropic Media," *J. Electromagn. Waves Appl*. **12**, 481 (1998).
9. S. A. Tretyakov, S. I. Maslovski, I. S. Nefedov, A. J. Viitanen, P. A. Belovand, and A. Sanmartin, "Artificial Tellegen Particle," *Electromagnetics* **23**, 665-680 (2003).

10. I. V. Lindell, A. H. Sihvola, S. A. Tretyakov, and A. J. Viitanen, *Electromagnetic Waves in Chiral and Bi-Isotropic Media*, MA: Artech, 1994.
11. M. Husnik, M. W. Klein, N. Feth, M. König, J. Niegemann, K. Busch, S. Linden, and M. Wegener, "Absolute extinction cross-section of individual magnetic split-ring resonators," *Nat. Photonics* **2**, 614 (2008).
12. P. Banzer, U. Peschel, S. Quabis, and G. Leuchs, "On the experimental investigation of the electric and magnetic response of a single nano-structure," *Opt. Express* **18**, 10905 (2010).
13. E. Plum, X.-X. Liu, V. A. Fedotov, Y. Chen, D. P. Tsai, and N. I. Zheludev, "Metamaterials: Optical Activity without Chirality," *Phys. Rev. Lett.***102**, 113902 (2009).
14. S. Zhang, Y.-S. Park, J. Li, X. Lu, W. Zhang, and X. Zhang, "Negative Refractive Index in Chiral Metamaterials," *Phys. Rev. Lett.***102**, 023901 (2009).
15. S.A. Tretyakov, F.Mariotte, C.R. Simovski, T. G. Kharina, and J.-P. Heliot, "Analytical antenna model for chiral scatterers: comparison with numerical and experimental data," *IEEE Trans. Antennas Propag.* **44**, 1006-1014 (1996).
16. S. Tretyakov, *Analytical Modeling in Applied Electromagnetics*, Artech House 2003.
17. H. Liu, D. A. Genov, D. M. Wu, Y. M. Liu, Z. W. Liu, C. Sun, S. N. Zhu, and X. Zhang, "Magnetic plasmon hybridization and optical activity at optical frequencies in metallic nanostructures," *Phys. Rev. B* **76**, 073101 (2007).
18. N. Liu, H. Liu, S. Zhu, and H. Giessen, "Stereometamaterials," *Nat. Photonics* **3**, 157-162 (2009).
19. I. Sersic, M. Frimmer, and A. F. Koenderink, "Electric and Magnetic Dipole Coupling in Near-Infrared Split-Ring Metamaterial Arrays," *Phys. Rev. Lett*. **103**, 213902 (2009).
20. S. Linden, C. Enkrich, M. Wegener, J. Zhou, T. Koschny, and C. M. Soukoulis, "Magnetic Response of Metamaterials at 100 Terahertz," *Science* **306**, 1351-1353 (2004).
21. R. Marqués, F. Mesa, J. Martel, and F. Medina, "Comparative Analysis of Edge- and Broadside-Coupled Split Ring Resonators for Metamaterial Design—Theory and Experiments,"*IEEE Trans. Antennas Propag.* **51**, 2572-2581 (2003).
22. J. D. Baena, J. Bonache, F. Martín, R. M. Sillero, F. Falcone, T. Lopetegi, M. A. G. Laso, J. García–García, I. Gil, M. F. Portillo, and M. Sorolla, "Equivalent-Circuit Models for Split-Ring Resonators and Complementary Split-Ring Resonators Coupled to Planar Transmission Lines," *IEEE Trans. Microwave Theory Tech.* **53**, 1451-1461 (2005).
23. R. E. Collin, *Field Theory of Guided Waves*, Wiley-IEEE Press (1990).
24. A. Alù and N. Engheta, "Theory of linear chains of metamaterial/plasmonic particles as subdiffraction optical nanotransmission lines," *Phys. Rev. B* **74**, 205436 (2006).

25. I. Sersic, C. Tuambilangana, T. Kampfrath, and A. F. Koenderink, "Magneto-electric point scattering theory for metamaterial scatterers," *Phys. Rev. B* **83**, 245102 (2011).
26. A. Ishimaru, S.-W. Lee, Y. Kuga, V. Jandhyala, "Generalized constitutive relations for metamaterials based on the quasi-static Lorentz theory," *IEEE Trans. Antennas Propag.***51**, 2550-2557 (2003).
27. H.-X. Ye and Y.-Q. Jina, "Polarimetric scattering from a layer of spatially oriented metamaterial small spheroids," *Eur. Phys. J. Appl. Phys.* **31**, 3-9 (2005).
28. X. Cheng, H. Chen, L. Ran, B.-I. Wu, T. M. Grzegorczyk, and J. A. Kong, "Negative refraction and cross polarization effects in metamaterial realized with bianisotropicS-ring resonator,"*Phys. Rev. B* **76**, 024402 (2007).
29. A. J. Bahr and K. R. Clausing, "An Approximate Model for Artificial Chiral Material," *IEEE Trans. Antennas Propag*. **42**, 1592-1599 (1994).
30. A. D. Scher and E. F. Kuester, "Extracting the bulk effective parameters of a metamaterial via the scattering from a single planar array of particles,"*Metamaterials* **3**, 44-55 (2009).
31. L. Jelinek and J. Machac, "Free space polarizability measurement method," *Proc. Metamaterials '2011: The Fifth International Congress on Advanced Electromagnetic Materials in Microwaves and Optics*, Barcelona, 967-969 (2011).
32. A. I. Dimitriadis, D. L. Sounas, N. V. Kantartzis, C. Caloz, and T. D. Tsiboukis, "Surface Susceptibility Bianisotropic Matrix Model for Periodic Metasurfaces of Uniaxially Mono-Anisotropic Scatterers Under Oblique TE-Wave Incidence," *IEEE Trans. Antennas Propag.* **60**, 5753-5767 (2012).
33. A. Alù and N. Engheta, "Achieving transparency with plasmonic and metamaterial coatings," *Phys. Rev. E* **72**, 016623 (2005).
34. N. Papasimakis, V. A. Fedotov, N. I. Zheludev, and S. L. Prosvirnin, "Metamaterial analog of electromagnetically induced transparency," *Phys. Rev. Lett.* **101**, 253903 (2008).
35. N. Fang, H. Lee, C. Sun, and X, Zhang, "Sub–Diffraction-Limited Optical Imaging with a Silver Superlens," *Science* **308**, 534-537 (2005).
36. V. M. Shalaev, "Optical negative-index metamaterials," *Nat. Photonics* **1**, 41-48 (2007).
37. A. Aubry, D. Y. Lei, A. I. Fernández-Domínguez, Y. Sonnefraud, S. A. Maier and J. B. Pendry, "Plasmonic Light-Harvesting Devices over the Whole Visible Spectrum," *Nano Lett*. **10**, 2574-2579 (2010).
38. P. B. Johnson and R. W. Christy, "Optical Constants of the Noble Metals," *Phys. Rev. B* **6**, 4370-4379 (1972).

Chapter 3 Homogenization of One-Dimensional Metamaterials: Linear Particle Arrays as Sub-diffractive Waveguides and Leaky-wave Antennas

3.1 INTRODUCTION

One-dimensional linear particle arrays are the simplest metamaterial structures composed of nonconnected elements. The recent applications based on this type of metamaterial have provided novel possibilities for subwavelength waveguide and leaky-wave antenna design and operation at microwave frequencies [1-4]. As one of the interesting applications of periodic arrays at radio frequencies for radiation applications, leaky-wave antennas are a well-studied technology that provides directive radiation and frequency beam scanning [1,6-7]. Translating these concepts to the optical regime may open new areas in optical communications, control of radiation and optical computing. In this regard, periodic arrays of nanoparticles have already been considered by various fields as optical waveguides with confined beams, overcoming the optical diffraction limit [8-17]. The coated-particle arrays may also be considered as optical reflector arrays on layered structures to achieve directive radiation [18-19]. The use of plasmonic materials and linear arrays of subwavelength plasmonic nanoparticles [8-17] may overcome the diffraction limit of waves and confine a guided optical beam over a transverse cross-section significantly smaller than the wavelength of operation. Therefore, the 1-D linear array may support *sub-diffractive propagation* with relevant applications in optical computing and communications.

In order to theoretically investigate wave propagation on the 1-D linear array, we derive in this chapter a closed-form dispersion relation for real and complex dipolar modes supported by such infinitely extended structures, with the only approximation being the neglect of higher-order multipoles beyond the dominant dipole terms for each

particle. In particular, this formulation makes it possible to deal with the presence of realistic losses and damping for the guided modes, extending previous analyses that were limited to real wave numbers to the complex domain by an analytic continuation technique [20]. Similarly, this technique may be applied to problems involving radiation losses, which are significant when the wave energy is not totally guided along the particle chain, but partially leaked out, as it happens in the leaky modes.

As mentioned above, the idea of energy leakage is widely applied in microwave engineering to design directive radiators with beam scanning capabilities. Moreover, in optics, the applications of energy leakage on thin film associated with surface plasmon waves are also applied in near field microscopy [21, 22]. The leaky mode is a fast eigenmode of the structure with complex wave number, whose real part is smaller than the free-space wave number [23]. This ensures that the energy is not confined along the array, and the Poynting (power flux) vector points towards the lateral direction. Provided that the imaginary part of the leaky wave number is sufficiently small, the radiation from the chain may become very directive, producing a conical directive beam at a given angle from the array axis. At microwaves, leaky-wave antennas are usually obtained by perturbing a guided wave with periodic defects, as in a periodically loaded micro-strip line [24-26]. In optics, the studies of modal analysis for metallic thin film also report radiating property due to surface-polariton waves [27]. It is challenging, however, to produce precisely defects within a sub-wavelength transverse cross-section, since in such case they tend to weakly interact with the mode of interest, which is usually weakly confined. This is another clear symptom of the diffraction limit of guided beams in free-space. For this reason, the leaky-wave antenna transverse cross section is usually comparable with the wavelength of operation.

In this Chapter, we investigate the potential of periodic linear arrays to support guided- and leaky-waves with energy confinement and directive radiation properties in the optical regime. Even in the limit in which the array has sub-wavelength (i.e., not limited by the diffraction limitations mentioned above) lateral cross section, the structure may be applied as a *sub-diffractive* optical waveguide and leaky-wave nanoantenna. Both applications may lead to the possibility to connect distant points of an optical nanocircuit board [28] and create point-to-point links at the nanoscale. In the following we derive relevant design parameters and underline the fundamental and general limitations and challenges to the practical realization of such devices. Our general analysis is particularly focused on plasmonic nanoparticles as the linear chain elements, which may ensure the application of these concepts at optical frequencies and may provide inherent advantages associated with their anomalous light interaction.

This chapter is organized as follows. In section 3.2, we derive the dispersion equations of single and parallel linear periodic arrays and for both longitudinal and transverse leaky modes. We identify the typical properties of wave vector in leaky modes and discuss the associated radiation properties for linear arrays. In section 3.3, we solve the dispersion equations for the wave number of guided- and leaky-waves in real and complex domains, respectively. In particular, we give a detailed discussion on the transition of wave vector solutions between guided and leaky regime. The general guided and leaky-regime for linear array is analyzed in terms of dimensionless parameters. We also provide a figure of merit to evaluate the radiation and propagation performance of leaky waves. In section 3.4, spheres of various materials are considered as array inclusions. We determine the permittivity value that can support guided and leaky modes and discuss the effect of loss or absorption along the chain. Moreover, realistic plasmonic and dielectric materials are considered to draw the comparison of wave propagation and

radiation in various types of arrays. Finally, we provide full wave simulations in section 3.5 to validate our results and graphically show how the electromagnetic fields behave in both guided and leaky scenarios.

3.2. FORMULATION

3.2.1 Single linear particle array

Consider an infinite linear array of particles oriented along the z axis, periodically located at $z = Nd$, with d being the center-to-center distance and N being any positive or negative integer.

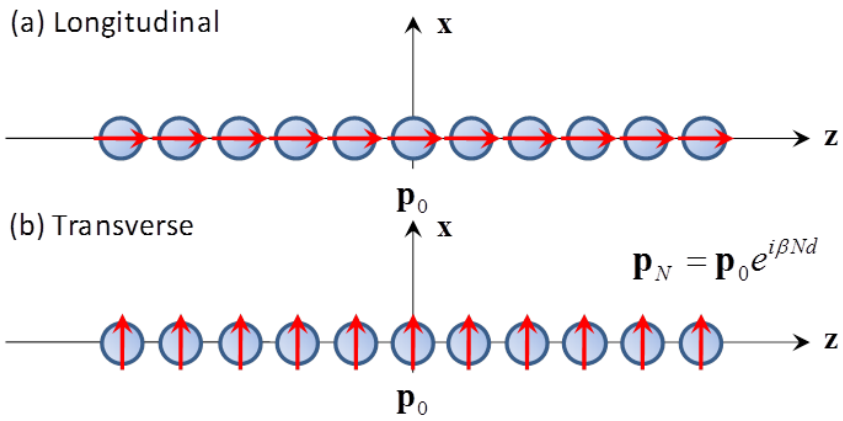

Figure 3.1 Geometry under consideration: a single linear array of spherical particles supporting a longitudinal (a) or a transverse (b) eigenmode.

Provided that the nanoparticle size is much smaller than the wavelength of operation, its wave interaction is dominated by the dipolar scattering and each element may be safely modeled as a polarizable dipole and fully characterized by its electric polarizability α_{ee}. As the formulation widely applied in Ref. 29, if $\mathbf{p}_0 = \alpha_{ee}\mathbf{E}_0$ is the dipole moment induced by a local electric field $\mathbf{E}_0$ on the particle at $z = 0$, it is possible to derive a self-sustained eigensolution traveling along the array in the form $\mathbf{p}_N = \mathbf{p}_0 e^{i\beta Nd}$, under an

$e^{-i\omega t}$ time-harmonic convention. Here, β is the complex propagation factor, fully characterizing its propagation and radiation properties. As reported in several papers on the topic [9-20], the complete eigenmode spectrum may be split into longitudinal and transverse polarizations, consistent with Fig. 3.1a and b, respectively. The dispersion relations for these two polarizations may be respectively written [20]:

$$\begin{aligned} L &: 3\bar{d}^{-3}\left[f_3\left(\bar{\beta},\bar{d}\right) - i\bar{d}\ f_2\left(\bar{\beta},\bar{d}\right)\right] = \bar{\alpha}_{ee}^{-1} \\ T &: -\frac{3}{2}\bar{d}^{-3}\left[f_3\left(\bar{\beta},\bar{d}\right) - i\bar{d}\ f_2\left(\bar{\beta},\bar{d}\right) - \bar{d}^2 f_1\left(\bar{\beta},\bar{d}\right)\right] = \bar{\alpha}_{ee}^{-1} \end{aligned} \tag{3.1}$$

where we introduce the normalized parameters $\bar{d} \equiv k_0 d$, $\bar{\beta} \equiv \beta / k_0$, $\bar{\alpha}_{ee} \equiv k_0^3 \alpha_{ee} / \left(6\pi\varepsilon_0\right)$, $k_0 \equiv \omega\sqrt{\varepsilon_0\mu_0}$, and ε_0, μ_0 are the permittivity and permeability of background medium, respectively. In addition, we use a special function

$$f_N\left(\bar{\beta},\ \bar{d}\right) = \mathrm{Li}_N\left(e^{i\left(\bar{\beta}+1\right)\bar{d}}\right) + \mathrm{Li}_N\left(e^{-i\left(\bar{\beta}-1\right)\bar{d}}\right) \tag{3.2}$$

in which $\mathrm{Li}_N\left(x\right)$ is the polylogarithm function, as defined in Ref. 31. Due to the inherent periodicity of the Floquet modes of the linear chain, we limit our analysis to the principal period $\left|\mathrm{Re}\left[\bar{\beta}\right]\right| \le \pi/\bar{d}$.

The form of dispersion relation in Eq. (3.1) is valid for any real or complex value of β, ensuring that it may be employed to study guided as well as leaky-wave propagation along the linear chains. For a lossless case, it is required the condition $\mathrm{Im}\left[\bar{\alpha}_{ee}^{-1}\right] = -1$ for the involved nanoparticles to support a real solution for β (guided modes without decay) [20]. This condition is identically met for passive dipolar particles only when absorption may be neglected [29, 32] as physically expected, and it implies that $\mathrm{Re}\left[\bar{\beta}\right] \ge 1$ in Eq. (3.1). If the lossless condition is not satisfied ($\mathrm{Im}\left[\bar{\alpha}_{ee}^{-1}\right] < -1$), then absorption takes place in the nanoparticle array and the eigenwave numbers are

necessarily complex, whose imaginary part is associated with the damping caused by Ohmic loss.

Even in the lossless scenario, however, complex solutions are allowed when $\left|\mathrm{Re}\left[\bar{\beta}\right]\right|<1$ (fast leaky modes), when $1<\left|\mathrm{Re}\left[\bar{\beta}\right]\right|<\pi/\bar{d}$ (complex modes) or when $\left|\mathrm{Re}\left[\bar{\beta}\right]\right|=\pi/\bar{d}$ (stop-band). In the following, we are interested in the leaky modes with sufficiently small $\mathrm{Im}\left[\bar{\beta}\right]$, which may provide directive radiation and sustain propagation over a reasonable electrical length, analogous to the operation of microwave leaky-wave antennas []. For $\bar{d}<\pi$ (sufficiently tight arrays, which is required for leaky radiation, as we note in the following), the first-order Bloch mode dominates the far-field pattern, which may be therefore evaluated by simply assuming an averaged current line distribution along the z axis with amplitude $-i\omega\mathbf{p}_0 e^{i\beta z}/d$, consistent with Ref. 30. In this case, the magnetic potential $\mathbf{A}$ may be written in the two polarizations as:

$$\mathbf{A}=\frac{\omega\mu_0\mathbf{p}_0}{4d}H_0^{(1)}\left(\sqrt{k_0^2-\beta^2}\,\rho\right)e^{i\beta z} \tag{3.3}$$

where ρ is the radial coordinate in the suitable cylindrical reference system with axis along the cylinder. The electric and magnetic far-field distributions may be easily derived as $\mathbf{H}=\nabla\times\mathbf{A}/\mu_0$, $\mathbf{E}=\nabla\times\mathbf{H}/\left(-i\omega\varepsilon_0\right)$.

This implies that a complex value of β necessarily requires a non-zero power flux and phase propagation along the radial direction. In particular, for sufficiently small $\mathrm{Im}\left[\beta\right]$, Eq. (3.3) represents a standard guided-wave mode for $\mathrm{Re}\left[\beta\right]>k_0$, with exponential decay rate in the radial direction given by Ref. 20:

$$\begin{cases} L: & K_1\left(\sqrt{\mathrm{Re}\left[\beta\right]^2-k_0^2}\,\rho\right) \\ T: & K_2\left(\sqrt{\mathrm{Re}\left[\beta\right]^2-k_0^2}\,\rho\right) \end{cases} \tag{3.4}$$

and a leaky mode when $\mathrm{Re}[\beta] < k_0$, with conical beam radiation at an angle $\theta = \cos^{-1}\left[\mathrm{Re}[\bar{\beta}]\right]$ from the z axis. In such case, the decay rate is comparable to a cylindrical wave $1/\sqrt{\rho}$ and the corresponding intensity pattern is well approximated by [6]:

$$I(\theta) = \frac{\sin^2\theta}{\left(\cos\theta - \mathrm{Re}[\bar{\beta}]\right)^2 + \left(\mathrm{Im}[\bar{\beta}]\right)^2}. \tag{3.5}$$

The radiation beamwidth of the main conical lobe is calculated as:

$$BW = 2\,\mathrm{Im}\,\bar{\beta} / \sin\theta_0, \tag{3.6}$$

which ensures that the *directivity* of radiation, a measure of how oriented and narrow the far-field radiation pattern is towards the desired direction, is inversely proportional to $\mathrm{Im}[\bar{\beta}]$.

It should be emphasized that the leaky-wave solutions do not represent proper contributions to the radiated spectrum of the chain, but they indeed dominate the steepest-descent approximation in specific angular regions of the visible spectrum, and therefore, they constitute an accurate and effective description of the far-field distribution of the chain in a variety of realistic applications [1]. In practice, their divergence does not lead to a numerical issue, since we are interested in solutions with small $\mathrm{Im}[\beta]$ and finite chain lengths, for which the localized excitation (which practically may be represented by an emitting molecule or a quantum dot in this scenario at optical frequencies) is at a finite location along the array [33].

3.2.2 Parallel linear particle arrays

Based on the formulation for the single linear particle array, we may extend the discussion to the dipole coupling among parallel arrays in this section. For this case,

consider two identical linear arrays of nanoparticles with radius a, periodic interparticle distance $d > 2a$ and interchain distance l, as shown in Fig 3.2. Since we are interested in wave propagation along the chain, we limit the structure to the condition $l > d$, which ensures the mutual coupling between particles along the axial direction is stronger than the interaction between the two chains. For the case of parallel arrays, we expect that the mutual coupling between particle chains may allow efficient energy confinement [34, 35], and therefore, the propagation along parallel arrays may be longer than for a single chain.

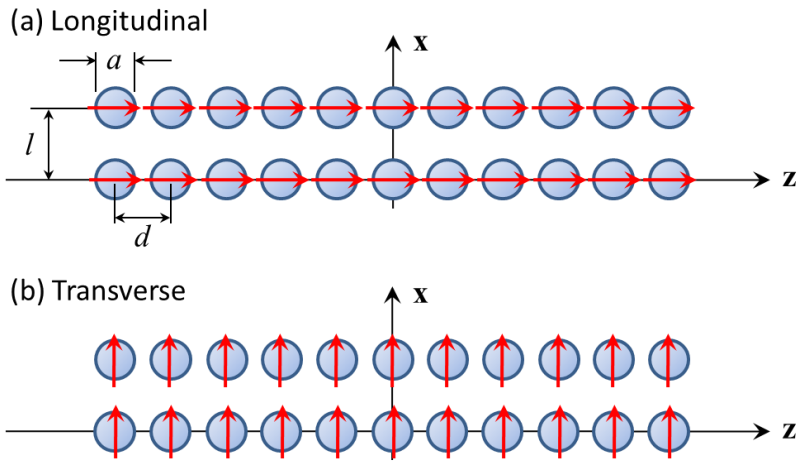

Figure 3.2 Geometry under consideration: a parallel linear array of nanoparticles supporting longitudinal (a) or a transverse (b) eigenmode.

Similar to the previous scenario, we may express the total displacement current distribution on a single chain as the summation of the dipole moments in Bloch form:

$$\mathbf{J}(x) = -i\omega\mathbf{p}\sum_{m=-\infty}^{\infty} e^{i\beta md}\delta(x - md), \tag{3.7}$$

where δ is the Dirac delta function. In order to simplify the computation, we can further define the averaged line current in Eq. (3.7) as

$$\mathbf{J}_{av}\left(x\right)=i\omega\mathbf{p}e^{i\beta z}/d\,. \tag{3.8}$$

To determine the field coupling between parallel chains, we can expand the radiation field of the equivalent line current into cylindrical waves and evaluate the interaction with particles of dipole moment $\mathbf{p}_2 e^{i\beta md}$ in another chain to obtain the coupling coefficients [35]

$$\begin{aligned}
C_{xx} &= -\frac{3}{\bar{d}}\sum_{m=-\infty}^{\infty}\bar{b}_m^2 K_0\left[\bar{b}_m\bar{l}\right] \\
C_{xz} &= C_{zx} = -\frac{3i}{\bar{d}}\sum_{m=-\infty}^{\infty}\sqrt{\bar{b}_m^2+1}\,\bar{b}\;K_1\left[\bar{b}_m\bar{l}\right] \\
C_{zz} &= \frac{3i}{\bar{l}\;\bar{d}}\sum_{m=-\infty}^{\infty}\left(\bar{b}_m^2+1\right)\bar{l}K_0\left[\bar{b}_m\bar{l}\right]+\bar{b}_m\;K_1\left[\bar{b}_m\bar{l}\right] \\
C_{yy} &= \frac{3}{2\bar{d}}\sum_{m=-\infty}^{\infty}\left(\bar{b}_m^2+2\right)K_0\left[\bar{b}_m\bar{l}\right]-\bar{b}_m^2 K_2\left[\bar{b}_m\bar{l}\right] \\
C_{xy} &= C_{yx} = C_{zy} = C_{yz} = 0
\end{aligned} \tag{3.9}$$

where $\bar{b}_m=\sqrt{\left(\bar{\beta}+\frac{2\pi m}{\bar{d}}\right)^2-1}$ and $K_m\left[.\right]$ are the modified Bessel functions of order *m*. The coupling coefficient C_{ij} stands for the polarization in *i* direction on one chain induced by the polarization in the *j* direction on the other chain. We omit some other null coefficient such as C_{xz} and C_{yz} in (3.9), because the transverse mode polarized in z direction is not coupled with the orthogonal polarizations. Due to the fast convergence behavior of the expansion in (3.9), it is sufficient to consider the leading term ($m = 0$) to analyze the coupling between chains [35].

The dispersion relation can be organized as an eigensystem:

$$\det\begin{pmatrix} L & 0 & C_{xx} & C_{xz} \\ 0 & T & C_{xz} & C_{zz} \\ C_{xx} & -C_{xz} & L & 0 \\ -C_{xz} & C_{zz} & 0 & T \end{pmatrix}\det\begin{pmatrix} T & C_{yy} \\ C_{yy} & T \end{pmatrix}=0 \tag{3.10}$$

where L and T are the longitudinal and transverse dispersion relations for an isolated chain in Eq. (3.1). The first determinant in (3.10) gives the dispersion of the coupled modes polarized in *xz*-plane, while the second denotes the coupling of transverse modes which lay in *yz*-plane. We can further derive the dispersion relations by expanding the determinants, which can be organized as:

$$\left(L+C_{xx}\right)\left(T-C_{zz}\right)+C_{xz}^2=0, \tag{3.11}$$

$$\left(L-C_{xx}\right)\left(T+C_{zz}\right)+C_{xz}^2=0, \tag{3.12}$$

providing the following constraints on the polarization eigenvectors:

$$\begin{cases} \mathbf{p}_1\cdot\hat{\mathbf{x}}=\mathbf{p}_2\cdot\hat{\mathbf{x}} \\ \mathbf{p}_1\cdot\hat{\mathbf{y}}=-\mathbf{p}_2\cdot\hat{\mathbf{y}} \end{cases} \tag{3.13}$$

$$\begin{cases} \mathbf{p}_1\cdot\hat{\mathbf{x}}=-\mathbf{p}_2\cdot\hat{\mathbf{x}} \\ \mathbf{p}_1\cdot\hat{\mathbf{y}}=\mathbf{p}_2\cdot\hat{\mathbf{y}} \end{cases} \tag{3.14}$$

for Eq. (3.11) and (3.12), respectively.

3.3 GENERAL PROPERTIES OF THE EIGENSOLUTIONS

In this section, we show our investigation on the general properties of the complex solutions of dispersion relations Eqs. (3.1) and (3.10), with special attention to the leaky-wave regime. In order to make the analysis very general, we focus in this section on the variation of complex $\overline{\beta}$ with the normalized quantity $\mathrm{Re}\left[\overline{\alpha}_{ee}^{-1}\right]$, which compactly describes the general properties of the individual subwavelength particles forming the array. It is noticed, in particular, that $\mathrm{Im}\left[\overline{\alpha}_{ee}^{-1}\right]$ is simply associated with the

absorption properties of the particles, and it is forced to be $\mathrm{Im}\left[\bar{\alpha}_{ee}^{-1}\right]=-1$ when the particles are lossless. The available degrees of freedom to tailor the leaky-wave properties of the array are therefore elegantly represented by $\mathrm{Re}\left[\bar{\alpha}_{ee}^{-1}\right]$, which is a function of the geometrical and material properties of the particles.

3.3.1 Single Particle Chains

As a first example, in Fig. 3.3 we present the variation of complex $\bar{\beta}$ as a function of the normalized parameter $\bar{d}^3\,\mathrm{Re}\left[\bar{\alpha}_{ee}^{-1}\right]$, for an interparticle distance $\bar{d}=0.2$. We consider here lossless particles with $\mathrm{Im}\left[\bar{\alpha}_{ee}^{-1}\right]=-1$. As seen in Fig. 3.2a, the longitudinally polarized eigenmodes have a smooth transition from the guided-wave to the leaky-wave region at $\mathrm{Re}\left[\bar{\beta}\right]=1$. The lossless nature of the particles ensures $\mathrm{Im}\left[\bar{\beta}\right]=0$ in the guided region $\mathrm{Re}\left[\bar{\beta}\right]>1$. As the wave number enters the region $\mathrm{Re}\left[\bar{\beta}\right]<1$, the imaginary part starts increasing, due to the *conical radiation* of the leaky mode at an angle $\theta_0=\cos^{-1}\left[\mathrm{Re}\left[\bar{\beta}\right]\right]$. It is recognized that the guided modes in this longitudinal polarization are *inherently forward* in nature, since the slope $\partial\,\mathrm{Re}\left[\bar{\beta}\right]/\partial\,\mathrm{Re}\left[\bar{\alpha}_{ee}^{-1}\right]$ is negative. As explicitly proven in Ref. 20, in fact, the slope of the curves in Fig. 3.3 is directly related to whether the modes are forward (negative slope) or backward (positive), which directly determines the sign of $\partial\,\mathrm{Re}\left[\beta\right]/\partial\omega$ for passive particles in regions in which $\mathrm{Im}\left[\bar{\beta}\right]$ is negligible.

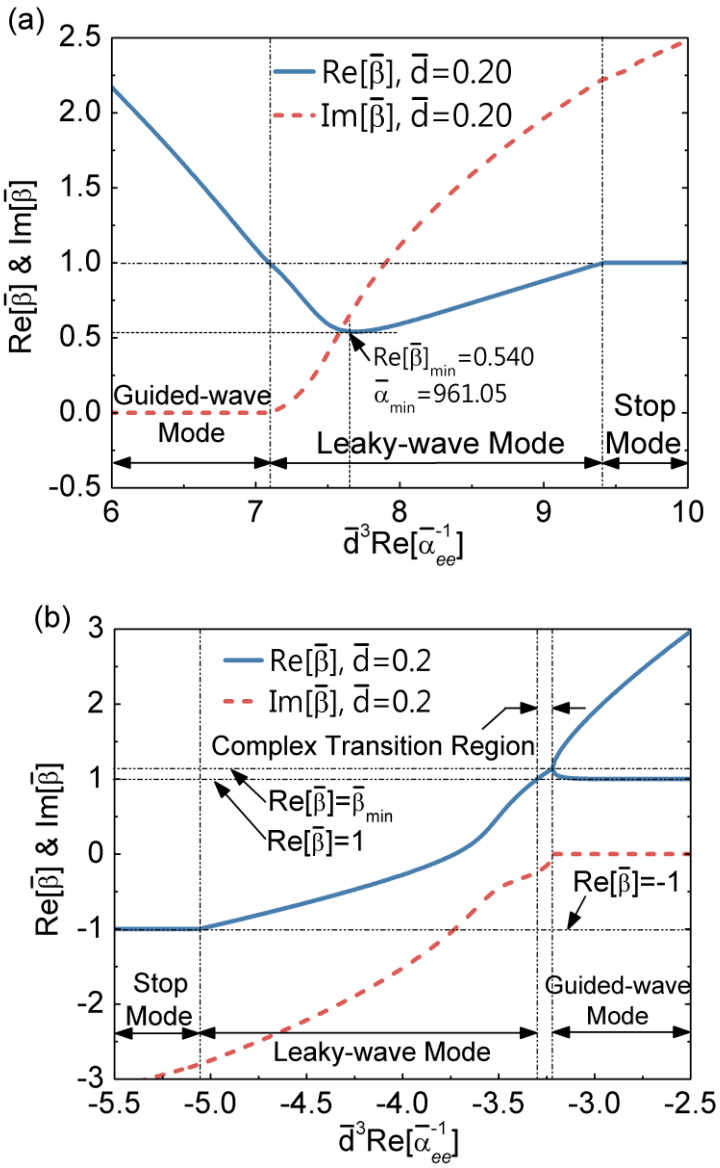

Figure 3.3 Variation of complex $\bar{\beta}$ in (a) longitudinal and (b) transverse polarizations versus the normalized inverse polarizability of the nanoparticles composing the array. Here, a normalized center-to-center distance between particles $\bar{d}=0.2$ is considered.

Also in the leaky-wave regime, for low $\mathrm{Im}\left[\bar{\beta}\right]$ negative slope is preserved, but, for the value $\bar{\alpha}_{ee}^{-1}=\bar{\alpha}_{\min}^{-1}$, the real part of $\bar{\beta}$ reaches a minimum at $\bar{\beta}_{\min}$ and then returns to $\mathrm{Re}\left[\bar{\beta}\right]=1$. Similar arguments apply in the low-damping region $\bar{\alpha}_{ee}^{-1}>\bar{\alpha}_{\min}^{-1}$,

ensuring that the supported longitudinal leaky-wave modes are forward, *improper*, in nature, as also verified by the fact that $\mathrm{Re}\left[\bar{\beta}\right]/\mathrm{Im}\left[\bar{\beta}\right]>0$, (phase and group velocities are parallel with each other) in the region with small $\mathrm{Im}\left[\bar{\beta}\right]$. As it follows from the conventional properties of leaky modes [1,6], these forward modes are inherently improper, since they grow in the transverse direction away from the array axis. Although this would violate the radiation condition for infinite arrays, these eigenmodes indeed dominate the far-field pattern of finite arrays for small $\mathrm{Im}\left[\bar{\beta}\right]$. The fact that $\mathrm{Re}\left[\bar{\beta}\right]/\mathrm{Im}\left[\bar{\beta}\right]>0$ also ensures the phase propagation is in the same direction as the power flow and energy decay.

The level of radiation damping monotonically increases with $\mathrm{Re}\left[\alpha_{ee}^{-1}\right]$, implying that the range $\mathrm{Re}\left[\alpha_{ee}^{-1}\right]<\alpha_{\min}^{-1}$ is preferable for more directive radiation. This is physically expected, since this region is closer to the resonance condition ($\mathrm{Re}\left[\alpha_{ee}^{-1}\right]=0$) of the individual nanoparticles among the array. Longitudinal leaky modes are inherently supported for positive values of $\mathrm{Re}\left[\alpha_{ee}^{-1}\right]$, due to their forward nature, since causality requires $\partial\,\mathrm{Re}\left[\alpha_{ee}^{-1}\right]\big/\partial\omega\le 0$ [20].

It is worth noticing that the point of minimum $\mathrm{Re}\left[\bar{\beta}\right]=\bar{\beta}_{\min}$ arises close to the crossing $\mathrm{Re}\left[\bar{\beta}\right]=\mathrm{Im}\left[\bar{\beta}\right]$ in Fig. 3.3a. This point may be considered the cut-off of the leaky-wave regime, since for condition $\bar{\alpha}_{ee}^{-1}>\alpha_{\min}^{-1}$ the leaky-wave radiation is damped by rapid longitudinal decay, and its directivity becomes very limited. The occurrence of a cut-off for leaky modes close to where $\mathrm{Re}\left[\bar{\beta}\right]=\mathrm{Im}\left[\bar{\beta}\right]$ is well-known in a variety of leaky-wave antennas [7], and it is verified in this geometry for different values of $\bar{d}$ in Fig. 3.3. It is interesting to note that this cut-off arises here around the region of minimum $\bar{\beta}$.

In the transverse polarization (Fig. 3.3b), the guided branch (right in the figure) is inherently *backward* in nature, since $\partial\,\mathrm{Re}\left[\bar{\beta}\right]/\partial\,\mathrm{Re}\left[\bar{\alpha}_{ee}^{-1}\right]>0$ and they decay in the

transverse direction away from the array axis. These may be considered proper physical eigensolutions of the array even in the limit of infinite geometries. As outlined in Ref. 20, a second, less confined, forward branch is also present in the guided regime, of less interest from the practical point of view, since it is very similar to a plane wave traveling unperturbed in the background with very limited confinement. A complex branch stems from the contact point between these two guided modes, which enters the leaky-wave regime for sufficiently negative $\mathrm{Re}\left[\alpha_{ee}^{-1}\right]$. The dispersion of $\mathrm{Re}\left[\bar{\beta}\right]$ with frequency in this regime decreases monotonically from +1 to -1, for decreasing $\mathrm{Re}\left[\alpha_{ee}^{-1}\right]$, crossing the axis $\mathrm{Re}\left[\bar{\beta}\right]=0$. For this specific value of inverse polarizability, the leaky mode passes from backward *proper* (for less negative $\mathrm{Re}\left[\alpha_{ee}^{-1}\right]$) to forward *improper* operation. It is evident that in this polarization we are mostly interested in the backward region, which ensures smaller damping factor $\mathrm{Im}\left[\bar{\beta}\right]$. As expected, in this polarization the most interesting region arises closer to the resonance of the individual nanoparticles, i.e., here for less negative values of $\mathrm{Re}\left[\alpha_{ee}^{-1}\right]$. The leaky-wave branch is connected to the guided branches through a complex modal regime, which is typical of a transition between leaky-wave modes and a two-branch guided-wave regime [7]. In this transition region, the mode does not radiate and propagates with complex wave number, whose real part is very close to the one of free-space, and imaginary part is non-zero.

It is interesting to stress that the inherent backward propagation of guided and leaky-wave modes with transverse polarization may be appealing in the framework of negative-index propagation, and this guided regime has been exploited to realize double-negative metamaterials in the visible [36]. In terms of leaky-wave radiation, backward radiation may be of interest to increase the degrees of freedom in tailoring and directing the optical radiation, but, as we show in the following, it is intrinsically less efficient than the forward longitudinal mode. Farther from resonance, outside the leaky-wave regime,

both polarizations have a stop-band region with $\left|\mathrm{Re}\left[\bar{\beta}\right]\right|=1$, in which the imaginary part grows in magnitude, the propagation is evanescent in nature and the damping is significantly large. In the following, we analyze more in detail the dispersion of the leaky-wave modes as a function of the interparticle distance $\bar{d}$ and of the nanoparticle polarizability, with the goal of optimizing the leaky-wave radiation in the two polarizations, and of analyzing the fundamental limitations and possibilities of leaky radiation at optical frequencies.

3.3.1.1 Longitudinally polarized modes

Being consistent with Fig 3.3a, $\mathrm{Re}\left[\bar{\beta}\right]=1$ constitutes the boundary between guided-wave and leaky-wave operation for longitudinal polarization. Literally, the leaky-wave regime is bounded by the following conditions on the nanoparticle inverse polarizability:

$$\xi(3)+Cl_3\left(2\bar{d}\right)+\bar{d}\,Cl_2\left(2\bar{d}\right)<\frac{\bar{d}^3\,\mathrm{Re}\left[\bar{\alpha}_{ee}^{-1}\right]}{3}<\mathrm{Re}\left[\,f_3\left(\bar{\beta},\bar{d}\right)-i\bar{d}f_2\left(\bar{\beta},\bar{d}\right)\right]\Big|_{\substack{\bar{\beta}\in\square\\ \mathrm{Re}\left[\bar{\beta}\right]=1}} \quad ,(3.15)$$

where $f_N\left(\bar{\beta},\bar{d}\right)$ are defined in Eq. (3.2), $Cl_N\left(\theta\right)$ are the Clausen's functions [31], which are real for real argument and $\zeta(.)$ is the Riemann Zeta function. The left-hand side has been written in closed-form using the properties of the polylogarithm functions for real argument:

$$\begin{cases} Li_1\left(e^{i\theta}\right)=Cl_1\left(\theta\right)+i\dfrac{\left(\pi-\theta\right)}{2} \\ Li_2\left(e^{i\theta}\right)=\dfrac{\pi^2}{6}-\dfrac{\theta\left(2\pi-\theta\right)}{4}+i\;Cl_2\left(\theta\right) \\ Li_3\left(e^{i\theta}\right)=Cl_3\left(\theta\right)+i\dfrac{\theta\left(\pi-\theta\right)\left(2\pi-\theta\right)}{12} \end{cases} \qquad 0\le\theta\le 2\pi\,. \qquad (3.16)$$

Figure 3.4 shows a map of the different ranges of guided-wave, leaky-wave radiation, or stop-band, as a function of $\bar{d}$ and $\mathrm{Re}\left[\bar{\alpha}_{ee}^{-1}\right]$. The dashed red line in this

plot represents the locus $\bar{\beta}=1$, which separates the guided-wave propagation (below) and leaky-wave radiation (above). The dotted green line represents the upper boundary of the leaky-wave regime, for which $\bar{\beta}\in$ and $\mathrm{Re}\left[\bar{\beta}\right]=1$. In this plot, we have also considered the locus $\mathrm{Re}\left[\bar{\beta}_{\min}\right]$ (black dotted line), which may be considered the cut-off for leaky-wave propagation, as discussed above. The solid blue line corresponds to $\bar{\beta}=\pi/\bar{d}$, which is the lower boundary of the guided regime. The regions above the leaky-wave region and below the guided-wave region are stop-band regions, where modes decay very fast along *z*-direction, and are not of interest for guidance or radiation purposes

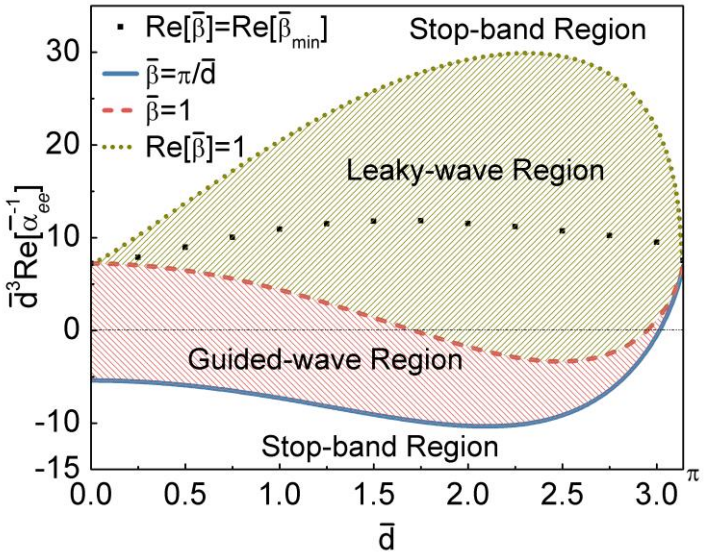

Figure 3.4 Guided- and leaky-wave regions for longitudinal polarization. The solid blue and dashed red curves are respectively the loci of real solutions $\bar{\beta}=\pi/\bar{d}$ and $\bar{\beta}=1$, which define the guided-wave regime. The dotted green line defines the upper limit of the leaky-wave regime. The black dots denote the locus $\mathrm{Re}\left[\bar{\beta}\right]=\bar{\beta}_{\min}$, which may be considered the cut-off of the leaky-wave regime.

It is seen how all the boundary curves converge at $\bar{d} = \pi$ which represents the maximum interparticle distance for supporting guided or leaky modes along arrays of sub-wavelength nanoparticles. Moreover, the leaky-wave region widens up around $\bar{d} = 2$ and it is centered above the resonance condition for the individual nanoparticles $\mathrm{Re}\left[\bar{\alpha}_{ee}^{-1}\right] = 0$. In the limit $\bar{d} \to 0$, the leaky-wave range Eq. (3.15) tends to a single point with value $\bar{d}^3 \,\mathrm{Re}\left[\bar{\alpha}_{ee}^{-1}\right] = 6\zeta(3) \approx 7.21$, implying that too closely packed chains provide a very limited leaky-wave radiation bandwidth.

One of the useful figures of merit for leaky modes is the ratio $\xi = \mathrm{Re}\left[\bar{\beta}\right] / \mathrm{Im}\left[\bar{\beta}\right]$. A lower $\mathrm{Re}\left[\bar{\beta}\right]$ may be desirable for radiation closer to the normal to the array, but this is usually accompanied by a larger $\mathrm{Im}\left[\bar{\beta}\right]$, which implies shorter propagation distance, and inherently lower directivity. As mentioned above, the cut-off of the leaky mode may be defined by $\xi = 1$. Overall, a larger value of ξ ensures larger directivity and radiation farther from the array axis, both desirable features of a leaky-wave antenna.

Figure 3.5 shows the variation of $\log \xi$ versus $\mathrm{Re}\left[\bar{\beta}\right]$ for different values of interparticle distance. The ratio ξ tends to infinity for $\mathrm{Re}\left[\bar{\beta}\right] \approx 1$, since we are operating near the guided-wave regime and lossless particles are being considered here. This region is characterized by *endfire* radiation, consistent with the limit of a surface mode propagating along the chain. A wider range of $\mathrm{Re}\left[\bar{\beta}\right]$ implies that energy may be coupled into a broader angular spectrum, which is more appealing for antenna applications. Figure 3.4 confirms that better ratios ξ and wider variation along $\mathrm{Re}\left[\bar{\beta}\right]$ may be obtained by choosing a smaller value of $\bar{d}$. This is to be expected, since the nanoparticles in this regime are tightly coupled, ensuring more flexibility in terms of guidance and radiation. Consistent with Fig. 3.3, however, the available

bandwidth of leaky-wave operation shrinks down for smaller values of $\bar{d}$. It should be stressed, in addition, that small interparticle distance necessarily requires nanoparticles with smaller diameters, which in turn implies higher individual Q factors and more sensitivity to losses.

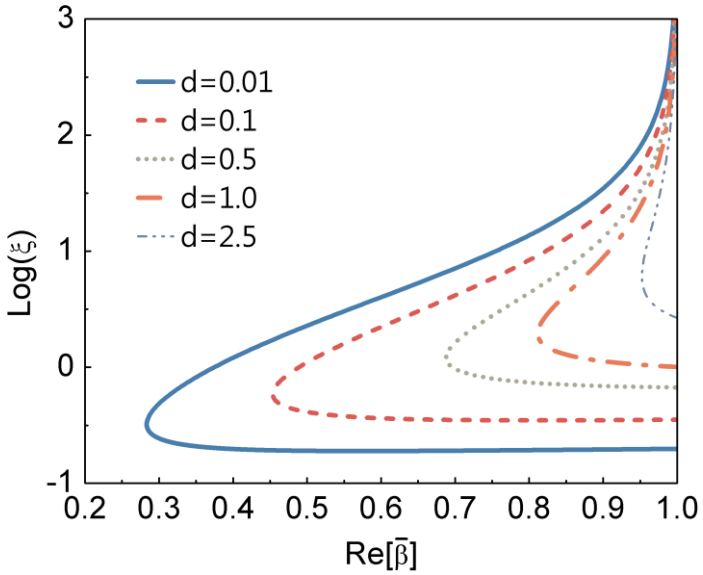

Figure 3.5 Variation of the ratio $\xi = \mathrm{Re}\left[\bar{\beta}\right]/\mathrm{Im}\left[\bar{\beta}\right]$ for the supported leaky-wave modes of the nanoparticle chain of Fig. 3.1 for longitudinal polarization, varying the center-to-center distance.

3.3.1.2 Transversely polarized modes

Transversely polarized leaky modes behave quite differently. As discussed above, guided-wave and leaky-wave regions are separated by a complex transition region, not existing in the longitudinal polarization. By setting $\mathrm{Re}\left[\bar{\beta}\right] = \pm 1$ and solving for the corresponding $\mathrm{Im}\left[\bar{\beta}\right]$ in Eq. (3.1), we can obtain the range of polarizability values that support leaky-wave propagation in this regime. This condition may be formally expressed as:

$$\left[f_3\left(\bar{\beta},\bar{d}\right) - i\bar{d}\, f_2\left(\bar{\beta},\bar{d}\right) - \bar{d}^2 f_1\left(\bar{\beta},\bar{d}\right) \right]\Big|_{\mathrm{Re}\left[\bar{\beta}\right]=-1}$$
$$< -\frac{2}{3}\bar{d}^3\bar{\alpha}_{ee}^{-1} < \left[f_3\left(\bar{\beta},\bar{d}\right) - i\bar{d}\, f_2\left(\bar{\beta},\bar{d}\right) - \bar{d}^2 f_1\left(\bar{\beta},\bar{d}\right) \right]\Big|_{\mathrm{Re}\left[\bar{\beta}\right]=1} , \quad (3.17)$$

where $f_N\left(\bar{\beta},\bar{d}\right)$ are defined in Eq. (3.2).

Figure 3.6 shows the different modal regions for transversely polarized modes as a function of $\bar{d}$ and $\bar{\alpha}_{ee}^{-1}$, analogous to Fig. 3.4. Like the longitudinal case, the leaky-wave regime converges to a single point for $\bar{d} \to 0$, implying that also in this polarization the leaky-wave regime is of narrow bandwidth for very tight nanoparticle arrangement. On the other extreme, towards $\bar{d} = \pi$, the modal region widens, ensuring a relatively broad range of normalized polarizability values that support leaky modes. As we will point out in the following, however, the corresponding $\mathrm{Im}\left[\bar{\beta}\right]$ is rather large for this range of interparticle distance.

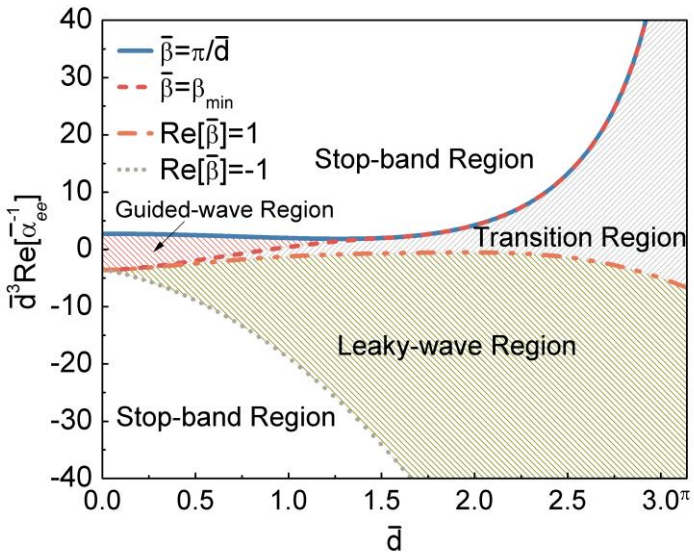

Figure 3.6 Analogous to Fig. 3.4, guided- and leaky-wave regions for transversely polarized modes.

Figure 3.7 presents the variations of ξ with the array properties in this polarization, analogous to Fig. 3.5. It is evident comparing these two figures that it is more challenging to obtain a reasonably large figure of merit in the transverse polarization. As anticipated earlier, the region of most interest is localized in the backward-wave region, for positive $\mathrm{Re}\left[\bar{\beta}\right]$ (right portion of Fig. 3.7). Due to the presence of a complex transition region between guided-wave and leaky-wave modes, in this polarization the imaginary part $\mathrm{Im}\left[\bar{\beta}\right]$ is not negligible even for values $\mathrm{Re}\left[\bar{\beta}\right] \square 1^{-}$, and the ratio ξ is never remarkably large. These results confirm the general dispersion properties of transverse modes highlighted in Fig. 3.3b.

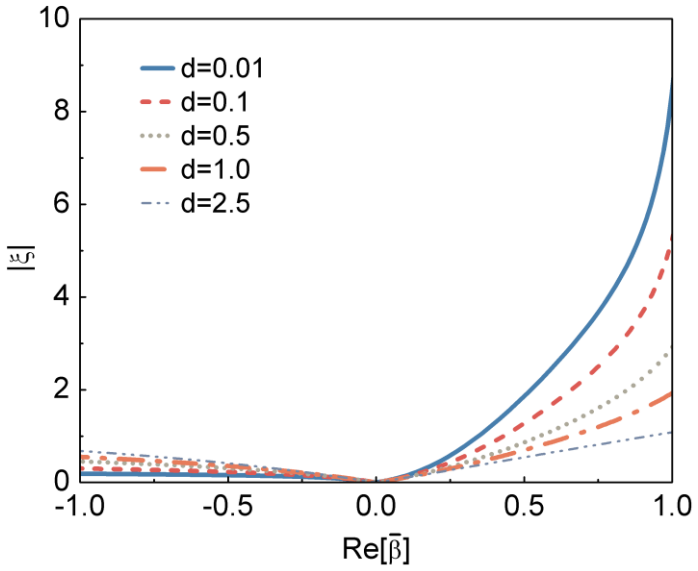

Figure 3.7 Analogous to Fig. 3.5, variation of ξ vs. $\mathrm{Re}\left[\bar{\beta}\right]$ for transversely polarized leaky modes, varying the center-to-center distance.

3.3.1.3 Realistic models for nanoparticles

In the previous sections, we have analyzed the general conditions and limitations for leaky-wave propagation along sub-wavelength nanoparticle chains, considering a general

model for the nanoparticle polarizability. In particular, we have shown that longitudinal forward leaky-wave modes may provide better directivity properties than transverse modes, due to their significantly larger value of ξ for the same interparticle distance. Moreover, we have outlined the range of $\mathrm{Re}\left[\bar{\alpha}_{ee}^{-1}\right]$ required to sustain leaky-wave radiation. In the following, we consider *realistic* nanoparticle geometries and materials to apply the previous general results to several practical designs for optical leaky-wave arrays.

In practice, $\mathrm{Re}\left[\bar{\alpha}_{ee}^{-1}\right]$ is determined by the specific design and shape of the nanoparticles forming the array. In the case of spherical nanoparticles of radius *a* and permittivity ε, for instance, we obtain [38]:

$$\mathrm{Re}\left[\bar{\alpha}_{ee}^{-1}\right] \approx \frac{3}{2}\left(k_0 a\right)^{-3} \frac{\varepsilon + 2\varepsilon_0}{\varepsilon - \varepsilon_0}, \tag{3.18}$$

in the quasi-static limit of interest here. It is evident that there is a wide range of flexibility in the shape and material properties of the nanoparticles to tailor the value of $\mathrm{Re}\left[\bar{\alpha}_{ee}^{-1}\right]$ at the frequencies of interest. In the following, we focus on homogeneous nanospheres in Eq. (3.18) and analyze how their design parameters affect the leaky-wave dispersion.

Before analyzing in detail the nanosphere problem, it is relevant to highlight a common trend in the previous Eq. (3.18): the value of $\mathrm{Re}\left[\bar{\alpha}_{ee}^{-1}\right]$ tends to diverge for small nanoparticles $\left(k_0 a\right) \to 0$. On the other hand, leaky-wave radiation requires finite values of $\mathrm{Re}\left[\bar{\alpha}_{ee}^{-1}\right]$, as shown in the previous section. This implies that the operation of these leaky-wave nanoantennas with sub-diffractive lateral cross section will arise in the frequency range for which the numerator in the right-hand side of Eqs. (3.18) is closed to zero, i.e., near a plasmonic resonance for the specific shape of interest. For larger $\bar{d}$

this condition becomes more and more stringent, since $\mathrm{Re}\left[\bar{\alpha}_{ee}^{-1}\right]$ is required to be closer to zero. This is reflected in a general trade-off between size of these leaky-wave antennas and their bandwidth and robustness to the presence of loss and disorder.

3.3.1.4 Leaky-wave modal dispersion with the nanosphere permittivity

For spherical nanoparticles, we may use Eq. (3.18) to determine the range of permittivities ε that may allow leaky-wave propagation along the nanoparticle chain. Figure 3.8a shows the longitudinal guided and leaky modal regions in the diagram of $\varepsilon/\varepsilon_0$ versus $\bar{d}$, for different values of the nanosphere radius a. The different curves refer to different ratios $\eta = d/a$ and we have used shadowing to highlight the guided-wave and leaky-wave regions in the case $\eta = 3$. As it may be seen, the leaky-wave region requires more negative permittivity values than the guided-wave region, which is centered at the resonance condition of the individual nanospheres $\varepsilon = -2\varepsilon_0$. Denser chains support a wider range of permittivities to achieve leaky-wave propagation, since the permittivity range gets wider for smaller values of η (of course there is a geometrical limit of $\eta > 2$ to consider in the design). This is reflected in wider bandwidths, as negative permittivity is necessarily dispersive with frequency [38]. Consistent with the previous section, in the mathematical limit $\bar{d} \to 0$ leaky waves are not supported, but the permittivity region rapidly widens up for slightly larger values of $\bar{d}$. Figure 3.8b shows the loci of constant $\xi = \mathrm{Re}\left[\bar{\beta}\right]/\mathrm{Im}\left[\bar{\beta}\right]$ for $\eta = 2.2$, as an example. Consistent with the results of the previous section, it is seen that low attenuation rate is achieved close to the boundary of the guided-wave mode region, corresponding to end-fire radiation. However, relatively large values of ξ may be achieved even farther away from the guided-wave regime, which may provide conical off-axis radiation.

Moreover, the natural permittivity dispersion of metals may provide frequency scanning for the conical beams radiated by the chain.

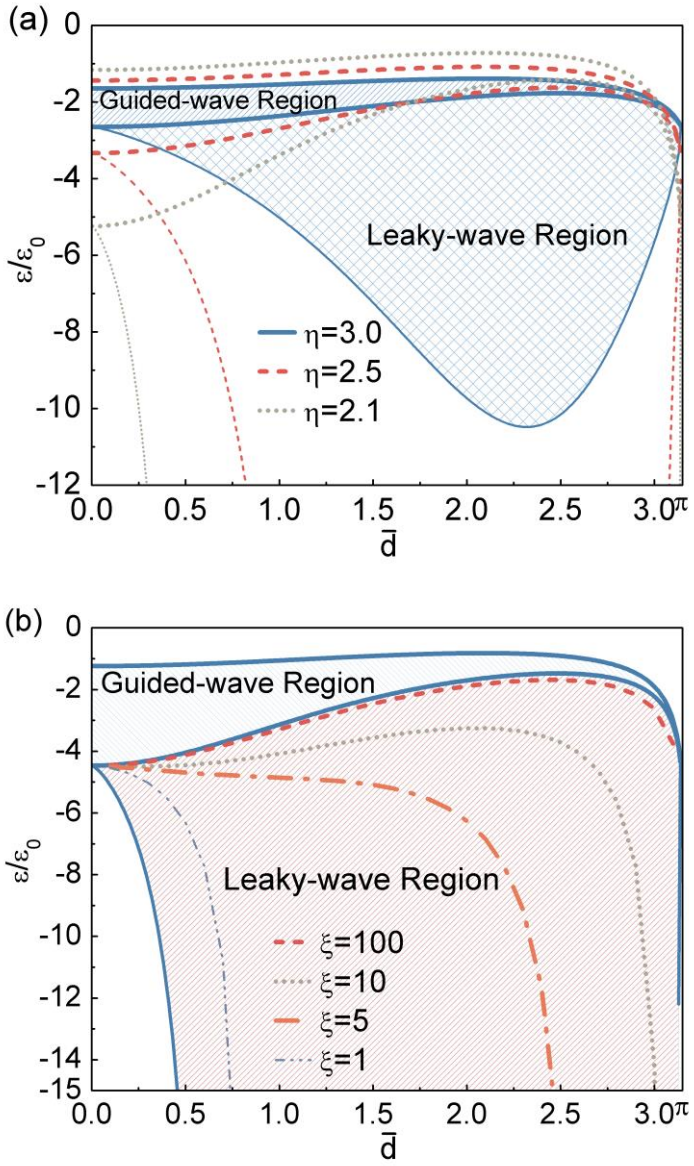

Figure 3.8 (a) Guided-wave and leaky-wave regions for longitudinal polarization, as a function of nanosphere permittivity and interparticle distance. The guided-wave regime is supported between the bold lines, while the leaky-wave region is bounded by thinner lines. (b) Loci of constant $\xi = \mathrm{Re}[\bar{\beta}]/\mathrm{Im}[\bar{\beta}]$ in the leaky-wave region for $\eta = 2.2$. Blue solid lines delimit the guided-wave and leaky-wave regions.

Figure 3.9 shows analogous plots for the transverse polarization mode. Due to the backward nature of guided and leaky modes in this polarization, less negative values of permittivity are required as compared to the guided regime. Also in this case, by

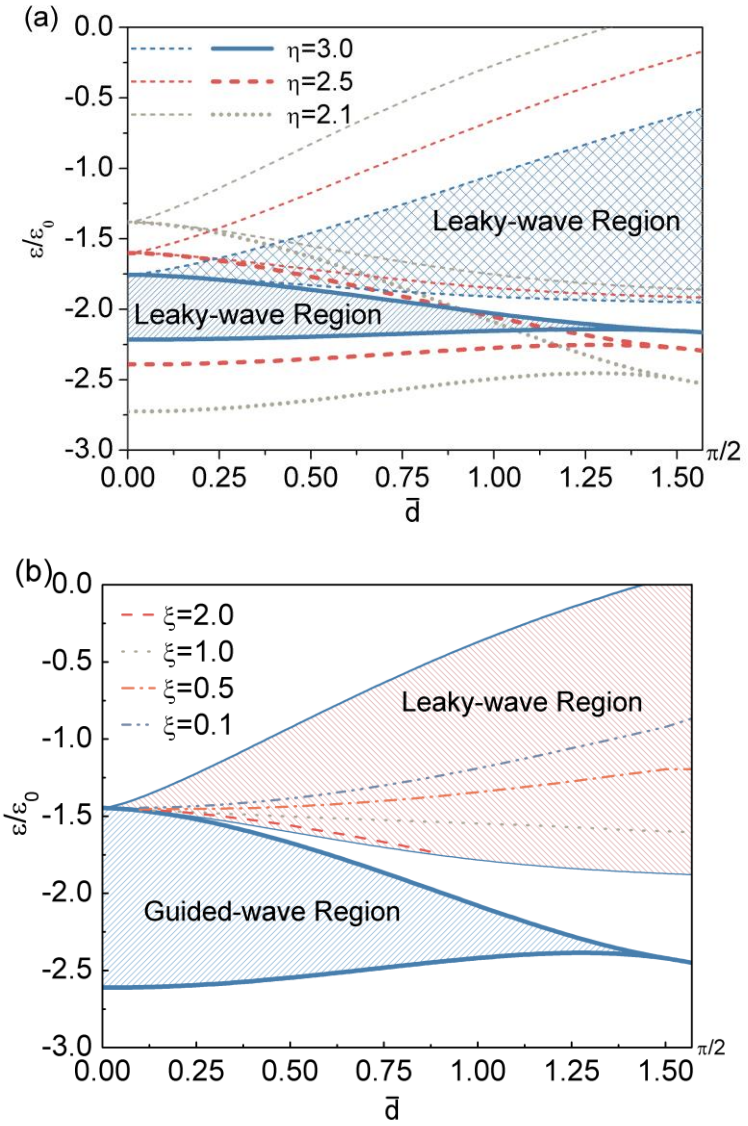

Figure 3.9 Analogous to Fig. 3.8, but for transverse polarization.

decreasing the value of η the leaky-wave operation broadens in bandwidth. Comparing Figs. 3.8 and 3.9, it is seen that longitudinal leaky modes have a broader leaky-wave region and obviously larger values of ξ, implying that they may outperform the transverse backward-wave leaky modes in terms of directivity and bandwidth of operation. These results are consistent with the discussion in the previous section, but applied here specifically to the nanosphere geometry.

3.3.1.5 Realistic plasmonic materials

The previous results suggest that chains of metamaterial or plasmonic nanoparticles with negative permittivity and moderate losses may provide a promising mean to realize a leaky-wave nanoantenna with subwavelength transverse cross-section. For this purpose, noble metals, or combinations of noble metals and dielectrics, may be chosen to realize such nanochains, following the design guidelines represented by Eqs. (3.18). Metallic nanoparticles made of silver or gold, for instance, have shown moderate guidance properties in the optical regime [12]. In this subsection, we consider the realistic properties of noble metals in the realization of these nanoantennas. For simplicity, we focus on nanospheres and on longitudinally polarized modes, which ensure better radiation performance and more robustness to the effect of absorption in the materials under consideration.

Figure 3.10 shows the complex dispersion relations $\beta d - k_0 d$ for linear arrays composed of silver nanospheres, considering experimental values of permittivity [42], frequency dispersion and loss. In this case, we have chosen $\eta = 2.1$ and nanosphere radii of 25 (blue solid line) and 50 nm (red dashed). Figure 3.10a and b report the real and imaginary parts of βd, respectively. It is seen that larger particles may provide wider bandwidth of leaky-wave radiation, due to the inherently larger period, and they are

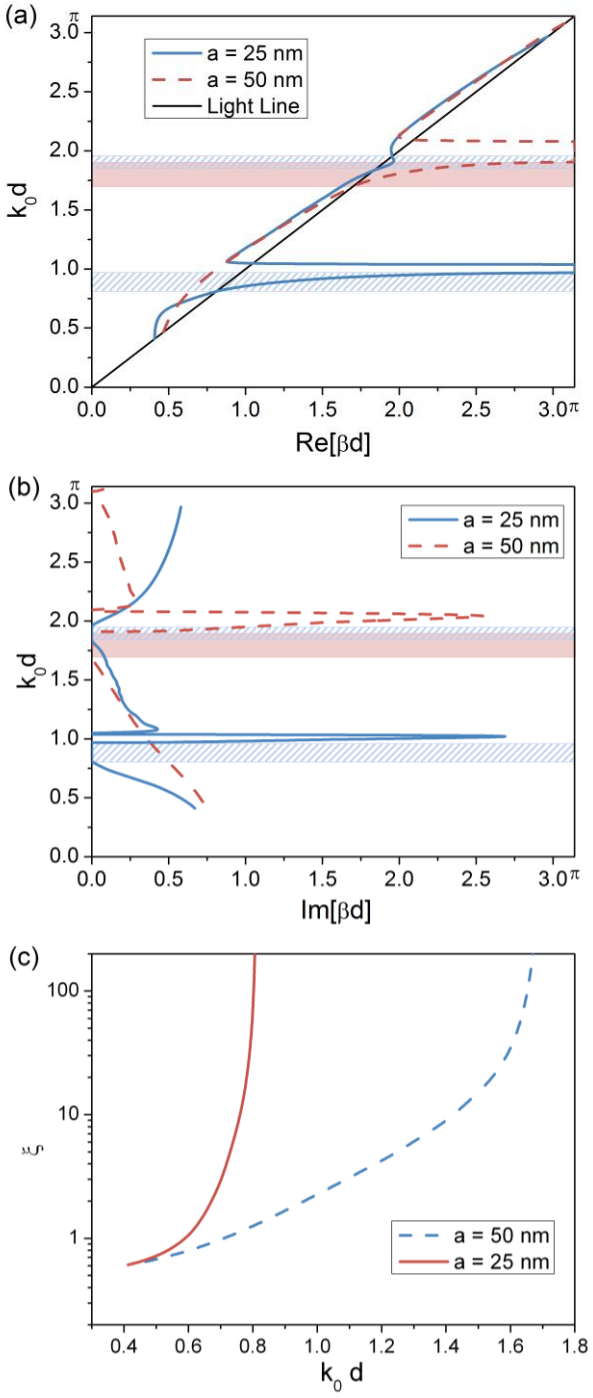

Figure 3.10 $\bar{\beta}d$ vs. $k_0 d$ diagrams and ξ for longitudinal modes supported by silver arrays with $\eta = 2.1$.

inherently more robust to the presence of loss, consistent with analogous results in the guided region [20]. The shadowed regions in the figure indicate these guidance regions. Figure 3.10c reports the calculated values of ξ for the leaky-wave operation. Significantly large values may be achieved near the endfire radiation, despite the presence of loss and the overall sub-diffractive lateral cross-section of these nanoantennas. These results are particularly encouraging for the realization of these concepts using arrays of subwavelength silver nanoparticles.

3.3.1.6 Comparison with dielectric nanosphere arrays

The previous results imply that plasmonic nanoparticles may represent a promising means for the realization of sub-diffractive leaky-wave nanoantennas. In this subsection we compare their performance with the one of dielectric nanoparticles, focusing in the range $\bar{d} < \pi$. Figure 3.11 shows the dispersion of complex modes along a dense array ($\eta = 2.1$) of dielectric spheres with $\varepsilon = 5\varepsilon_0$ and with $\varepsilon = 45\varepsilon_0$. For consistency with the previous results, we show only guided modes supported by the induced electric dipoles along the array for longitudinal polarization, although for large dielectric constants magnetic modes are also available. Fig. 3.11a and 3.11b report the dispersion diagrams for $\mathrm{Re}\left[\bar{\beta}\right]$ and the corresponding $\mathrm{Im}\left[\bar{\beta}\right]$, respectively. For the low permittivity spheres (blue line), guided modes are not available in this low-frequency regime, as expected, and a small complex branch is visible near the light line. Since we are far from resonance, however, the value of ξ is always less than unity, implying poor radiation properties, as expected. Drastically increasing the nanosphere permittivity it is possible to induce electric dipole resonances, despite the deep subwavelength size of the particles. In this situation, both guided-wave and leaky-wave regimes are available, and the dispersion

diagrams are characterized by narrow guided-wave regions (highlighted by the shadowed regions) connected by leaky-wave branches.

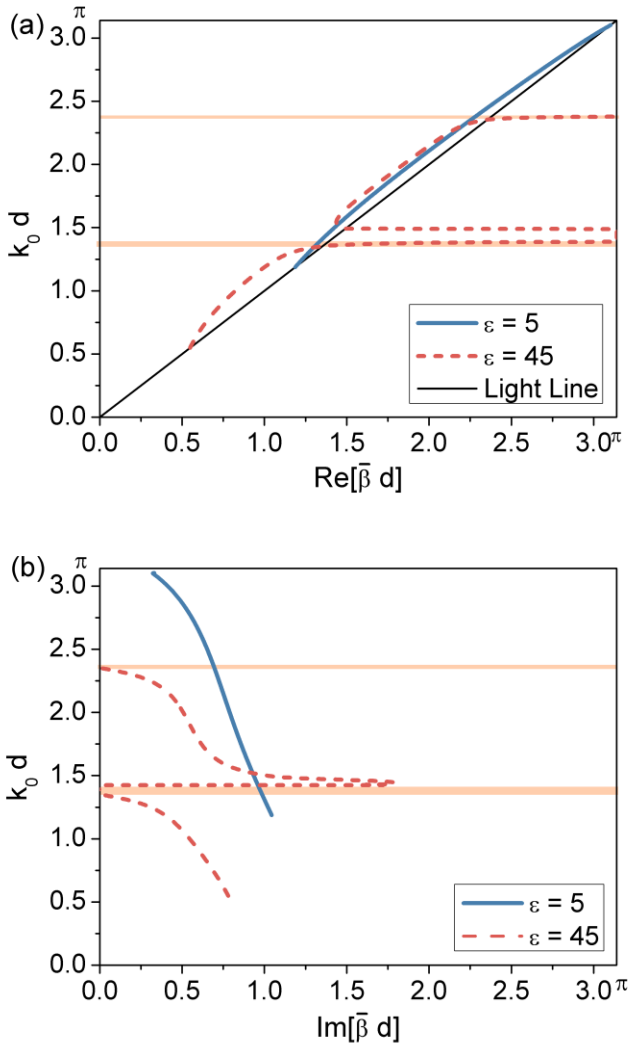

Figure 3.11 Dispersion diagrams $\bar{\beta}d$ vs. $k_0 d$ for longitudinal modes supported by dielectric particle arrays with $\eta = 2.1$.

In some frequency ranges, significant directivity may be achieved, although the radiation is limited to grazing angles, close to the light line in the diagrams of Fig. 3.11. It

is evident that large permittivity spheres may be also effective in supporting sub-diffractive leaky radiation, although the efficiency and directivity values achieved in this example are lower than for plasmonic particles and it may be challenging to realize such large values of permittivity at visible wavelengths. Plasmonic materials with the required values of permittivity, on the contrary, are naturally available at these frequencies, and their dispersion may naturally provide a larger degree of frequency scanning compared to large permittivity materials.

3.3.2 Parallel Particle Chains

Based on the physical and numerical analyses presented in the previous section, we extend our discussion to the parallel particle arrays analyzed in the previous section. Again, we focus our study on the leaky-wave regime and draw comparison with the results of isolated particle chains. In this part, we directly apply realistic material silver with experimental values of permittivity (see Appendix B and Ref. 43). The mutual coupling between the parallel arrays affects the propagation and radiation properties by splitting and coupling the modes of an isolated chain into symmetric and anti-symmetric types on the parallel structures.

3.3.2.1 Longitudinally polarized modes

Figure 3.12 shows the dispersion of the complex wave number versus optical frequencies from 350 to 600 THz (or from 857 to 500 nm in wavelength) for the single and parallel chains composed of silver nanoparticles with radius 10 nm and interparticle distance $\eta = 2.1$. Various interchain distances are considered to reveal how the field coupling between particle chains induces mode splitting in the dispersion relations. As discussed previously for a single array, when the wave number enters the region $\mathrm{Re}\left[\bar{\beta}\right] < 1$, the imaginary part monotonically increases, due to the conical radiation of the leaky-mode at

an angle $\theta = \cos^{-1}\left[\mathrm{Re}\left[\bar{\beta}\right]\right]$. Two different loci corresponding to symmetric and anti-symmetric modes are shown in the parallel array case. For the symmetric mode, the induced dipole moments on two individual chain point at the same direction, while the anti-symmetric mode has opposite dipole moment pairs in the arrays. Although these two modes have different field characteristics, they are both forward propagating along the parallel chains for longitudinal polarization.

By comparing Fig. 3.12a, b and c, we can see obvious mode splitting when we pull the arrays closer, because smaller interchain distance may result in stronger coupling between parallel chains. In general, the symmetric mode has larger leaky-wave efficiency $\xi = \mathrm{Re}\left[\bar{\beta}\right]/\mathrm{Im}\left[\bar{\beta}\right]$, which provides better performance in terms of leaky-wave radiation. Therefore, this mode is more promising than the single array for directive radiation application, especially in the region around 550 THz with slow variation of $\mathrm{Im}\left[\bar{\beta}\right]$, as shown in Fig. 3.12a and b. On the other hand, the anti-symmetric mode corresponds to a smaller ratio $\mathrm{Re}\left[\bar{\beta}\right]/\mathrm{Im}\left[\bar{\beta}\right]$, which limits the efficiency of leaky-wave radiation and propagation. In general, for larger interchain distance, it is easier to excite the symmetric mode. In the single-chain system, we may see that the minimum point $\mathrm{Re}\left[\bar{\beta}\right] = \bar{\beta}_{\min}$ arises around the crossing $\mathrm{Re}\left[\bar{\beta}\right] = \mathrm{Im}\left[\bar{\beta}\right]$ of solution loci. This condition is considered as the "cut-off" for the leaky-wave antennas, as noticed above. However, this condition is not shown in the parallel-chain system with mode splitting, especially for larger interchain distance.

3.3.2.2 Transversely polarized modes

The transverse case also experiences mode splitting for parallel linear chains, as shown in Fig 3.13a and b. Like the longitudinal modes, the level of mode splitting for the transverse polarization depends on the interchain distance. It is worth noting that the loci

of the real part of wave number are more sensitive than those for the imaginary part to the array coupling.

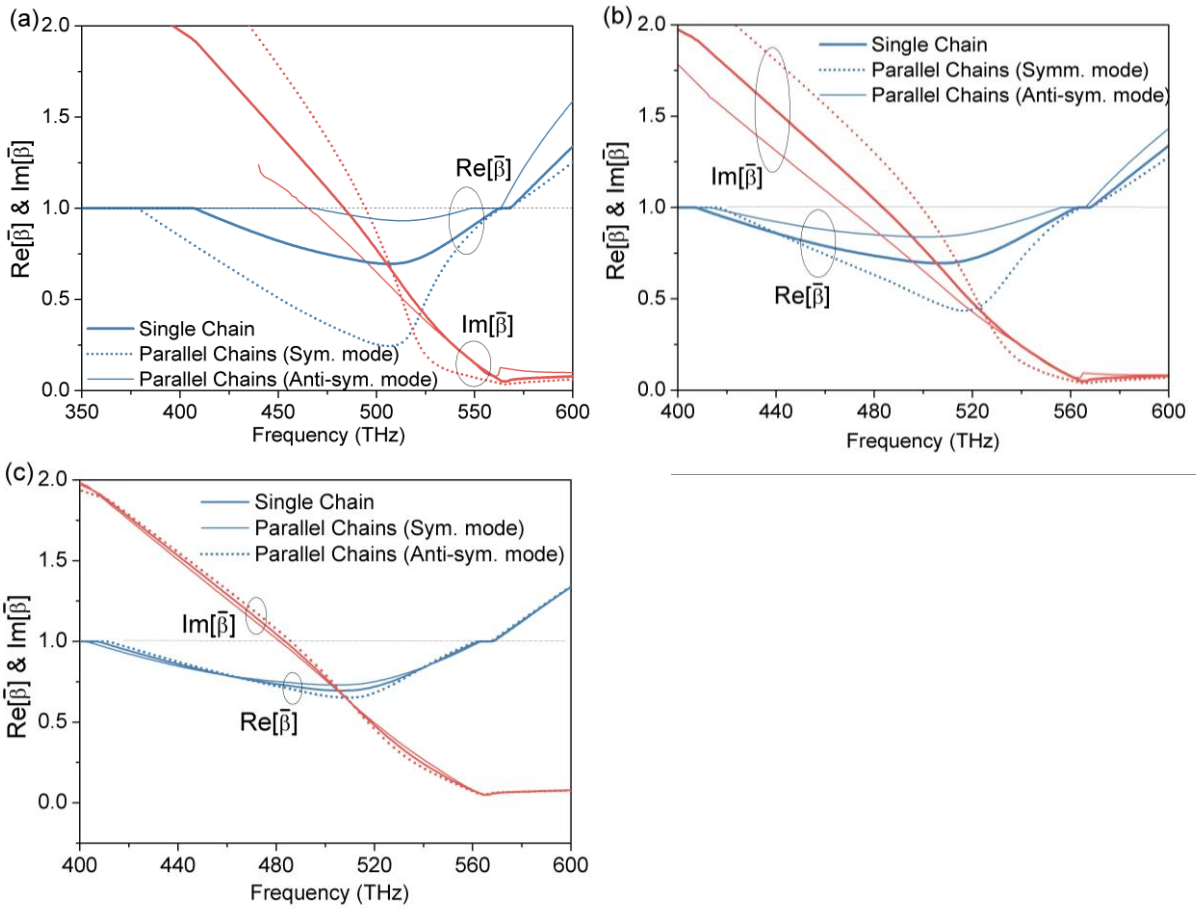

Figure 3.12 Dispersions of complex $\bar{\beta}$ versus frequency for single- and parallel-chains and longitudinal polarization. Here, we consider silver particles with radius 10 nm, normalized interparticle distance $\eta = 2.1$, and interchain distance (a) $\bar{l}$=3, (b) $\bar{l}$=5 and (b) $\bar{l}$=20, respectively.

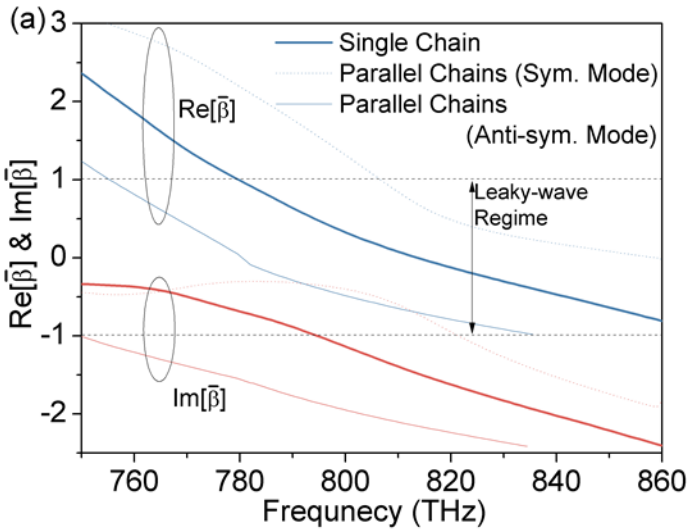

Figure 3.13 Dispersions of complex $\bar{\beta}$ in transverse versus frequency of single- and parallel-chain systems. Here, we consider silver particles with radius 10 nm, normalized interparticle distance $\eta = 2.1$, and interchain distance (a) $\bar{l}$=3 and (b) $\bar{l}$=5, respectively.

Generally, the real part, which determines wave propagation or radiation, is largely affected by the array coupling, while the imaginary part is mainly decided by intrinsic material losses in this case. Both the symmetric and anti-symmetric modes are backward

propagating due to $\mathrm{Im}\left[\bar{\beta}\right] < 0$, as we discussed in the single chain system. In this transverse mode, complex wave numbers have much larger imaginary parts, which limits long-distance wave propagation. This feature makes the leaky-wave phenomena in transverse polarization less promising for communication purposes. Therefore, we concentrate our analysis on longitudinal mode in the following discussion.

3.3.2.3 Modal analysis in longitudinal polarization

As shown in Fig 3.4, guided and leaky wave regions share the same border line and the condition $\mathrm{Re}\left[\bar{\beta}\right] = 1$ constitutes the boundary of leaky-mode operation. For the parallel chains, however, the additional mutual coupling between linear arrays makes the linear eigensystem rather complicated, such that an elegant form similar to Eq. (3.15) in the single chain system for defining mode regime is not available. Therefore, we employ the numerical process to find the roots in the leaky-wave regime boundary $\mathrm{Re}\left[\bar{\beta}\right] = 1$.

Figure 3.14 presents the regime for leaky-wave modes under longitudinal polarization. It is obvious that the regions of symmetric and anti-symmetric modes saturate for large interchain distances (around $\bar{l} \approx 7$). This is because when the parallel chains are pulled apart to a certain distance, the coupling becomes less important than the neighboring particle interactions along a single chain. Therefore, the mutual polarization does not influence the leaky-wave region for large $\bar{l}$. However, this interchain weak coupling still provides the mechanism for mode-splitting. If we further increase $\bar{l}$, for instance $\bar{l} = 20$, the symmetry and anti-symmetric modes would degenerate to the simple longitudinal mode of a single chain due to the negligible coupling effect. This degeneration can be easily understood in analytical way by applying very large $\bar{l}$ in Eq. (3.9), where all the generic coupling coefficients reduce to zero due to the nature of modified Bessel function of the second kind, $\lim_{x \to 0} K_n\left[x\right] = 0$. Moreover, all the off-

diagonal terms in the first determinant of Eq. (3.10) become zero, and the polarizations $\mathbf{p}_1$ and $\mathbf{p}_2$ on two individual chains become independent.

On the other hand, for smaller values of $\bar{l}$, the window of anti-symmetric mode shrink down, but the region for symmetric mode is widened. The induced magnetic fields (red arrows in Fig 3.14c and d) around $\mathbf{p}_1$ and $\mathbf{p}_2$ for symmetric and anti-symmetric modes help to explain this phenomenon: in the symmetric case, the induced magnetic fields point in opposite directions in the gap and they cancel each other in the chain gaps, provided that the magnitude of $\mathbf{p}_1$ and $\mathbf{p}_2$ are identical. As the chains are placed closer, the magnetic field distribution may reduce to the single chain scenario and the closed arrangement may allow us to treat the parallel chains as a dimer array. The dimer elements may show larger frequency window for leaky mode. On the other hand, the anti-symmetric configuration can confine much stronger field between the parallel chains, instead of leaking the wave out. The field concentration therefore leads to a smaller window in Fig. 3.14a.

Although we can have a spectrum of leaky-wave modes as wide as 100 THz for parallel chains, it is worth noticing that the leaky-wave efficiency $\xi = \mathrm{Re}\left[\bar{\beta}\right]/\mathrm{Im}\left[\bar{\beta}\right]$ is rather important when we consider its radiation applications. In Fig. 3.15, we show the efficiency for parallel chains and demonstrate how the ratio of real and imaginary part of wave number varies in the leaky-wave window. In this figure, we also show the efficiency for a single chain (black line) as a reference. It is obvious that the curves of symmetric and anti-symmetric modes are split toward opposite directions compared to the single-chain reference line. The curves corresponding to large $\bar{l}$ are just slightly separated apart from the solid line. This is can be understood by the strength of coupling between chains, as mentioned above. The weaker interaction does not significantly change the results of a single isolated chain. For the closely arranged pair, we see the

curves move to extreme regions. The anti-symmetric mode, with $\bar{l} = 2.5$ and $\xi < 5$, may lose its leaky-wave features because the wave cannot propagate very long and the energy is rapidly dissipated within one wavelength.

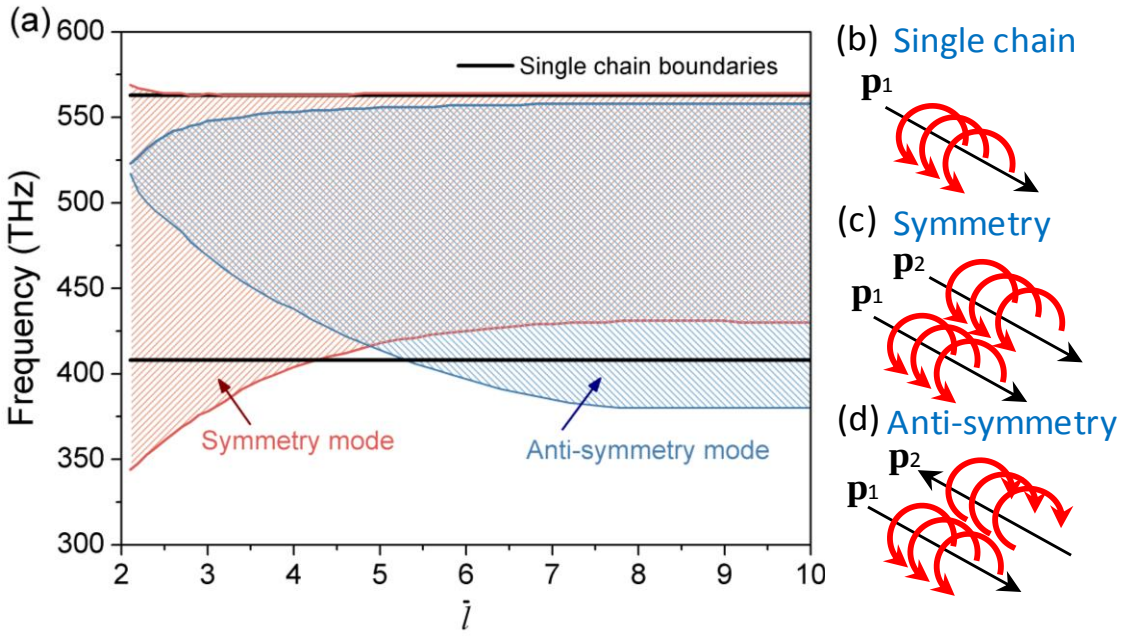

Figure 3.14 (a) Valid frequency regions of leaky-wave modes for longitudinal polarization. The red and blue regions are the valid frequencies for symmetric and anti-symmetric modes with various interchain distances $\bar{l}$. We assumed a normalized interparticle distance $\eta = 2.1$. The leaky-wave boundary for single chain with the same geometry parameters is also shown by black solid lines. (b), (c) and (d) schematically show the induced polarizations on single and parallel chains and their associated magnetic field circulation.

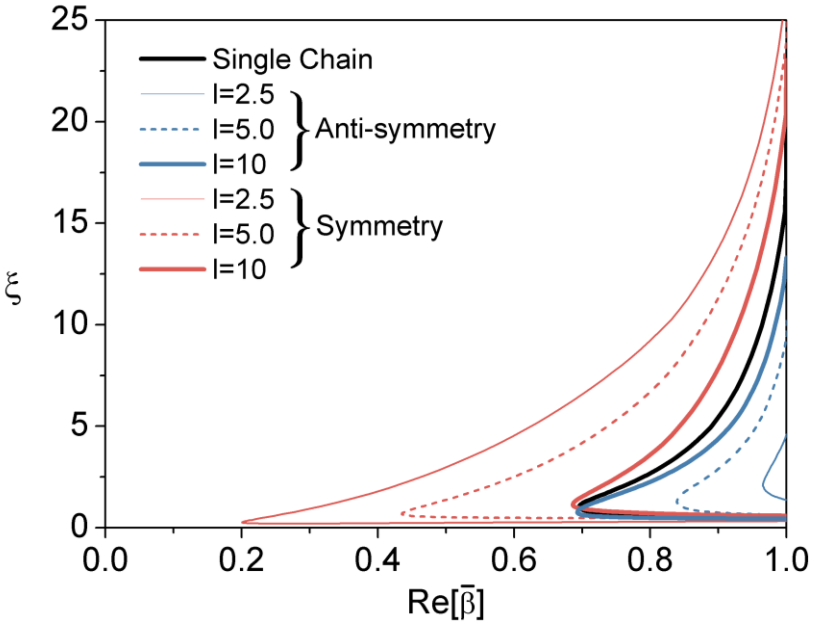

Figure 3.15 Leaky-wave efficiency $\xi = \mathrm{Re}\left[\bar{\beta}\right]/\mathrm{Im}\left[\bar{\beta}\right]$ on single and parallel chains. Here, we used the silver particle of radius 10 nm and normalized interparticle distance $\eta = 2.1$ with various interchain distances.

Compared with the anti-symmetric mode, the symmetric configuration is more promising for leaky-wave radiation applications. The curves may extend to the region with large $\mathrm{Re}\left[\bar{\beta}\right]$ and ξ, or the top-right region in Fig 3.15. By checking the efficiency curves of leaky-wave modes, we realize that only a portion of the valid leaky-wave region in Fig 3.13 provides a useful condition for radiation. Generally, when designing leaky-wave nanoantennas based on this particle arrays, we may prefer wave numbers with smaller imaginary parts closer to the guidance region.

3.4 Effects of Absorption and Material Loss

In this section, we focus on the effects of material absorption and loss and discuss how this physical limitation affects wave propagation and radiation on a single particle chain. This is a crucial aspect to consider, since negative permittivity, required to support

subdiffractive leaky-wave operation, is usually combined with finite absorption [38]. Material losses are known to play an important role in plasmonic devices with subwavelength cross sections, such as nanoparticle waveguides [20, 40-41]. In the case of lossy materials, the quasi-static inverse polarizability is related to the complex permittivity $\varepsilon = \varepsilon_r + i\varepsilon_i$ as:

$$\begin{aligned} \mathrm{Re}\left[\bar{\alpha}_{ee}^{-1}\right] &= \frac{3}{2}\left(k_0 a\right)^{-3} \frac{\left(\varepsilon_r + 2\varepsilon_0\right)\left(\varepsilon_r - \varepsilon_0\right) + \varepsilon_i^2}{\left(\varepsilon_r - \varepsilon_0\right)^2 + \varepsilon_i^2} \\ \mathrm{Im}\left[\bar{\alpha}_{ee}^{-1}\right] &= -1 - \frac{9}{2}\left(k_0 a\right)^{-3} \frac{\varepsilon_0 \varepsilon_i}{\left(\varepsilon_r - \varepsilon_0\right)^2 + \varepsilon_i^2} \end{aligned} \quad . \tag{5.19}$$

For low-loss particles, of interest here, ε_i is small and the associated additional contribution to $\mathrm{Im}\left[\bar{\alpha}_{ee}^{-1}\right]$ provides a first-order perturbation of the lossless results derived above.

Figure 3.16 reports the dispersion of $\mathrm{Re}\left[\bar{\beta}\right]$ and $\mathrm{Im}\left[\bar{\beta}\right]$ versus ε_r for longitudinally polarized modes, for $\bar{d} = 0.1$, $\eta = d/a = 2.1$ and different levels of material absorption ε_i. It is interesting to see how in the guided-wave region a moderate increase of ε_i principally affects $\mathrm{Im}\left[\bar{\beta}\right]$, but leaves unaltered $\mathrm{Re}\left[\bar{\beta}\right]$ and correspondingly the phase velocity. Since the transition towards the leaky-wave regime is continuous for longitudinal polarization, the presence of material loss implies a reduction of the achievable values of ξ, even near the guided-wave region. In the leaky-wave region, however, the trend is opposite: $\mathrm{Im}\left[\bar{\beta}\right]$ is not sensibly altered, being mainly dominated by radiation losses (the mode is less confined to the particles), and the additional small loss mainly affects the angle of radiation and $\mathrm{Re}\left[\bar{\beta}\right]$. It is worth noticing that a complex-valued transition region may arise for relatively larger values of ε_i, for which $\mathrm{Re}\left[\bar{\beta}\right] = 1$. A zoom of this transition region for $\varepsilon_i = 0.1$ is reported in

the inset of Fig. 3.16. The figure confirms that realistic levels of absorption in optical materials may provide the possibility to realize nanoantennas with sub-diffractive lateral cross section able to sustain such longitudinal leaky modes with directive radiation properties.

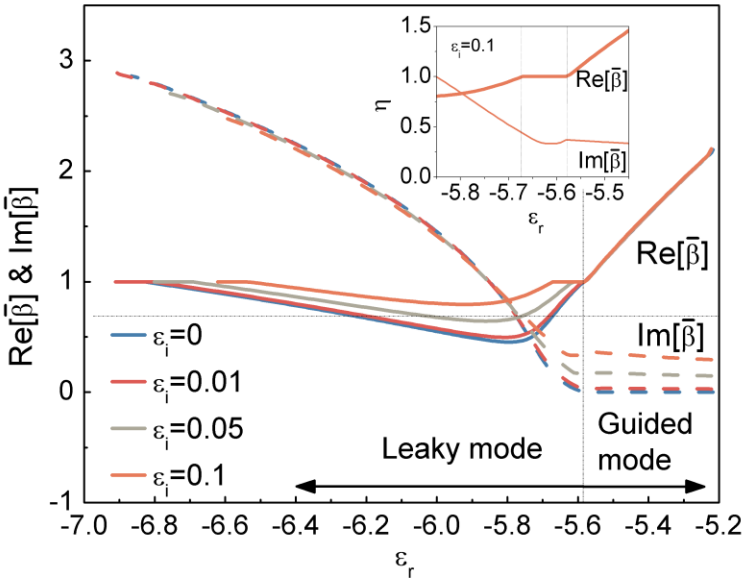

Figure 3.16 Variations of $\mathrm{Re}[\bar{\beta}]$ and $\mathrm{Im}[\bar{\beta}]$ for $\bar{d}=0.1$ and $\eta=d/a=2.1$ in the longitudinal polarization regime, varying the imaginary part of permittivity. The inset plot shows a zoom-in view in the transition region for the case $\varepsilon_i=0.1$.

3.5 FULL-WAVE NUMERICAL SIMULATIONS

In the previous sections, we have used the analytical formulation (3.1) to derive the fundamental properties of leaky-wave propagation and radiation along infinite arrays of subwavelength plasmonic nanoparticles to within a dipolar approximation. In this section, we validate the previous analytical model by simulating realistic finite arrays of silver nanoparticles with finite-integration technique in CST Microwave Studio, in order to

determine the radiation patterns of such leaky modes in a practical realization, considering also the complete multipolar coupling among closely spaced nanoparticles.

In our numerical simulations, we have fixed the particle size to $a = 50nm$, center-to-center distance $d = 110nm$, and we have used a Drude permittivity model (See Appendix B), which describes with good approximation the silver dispersion in the range of frequencies of interest [43]. The overall length of the chain is L=7μm, sufficiently long to ensure that significant part of the power coupled to the leaky mode has been radiated. The array is excited by an optical source (i.e. an emitting molecule or a quantum dot) longitudinally polarized along the array axis, to ensure proper coupling with the longitudinal leaky modes supported by the array.

We have verified in our simulations that the dispersion of leaky and guided modes along the array is qualitatively consistent with our analytical predictions. Clearly, the nature of our analytical technique neglects higher-order multipolar coupling between the closely spaced nanoparticles, which is reflected in a quantitative difference in the prediction of the frequency range for leaky-wave radiation, but qualitatively the results are in good agreement with the previous sections. As an example, Figure 3.17a reports the normal magnetic field (absolute value of real part) distribution at the operating wavelength $\lambda_0 = 690\,\text{nm}$, which is in the leaky-wave regime for this array. Similarly, Fig. 3.17b reports the corresponding distribution at $\lambda_0 = 600\,\text{nm}$, for which the chain is in its guided regime. It is evident that the permittivity dispersion of silver allows tuning the guidance properties of the supported mode from a slow mode with short guided wavelength, as in Fig. 3.17b, confined along the structure, to a much faster mode, which produces leaky-wave radiation in free-space with conical directive properties. The difference in phase velocity between the two simulations is striking, considering that the free-space wavelength difference between the two cases is only 15%, and it is

consistent with our analytical theory. Away from the chain, the leaky-wave (Fig 3.17a) couples to free-space radiation, drastically different from the guided propagation in Fig. 3.17b, which decays exponentially far away from the chain axis. The leaky-wave far-field extends laterally and propagates with oblique wave fronts, consistent with the previous analytical results. Figs. 3.17c and 3.17d show a zoom in the dashed regions of the two panels of Figs. 3.17a and 3.17b, reporting the power flow (Poynting vector) distribution. The power flow shows significant lateral energy leakage in the leaky-wave scenario of Fig. 3.17c. In contrast, at the wavelength $\lambda_0 = 600\,\mathrm{nm}$ (Fig. 3.17d), the power flow is confined and bounded parallel to the chain, rapidly decaying away from its axis. It is remarkable that these full-wave results qualitatively confirm with very good precision the analytical results in the previous sections, and in particular the possibility to create a leaky-wave nanoantenna composed of subwavelength nanoparticles composed of realistic plasmonic materials. The fact that our full-wave results take into account the full coupling among the neighboring particles, and not just their dipolar (dominant) contribution, slightly shifts the guidance and leaky-wave frequency ranges from our analytical predictions in Fig. 3.4, but qualitatively these results confirm the possibilities noted in the previous sections.

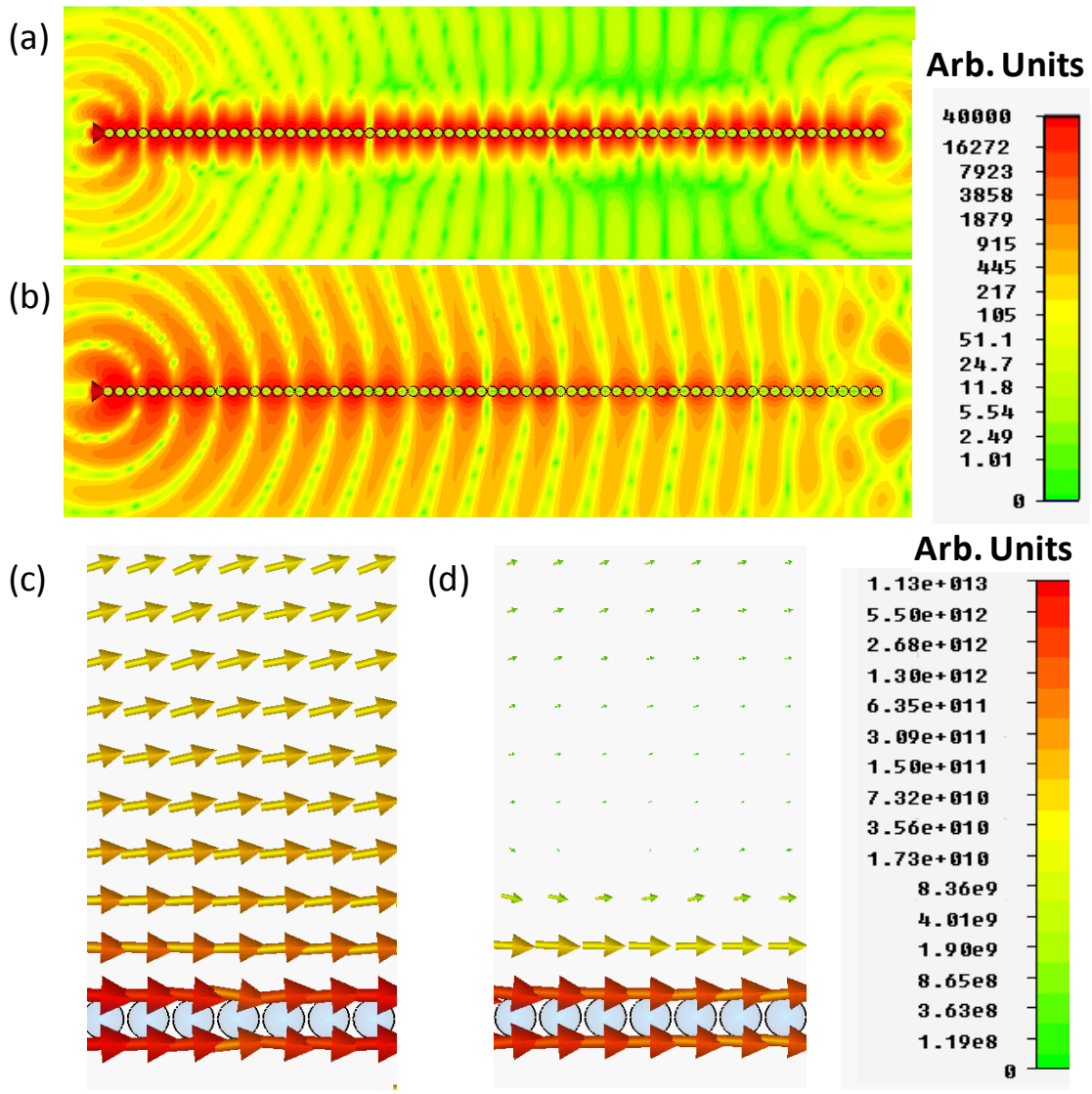

Figure 3.17 Magnetic field (absolute value of real part) and power flow distribution for a nanoparticle chain operating in the leaky-wave regime [(a) and (c), at 690nm wavelength] and in the guided propagation regime [(b) and (d), at 600nm].

Figure 3.18a shows the corresponding far-field radiation patterns in the E plane at various wavelengths. It is seen that, in the leaky-wave regime, the conical beam may scan the angle with frequency, as predicted in the previous sections. The patterns show a significant directivity that may be tuned by changing the frequency of operation (i.e., the

material permittivity). It is seen that, consistent with the previous analytical results, better directivity is achieved for radiation closer to the chain axis, for which ξ is larger. The scan of the main lobe direction with frequency confirms the forward nature of these longitudinal leaky-wave modes, as predicted by the previous analysis. For comparison, the radiation at $\lambda_0 = 600\,\text{nm}$ is very poor, due to the guided-wave properties of the chain at this wavelength. The sub-diffractive nature and subwavelength period of the chain ensure absence of significant side lobes. These results confirm the realistic possibility of using a silver nanoparticle chain as a leaky-wave nanoantenna. Different nanoparticle size and geometry may be used to tune and shift the leaky-wave operation at different wavelengths.

Figure 3.18b reports the three-dimensional far-field radiation pattern at 714 nm, together with the geometry of the chain, to highlight the directive conical radiation at 18 degrees from the chain axis, consistent with Fig. 3.18a. Smaller side lobes are visible, associated to the finite length of the chain. As reported in Fig. 3.18c, the nanoparticle chain supports a smooth linear scanning region between the wavelengths of 680 to 740 nm (highlighted in the figure), which delimit the leaky-wave operation of this nanoantenna.

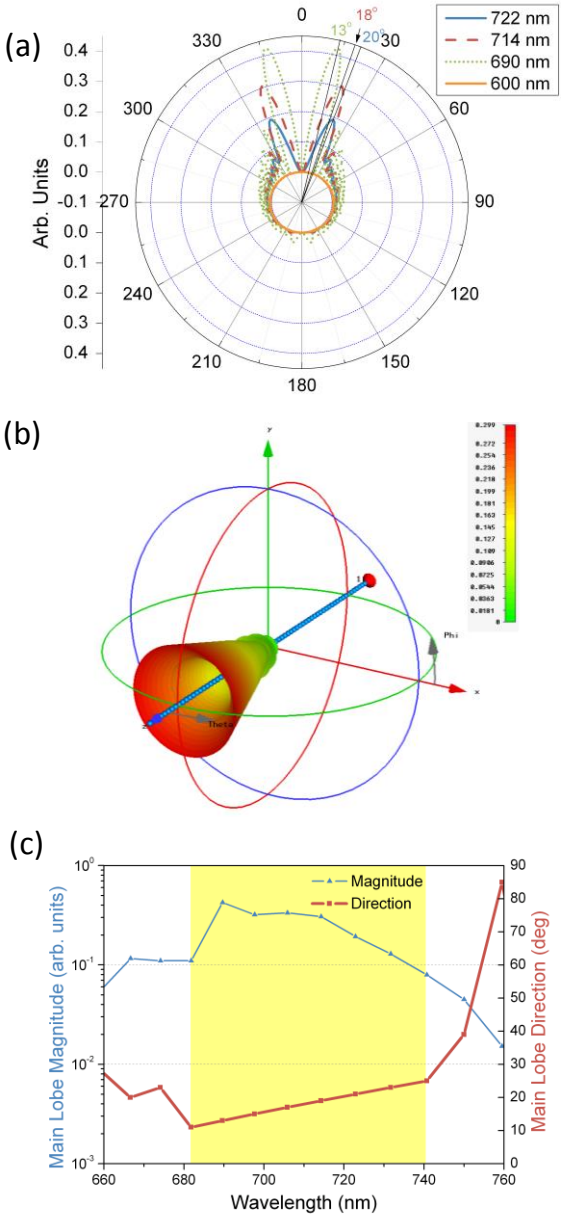

Figure 3.18 (a) Far-field radiation patterns vs. wavelength of operation. At 722 nm (solid blue line), 714 nm (dashed red line) and 690nm (dotted green line), directional far-field radiation patterns are obtained, pointing at 20°, 18°, and 13° respectively. At 600nm, the guided-wave mode does not significantly contribute to the far-field radiation. (b) Calculated three-dimensional leaky-wave radiation pattern at the wavelength of 690nm. (c) Scanning of the main lobe radiation pattern (magnitude and main direction) versus wavelength. The highlighted region corresponds to leaky-wave operation.

3.6 CONCLUSIONS

In this Chapter, we have analyzed the leaky-wave radiation properties of single and parallel linear arrays of subwavelength plasmonic nanoparticles. Starting from closed-form analytical dispersion relations for real and complex modes supported by the linear chains, we have analyzed the leaky-mode properties in the complex domain and the conditions for supporting this leaky wave regime. To evaluate the radiation and propagation capability of leaky wave, the figure of merit has been provided, which is based on the ratio of real and imaginary parts of wave number. The general conditions for guided and leaky modes for longitudinal and transverse conditions have also been determined in terms of dimensionless parameters. Based on the plots of leaky-wave region and figure of merit, we have verified that the longitudinal polarization is the best candidate for achieving significantly directive conical radiation with scanning capabilities. We also considered the effects of varying the center-to-center distance, and studied the array characteristic of realistic plasmonic and dielectric materials. Our analysis showed that plasmonic materials may provide a wide frequency range for leaky-wave mode. On the contrary, dielectric arrays do not sustain leaky-wave propagation unless the permittivity value is drastically large. Finally, we have simulated the leaky-wave propagation of silver nanoparticle chains to verify that these effects may be achieved in realistic geometries. Our full-wave simulations confirm and validate that plasmonic leaky-wave nanoantennas with sub-diffractive lateral cross section are indeed possible in the realm of current nanotechnology and may be applied to novel devices for optical communications and computing.

3.7 REFERENCES

1. R. E. Collin and F. J. Zucker, *Antenna Theory*, (McGraw-Hill, New York, 1969).
2. A. G. Curto, G. Volpe, T. H. Taminiau, M. P. Kreuzer, R. Quidant, and N. F. van Hulst, "Unidirectional Emission of a Quantum Dot Coupled to a Nanoantenna,"

Science **329**, 930 (2010).
3. A. Lai, T. Itoh, and C. Caloz, "Composite right/left-handed transmission line metamaterials," *IEEE Microw. Mag*. **5,** 34 (2009).
4. Liu, L., C. Caloz, and T. Itoh, "Dominant mode leaky-wave antenna with backfire-to-endfire scanning capability," *Electr. Lett*. **38**, 1414-1416 (2002).
5. L. Sungjoon, C. Caloz, and T. Itoh, "A reflectodirective system using a composite right/left-handed (CRLH) leaky-wave antenna and heterodyne mixing," *IEEE Microw. Wireless Compon. Lett*. **14,** 183 (2004).
6. D. R. Jackson, A. A. Oliner, "Leaky-Wave Antennas," in *Modern Antenna Handbook*, C. A. Balanis ed. (Wiley, 2008).
7. P. Lampariello, F. Frezza, and A. A. Oliner, "The transition region between bound-wave and leaky-wave ranges for a partially dielectric-loaded open guiding structure," *IEEE Trans. Microwave Theory Tech*. **38**, 1831 (1990).
8. S. A. Maier, M. L. Brongersma, P. G. Kik, S. Meltzer, A. A. G. Requicha, and H. A. Atwater, "Plasmonics—A Route to Nanoscale Optical Devices," *Adv. Mater*. **13**, 1501 (2001).
9. R. A. Shore, and A.D. Yaghjian, "Travelling electromagnetic waves on linear periodic arrays of lossless spheres," *Electr. Lett*. **41**, 578 (2005).
10. W. H. Weber and G. W. Ford, "Propagation of optical excitations by dipolar interactions in metal nanoparticle chains," *Phys. Rev. B* **70**, 125429 (2004).
11. R. A. Shore, and A. D. Yaghjian, "Traveling Electromagnetic Waves on Linear Periodic Arrays of Lossless Penetrable Spheres," *IEICE Trans. Commun*. **E88-B**, 2346 (2005).
12. S. A. Maier, P. G. Kik, H. A. Atwater, S. Meltzer, E. Harel, B. E. Koel and A. A. G. Requicha, "Local detection of electromagnetic energy transport below the diffraction limit in metal nanoparticle plasmon waveguides," *Nat. Mater*. **2**, 229 (2003).
13. M. Quinten, A. Leitner, J. R. Krenn, and F. R. Aussenegg, "Electromagnetic energy transport via linear chains of silver nanoparticles," *Opt. Lett*., **23**, 1331 (1998).
14. M. L. Brongersma, J.W. Hartman, and H.A. Atwater, "Electromagnetic energy transfer and switching in nanoparticle chain arrays below the diffraction limit," *Phys. Rev. B* **62**, R16356 (2000).
15. A. L. Aden, and M. Kerker, "Scattering of Electromagnetic Waves from Two Concentric Spheres," *J. Appl. Phys*. **22**, 1242 (1951).
16. J. R. Krenn, M. Salerno, N. Felidj, B. Lamprecht, G. Schider, A. Leitner, F. R. Aussenegg, J. C. Weeber, A. Dereux, and J. P. Goudonnet, "Light field propagation by metal micro- and nanostructures," *J. Microscopy* **202**, 122 (2001)
17. S. A. Maier, P. G. Kik, and H. A. Atwater, "Optical pulse propagation in metal nanoparticle chain waveguides," *Phys. Rev. B* **67**, 205402 (2003).
18. S. Ghadarghadr, Z. Hao, and H. Mosallaei, "Plasmonic array nanoantennas on layered substrates: modeling and radiation characteristics," *Opt. Express* **17**, 18556 (2009).
19. A. Ahmadi, S. Ghadarghadr, and H. Mosallaei, "An optical reflectarray nanoantenna:

The concept and design," *Opt. Express* **18**, 123 (2010).
20. A. Alù, and N. Engheta, "Theory of linear chains of metamaterial/plasmonic particles as subdiffraction optical nanotransmission lines," *Phys. Rev. B* **74**, 205436 (2006).
21. A. Drezet, A. Hohenau, A. L. Stepanov, H. Ditlbacher, B. Steinberger, N. Galler, F. R. Aussenegg, "How to erase surface plasmon fringes," *Appl. Phys. Lett*. **89**, 091117 (2006)
22. A. Bouhelier, Th. Huser, H. Tamaru, H.-J. Guntherodt, and D. W. Pohl, "Plasmon optics of structured silver films," *Phys. Rev. B* **63**, 155404 (2001).
23. J. Hu and C. R. Menyuk, "Understanding leaky modes: slab waveguide revisited," *Adv. Opt. Photon*. **1**, 58 (2009).
24. L. Huang, J.-C. Chiao, and M. P. De Lisio, "An electronically switchable leaky wave antenna," *IEEE Trans. Antennas Propag*. **48**, 1769 (2000).
25. P.-W. Chen, C. S. Lee, and V. Nalbandian, "Planar double-layer leaky-wave microstrip antenna," *IEEE Trans. Antennas Propag.* **50**, 832 (2002).
26. W. Hong, T.-L. Chen, C.-Y. Chang, J.-W. Sheen, Y.-D. Lin, "Broadband tapered microstrip leaky-wave antenna," *IEEE Trans. Antennas Propag*. **51,** 1922 (2003).
27. J. J. Burke, G. I. Stegeman, and T. Tamir, "Surface-polariton-like waves guided by thin, lossy metal films," *Phys. Rev. B* **33,** 5186 (1986).
28. A. Alù, and N. Engheta, "Wireless at the Nanoscale: Optical Interconnects using Matched Nanoantennas," *Phys. Rev. Lett*. **104**, 213902 (2010).
29. S. A. Tretyakov, *Analytical Modeling in Applied Electromagnetics*, Artech House (2003).
30. S. A. Tretyakov, and A. J. Viitanen, "Line of periodically arranged passive dipole scatterers," *Electr. Eng*. **82**, 35 (2000).
31. L. Lewin, *Polylogarithms and Associated Functions*, (Elsevier, New York, 1981).
32. J. E. Sipe, and J. V. Kranendonk, "Macroscopic electromagnetic theory of resonant dielectrics," *Phys. Rev. A* **9**, 1806 (1974).
33. O. Zhuromskyy, O. Sydoruk, E. Shamonina, and L. Solymar, "Slow waves on magnetic metamaterials and on chains of plasmonic nanoparticles: Driven solutions in the presence of retardation," *J. Appl. Phys*. **106**, 104908 (2009).
34. A. Alù, P. A. Belov, and N. Engheta, "Parallel-chain optical transmission line for a low-loss ultraconfined light beam," *Phys. Rev. B* **80**, 113101 (2009).
35. A. Alù, P. A. Belov and N. Engheta, "Coupling and guided propagation along parallel chains of plasmonic nanoparticles," *New J. Phys.* **13**, 033026 (2011).
36. A. Alù, and N. Engheta, "Three-dimensional nanotransmission lines at optical frequencies: A recipe for broadband negative-refraction optical metamaterials," *Phys. Rev. B* 75, 024304 (2007).
37. R. E. Collin, *Field Theory of Guided Waves* (Wiley-IEEE Press, 1990).
38. Bohren, C. F. and D. R. Huffman, *Absorption and Scattering of Light by Small Particles* (Wiley, New-York, 1983).
39. L. D. Landau, E. M. Lifshitz, and L. P. Pitaevskii, *Electrodynamics of Continuous Media* (Butterworth-Heinemann, Oxford, 1982).

40. S. A. Maier, P. E. Barclay, T. J. Johnson, M. D. Friedman, and O. Painter, “Low-loss fiber accessible plasmon waveguide for planar energy guiding and sensing,” *Appl. Phys. Lett.* **84**, 3990 (2004).
41. S. A. Maier, P. G. Kik, and H. A. Atwater, “Observation of coupled plasmon-polariton modes in Au nanoparticle chain waveguides of different lengths: Estimation of waveguide loss,” *Appl. Phys. Lett*. **81**, 1714 (2002).
42. E. Palik, *Handbook of Optical Constants of Solids*. (New York: Academic Press, 1985).
43. P. B. Johnson and R.W. Christy, “Optical Constants of the Noble Metals,” *Phys. Rev. B* **6**, 4370 (1972).

Chapter 4 Homogenization of Two-Dimensional Metamaterials and Metasurfaces

4.1 INTRODUCTION

Two-dimensional metamaterials, also known as metasurfaces, are the most popular category of metamaterials, due to their simplicity of realization, and have attracted a great deal of attention for microwave, terahertz and optical applications [1-12]. Typically, metasurfaces are planar periodic structures composed of subwavelength unit cells with in-plane or out-of-plane inclusions. Compared to fully 3-D metamaterials, metasurfaces offer the advantages of simpler fabrication processes, smaller physical space and less influence on material loss.

It is worth mentioning the relations between metasurfaces and more conventional frequency-selective surface (FSS), which are both artificial planar structures that can be designed to achieve specific transmission, reflection, and polarization under proper excitations. Generally, metasurfaces are extending applications of FSS, and they are particularly composed of stereo-inclusion and applied at optical frequencies. In addition, FSS usually has unit cell size comparable to the wavelength ($d \sim \lambda$), and metasurfaces have much smaller elements, operating in the regime $k_0 d < 1$ or $d < \lambda/2\pi$ (with k_0 being the free-space wave number) [13]. This implies that the metasurface inclusions may be more often treated as electric and magnetic dipole moments, whose values are determined by the particle geometry, constituent materials, lattice structure and external excitation. We can therefore use the tools derived in the previous sections to analyze metasurfaces and describe them with some macroscopic physical quantities, such as the average surface impedance and susceptibility [14].

The situation is rather different for FSS, for which the size of the unit cell is often comparable to the working wavelength, such that the induced currents on the inclusions

are more complicated than simply electric or magnetic dipoles. In any case, also FSS are in many instances described using homogenized surface impedance or susceptibility, and with lumped circuit elements like inductors (L) and capacitors (C) [15, 16]. We can use some of these tools in the case of metasurfaces.

The characterization of metasurfaces is crucial not only for understanding their macroscopic properties and but also for their efficient design and applications. There are two main approaches to determine the surface average properties of metasurfaces, similar to the ones described for bulk metamaterials in Chapter 1: the retrieval method and homogenization theory, respectively. The former technique is usually considered as a counterpart of the Nicolson-Ross-Weir (NRW) method used in 3-D metamaterials. The main difference in 2-D and 3-D retrieval methods is the assumption of a certain thickness for the equivalent homogeneous structures. In a 3-D array, the effective thickness of the sample is directly chosen to match the total number of unit cells along the direction of wave propagation. For the 2-D array, however, we assume the thickness of the structure to be zero (i.e., the array is homogenized as a uniform sheet), and we may interpret the transmission and reflection in terms of induced surface currents [17].

The homogenization of metasurfaces determines the surface constitutive parameters analyzing their microscopic structure. It considers the induced microscopic currents and takes into account the field interaction in the planar array. Based on these average quantities, such as electric and magnetic sheet currents, we can then define homogenized parameters, such as surface susceptibilities, to relate the fields and induced currents on the plane. Based on the proper definition of susceptibility, we may be able to predict the transmission and reflection coefficients under various oblique incident angles and polarizations.

Many previous works have reported the homogenization of metasurfaces composed of simple inclusions [1,13,18-25], such as spheres or planar inclusions. In general, the surface susceptibility of an arbitrary metasurface is a six-by-six tensor which is governed by co- and cross-polarization coupling between electric and magnetic induced currents. All the available models only formulate this quantity in either scalar [1] or a three-by-three tensor [19] form, due to specific assumptions on the symmetry of the inclusions and illumination. So far, a complete model for arbitrary metasurfaces is not available. This generalized model should take into account all possible coupling effects between electric and magnetic fields on the metasurface, including anisotropic and bianisotropic effects produced in the 2-D array.

In this chapter, we develop such homogenization theory for 2-D metasurfaces and extend the existing models to more general conditions. We consider a periodic metasurface with subwavelength rectangular unit cells composed of arbitrary nonconnected inclusions excited by plane waves with arbitrary incident and polarization angles. We extend the concepts introduced in previous works [1, 13, 18, 19] to derive a general definition of surface susceptibility to describe the array, and we further generalize this parameter to a six-by-six tensor to model the complete wave phenomena in metasurfaces.

This chapter is organized as follows. In section 4.2, we give the definition and detail formulations of homogenized surface susceptibility of a general metasurface. The inclusions in a metasurface are described by a set of electric and magnetic dipole moments based on the six-by-six polarizability derived in chapter 2, and the complete interaction among these dipole moments are expressed by dyadic Green's functions. In section 4.3, the transmission and reflection of a metasurface is studied based on the surface susceptibility derived earlier. By using this formulation we are able to

analytically predict the transmission and reflection coefficients of a metasurface with arbitrary inclusion polarizability.

4.2 FORMULATION

In this section, we present the definition and derivation of surface susceptibility of a planar metasurface, composed of a 2-D array of nonconnected arbitrary subwavelength scatterers. Similar to the previous section, the metasurface inclusions are described by a set of electric and magnetic dipoles. After defining the surface susceptibility, we are able to determine the transmission and reflection for arbitrary incident TE/TM plane wave impinging on the metasurfaces. Since the size of the unit cell is considered smaller than the wavelength of operation, we do not need to consider the higher-order scattering modes. In other words, we assume the transmitted and incident waves to be propagating in the same direction (with the same transverse momentum compared to the metasurface normal), even though their magnitudes and polarizations may be in general different.

4.2.1 Surface Susceptibility

Consider a periodic infinite 2-D array (see Fig. 4.1) composed of subwavelength unit cells with period *d* filled by arbitrary nonconnected inclusions. The array plane is normal to the z-axis and the unit cell dimensions are *a* and *b* in *x*- and *y*-directions, respectively. As in the previous sections, we are interested in the wave interaction of this metasurface within the subwavelength regime $k_0 d < 1.5$. Since the unit cell and the inclusions are smaller than the wavelength of operation, the scattering behavior of the inclusions under electromagnetic excitation can be treated as induced electric and magnetic dipoles. For an isolated unit cell, these induced dipoles, $\mathbf{p}_0$ and $\mathbf{m}_0$, can be expressed by

$$\begin{Bmatrix} \mathbf{p}_0 \\ \mathbf{m}_0 \end{Bmatrix} = \boldsymbol{\alpha} \begin{Bmatrix} \mathbf{E}^{loc} \\ \mathbf{H}^{loc} \end{Bmatrix} = \begin{bmatrix} \boldsymbol{\alpha}^{ee} & \boldsymbol{\alpha}^{em} \\ \boldsymbol{\alpha}^{me} & \boldsymbol{\alpha}^{mm} \end{bmatrix} \begin{Bmatrix} \mathbf{E}^{loc} \\ \mathbf{H}^{loc} \end{Bmatrix} \tag{4.1}$$

where $\boldsymbol{\alpha}$ is a six-by-six polarizability tensor of array element and $\mathbf{E}^{loc}$ and $\mathbf{H}^{loc}$ are the local fields at the phase (or geometry) center of inclusions. The polarizability tensor is composed of sub-tensors responsible for co- and cross-polarization between electric and magnetic fields, and these quantities can be determined by either analytical approaches (e.g., Mie theory for spherical particles) or numerical methods (e.g. generalized polarizability retrieval reported in Chapter 2.)

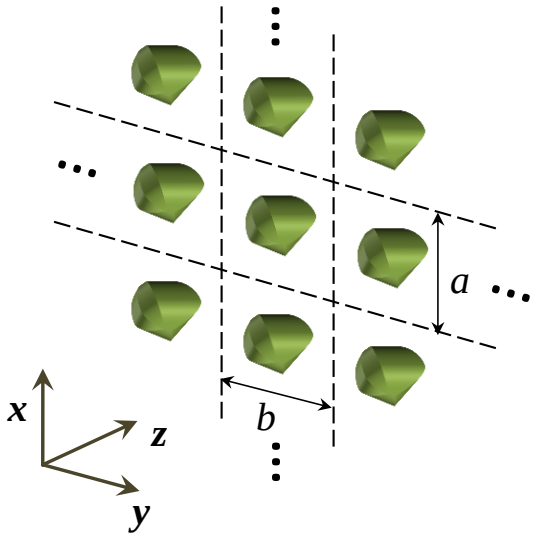

Figure 4.1 A 2-D periodic infinite metasurface with rectangular unit cell and nonconnected inclusions. The plane of array is normal to z-axis, and the dimensions of unit cell are *a* and *b* in *x*- and *y*-directions, respectively.

As we consider the induced dipoles among a 2-D array, the local fields for a certain unit cell are contributed by the incident fields and the coupling with all the other elements in the array, and they can be written as

$$\begin{Bmatrix} \mathbf{E}^{loc} \\ \mathbf{H}^{loc} \end{Bmatrix} = \begin{Bmatrix} \mathbf{E}^{inc} \\ \mathbf{H}^{inc} \end{Bmatrix} + \begin{Bmatrix} \mathbf{E}^{Array} \\ \mathbf{H}^{Array} \end{Bmatrix}, \tag{4.2}$$

where

$$\begin{Bmatrix} \mathbf{E}^{Array} \\ \mathbf{H}^{Array} \end{Bmatrix} = \mathbf{C}^{2D} \begin{Bmatrix} \mathbf{p}_0 \\ \mathbf{m}_0 \end{Bmatrix} \tag{4.3}$$

is the scattering from neighboring unit cells that can be determined by the Green's dyads $\mathbf{C}^{2D}$ based on Bloch theorem [19-27]. The closed-form expression of each elements in $\mathbf{C}^{2D}$ are reported in Appendix C. We stress that many of these analytical expressions are new, and have never been derived before. We may combine Eqs. (4.1), (4.2) and (4.3) to obtain the relations between dipole moments and incident fields, which yields

$$\begin{Bmatrix} \mathbf{p}^0 \\ \mathbf{m}^0 \end{Bmatrix} = \left(\boldsymbol{\alpha}^{-1} - \mathbf{C}^{2D} \right)^{-1} \begin{Bmatrix} \mathbf{E}^{inc} \\ \mathbf{H}^{inc} \end{Bmatrix}. \tag{4.4}$$

Since the unit cells and inclusions on the 2-D metasurface are smaller than the wavelength, we are able to macroscopically treat the unit cell as a uniform surface with averaged surface susceptibility [14], which relates the *surface* average polarization and the fields on the surface by

$$\begin{Bmatrix} \mathbf{P} \\ \mathbf{M} \end{Bmatrix} = \boldsymbol{\chi}^{2D} \begin{Bmatrix} \mathbf{E}^{surf} \\ \mathbf{H}^{surf} \end{Bmatrix} = \boldsymbol{\chi}^{2D} \left(\begin{Bmatrix} \mathbf{E}^{inc} \\ \mathbf{H}^{inc} \end{Bmatrix} + \begin{Bmatrix} \mathbf{E}^{scat} \\ \mathbf{H}^{scat} \end{Bmatrix} \right), \tag{4.5}$$

where the average polarizations are $\mathbf{P} = \mathbf{p}_0 / ab$ and $\mathbf{M} = \mathbf{m}_0 / ab$, and the fields $\mathbf{E}^{surf}$ and $\mathbf{H}^{surf}$ are contributed by incident waves ($\mathbf{E}^{inc}$ and $\mathbf{H}^{inc}$) and scattering fields ($\mathbf{E}^{scat}$ and $\mathbf{H}^{scat}$) generated by all the induced dipoles among the array.

In principle, the scattering fields on a metasurface can be treated as the radiation fields generated by the surface currents induced by external excitations. Therefore, in order to formulate the scattering fields, we should consider all the possible components of induced electric and magnetic surface currents on a plane. In Fig. 4.2a, we illustrate the fields on both sides of the array plane generated by the electric current component J_{sx}.

J_{sx} generates opposite transverse magnetic fields ($\mathbf{H}^{0-} = -\mathbf{H}^{0+}$) across the plane, and also produces propagating electric fields ($\mathbf{E}^{0+} = \mathbf{E}^{0-}$) along the *x*-direction on both sides of surface. The surface electric currents can be related by the discontinuity of the tangential magnetic fields across the plane

$$\begin{aligned}\hat{\mathbf{z}}\times\left(\mathbf{H}^{0+}-\mathbf{H}^{0-}\right)&=\hat{\mathbf{z}}\times\left(2H^{0+}\right)\hat{\mathbf{y}}=-2H^{0+}\hat{\mathbf{x}}=J_{sx}\hat{\mathbf{v}},\\ \hat{\mathbf{z}}\times\left(\mathbf{H}^{0+}-\mathbf{H}^{0-}\right)&=\hat{\mathbf{z}}\times\left(-2H^{0-}\right)\hat{\mathbf{y}}=2H^{0-}\hat{\mathbf{x}}=J_{sx}\hat{\mathbf{v}},\end{aligned} \tag{4.6}$$

and we may obtain $H^{0+} = -J_{sx}/2$ and $H^{0-} = J_{sx}/2$, respectively. Moreover, we can relate the electric and magnetic fields through the wave impedances [28]

$$\begin{aligned}Z_0^{TE}&=\frac{E_x}{H_y}=\frac{-E_y}{H_x}=\frac{\omega\mu_0}{k_z}=\frac{k_0\eta_0}{k_z},\\ Z_0^{TM}&=\frac{E_x}{H_y}=\frac{-E_y}{H_x}=\frac{k_z}{\omega\varepsilon_0}=\frac{k_z\eta_0}{k_0}.\end{aligned} \tag{4.7}$$

In this case, we choose Z_0^{TE} for the current component J_{sx} and K_{sy}, and Z_0^{TM} for J_{sy} and K_{sx}. Therefore, as illustrated in Fig 4.2a, the average scattered fields stemming from J_{sx} on the plane are

$$\begin{aligned}E_x^{scat\_J_{sx}}&=\frac{E_x^{0+}+E_x^{0-}}{2}=-\frac{Z_0^{TE}}{2}J_{sx},\\ H_y^{scat\_J_{sx}}&=\frac{H_y^{0+}+H_y^{0-}}{2}=0,\end{aligned} \tag{4.8}$$

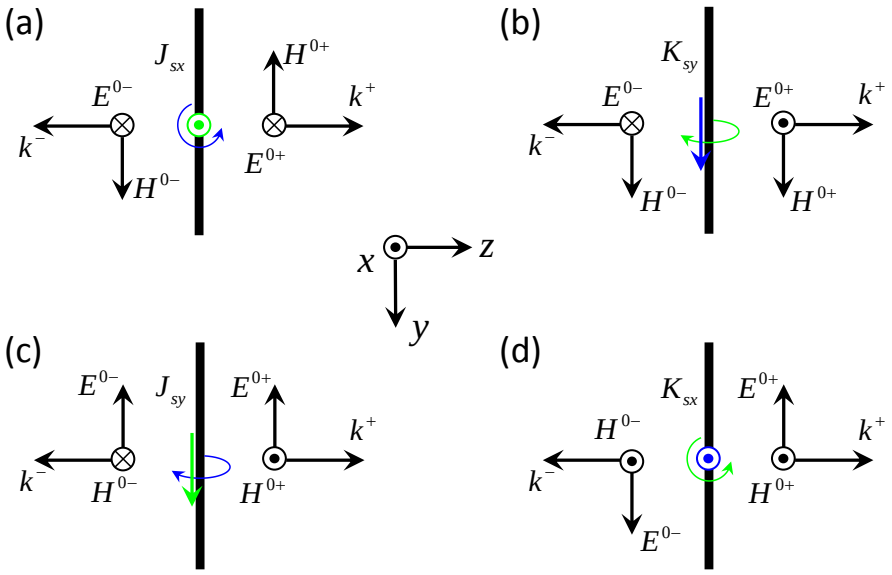

Figure 4.2 Induced surface currents and the associated radiation fields on a metasurface.

Similarly, the average scattered fields contributed by the other surface current components are:

$$\begin{aligned} E_x^{scat\_K_{sy}} &= \frac{E_x^{0+} + E_x^{0-}}{2} = 0, \\ H_y^{scat\_K_{sy}} &= \frac{H_y^{0+} + H_y^{0-}}{2} = -\frac{1}{2Z_0^{TE}} K_{sy}, \end{aligned} \tag{4.9}$$

$$\begin{aligned} E_y^{scat\_J_{sy}} &= \frac{E_y^{0+} + E_y^{0-}}{2} = -\frac{Z_0^{TM}}{2} J_{sy}, \\ H_x^{scat\_J_{sy}} &= \frac{H_y^{0+} + H_y^{0-}}{2} = 0, \end{aligned} \tag{4.10}$$

and

$$\begin{aligned} E_y^{scat\_K_{sx}} &= \frac{E_y^{0+} + E_y^{0-}}{2} = 0, \\ H_x^{scat\_K_{sx}} &= \frac{H_y^{0+} + H_y^{0-}}{2} = -\frac{1}{2Z_0^{TM}} K_{sx}. \end{aligned} \tag{4.11}$$

By considering Eqs. (4.8)-(4.11) as well as the relations between induced dipole moments and currents [29]

$$\begin{aligned}\mathbf{J} &= j\omega\mathbf{P}_{\square} - \frac{1}{\mu_0}\hat{\mathbf{z}}\times\nabla M_{\perp},\\ \mathbf{K} &= j\omega\mathbf{M}_{\square} + \frac{1}{\varepsilon_0}\hat{\mathbf{z}}\times\nabla P_{\perp},\end{aligned} \tag{4.12}$$

we may express the scattered fields in terms of average surface polarizations, which yield

$$\begin{Bmatrix}\mathbf{E}^{scat}\\ \mathbf{H}^{scat}\end{Bmatrix} = \mathbf{Q}\begin{Bmatrix}\mathbf{P}\\ \mathbf{M}\end{Bmatrix} \tag{4.13}$$

where

$$\mathbf{Q} = \begin{Bmatrix} -\frac{jk_0^2}{2k_z\varepsilon_0} & 0 & 0 & 0 & 0 & \frac{jk_yk_0c}{2k_z} \\ 0 & -\frac{jk_z}{2\varepsilon_0} & 0 & 0 & 0 & 0 \\ 0 & 0 & \frac{jk_y^2}{2k_z\varepsilon_0} & \frac{jk_yk_0c}{2k_z} & 0 & 0 \\ 0 & 0 & \frac{jk_yk_0c}{2k_z} & \frac{jk_0^2}{2k_z\mu_0} & 0 & 0 \\ 0 & 0 & 0 & 0 & \frac{jk_z}{2\mu_0} & 0 \\ \frac{jk_0k_yc}{2k_z} & 0 & 0 & 0 & 0 & -\frac{jk_y^2}{2k_z\mu_0} \end{Bmatrix}. \tag{4.14}$$

Therefore, we can rewrite Eq. (4.5) as

$$\begin{Bmatrix}\mathbf{P}\\ \mathbf{M}\end{Bmatrix} = \boldsymbol{\chi}^{2D}\begin{Bmatrix}\mathbf{E}^{surf}\\ \mathbf{H}^{surf}\end{Bmatrix} = \left(ab\left(\boldsymbol{\alpha}^{-1} - \mathbf{C}^{2D}\right) + \mathbf{Q}\right)\begin{Bmatrix}\mathbf{P}\\ \mathbf{M}\end{Bmatrix} \tag{4.15}$$

and the homogenized surface susceptibility is

$$\boldsymbol{\chi}^{2D} = \left(ab\left(\boldsymbol{\alpha}^{-1} - \mathbf{C}^{2D} \right) + \mathbf{Q} \right)^{-1}. \tag{4.16}$$

A similar result was derived for the more simplified cases of uniaxially mono-anisotropic inclusions under TE-wave incidence in Ref. 19. In this uniaxial case, the effective surface susceptibility is formulated as a three-by-three matrix and the applicable inclusions are only allowed to lie on the plane of the metasurfaces. In this generalized model we may model arbitrary nonconnected subwavelength inclusions and describe the complete field coupling in an arbitrary array, as we discuss in the following sections.

4.2.2 Transmission and Reflection Coefficients

From a macroscopic point of view, we may also express the average field on the surface in Eq. (4.5) in terms of incident, reflection and transmission waves across the plane:

$$\begin{aligned} \begin{Bmatrix} \mathbf{P} \\ \mathbf{M} \end{Bmatrix} &= \boldsymbol{\chi}^{2D} \begin{Bmatrix} \mathbf{E}^{surf} \\ \mathbf{H}^{surf} \end{Bmatrix} \\ &= \frac{1}{2} \boldsymbol{\chi}^{2D} \left(\left. \begin{Bmatrix} \mathbf{E}^{inc} \\ \mathbf{H}^{inc} \end{Bmatrix} \right|_{z=0^-} + \left. \begin{Bmatrix} \mathbf{E}^{refl} \\ \mathbf{H}^{refl} \end{Bmatrix} \right|_{z=0^-} + \left. \begin{Bmatrix} \mathbf{E}^{tran} \\ \mathbf{H}^{tran} \end{Bmatrix} \right|_{z=0+} \right). \end{aligned} \tag{4.17}$$

Here, we may separate the incident fields into TE and TM modes, which have transverse electric and magnetic fields in the plane of the metasurface, respectively. These transverse fields are not necessarily in the *x*- or *y*-directions. For the general TE mode, the incident, reflection and transmission fields are

$$\begin{aligned} \mathbf{E}_{TE}^{inc} &= E_{TE0} e^{-j(k_w w + k_z z)} \begin{bmatrix} 1 & 0 & 0 \end{bmatrix}^T \\ \mathbf{H}_{TE}^{inc} &= \frac{E_{TE0} e^{-j(k_w w + k_z z)}}{\eta_0} \begin{bmatrix} 0 & \cos\theta & -\sin\theta \end{bmatrix}^T \end{aligned} \tag{4.18}$$

$$\begin{aligned} \mathbf{E}_{TE,TE}^{refl} &= E_{TE0} R_{TE,TE} e^{-j(k_w w - k_z z)} \begin{bmatrix} 1 & 0 & 0 \end{bmatrix}^T \\ \mathbf{H}_{TE,TE}^{refl} &= \frac{E_{TE0} R_{TE,TE}}{\eta_0} e^{-j(k_w w - k_z z)} \begin{bmatrix} 0 & -\cos\theta & -\sin\theta \end{bmatrix}^T \end{aligned} \tag{4.19}$$

$$\mathbf{E}_{TE,TE}^{tran} = E_{TE0}T_{TE,TE}e^{-j(k_w w+k_z z)}\begin{bmatrix}1 & 0 & 0\end{bmatrix}^T$$
$$\mathbf{H}_{TE,TE}^{tran} = \frac{E_{TE0}T_{TE,TE}}{\eta_0}e^{-j(k_w w+k_z z)}\begin{bmatrix}0 & \cos\theta & -\sin\theta\end{bmatrix}^T \tag{4.20}$$

$$\mathbf{E}_{TM,TE}^{refl} = \frac{E_{TE0}R_{TM,TE}}{\eta_0}e^{-j(k_w w-k_z z)}\begin{bmatrix}0 & \cos\theta & \sin\theta\end{bmatrix}^T$$
$$\mathbf{H}_{TM,TE}^{refl} = E_{TE0}R_{TM,TE}e^{-j(k_w w-k_z z)}\begin{bmatrix}1 & 0 & 0\end{bmatrix}^T \tag{4.21}$$

$$\mathbf{E}_{TM,TE}^{tran} = \frac{E_{TE0}T_{TM,TE}}{\eta_0}e^{-j(k_w w+k_z z)}\begin{bmatrix}0 & -\cos\theta & \sin\theta\end{bmatrix}^T$$
$$\mathbf{H}_{TM,TE}^{tran} = E_{TE0}T_{TM,TE}e^{-j(k_w w+k_z z)}\begin{bmatrix}1 & 0 & 0\end{bmatrix}^T \tag{4.22}$$

where E_{TE0} is the amplitude of fields, the subscripts *TE,TE* and *TM,TE* stand for TE and TM fields produced by TE incident waves, respectively. Importantly, we use a *vwz* coordinate system which is defined along the transverse electric component in the TE mode as illustrated in Fig. 4.3. The reason for employing this new coordinate system is to simplify the expression for the electromagnetic fields in the above equations. We can to transform field components from the *xyz* coordinate system to the *vwz* system using the transformation matrix

$$\mathbf{T} = \begin{Bmatrix} \cos\phi & \sin\phi & & & \\ -\sin\phi & \cos\phi & & 0 & \\ & & 1 & & \\ & & & \cos\phi & \sin\phi \\ & 0 & & -\sin\phi & \cos\phi \\ & & & & 1 \end{Bmatrix}. \tag{4.23}$$

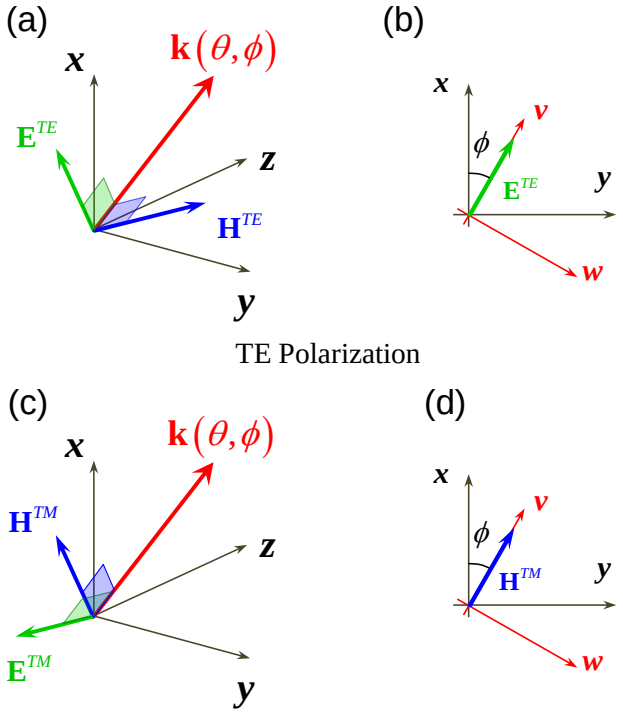

Figure 4.3 General TE and TM modes and their coordinate system considered in calculating the transmitted and reflected fields for a 2-D metasurface. In both cases, the waves are propagating in the same direction. For the general TE mode shown in (a) and (b), the transverse field component $\mathbf{E}^{TE}$ is lying in the *xy*-plane and pointing in the assigned *v*-axis. Similarly, in (c) and (d) the component $\mathbf{H}^{TM}$ of the general TM mode is lying in the *xy*-plane and pointing in the *v*-axis.

Similarly, the incident, reflected and transmitted fields for TM polarization are

$$\begin{aligned}\mathbf{H}_{TM}^{inc} &= H_{TM0}e^{-j(k_w w+k_z z)}\begin{bmatrix}1 & 0 & 0\end{bmatrix}^T,\\ \mathbf{E}_{TM}^{inc} &= \frac{H_{TM0}e^{-j(k_w w+k_z z)}}{\eta_0}\begin{bmatrix}0 & -\cos\theta & \sin\theta\end{bmatrix}^T,\end{aligned} \tag{4.24}$$

$$\begin{aligned}\mathbf{H}_{TM,TM}^{refl} &= H_{TM0}R_{TM,TM}e^{-j(k_w w-k_z z)}\begin{bmatrix}1 & 0 & 0\end{bmatrix}^T,\\ \mathbf{E}_{TM,TM}^{refl} &= \frac{H_{TM0}R_{TM,TM}}{\eta_0}e^{-j(k_w w-k_z z)}\begin{bmatrix}0 & \cos\theta & \sin\theta\end{bmatrix}^T,\end{aligned} \tag{4.25}$$

$$\begin{aligned}
\mathbf{H}_{TM,TM}^{tran} &= H_{TM0}T_{TM,TM}e^{-j(k_w w+k_z z)}\begin{bmatrix}1 & 0 & 0\end{bmatrix}^T, \\
\mathbf{E}_{TM,TM}^{tran} &= \frac{H_{TM0}T_{TM,TM}}{\eta_0}e^{-j(k_w w+k_z z)}\begin{bmatrix}0 & -\cos\theta & \sin\theta\end{bmatrix}^T,
\end{aligned} \tag{4.26}$$

$$\begin{aligned}
\mathbf{H}_{TE,TM}^{refl} &= \frac{H_{TM0}R_{TE,TM}}{\eta_0}e^{-j(k_w w-k_z z)}\begin{bmatrix}0 & -\cos\theta & -\sin\theta\end{bmatrix}^T, \\
\mathbf{E}_{TE,TM}^{refl} &= H_{TM0}R_{TE,TM}e^{-j(k_w w-k_z z)}\begin{bmatrix}1 & 0 & 0\end{bmatrix}^T,
\end{aligned} \tag{4.27}$$

$$\begin{aligned}
\mathbf{H}_{TE,TM}^{tran} &= \frac{H_{TM0}T_{TE,TM}}{\eta_0}e^{-j(k_w w+k_z z)}\begin{bmatrix}0 & \cos\theta & -\sin\theta\end{bmatrix}^T, \\
\mathbf{E}_{TE,TM}^{tran} &= H_{TM0}T_{TE,TM}e^{-j(k_w w+k_z z)}\begin{bmatrix}1 & 0 & 0\end{bmatrix}^T,
\end{aligned} \tag{4.28}$$

where H_{TM0} is the amplitude of the impinging magnetic field, the subscripts *TE,TM* and *TM,TM* stand for the TE and TM fields produced by TM excitation, respectively.

Applying the boundary conditions for tangential electric and magnetic fields, we are able to define surface currents by comparing the fields across the surface

$$\begin{aligned}
\mathbf{J}_{s1} &= \hat{\mathbf{z}}\times\left(\mathbf{H}_{z=0^+}-\mathbf{H}_{z=0^-}\right)=\hat{\mathbf{z}}\times\left[\mathbf{H}^{tran}-\left(\mathbf{H}^{inc}+\mathbf{H}^{refl}\right)\right], \\
\mathbf{K}_{s1} &= -\hat{\mathbf{z}}\times\left(\mathbf{E}_{z=0^+}-\mathbf{E}_{z=0^-}\right)=-\hat{\mathbf{z}}\times\left[\mathbf{E}^{tran}-\left(\mathbf{E}^{inc}+\mathbf{E}^{refl}\right)\right].
\end{aligned} \tag{4.29}$$

On the other hand, we can also obtain another set of surface currents $\left(\mathbf{J}_{s2},\mathbf{K}_{s2}\right)$ in terms of average fields on the plane by using Eqs. (4.12) and (4.17). It is important to note that the surface susceptibility in Eq. (4.16) are derived in the *xyz* coordinate system due to the definition of $\boldsymbol{\alpha}$ and $\mathbf{C}^{2D}$, which are defined with respect to the rectangular grid in the metasurface. Therefore, as we consider general TE and TM polarization (whose polarization direction are rotated by ϕ with respect to the *x*-axis, as shown in Fig. 4.3b and 4.3d) on the structures, a new form of susceptibility

$$\boldsymbol{\chi}^{2D}=\left(ab\left(\boldsymbol{\alpha}^{-1}-\mathbf{C}^{2D}\right)+\mathbf{T}^{-1}\mathbf{Q}\,\mathbf{T}\right)^{-1} \tag{4.30}$$

with proper coordinate transformation for $\underline{\underline{\mathbf{Q}}}$ (which is originally defined along the transverse fields and surface currents) should be considered.

For TE excitation, we can consider the surface currents as a set of simultaneous equations

$$\begin{aligned} \mathbf{J}_{s1} &= \mathbf{J}_{s2}, \\ \mathbf{K}_{s1} &= \mathbf{K}_{s2}, \end{aligned} \tag{4.31}$$

in which there are four unknowns for the transmission and reflection coefficients $R_{TE,TE}$, $T_{TE,TE}$, $R_{TM,TE}$ and $T_{TM,TE}$ for TE and TM waves in terms of surface susceptibility defined in Eq. (4.16). We can solve for these simultaneous equations to derive the transmission and reflection coefficients of a given metasurface. Because this generalized solution involves a complete surface susceptibility tensor, these coefficients may not be analytically solved in closed-form. In the practical implementation as shown in the following section, we numerically solve for these unknowns. Similarly, we can also solve for $R_{TE,TM}$, $T_{TE,TM}$, $R_{TM,TM}$ and $T_{TM,TM}$ for TM excitation by collecting surface current components in terms of fields in Eqs (4.24)-(4.28).

To summarize, given a metasurface composed of arbitrary inclusions with a polarizability tensor $\boldsymbol{\alpha}$ and incident and polarization angles defining the $\mathbf{Q}$ matrix, this analytical method allows to analytically determine the transmission and reflection coefficients of the scattered TE and TM waves across the metasurface.

4.3 Examples of 2-D Metasurface Homogenization

In this section, instead of showing effective surface susceptibilities, we directly validate that the homogenization model of 2-D metasurfaces by comparing the analytical transmission and reflection coefficients to the results obtained from numerical

simulations. In particular, we use CST Microwave Studio and Ansoft HFSS to verify our analytical results. In order to simulate infinitely periodic

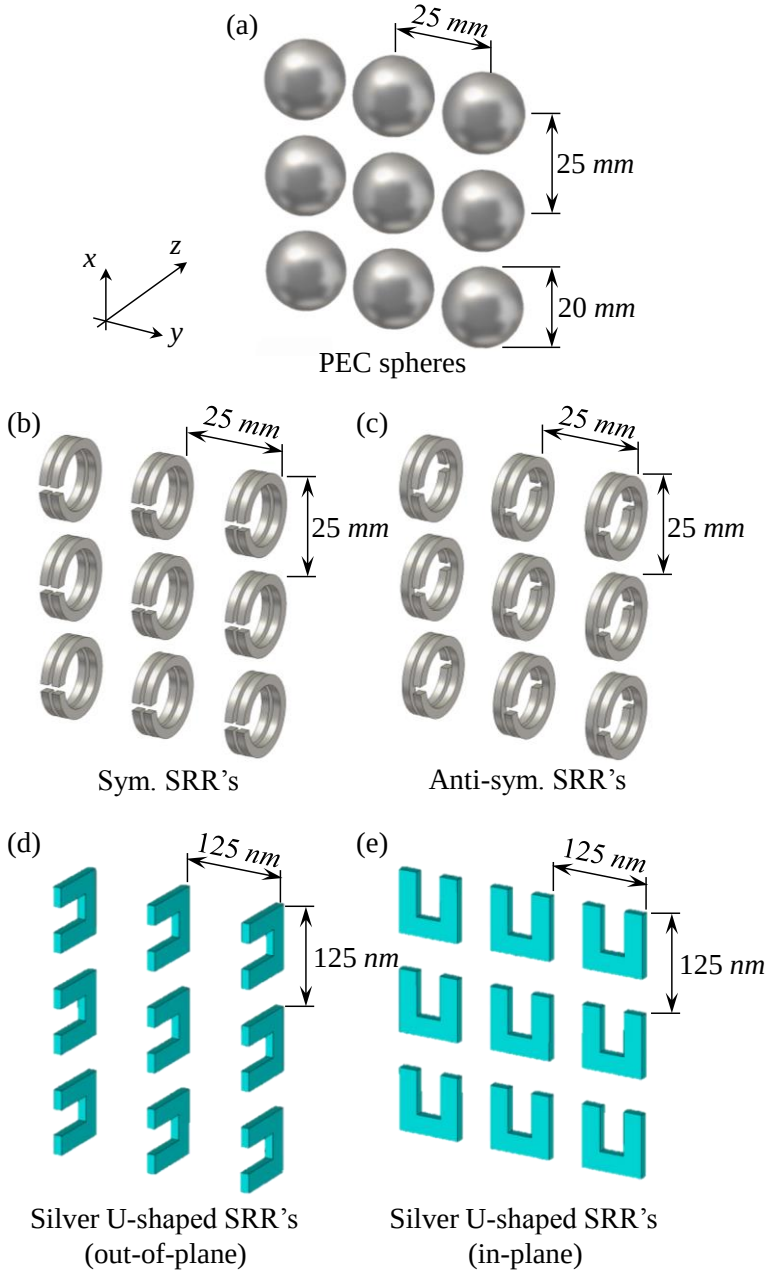

Figure 4.4 The investigated 2-D infinitely periodic metasurfaces composed of (a) PEC spheres, (b) symmetric conducting SRRs, (c) anti-symmetric conducting SRRs, and (d-e) silver U-shape SRRs arranged out-of-plane and in-plane, respectively. The detailed geometrical parameters are identical to the inclusions presented in Fig. 2.3.

metasurfaces in both tools, we use the unit-cell moduli with Floquet boundaries in frequency domain. In this type of moduli, we may directly obtain the reflection and transmission coefficients for arbitrary TE and TM incidence, respectively, as we assign the plane wave incident direction. Here, we investigate the transmission and reflection coefficients of metasurfaces composed by various inclusions, including PEC spheres, conducting SRRs pairs and silver U-shape SRRs, as shown in Fig. 4.4. For the SRR-like elements, their polarizability tensors are obtained from the retrieval procedure developed in Chapter 2.

4.3.1 Metasurfaces composed of PEC spheres

In this example, we consider a metasurface with array period $d = 25mm$ and inclusions consisting of conducting spheres with radius $a = 10mm$, as shown in Fig. 4.4a. For this structure, the polarizability tensor $\boldsymbol{\alpha}$ is diagonal, and only contains non-zero elements in the subtensors $\boldsymbol{\alpha}^{ee}$ and $\boldsymbol{\alpha}^{mm}$. In other words, there are no bianisotropic effects in this structure. Figure 4.5 shows reflection and transmission coefficients when the metasurface is illuminated by plane waves with frequency varying from 0.1 to 2.0 GHz (or $k_0 d = 0.05 \sim 1.05$) coming from directions $(\theta = 0°, \phi = 0°)$, $(\theta = 30°, \phi = 0°)$ and $(\theta = 45°, \phi = 0°)$.

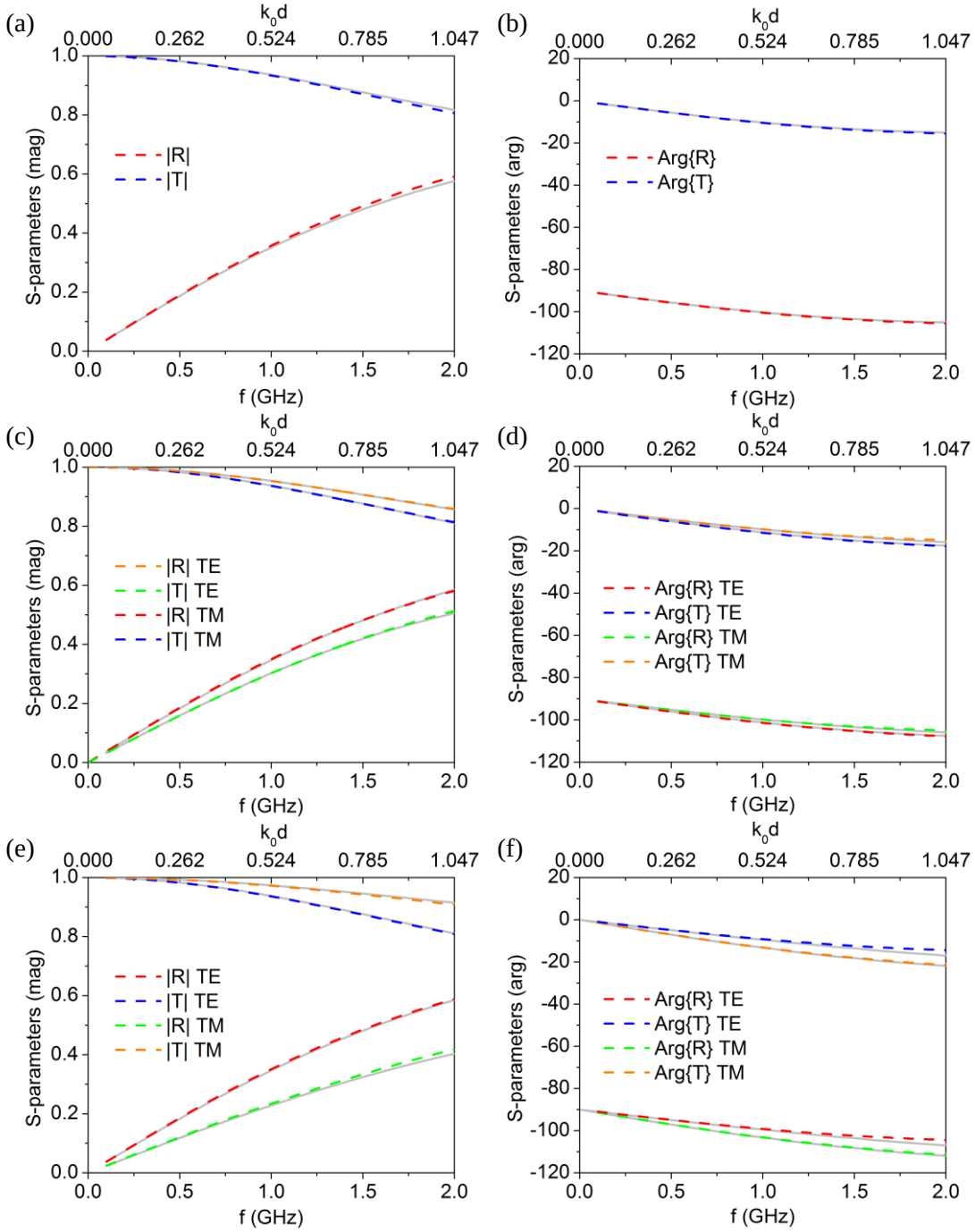

Figure 4.5 Reflection and transmission coefficients for metasurfaces made of 2-D PEC spheres, as illustrated in Fig 4.4a. The gray curves behind each color line are the corresponding results obtained from numerical simulations in CST Microwave Studio.

In these figures, we also present the numerical results calculated with CST Microwave Studio, corresponding to the gray curves in each panel. They show nice agreement with our analytical data in both magnitude and phase, validating our numerical approach. Except for the normal incidence case (Fig. 4.5a and b), oblique illumination produces different results for TE and TM illumination. As expected, larger oblique angles lead to more different transmission and reflection coefficients for TE and TM excitation. These results imply that our proposed model of generalized surface susceptibility in Eq. (4.30) correctly captures the wave propagation along these 2-D arrays.

4.3.2 Metasurfaces composed of conducting SRR pairs

To test more complicated metasurfaces, we use conducting SRR pairs in symmetric and anti-symmetric configurations (see Fig. 2.3d), and apply their tensorial polarizability $\boldsymbol{\alpha}$ (with dimension six-by-six) in Eq. (4.30) based on the retrieved results obtained in Chapter 2. The frequency range considered in this example is identical to the previous PEC sphere examples. Unlike previous studies [4, 19, 20], we consider here SRRs arranged out-of-plane, which allows out-of-plane electric dipoles in the metasurface and in-plane magnetic excitation, which is interesting for a variety of applications.

Due to bianisotropic effects on the isolated symmetric SRR pairs, our results show that even for normal incidence we may couple TE into TM modes and vice versa, as presented in Fig. 4.6a and b. In Fig. 4.6c-f, we further evaluate the transmission and reflection coefficients for symmetric SRR pairs and oblique incidence with $\theta = 30°$ and $\phi = 30°$. In all cases, the analytical and numerical results nicely match each other, validating our theory also in this more challenging scenario (and also further validating our polarizability retrieval method).

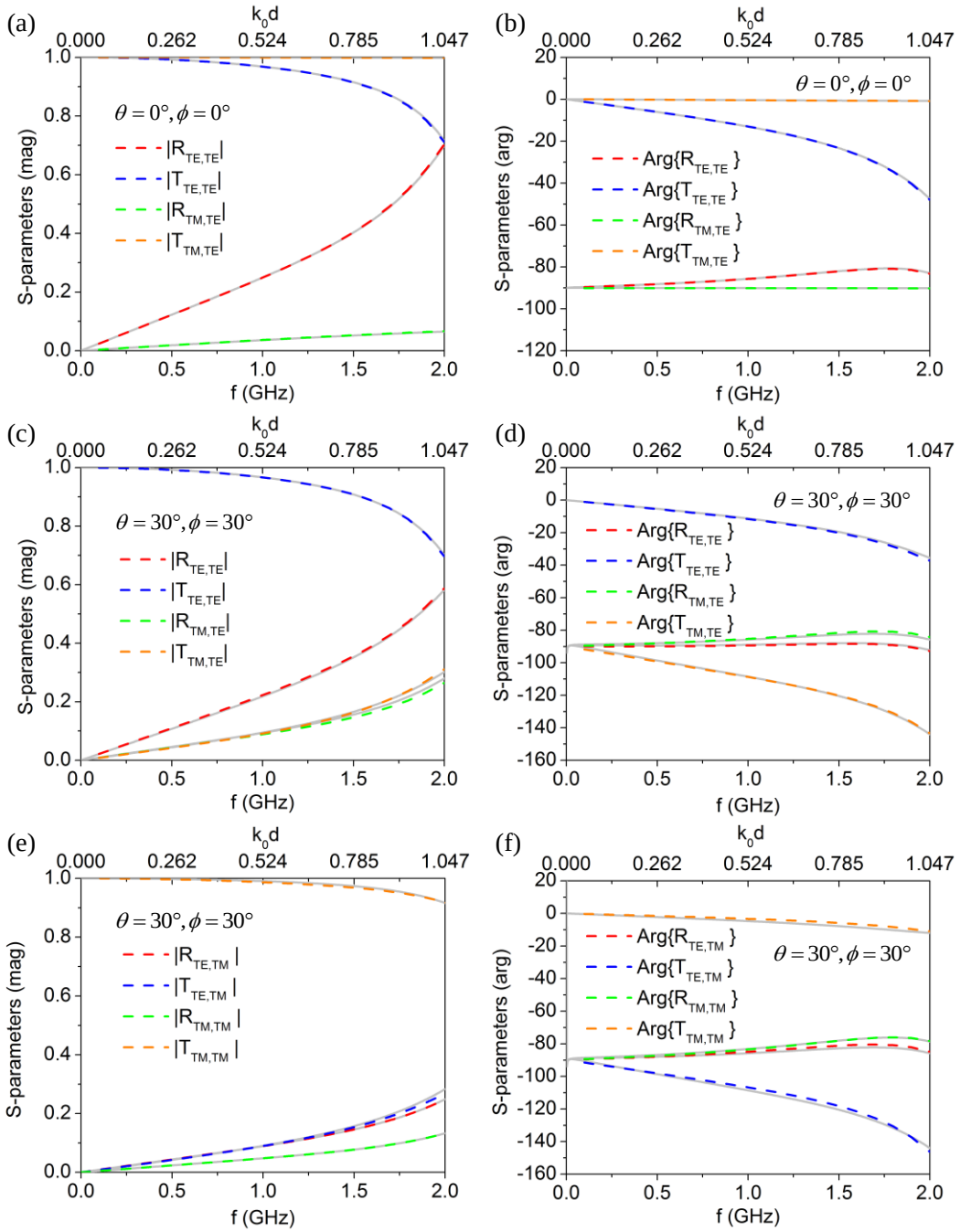

Figure 4.6 Reflection and transmission coefficients for metasurfaces composed of symmetric SRRs, as illustrated in Fig 4.4c. The gray curves in each panel show the corresponding results obtained from numerical simulations in CST Microwave Studio.

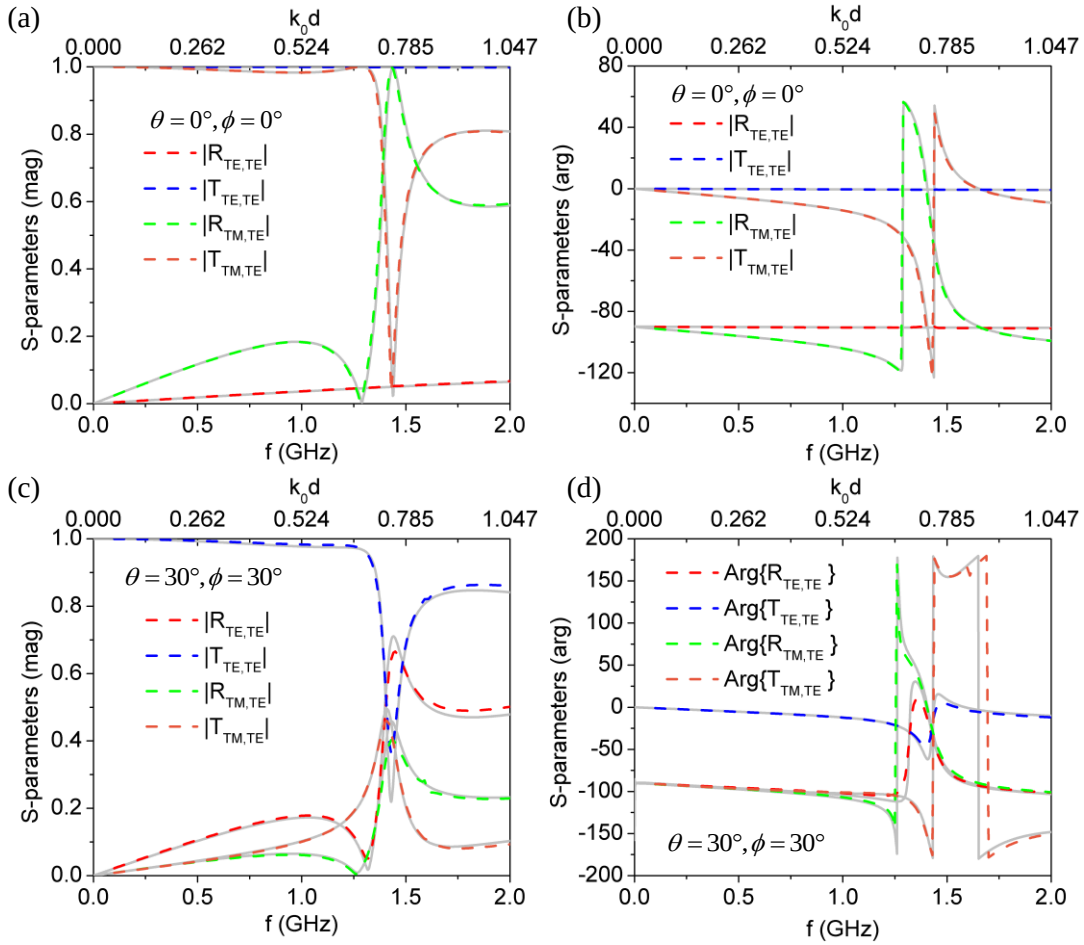

Figure 4.7 Reflection and transmission coefficients of metasurfaces composed of anti-symmetric SRRs, as illustrated in Fig 4.4b. The gray curves in each panel show the corresponding results obtained from numerical simulations in CST Microwave Studio.

The metasurfaces composed of anti-symmetric SRR pairs show interesting resonant features in the calculated transmission and reflection coefficients around $k_0 d = 0.7$, as shown in Fig. 4.7. The resonances in Fig. 4.7a and b are related to the magnetic resonance of an isolated inclusion characterized by the peaks of polarizability α_{zz}, as shown in Fig. 2.9. At oblique incidence, the resonances are still located around the same frequency, but the peak magnitudes become much weaker due to energy being split between TE and TM waves.

The good matching in Fig. 4.6 and 4.7 between analytical and numerical results suggests two important considerations: first, the polarizability tensors of SRR pairs retrieved by the system reported in Chapter 2 are physically and numerically accurate. These full-size tensors can successfully capture the induced dipole behavior of arbitrary subwavelength complex inclusions. Second, the homogenization model for 2-D metasurfaces is also correct, and the definition of generalized surface susceptibility can physically capture the average properties of complex artificial surfaces. Only provided that both models are accurate, we may obtain the degree of accuracy and consistent results shown in these figures.

4.3.3 Metasurfaces composed of plasmonic U-shape SRR

In this example, we verify and apply our model to plasmonic inclusions, considering material losses and frequency dispersion in the optical regime. Figure 4.8a and b shows the transmission and reflection coefficients for metasurfaces composed of out-of-plane silver U-shape SRRs excited by x-polarized plane waves (see Fig. 4.4d). It can be seen that, for normal incidence, the electromagnetic wave is hardly affected by the structure, even if the inclusions themselves are lossy. As we tilt the incident direction to $\theta = 30°$ and $\phi = 30°$, we can see strong resonant reflection peaks at $k_0 d \cong 0.55$ and $k_0 d \cong 1.2$, due to the resonances in α_{yy} in Fig. 2.10 (here, we are using different coordinate systems for inclusions and 2-D arrays). Moreover, wave coupling between TE and TM modes is evident for oblique excitation. It is interesting to mention that even if the magnitudes of $R_{TE,TM}$ and $T_{TE,TM}$ are near zero for normal incidence, the arguments of these coefficients shown in Fig. 4.8b are still numerically accurate, and denote some weak coupling with resonant modes.

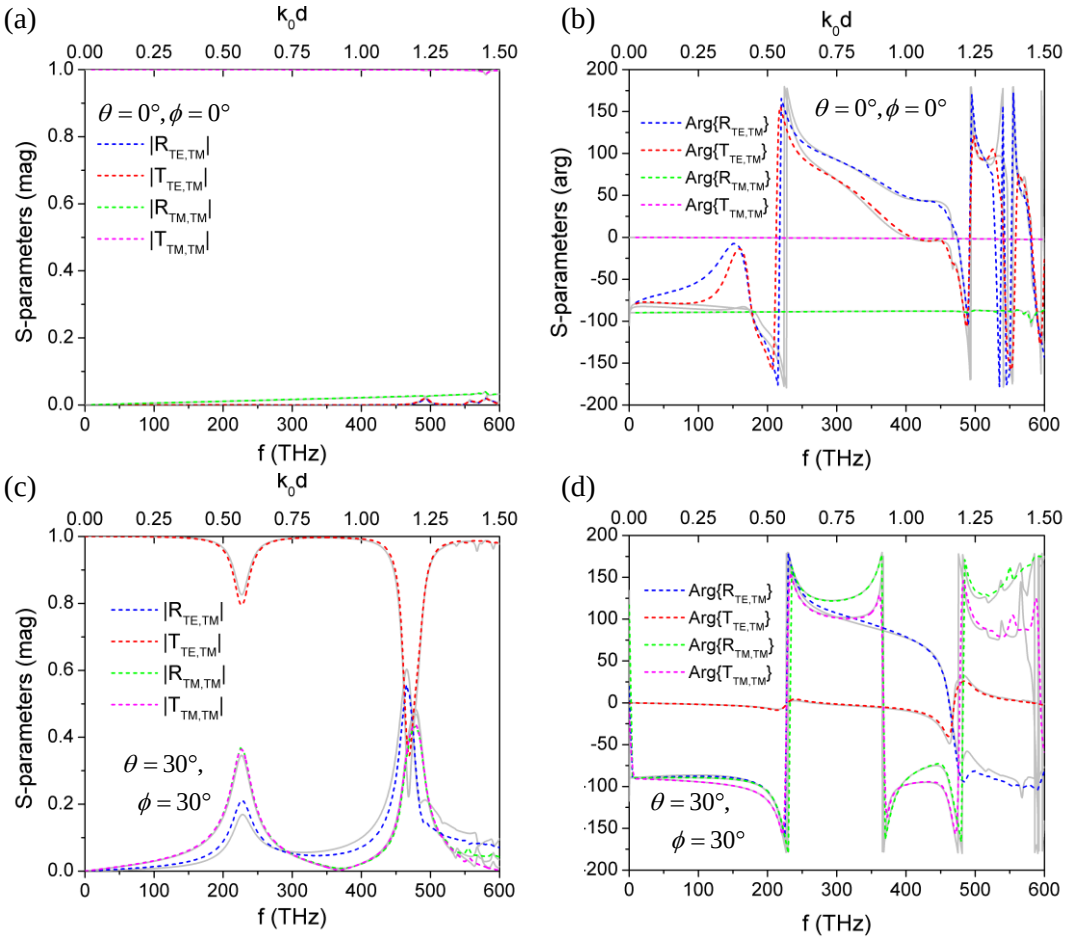

Figure 4.8 Reflection and transmission coefficients for metasurfaces composed of out-of-plane silver U-shape SRRs, as illustrated in Fig 4.4d. The gray curves in each panel show the corresponding results obtained from numerical simulations in CST Microwave Studio.

In Fig. 4.9, we analyze similar plasmonic metasurfaces, but here the inclusions are lying in the plane of the array, as more common for structures fabricated with e-beam lithography [30, 31]. In this case, we only present the results for TE excitation, as a comparison to the previous out-of-plane configuration. For normal incidence, the two reflection peaks are directly related to α_{yy} in Fig. 2.10. However, as we choose oblique incidence at $\theta = 30°$ and $\phi = 30°$, we see that broad peaks appear at $k_0 d \cong 1.0$, caused by the coupling between electric dipoles, consistent with the response of α_{xx} and α_{yy}

in Fig. 2.10. Also, in this case, we obtain significant dispersion in $\left|R_{TM,TE}\right|$ and $\left|T_{TM,TE}\right|$ due to the bianisotropic effects in the inclusions.

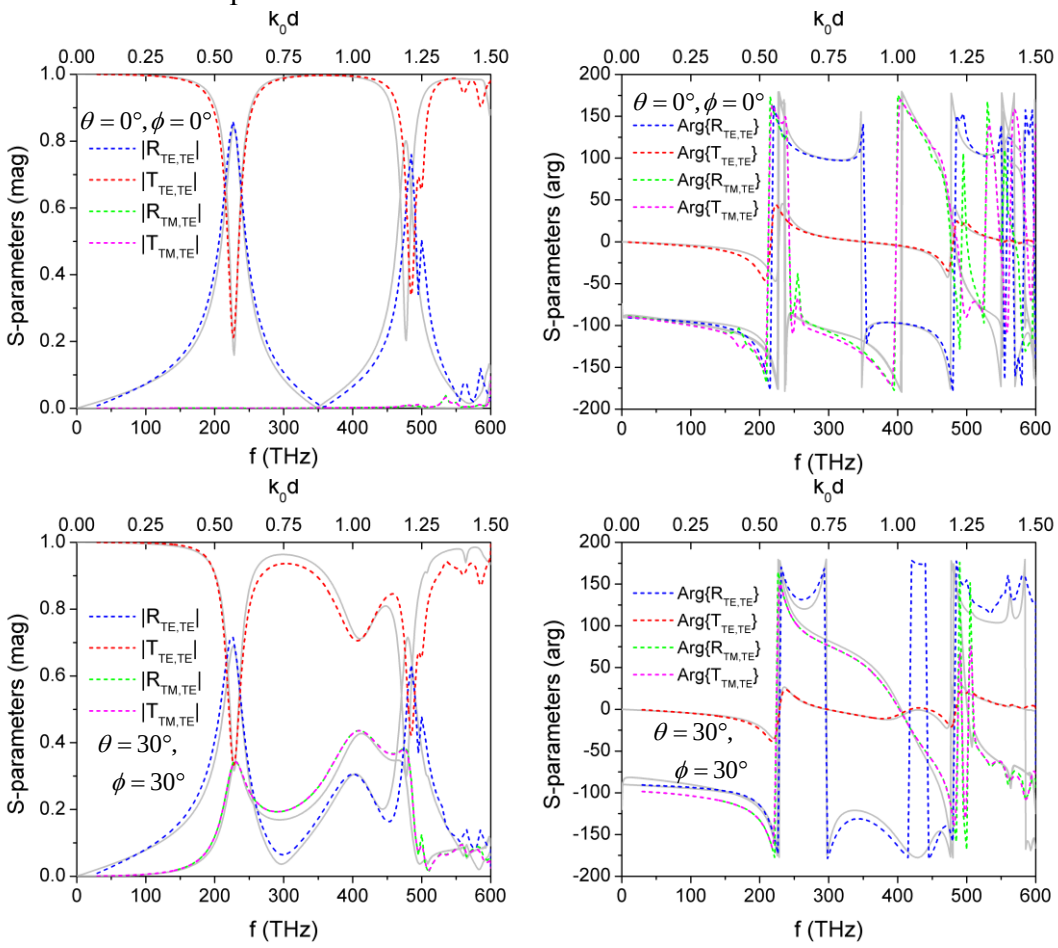

Figure 4.9 Reflection and transmission coefficients of metasurfaces composed of in-plane silver U-shape SRRs, as illustrated in Fig 4.4e. The gray curves in each panel show the corresponding results obtained from numerical simulations in CST Microwave Studio.

It appears that the developed homogenization model for planar metasurfaces is also reliable for the lossy inclusions. The numerical and analytical results not only agree very well in magnitude, but also in the arguments of the coefficients. In some frequency regimes for which the phase of the coefficients varies rapidly with frequency, the homogenization model can still offer quite accurate results.

4.4 CONCLUSIONS

In this chapter, we have presented a generalized homogenization model for metasurfaces to define and determine the complete effective surface susceptibility of 2-D arrays with arbitrary inclusion polarizability tensors. In this model, we consider all the possible interaction between induced electric and magnetic dipoles on the metasurfaces, and take into account the coupling of general TE and TM impinging waves for arbitrary oblique incidence. We have derived analytical expressions for the reflection and transmission coefficients of several metasurfaces and validated the results with CST Microwave Studio. We have shown that our model can accurately capture the effective surface susceptibility and precisely predict the transmission and reflection spectra in the subwavelength regime.

4.5 REFERENCES

1. C. L. Holloway, M. A. Mohamed, E. F. Kuester and A. Dienstfrey, "Reflection and Transmission Properties of a Metafilm: With an Application to a Controllable Surface Composed of Resonant Particles," *IEEE Trans. Electromag. Compat.* **47**, 853-865 (2005).
2. C. L. Holloway, P. Kabos, M. A. Mohamed, E. F. Kuester, J. Gordon, M. D. Janezic and J. Baker-Jarvis, "Realization of a Controllable Metafi lm/Metasurface Composed of Resonant Magnetodielectric Particles: Measurements and Theory," *IET Microwaves Antennas Propag.* **4**, 1111-1122 (2010).
3. J. F. O'Hara, E. Smirnova, A. K. Azad, H.-T. Chen, and A. J. Taylor, "Effects of Microstructure Variations on Macroscopic Terahertz Metafilm Properties," *Act. Passive Electron. Compon*. art. 49691 (2007).
4. N. Papasimakis, V. A. Fedotov, N. I. Zheludev and S. L. Prosvirnin, "Metamaterial Analog of Electromagnetically Induced Transparency," *Phys. Rev. Lett*. **101**, 253903 (2008).
5. N. Papasimakis, Y. H. Fu, V. A. Fedotov, S. L. Prosvirnin, D. P. Tsai, and N. I. Zheludev, "Metamaterial with polarization and direction insensitive resonant transmission response mimicking electromagnetically induced transparency," *Appl. Phys. Lett*. **94**, 211902 (2009).
6. J. Han, A. Lakhtakia and C.-W. Qiu, "Terahertz metamaterials with semiconductor split-ring resonators for magnetostatic tunability," *Opt. Express* **16**, 14390-14396 (2008).

7. Y. Zhao, M.A. Belkin and A. Alù, "Twisted optical metamaterials for planarized ultrathin broadband circular polarizers," Nat. Commun. **3**, 870 (2012).
8. W. J. Padilla, D. N. Basov and D. R. Smith, "Negative Refractive Index Metamaterials," *Mater. Today* **9**, 28-35 (2006).
9. D. R. Smith, D. Schurig, and J. J. Mock, "Characterization of a Planar Artifi cial Magnetic Metamaterial Surface," *Phys. Rev. E* **74**, 036604 (2006).
10. C. Highstrete, M. Lee, and W. Padilla, "Complementary Planar Terahertz Metamaterials," *Opt. Express* **15**, 1084-1095 (2007).
11. W. J. Padilla, A. J. Taylor, C. Highstrete, M. Lee, and R. D. Averitt, "Dynamical Electric and Magnetic Metamaterial Response at Terahertz Frequencies," *Phys. Rev. Lett.* **96**, 107401 (2006).
12. H. Tao, A. C. Strikwerda, K. Fan, W. J. Padilla, X. Zhang, and R. D. Averitt, "Reconfi gurable Terahertz Metamaterials," *Phys. Rev. Lett.* **103**, 147401 (2009).
13. C. L. Holloway, E. F. Kuester, J. A. Gordon, J. O'Hara, J. Booth, D. R. Smith, "An Overview of the Theory and Applications of Metasurfaces: The Two-Dimensional Equivalents of Metamaterials," *IEEE Antennas Propag. Mag*. **54**, 10-35 (2012).
14. E. F. Kuester, M.A. Mohamed, M. Piket-May and C. L. Holloway, "Averaged transition conditions for electromagnetic fields at a metafilm," *IEEE Trans. Antennas Propag.* **51**, 2641-2651 (2003).
15. B. A. Munk, *Frequency Selective Surfaces: Theory and Design*, (Wiley-Interscience, 2000).
16. C. Caloz and T. Itoh, *Electromagnetic Metamaterials: Transmission Line Theory and Microwave Applications*, Wiley-IEEE Press (2005).
17. C. L. Holloway, E. F. Kuester, and A. Dienstfrey, "Characterizing Metasurfaces/Metafilms: The Connection Between Surface Susceptibilities and Effective Material Properties," *IEEE Antennas Wirel. Propag. Lett*. **10**, 1507-1511 (2011).
18. C. L. Holloway, A. Dienstfrey, E. F. Kuester, J. F. O'Hara, A. K. Azad, and A. J. Taylord, "A discussion on the interpretation and characterization of metafilms/metasurfaces: The two-dimensional equivalent of metamaterials," *Metamaterials* **3**, 100-112 (2009).
19. A. I. Dimitriadis, D. L. Sounas, N. V. Kantartzis, C. Caloz, and T. D. Tsiboukis, "Surface Susceptibility Bianisotropic Matrix Model for Periodic Metasurfaces of Uniaxially Mono-Anisotropic Scatterers Under Oblique TE-Wave Incidence," *IEEE Trans. Antennas Propag.* **60**, 5753-5767 (2012).
20. D. Morits and C. Simovski, "Electromagnetic characterization of planar and bulk metamaterials: A theoretical study," *Phys. Rev. B* **82**, 165114 (2010).
21. M. Albooyeh, D. Morits and C.R. Simovski, "Electromagnetic characterization of substrated metasurfaces," *Metamaterials* **5**, 178-205 (2011).
22. A. I. Dimitriadis, N. V. Kantartzis, I. T. Rekanos and T. D. Tsiboukis, "Efficient Metafilm/Metasurface Characterization for Obliquely Incident TE Waves via Surface Susceptibility Models," *IEEE Trans. Magn*. **48**, 367-370 (2012).

23. S. H. Mousavi, A. B. Khanikaev, and G. Shvets, "Optical properties of Fano-resonant metallic metasurfaces on a substrate," *Phys. Rev. B* **85**, 155429 (2012).
24. M. Beruete, M. Sorolla, R. Marqués, J. D. Baena and M. Freire, "Resonance and Cross-Polarization Effects in Conventional and Complementary Split Ring Resonator Periodic Screens," *Electromagnetics* **26**, 247-260 (2006).
25. D. L. Sounas and N. V. Kantartzis, "Systematic surface waves analysis at the interfaces of composite DNG/SNG media," *Opt. Express* **17**, 8513-8524 (2009).
26. R. E. Collin, *Field Theory of Guided Waves* (Wiley-IEEE Press, 1990).
27. P. A. Belov and C. R. Simovski, "Homogenization of electromagnetic crystals formed by uniaxial resonant scatterers," *Phys. Rev. E* **72**, 026615 (2005).
28. D. M. Pozar, *Microwave Engineering* 3rd ed., (Wiley & Sons, 2005).
29. M. Idemen, "Straightforward Derivation of Boundary Conditions on Sheet Simulating an Anisotropic Thin Layer," *Electron. Lett.* **24**, 663-665 (1988).
30. K. Aydin, I. M. Pryce, and H. A. Atwater, "Symmetry breaking and strong coupling in planar optical metamaterials," *Opt. Express* **18**, 13407-13417 (2010).
31. N. Liu, H. Guo, L. Fu, S. Kaiser, H. Schweizer, and H. Giessen, "Three-dimensional photonic metamaterials at optical frequencies," *Nat. Mater*. **7**, 31-37 (2008).

Chapter 5 Homogenization of Three-Dimensional Metamaterials

5.1 INTRODUCTION

Homogenization models for 3-D artificial composite materials have been developed and applied for several decades. Many classical mixing rules, including Clausius-Mossotti [1] , Maxwell-Garnett [2, 3], and Bruggeman formulations [4] have been widely used to predict material properties of composite dielectric media embedded or mixed with small impurities. These classical theories, usually applied at low frequencies or under quasi-static conditions [2], are based on the average of isomorphic dipolar scattering response generated by the embedded small dielectric or metal particles. Due to the assumptions of simple scattering patterns, these approaches have provided elegant analytical formulations and have become valuable tools to characterize the electromagnetic properties of conventional composite dielectric materials [5, 6].

However, there are many physical limitations for these models to be applicable to artificial media. For instance, in order to ensure isomorphic scattering, the geometry of the inclusions are required to be simple and sufficiently smaller than the wavelength of operation [2, 7], and the particle distribution density should be dilute enough such that field coupling or interaction between the particles are weak. Moreover, these mixing formulas and classical models only describe average material properties in the regimes of conventional dielectric and magnetic responses (i.e., positive permittivity and permeability). They are not able to describe the exotic electromagnetic mechanism, such as negative refraction and artificial bianisotropic effects, arising in modern composite media with novel phenomena or electromagnetic characteristics unavailable in nature.

Recently, the concept of metamaterials has received a great amount of attention and brought promising applications to optical, terahertz and microwave technologies. Metamaterials are artificial structures composed of specifically designed subwavelength

inclusions with certain polarization characteristics and they have shown several interesting phenomena, including negative refraction [8, 9], artificial magnetism [10], artificial chirality [11-13]. These novel material properties are mainly caused by the special scattering and polarization properties of complex inclusions, such as SRRs [10, 11], omega-shaped wires [4, 5] and helix wires [16]. Unlike the simple particles in conventional mixtures, these metamaterial inclusions are specifically engineered to produce certain polarizations or patterns of induced current circulation, and therefore, they usually generate interesting electric or magnetic response within the unit cells. Since their unit cell structures are still moderately smaller than the wavelength [7], metamaterials can be treated as macroscopically homogenized bulk materials which are characterized by some set of effective constitutive parameters.

From an engineering point of view, it is highly desirable to use physically meaningful parameters to describe the whole metamaterials and inversely design the geometry of inclusions to achieve certain values of parameters at the interesting frequency. However, the classical homogenization theories or mixing rules based on quasi-static conditions and simple small particles fail to predict the properties and incorrectly characterize the physical bulk parameters for the metamaterials. Since the conventional approaches cannot capture the sophisticated mechanism of field interactions within these complex arrays, more rigorous models are required.

In the past decade, many modern homogenization theories [17-40] have been put forward from analytical and numerical aspects to describe metamaterials with complex inclusions that support strong electric and/or magnetic resonances in electrodynamic regime. From these previous works, we can generally conclude that a few challenging issues appear in the modern metamaterial homogenization procedures that lead to dubious results or a nonphysical description of these novel structures.

Among these challenging issues, the first and most relevant one is the nonphysical nature of homogenized parameters. Many works applied conventional retrieval procedures [17, 18] (i.e., the NRW retrieval method [41, 42]) to extract effective parameters by treating the metamaterial as homogeneous bulk media with the same dimensions. However, these studies reported some retrieved parameters which violate the fundamental physical principles and assumptions, such as Kramers-Kronig relations and passivity [43]. This is because the exotic properties of metamaterials are usually supported by electric and magnetic resonances or strong interactions in the inclusion and lattice levels. In these resonant circumstances, however, the effective wavelengths are usually comparable to the feature size of the inclusions ($d \sim \lambda/2\pi$, d is the period size of unit cell), and therefore, the phase variation across the unit cell is not negligible [43]. As a consequence, the quasi-static assumption may lead to erroneous results and fully dynamic wave propagation has to be considered. These finite phase oscillations may affect the field homogenization within the unit cells and the induced dipoles or their couplings would become wavenumber-dependent. These phenomena are known as spatial dispersion, or non-local effects [44]. Without analytically capturing these detailed mechanisms, the homogenization procedure may not provide physically correct effective parameters, and the retrieved parameters are only valid under certain excitation conditions. Various recent studies have reported detailed discussions of these issues of non-locality and spatial dispersion [7, 24, 26, 29, 45]. Recently, a rigorous theory based on the dipolar approximation and first-principle-level derivations of dipole scattering and interactions has been reported [39]. This model derives both local and non-local parameters for metamaterials composed of isotropic inclusions, and it qualitatively elucidates the role of magneto-electric coupling at the unit cell and lattice levels, respectively. Based on this theory, we are able to restore the physically meaning of

effective parameters of metamaterials with cubic lattice for normal incidence. Generally this theory provides insightful viewpoints to approach the homogenization issues of general metamaterials.

Secondly, it is challenging to precisely quantify the microscopic scattering characteristics, or the polarizabilities, of the complex inclusions used in metamaterials. Unlike the simple particles in conventional mixing media, which are usually treated as small spherical scatterers, the inclusions of metamaterials may contain special magneto-electric effects and their polarizabilities and couplings are more complicated. Generally, in order to comprehensively describe the scattering characteristics, we need a six-by-six polarizability tensor to relate the local electromagnetic fields and co- and cross-polarizations, as described in Chapter 2. Many works have been presented to determine these quantities based on the concept of the circuit lumps with the *LC*-components [11, 25, 46-49] or the quasi-static approximation with conservation of radiation energy [49-51]. However, most of the procedures are still tricky due to the nature of complicated geometry, and it usually fails to accurately specify the polarizability in dynamic regime. In Chapter 2 of this dissertation, we have derived a retrieval method to determine the full polarizability dyads for arbitrary subwavelength inclusions based on a 2-D array configuration [30, 53]. This model can be applied to realistic metamaterials in any frequency regimes and it only requires the scattering parameters of a 2-D array composed of the complex inclusions to calculate the dyadic polarizability. Therefore, it is very efficient in numeric and is also providing physical insights of the inclusion couplings. We will apply this method to a fully general 3-D homogenization of metamaterials in this chapter.

The third challenging and interesting issue is the anisotropic and bianisotropic nature of metamaterials. Since metamaterials are composed of complex inclusions, it is

expected that the homogenized response may be highly anisotropic and the effective parameters should be expressed in dyadic forms [25-26,34-35]. Moreover, the constitutive relations for artificial materials should take into account the bianisotropic effect and be written in the Tellegen form [54]. Overall, the tensorial bianisotropic parameters that govern cross-coupling among electric and magnetic fields are generally required. Under some circumstances, the inclusion resonances or the array resonances may become very sensitive to the wave propagation directions, and therefore, different incident waves may see different homogenized results. Some previous approaches and theories [33-38] have been reported to determine dyadic constitutive parameters by purely numerical methods or quasi-static approximations. However, these works are designed for specific geometries and rely on numerical methods that are computationally inefficient. Some other difficult and practical issues, such as granular boundaries [55, 56] and disorder in the lattices and unit cells may also be discussed in metamaterial homogenization. However, these are secondary problems compared to the above three main issues, and their influence is of second-order in the homogenization problem.

In this chapter, we develop a general homogenization theory to overcome these challenging issues and explicitly derive the four dyadic effective parameters of metamaterials in the general bianisotropic constitutive relations. We take advantage of the results of dyadic polarizabilities from our retrieval method in Chapter 2 to model the inclusions as a combination of six orthogonal electric and magnetic dipoles. We explicitly present the analytical formulation for the effective parameters based on polarizabilities and dyadic interaction coefficients. We apply fast-convergent algorithms for dyadic Green's functions [20] and extend the scalar first-principle homogenization theory [39] to formulate dyadic effective parameters for generalized constitutive relations. The proposed theory comprehensively takes into account arbitrary propagation

directions and subwavelength inclusions that can induce any possible forms of anisotropic and bianisotropic effects in the unit cell and lattices. This method may deal with realistic lossy and dispersive materials and it is valid for complex dispersion relations due to the nature of the proposed algorithm. In order to validate the proposed theory, we apply it to two examples of metamaterials, which are composed of magnetodielectric spheres and conducting SRR pairs, respectively. We also compare the results of our analytical model to those from CST Microwave Studio, in order to demonstrate the accuracy of the proposed homogenization model and of the retrieved polarizability dyads. Moreover, we employ fundamental physical principles, such as reciprocal relations [43] to further validate the dyadic effective parameters.

After rigorously formulating the homogenization theory for general 3-D metamaterials, we revisit the conventional NRW retrieval method to discuss the issue of nonphysical effective parameters. As many previous works mentioned [7, 24, 26, 29, 43, 45], the nonphysical parameters of a homogenized metamaterial mainly results from the over-simplified consideration of magneto-electric coupling in the structure. Based on the presented generalized homogenization theory, we are able to take into account these complicated effects and modify the classical retrieval method to extract physically meaningful effective parameters of a given metamaterial. This new method not only provides the constitutive parameters, but also retrieves the polarizability of the inclusions even without their geometry and material information. Finally, we present an inverse design procedure for 3-D metamaterials based on our homogenization theory. This design method may seek for the geometry of inclusions and lattice dimensions that provide the desired exotic material properties, such as negative refraction index, at a specific frequency.

This chapter is organized as follows. In section 5.2, we present the generalized homogenization theory for 3-D periodic metamaterials composed of nonconnected elements. The effective parameters are explicitly expressed in terms of polarizability and Green's dyads. In section 5.3, two examples of metamaterials, composed of magnetodielectric spheres and conducting SRRs, are provided to demonstrate the dispersion relations and parameters predicted by the homogenization theory. In section 5.4, we present a modified retrieval method for metamaterials by simplifying the homogenization theory into a scalar form and re-arranging the formulation to be combined with the NRW retrieval method. This method can simultaneously provide retrieved parameters and polarizability of the embedded inclusions. In section 5.5, we report examples of full-wave simulation to demonstrate that we can use the exotic properties to design microwave lenses to achieve beam focusing and super-resolution. Finally, in the section 5.6, we present our inverse design method for metamaterials based on a simplified version of the proposed homogenization theory. The examples of core-shell particles are used to demonstrate that designers can use this concept to efficiently design metamaterials structures with exotic wave properties at the frequency of interest.

5.2 FORMULATION

Consider an orthorhombic crystal in free space, where the subwavelength unit cells are filled with arbitrary nonconnected inclusions, which are not touching the periodic boundaries, so that the elements within each unit cell can be treated as discrete scatterers. Generally, we can describe the macroscopic Maxwell equations in terms of average field quantities within inside the unit cell as [39]

$$\boldsymbol{\beta}\times\mathbf{E}_{av}=\omega\left(\mu_0\mathbf{H}_{av}+\mathbf{M}_{av}\right)+i\mathbf{K}_{ext\_av} \tag{5.1}$$

$$\boldsymbol{\beta}\times\mathbf{H}_{av}=-\omega\left(\varepsilon_0\mathbf{E}_{av}+\mathbf{P}_{av}\right)-i\mathbf{J}_{ext\_av} \tag{5.2}$$

where the spatially average fields quantities are defined as $\mathbf{E}_{av} = V_{cell}^{-1} \int_{cell} \mathbf{E} e^{-i\boldsymbol{\beta}\cdot\mathbf{r}} dv$ [23], and $\mathbf{P}_{av}$, $\mathbf{M}_{av}$, $\mathbf{J}_{ext\_av}$, and $\mathbf{K}_{ext\_av}$ denote the averaged polarization and magnetization of the dipole moments and averaged currents inside the unit cells, respectively. Here, it is important to note that there are impressed (external) fields with the same plane wave dependence $e^{i(\boldsymbol{\beta}\cdot\mathbf{r}-\omega t)}$, sustained by the impressed source distributions. These fields satisfy

$$\begin{aligned} \boldsymbol{\beta}\times\mathbf{E}_{ext} &= \omega\mu_0\mathbf{H}_{ext} + i\mathbf{K}_{ext\_av}, \\ \boldsymbol{\beta}\times\mathbf{H}_{ext} &= -\omega\varepsilon_0\mathbf{E}_{ext} - i\mathbf{J}_{ext\_av}. \end{aligned} \tag{5.3}$$

By taking the curl on both sides of the above equations and use the vector identity $\boldsymbol{\beta}\times\boldsymbol{\beta}\times\mathbf{E}_{av} = \boldsymbol{\beta}\left(\boldsymbol{\beta}\cdot\mathbf{E}_{av}\right) - |\boldsymbol{\beta}|^2 \mathbf{E}_{av}$, we may derive the decoupled relations for electric and magnetic fields in terms of the averaged dipole moments, which are

$$\left[\left(k_0^2 - |\boldsymbol{\beta}|^2\right)\mathbf{I} + \boldsymbol{\beta}\boldsymbol{\beta}\right]\left(\mathbf{E}_{av} - \mathbf{E}_{ext}\right) = -k_0^2 \frac{\mathbf{P}_{av}}{\varepsilon_0} + k_0\eta_0\boldsymbol{\beta}\times\frac{\mathbf{M}_{av}}{\mu_0}, \tag{5.4}$$

$$\left[\left(k_0^2 - |\boldsymbol{\beta}|^2\right)\mathbf{I} + \boldsymbol{\beta}\boldsymbol{\beta}\right]\left(\mathbf{H}_{av} - \mathbf{H}_{ext}\right) = -k_0^2 \frac{\mathbf{M}_{av}}{\mu_0} - k_0\frac{1}{\eta_0}\boldsymbol{\beta}\times\frac{\mathbf{P}_{av}}{\varepsilon_0}, \tag{5.5}$$

where

$$\boldsymbol{\beta}\boldsymbol{\beta} = \begin{bmatrix} \beta_x\beta_x & \beta_x\beta_y & \beta_x\beta_z \\ \beta_y\beta_x & \beta_y\beta_y & \beta_y\beta_z \\ \beta_z\beta_x & \beta_z\beta_y & \beta_z\beta_z \end{bmatrix}$$

Moreover, we use the inverse relation

$$\left[\left(k_0^2 - |\boldsymbol{\beta}|^2\right)\mathbf{I} + \boldsymbol{\beta}\boldsymbol{\beta}\right]^{-1} = \left(\underline{\underline{\mathbf{I}}} - \frac{1}{k_0^2}\boldsymbol{\beta}\boldsymbol{\beta}\right) \Big/ \left(k_0^2 - |\boldsymbol{\beta}|^2\right)$$

to re-write the Eqs. (5.4) and (5.5) as

$$\mathbf{E}_{av} = \mathbf{E}_{ext} + \frac{\overline{\overline{\mathbf{I}}} - k_0^{-2}\boldsymbol{\beta}\boldsymbol{\beta}}{\left(k_0^2 - |\boldsymbol{\beta}|^2\right)}\left[-k_0^2 \frac{\mathbf{P}_{av}}{\varepsilon_0} + k_0\eta_0\boldsymbol{\beta}\times\frac{\mathbf{M}_{av}}{\mu_0}\right], \tag{5.6}$$

$$\mathbf{H}_{av} = \mathbf{H}_{ext} + \frac{\overline{\overline{\mathbf{I}}} - k_0^{-2}\boldsymbol{\beta}\boldsymbol{\beta}}{\left(k_0^2 - |\boldsymbol{\beta}|^2\right)}\left[-k_0^2 \frac{\mathbf{M}_{av}}{\mu_0} - k_0\frac{1}{\eta_0}\boldsymbol{\beta}\times\frac{\mathbf{P}_{av}}{\varepsilon_0}\right]. \tag{5.7}$$

From the above equations, it is obvious that electric and magnetic fields are influenced by both polarization and magnetization as well as by the imposed electric and magnetic currents. It is also important to note that, from a general macroscopic point of view, we must consider both induced electric and magnetic effects regardless of the type of inclusion materials and geometry. For simplicity, Eqs. (5.6) and (5.7) can be expressed by using the normalized wave vector $\overline{\boldsymbol{\beta}} = \boldsymbol{\beta}/k_0$ which yield

$$\mathbf{E}_{av} = \mathbf{E}_{ext} + \frac{\mathbf{I} - \overline{\boldsymbol{\beta}}\overline{\boldsymbol{\beta}}}{\left(1 - |\overline{\boldsymbol{\beta}}|^2\right)}\left[-\frac{\mathbf{P}_{av}}{\varepsilon_0} + c_0\overline{\boldsymbol{\beta}}\times\mathbf{M}_{av}\right], \tag{5.8}$$

$$\mathbf{H}_{av} = \mathbf{H}_{av} + \frac{\overline{\overline{\mathbf{I}}} - \overline{\boldsymbol{\beta}}\overline{\boldsymbol{\beta}}}{\left(1 - |\overline{\boldsymbol{\beta}}|^2\right)}\left[-\frac{\mathbf{M}_{av}}{\mu_0} - \frac{1}{c_0}\overline{\boldsymbol{\beta}}\times\mathbf{P}_{av}\right]. \tag{5.9}$$

On the other hand, from the array point of view, we may express the local fields at the center of any unit cell in terms of the dyadic Green's function and the coupling with all the other cells as

$$\begin{Bmatrix}\mathbf{E}_{loc}\\ \mathbf{H}_{loc}\end{Bmatrix} = \mathbf{C}^{3D}\begin{Bmatrix}\mathbf{p}\\ \mathbf{m}\end{Bmatrix} + \begin{Bmatrix}\mathbf{E}_{ext}\\ \mathbf{H}_{ext}\end{Bmatrix} = \begin{bmatrix}\mathbf{C}_{ee}^{3D} & \mathbf{C}_{em}^{3D}\\ \mathbf{C}_{me}^{3D} & \mathbf{C}_{mm}^{3D}\end{bmatrix}\begin{Bmatrix}\mathbf{p}\\ \mathbf{m}\end{Bmatrix} + \begin{Bmatrix}\mathbf{E}_{ext}\\ \mathbf{H}_{ext}\end{Bmatrix}, \tag{5.10}$$

in which the electric and magnetic dipole moments can be related to the averaged polarization and magnetization in the unit cell by $\mathbf{P}_{av} = \mathbf{p}/V_{cell}$ and $\mathbf{M}_{av} = \mathbf{m}/V_{cell}$, respectively.

The coefficient matrix $\mathbf{C}$ is composed of the dyadic Green's functions governing the co- and cross-couplings among the electric and magnetic dipoles, and they can be analytically written as [57]

$$\mathbf{C}_{ee} = \mathbf{C}_{mm} = \frac{3}{2} \sum_{l,m,n \neq (0,0,0)} \left(\mathbf{I} + \nabla\nabla \right) \frac{e^{-jk_0 |\mathbf{r}_{lmn}|}}{|\mathbf{r}_{lmn}|} \Bigg|_{(x,y,z)=(0,0,0)} e^{-j\left(\beta_x al + \beta_y bm + \beta_z cn\right)}, \tag{5.11}$$

$$\mathbf{C}_{em} = -\mathbf{C}_{em} = \frac{3}{2j} \sum_{l,m,n \neq (0,0,0)} \nabla \frac{e^{-jk_0 |\mathbf{r}_{lmn}|}}{|\mathbf{r}_{lmn}|} \Bigg|_{(x,y,z)=(0,0,0)} \times \mathbf{I}\, e^{-j\left(\beta_x al + \beta_y bm + \beta_z cn\right)}, \tag{5.12}$$

where a, b and c are the dimensions of unit cell, and $|\mathbf{r}_{mnl}| = \sqrt{(la)^2 + (mb)^2 + (nc)^2}$. In their practical numerical implementation, we must employ alternative algorithms for these interaction coefficients due to slow convergence. Some useful fast-convergent algorithms [20, 29, 58] based on various numerical procedures have been reported to overcome this issue.

Importantly, the co- and cross-coupling dyads in Eqs. (5.11) and (5.12) have even and odd symmetric properties with respect to the wave vector $\boldsymbol{\beta}$, which are written as

$$\begin{aligned} \mathbf{C}_{ee}^{3D}(\boldsymbol{\beta}) &= \mathbf{C}_{ee}^{3D}(-\boldsymbol{\beta}), \\ \mathbf{C}_{em}^{3D}(\boldsymbol{\beta}) &= -\mathbf{C}_{me}^{3D}(-\boldsymbol{\beta}). \end{aligned} \tag{5.13}$$

The odd symmetry in $\mathbf{C}_{em}$ and $\mathbf{C}_{me}$ implies an opposite magneto-electric coupling for opposite propagating waves. In other words, this property is responsible for the nature of non-reciprocity in metamaterial arrays [26]. The local fields can also be related to the polarizability tensor of the isolated inclusion: by combining Eqs. (5.8), (5.9), and (5.10) together with the definition of polarizability, we obtain

$$\begin{Bmatrix} \mathbf{p} \\ \mathbf{m} \end{Bmatrix} = \begin{bmatrix} \boldsymbol{\alpha}^{ee} & \boldsymbol{\alpha}^{em} \\ \boldsymbol{\alpha}^{me} & \boldsymbol{\alpha}^{mm} \end{bmatrix} \begin{Bmatrix} \mathbf{E}_{loc} \\ \mathbf{H}_{loc} \end{Bmatrix} \tag{5.14}$$

and the local electric and magnetic fields yield

$$\mathbf{E}_{loc} = \mathbf{E}_{av} + V_{cell}\mathbf{C}_{ee} \cdot \mathbf{P}_{av} + \frac{\mathbf{I} - \bar{\boldsymbol{\beta}}\bar{\boldsymbol{\beta}}}{\varepsilon_0\left(1 - \left|\bar{\boldsymbol{\beta}}\right|^2\right)} \cdot \mathbf{P}_{av} + V_{cell}\mathbf{C}_{em} \cdot \mathbf{M}_{av} - \frac{\bar{\boldsymbol{\beta}} \times \mathbf{I}}{c_0\left(1 - \left|\bar{\boldsymbol{\beta}}\right|^2\right)} \cdot \mathbf{M}_{av}, \tag{5.15}$$

$$\mathbf{H}_{loc} = \mathbf{H}_{av} + V_{cell}\mathbf{C}_{mm} \cdot \mathbf{M}_{av} + \frac{\mathbf{I} - \bar{\boldsymbol{\beta}}\bar{\boldsymbol{\beta}}}{\varepsilon_0\left(1 - \left|\bar{\boldsymbol{\beta}}\right|^2\right)} \cdot \mathbf{M}_{av} + V_{cell}\mathbf{C}_{me} \cdot \mathbf{P}_{av} - \frac{\bar{\boldsymbol{\beta}} \times \mathbf{I}}{c_0\left(1 - \left|\bar{\boldsymbol{\beta}}\right|^2\right)} \cdot \mathbf{P}_{av}. \tag{5.16}$$

We can also express the new relations for the averaged fields as

$$\mathbf{E}_{av} = \mathbf{C}'_{ee} \cdot \mathbf{P}_{av} + \mathbf{C}'_{em} \cdot \mathbf{M}_{av}, \tag{5.17}$$

$$\mathbf{H}_{av} = \mathbf{C}'_{me} \cdot \mathbf{P}_{av} + \mathbf{C}'_{mm} \cdot \mathbf{M}_{av}, \tag{5.18}$$

where the generalized interaction dyads are

$$\mathbf{C}'_{ee} = V_{cell}\left(\boldsymbol{\alpha}'^{ee} - \mathbf{C}_{ee}\right) + \frac{\bar{\boldsymbol{\beta}}\bar{\boldsymbol{\beta}} - \mathbf{I}}{\varepsilon_0\left(1 - \left|\bar{\boldsymbol{\beta}}\right|^2\right)}, \tag{5.19}$$

$$\mathbf{C}'_{em} = V_{cell}\left(\boldsymbol{\alpha}'^{em} - \mathbf{C}_{em}\right) + \frac{\bar{\boldsymbol{\beta}} \times \mathbf{I}}{c_0\left(1 - \left|\bar{\boldsymbol{\beta}}\right|^2\right)}, \tag{5.20}$$

$$\mathbf{C}'_{mm} = V_{cell}\left(\boldsymbol{\alpha}'^{mm} - \mathbf{C}_{mm}\right) + \frac{\bar{\boldsymbol{\beta}}\bar{\boldsymbol{\beta}} - \mathbf{I}}{\mu_0\left(1 - \left|\bar{\boldsymbol{\beta}}\right|^2\right)}, \tag{5.21}$$

$$\mathbf{C}'_{me} = V_{cell}\left(\boldsymbol{\alpha}'^{me} - \mathbf{C}_{me}\right) - \frac{\bar{\boldsymbol{\beta}} \times \mathbf{I}}{c_0\left(1 - \left|\bar{\boldsymbol{\beta}}\right|^2\right)}, \tag{5.22}$$

and

$$\begin{bmatrix} \boldsymbol{\alpha}'^{ee} & \boldsymbol{\alpha}'^{em} \\ \boldsymbol{\alpha}'^{me} & \boldsymbol{\alpha}'^{mm} \end{bmatrix} = \begin{bmatrix} \boldsymbol{\alpha}^{ee} & \boldsymbol{\alpha}^{em} \\ \boldsymbol{\alpha}^{me} & \boldsymbol{\alpha}^{mm} \end{bmatrix}^{-1}. \tag{5.23}$$

It is interesting to note that the coefficients $\mathbf{C}'_{em}$ and $\mathbf{C}'_{me}$ lose their symmetric properties with respect to $\boldsymbol{\beta}$ when the inclusion is bianisotropic or with non-vanishing $\boldsymbol{\alpha}'^{em}$ and $\boldsymbol{\alpha}'^{me}$. This fact is important for metamaterials composed of complex inclusions, such as SRRs, and it may redefine the usual reciprocity relations for complex artificial media.

The expressions in Eqs. (5.17) and (5.18) relate the external fields in Eqs. (5.8) and (5.9) to the polarizability and interaction coefficients. Based on Eq. (5.3), the external fields are determined by the impressed sources $\mathbf{J}_{ext\_av}$ and $\mathbf{K}_{ext\_av}$ in Maxwell's equations. Therefore, we are able to apply any set of plane-wave-dependent sources in Eqs. (5.8) and (5.9) to change the proportions of $\mathbf{P}_{av}$ and $\mathbf{M}_{av}$ with respect to $\mathbf{E}_{av}$ and $\mathbf{H}_{av}$ (see Eqs. (5.17) and (5.18)). In other words, for a given k_0 (with $k_0 d < 1$), there are an infinite number of $\bar{\boldsymbol{\beta}}$ such that the Eqs. (5.17) and (5.18) can be satisfied, as a function of the impressed sources and external fields.

On the other hand, in the case without external sources (eigen-modal scenario), we may combine Eqs. (5.10) and (5.14) to obtain a dispersion relation for general 3-D metamaterial which yields

$$\boldsymbol{\alpha}^{-1} - \mathbf{C} = \mathbf{0}. \tag{5.24}$$

This equation restricts the relation between wave number in free space (k_0) and in the array ($\bar{\boldsymbol{\beta}}$) for each mode. Without the degree of freedom brought by external fields to independently manipulate electric and magnetic fields in the metamaterials, the problem becomes an eigenmodal analysis and the ratio of $\mathbf{P}_{av}$ and $\mathbf{M}_{av}$ is fixed. The valid

$k_0 - \boldsymbol{\beta}$ relation in the source-free condition is essentially the dispersion relation for the propagating eigenwaves in the metamaterial.

After some simple algebraic manipulations on Eqs. (5.17) and (5.18), we derive the averaged dipole moments in terms of electric and magnetic fields:

$$\left[\mathbf{I} - \mathbf{C}'^{-1}_{ee}\mathbf{C}'_{em}\mathbf{C}'^{-1}_{mm}\mathbf{C}'_{me}\right]\cdot\mathbf{P}_{av} = \mathbf{C}'^{-1}_{ee}\cdot\mathbf{E}_{av} - \mathbf{C}'^{-1}_{ee}\mathbf{C}'_{em}\mathbf{C}'^{-1}_{mm}\cdot\mathbf{H}_{av} \tag{5.25}$$

$$\left[\mathbf{I} - \mathbf{C}'^{-1}_{mm}\mathbf{C}'_{me}\mathbf{C}'^{-1}_{ee}\mathbf{C}'_{em}\right]\cdot\mathbf{M}_{av} = \mathbf{C}'^{-1}_{mm}\cdot\mathbf{H}_{av} - \mathbf{C}'^{-1}_{mm}\mathbf{C}'_{me}\mathbf{C}'^{-1}_{ee}\cdot\mathbf{E}_{av} \tag{5.26}$$

By considering the definition of displacement fields and general bianisotropic (also known as Tellegen form) constitutive relations

$$\mathbf{D}_{av} = \varepsilon_0\mathbf{E}_{av} + \mathbf{P}_{av} = \varepsilon_0\boldsymbol{\varepsilon}_{eff}\cdot\mathbf{E}_{av} + c_0^{-1}\boldsymbol{\xi}_{eff}\cdot\mathbf{H}_{av}, \tag{5.27}$$

$$\mathbf{B}_{av} = \mu_0\mathbf{H}_{av} + \mathbf{M}_{av} = c_0^{-1}\boldsymbol{\zeta}_{eff}\cdot\mathbf{E}_{av} + \mu_0\boldsymbol{\mu}_{eff}\cdot\mathbf{H}_{av}, \tag{5.28}$$

we may finally write the effective dyadic parameters of the given array composed of subwavelength unit cells as

$$\boldsymbol{\varepsilon}_{eff} = \mathbf{I} + \varepsilon_0^{-1}\left[\mathbf{I} - \mathbf{C}'^{-1}_{ee}\mathbf{C}'_{em}\mathbf{C}'^{-1}_{mm}\mathbf{C}'_{me}\right]^{-1}\mathbf{C}'^{-1}_{ee}, \tag{5.29}$$

$$\boldsymbol{\mu}_{eff} = \mathbf{I} + \mu_0^{-1}\left[\mathbf{I} - \mathbf{C}'^{-1}_{mm}\mathbf{C}'_{me}\mathbf{C}'^{-1}_{ee}\mathbf{C}'_{em}\right]^{-1}\mathbf{C}'^{-1}_{mm}, \tag{5.30}$$

$$\boldsymbol{\xi}_{eff} = -c_0\left[\mathbf{I} - \mathbf{C}'^{-1}_{ee}\mathbf{C}'_{em}\mathbf{C}'^{-1}_{mm}\mathbf{C}'_{me}\right]^{-1}\mathbf{C}'^{-1}_{ee}\mathbf{C}'_{em}\mathbf{C}'^{-1}_{mm}, \tag{5.31}$$

$$\boldsymbol{\zeta}_{eff} = -c_0\left[\mathbf{I} - \mathbf{C}'^{-1}_{mm}\mathbf{C}'_{me}\mathbf{C}'^{-1}_{ee}\mathbf{C}'_{em}\right]^{-1}\mathbf{C}'^{-1}_{mm}\mathbf{C}'_{me}\mathbf{C}'^{-1}_{ee}. \tag{5.32}$$

Equations (5.29)-(5.32) show the bianisotropic effective parameters used to describe the macroscopic electromagnetic fields and bianisotropic constitutive relations of the general 3-D metamaterials composed of arbitrary subwavelength inclusions.

By rearranging the wave equations of electric and magnetic fields, one can simplify the bianisotropic expressions into anisotropic forms without explicitly showing the magneto-electric dyads ξ_{eff} and ζ_{eff} [40]. In the previous work [39], the author has combined the magneto-electric coupling (bi-isotropic) terms in the constitutive relations into the alternative permittivity and permeability terms and defined the non-local *equivalent* parameters in scalar form for isotropic inclusions and propagation along the lattice axis. Similarly, we are able to arrange here Maxwell's equations to combine the magneto-electric dyads $\underline{\underline{\xi}}_{eff}$ and $\underline{\underline{\zeta}}_{eff}$ into the anisotropic permittivity and permeability dyads. In this way, we may write the curl equations of electric and magnetic fields in bianisotropic media as

$$i\boldsymbol{\beta}\times\mathbf{E}_{av} = i\boldsymbol{\beta}_m\mathbf{E}_{av} = i\omega\mu_0\boldsymbol{\mu}_{eff}\mathbf{H}_{av} + i\omega c_0^{-1}\boldsymbol{\zeta}_{eff}\mathbf{E}_{av}, \tag{5.33}$$

$$i\boldsymbol{\beta}\times\mathbf{H}_{av} = i\boldsymbol{\beta}_m\mathbf{H}_{av} = -i\omega\varepsilon_0\boldsymbol{\varepsilon}_{eff}\mathbf{E}_{av} - i\omega c_0^{-1}\boldsymbol{\xi}_{eff}\mathbf{H}_{av}, \tag{5.34}$$

where the vector cross operations on field quantities $\boldsymbol{\beta}\times\mathbf{E}_{av}$ are replaced by matrix multiplication $\underline{\underline{\boldsymbol{\beta}}}_m\mathbf{E}_{av}$ with a singular matrix

$$\boldsymbol{\beta}_m = \begin{bmatrix} 0 & -\beta_z & \beta_y \\ \beta_z & 0 & -\beta_x \\ -\beta_y & \beta_x & 0 \end{bmatrix}. \tag{5.35}$$

To rearrange the bianisotropic wave equations into anisotropic form, we could solve for $\mathbf{E}_{av}$ and $\mathbf{H}_{av}$ in Eqs. (5.33) and (5.34), and substitute them into Eqs. (5.33) and (5.34), respectively. With some straightforward manipulations, we can obtain

$$\boldsymbol{\beta}\times\mathbf{E}_{av} = \omega\mu_0\boldsymbol{\mu}_{eq}\mathbf{H}_{av}, \tag{5.36}$$

$$\boldsymbol{\beta}\times\mathbf{H}_{av} = -\omega\varepsilon_0\boldsymbol{\varepsilon}_{eq}\mathbf{E}_{av}, \tag{5.37}$$

with the equivalent parameters being

$$\boldsymbol{\varepsilon}_{eq} = \boldsymbol{\varepsilon}_{eff} + c_0 \boldsymbol{\xi}_{eff} \boldsymbol{\mu}_{eff}^{-1} \left(\omega^{-1} \boldsymbol{\beta}_m - c_0^{-1} \boldsymbol{\zeta}_{eff} \right), \tag{5.38}$$

$$\boldsymbol{\mu}_{eq} = \boldsymbol{\mu}_{eff} - c_0 \boldsymbol{\zeta}_{eff} \boldsymbol{\varepsilon}_{eff}^{-1} \left(\omega^{-1} \boldsymbol{\beta}_m + c_0^{-1} \boldsymbol{\xi}_{eff} \right). \tag{5.39}$$

These equivalent parameters explicitly contain the factor $\underline{\underline{\boldsymbol{\beta}}}_m$ and become spatially dispersive or *non-local*. Interestingly, we can see that both $\boldsymbol{\varepsilon}_{eff}$ and $\boldsymbol{\mu}_{eff}$ play roles in $\boldsymbol{\varepsilon}_{eq}$ and $\boldsymbol{\mu}_{eq}$, respectively, and these expressions become more complicated than the results in the isotropic cases [39]. To elucidate this issue, we can use either Eqs. (5.34) or (5.33) to determine the parameters by applying the cross operation $\boldsymbol{\beta}\times$ twice on the left side, and reorganize the leading coefficients of $\mathbf{E}_{av}$ and $\mathbf{H}_{av}$ as

$$\boldsymbol{\varepsilon}'_{eq} = \left(\boldsymbol{\beta}_m \boldsymbol{\beta}_m - \omega c_0^{-1} \boldsymbol{\beta}_m \boldsymbol{\xi}_{eff} \right)^{-1} \boldsymbol{\beta}_m \boldsymbol{\beta}_m \boldsymbol{\varepsilon}_{eff}, \tag{5.40}$$

$$\boldsymbol{\mu}'_{eq} = \left(\boldsymbol{\beta}_m \boldsymbol{\beta}_m - \omega c_0^{-1} \boldsymbol{\beta}_m \boldsymbol{\zeta}_{eff} \right)^{-1} \boldsymbol{\beta}_m \boldsymbol{\beta}_m \boldsymbol{\mu}_{eff}. \tag{5.41}$$

The two different expressions of equivalent parameters in Eqs. (5.38)-(5.39) and Eqs. (5.40)-(5.41) eventually return the same results of equivalent parameters for propagation along the axis, and we may also prove that these parameters are qualitatively coincident with the NRW retrieval for normal incidence [60]. However, the expressions (5.40) and (5.41) may encounter singularity in the inverse operations for certain specific values of $\boldsymbol{\beta}_m$.

The definition of these equivalent parameters suggests that we can always simplify the bianisotropic constitutive relations into the anisotropic form, but this inevitably returns $\boldsymbol{\beta}$-dependent homogenized parameters in these simplified expressions. In most of the traditional homogenization models, only the isotropic or anisotropic constitutive relations are considered. These models return nonphysical results that violate

Kramers-Kronig relations due to non-locality, and this issue has stirred many debates regarding the validity of homogenized parameters [43]. Here, our theory provides a complete interpretation of electromagnetic homogenization for general metamaterials and proves that we need to consider a general bianisotropic constitutive model to truly capture the magneto-electric coupling in the array and correctly characterize the bulk response of 3-D metamaterials.

5.3 Modal Analysis and Effective Parameters of Three-Dimensional Metamaterials

In this section, we apply the proposed homogenization theory to 3-D metamaterials to determine their dispersion relation and homogenized effective parameters. We focus our interest on the frequency range $k_0 d < 1.5$, which satisfies the subwavelength condition defined throughout this work. In order to demonstrate the validity of our homogenization procedure and the associated effective parameters, we consider two types of metamaterials, which are composed of cubic lattices filled with spheres and SRR inclusions, respectively. In both structures, we take into account normal and oblique wave propagation and present the sustained propagating eigenmodes. We also determine the complete effective dyadic parameters in the bianisotropic constitutive relations, including permittivity, permeability and the magneto-electric parameters. We take advantage of the numerical eigen-solver in CST Microwave Studio to verify the dispersion relations for 3-D metamaterials. Although this eigen-solver is convenient to use, it has many constraints on the materials that can be considered. For instance, dispersive, lossy or gainy media are not allowed in this solver. In addition, we verify that our derived effective parameters satisfy fundamental physical principles, such as reciprocity.

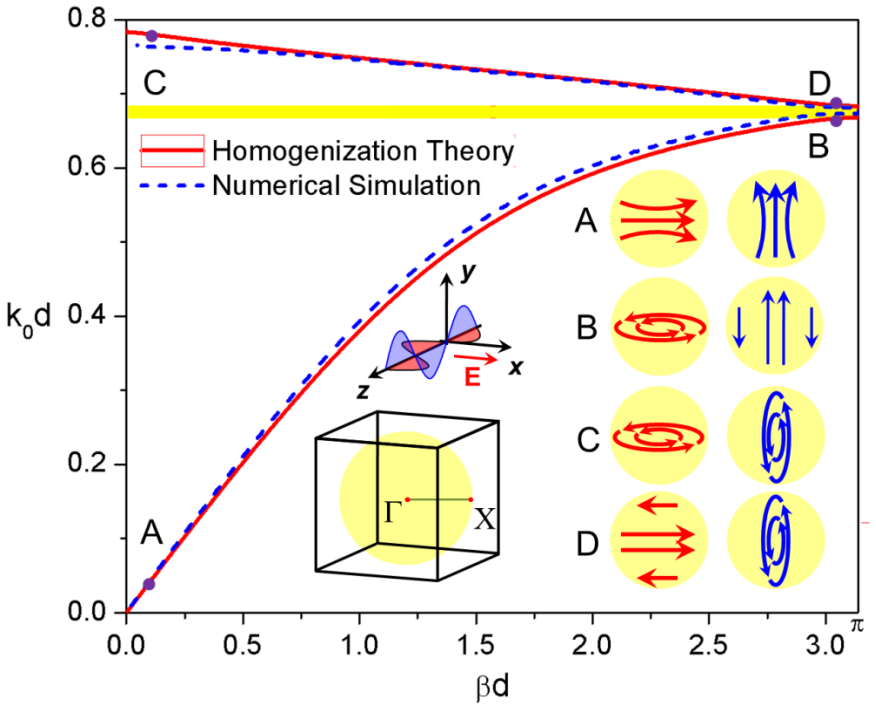

Fig. 5.1 Dispersion diagram obtained from homogenization theory and numerical simulations for propagation direction along the *z*-axis, as indicated in the legend. In the inset, we show electric (red lines) and magnetic (blue) polarization currents inside the sphere at sample frequency points A, B, C, D on the dispersion diagram. These schematic current plots are extracted from numerical simulations, in which the impinging polarization direction is along the *x*-axis.

5.3.1 Metamaterials composed of magnetodielectric spheres

Consider a 3-D metamaterial array composed of magnetodielectric spheres with relative permittivity $\varepsilon_r = 13.8$ and permeability $\mu_r = 11.0$, with a ratio of radius over period $a/d = 0.45$, as shown in the inset of Fig. 5.1. This array have been proposed to operate as a double-positive (DPS) and a double-negative (DNG) metamaterial at different frequencies in the range $k_0 d < 1$ [29]. In general, it was shown that magneto-electric coupling should be considered to determine physically meaningful homogenized parameters for this metamaterial [39], even if the inclusion geometry is simple and centrosymmetric and the propagation direction is along the principle axes of lattice.

In this example, we concentrate our discussion on the general dyadic case, considering the complete interaction coefficients in tensor form as in Eqs. (5.11)-(5.12), and we use the diagonal polarizability tensor obtained from Mie theory. For propagation along the lattice axes, this general case simplifies into the scalar form considered in Ref. 39. In order to find the dispersion curves in the general case, we numerically solve Eq. (5.24) in the complex domain and calculate the corresponding frequency k_0 for given $\underline{\underline{\boldsymbol{\beta}}}_m$ in the transcendental dispersion relation.

In Fig. 5.1, we show the calculated eigen-modal dispersion diagram for the magnetodielectric sphere array and propagation along one of the axes, calculated using the previous homogenization theory and full-wave simulations. It is seen how the dispersion curves agree very well for moderate values of βd within the frequency range $k_0 d < 0.8$. In the figure, we also schematically sketch the distributions of induced electric and magnetic currents, $\mathbf{J}$ (red arrows) and $\mathbf{K}$ (blue arrows), as observed in full-wave simulations, at the specific frequencies of interest which are indicated by the A, B, C, D points on the curves. At point A, the dispersion curve has positive slope, which corresponds to both positive effective permittivity and permeability, and the metamaterial in this regime can be well described by quasi-static models, such as Clausius-Mossotti formula [2]. At this frequency $\beta d \approx 0$ and each sphere indeed supports quasi-static distributions for both $\mathbf{J}$ and $\mathbf{K}$. The currents are almost uniformly polarized in orthogonal directions. At the other extreme of the first dispersion branch (point B) $\beta d \approx \pi$ and we hit the magnetic resonance of the array. In this case, $\mathbf{J}$ is circulating around the magnetic field, which is forcing $\mathbf{P}_{av} = 0$ and contributing only to $\mathbf{M}_{av}$. In the second dispersion branch, point C corresponds to a region in which both electric and magnetic effects are strong, causing a near-zero permittivity and permeability. In such case, both electric and magnetic currents circulate resonantly around the spheres,

contributing to both $\mathbf{P}_{av}$ and $\mathbf{M}_{av}$. Finally, point D refers to a dual configuration with respect to B, in which the array electric resonance arises near the bandgap edge. In this case, we have $\mathbf{M}_{av} \neq 0$, which causes a bend in the dispersion diagram.

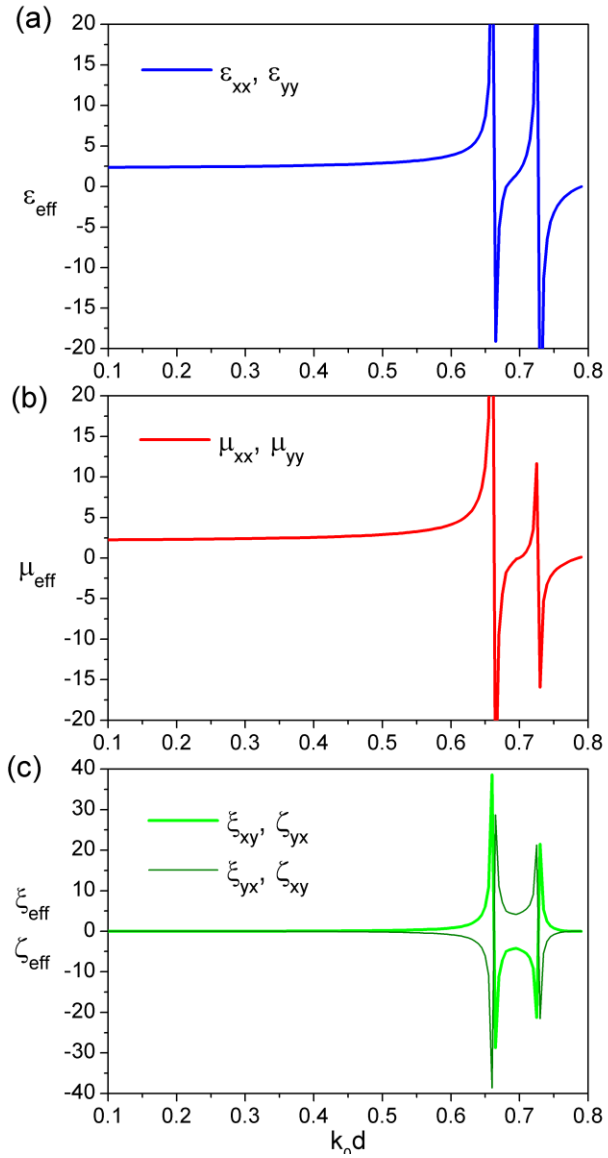

Figure 5.2 Dyadic effective parameters: (a) permittivity, (b) permeability and (c) bianisotropic terms for a metamaterial composed of magnetodielectric spheres for propagation along the axis. In this figure, only the non-zero terms in the dyads are shown.

5.3.1.1 Homogenized parameters for wave propagation along the lattice axes

In Fig. 5.2, we show the diagonal terms of dyadic permittivity, permeability and bianisotropic parameters calculated for wave propagation in the *z*-direction polarized in the *x*- or *y*-direction. Generally, ε_{xx} and ε_{yy} (μ_{xx} and μ_{yy}) terms are exactly consistent with the results determined in the scalar system [39, 60], but we can find the additional curves ε_{zz} and μ_{zz} when taking into account the dyadic formulation.

For the bianisotropic dyads, the diagonal terms are all zero and only the off-diagonal terms orthogonal to the propagation direction are nonvanishing. In addition, we observe that the reciprocity relations

$$\begin{aligned} \zeta_{eff} &= -\xi_{eff}^{\dagger}, \\ \xi_{eff} &= -\zeta_{eff}^{\dagger}, \end{aligned} \tag{5.42}$$

(the superscript † denotes a transpose and complex conjugate operator) valid for natural bianisotropy in continuum media [61, 62] do not hold in this case. This is consistent with the findings in Ref. [39] in the scalar case, and it indicates that the bianisotropic effect arising here is of odd nature with respect to $\boldsymbol{\beta}$, exclusively hidden in lattice effects. Indeed, the magneto-electric interaction produced by the cross-coupling coefficients $\mathbf{C}_{em}$ and $\mathbf{C}_{me}$, as shown in Eq. (5.13), has odd symmetry with respect to $\boldsymbol{\beta}$. In this case without chirality at the inclusion level ($\boldsymbol{\alpha}_{em} = \boldsymbol{\alpha}_{me} = \mathbf{0}$), we have the relations:

$$\begin{aligned} \boldsymbol{\varepsilon}_{eff}(-\boldsymbol{\beta}) &= \boldsymbol{\varepsilon}_{eff}(\boldsymbol{\beta}), \\ \boldsymbol{\mu}_{eff}(-\boldsymbol{\beta}) &= \boldsymbol{\mu}_{eff}(\boldsymbol{\beta}), \\ \boldsymbol{\xi}_{eff}(-\boldsymbol{\beta}) &= -\boldsymbol{\xi}_{eff}(\boldsymbol{\beta}), \\ \boldsymbol{\zeta}_{eff}(-\boldsymbol{\beta}) &= -\boldsymbol{\zeta}_{eff}(\boldsymbol{\beta}). \end{aligned} \tag{5.43}$$

It is also possible to convert the *effective* parameters into *equivalent* by using Eqs. (5.38) and (5.39) without explicitly taking into account the magneto-electric coupling terms in the constitutive relations. Figure 5.3 presents the equivalent parameters for the

same metamaterial and, in the same figure, we compare the results obtained by using the NRW retrieval method (based on a finite thickness sample composed of six unit cells in the propagating direction). The curves nicely match, but they both show evident nonphysical features. From Kramers-Kronig relations, we may expect the following general relations for lossless (or low loss) and passive media [43, 44] to hold:

$$\frac{\partial \mathrm{Re}[\varepsilon]}{\partial \omega}, \frac{\partial \mathrm{Re}[\mu]}{\partial \omega} \geq 0,$$

which means that the material dispersion curves, or the variation of ε and μ versus frequency, should always have positive slopes in regions with low loss. In Fig. 5.3, the curves experience nonphysical negative slopes near the bandgap region (marked by the yellow shade), and they considerably deviate from the effective parameters.

In a conventional retrieval, we only consider conventional constitutive relations $\mathbf{D} = \varepsilon_{eq}\mathbf{E}$ and $\mathbf{B} = \mu_{eq}\mathbf{H}$, implicitly assuming that these equivalent parameters are sufficient to describe all the electromagnetic response of the array. This is usually true for natural dielectric materials and mixtures, because their lattice structures much smaller than the wavelength of interest and the coupling among inclusions is not strong. For metamaterials, however, the rigorous theory presented above shows that most exotic phenomena arise around the resonant frequencies of the metamaterial, at which the wavelength is not sufficiently larger than the unit cell, and weak spatial dispersion effects are induced creating this anomalous magneto-electric coupling.

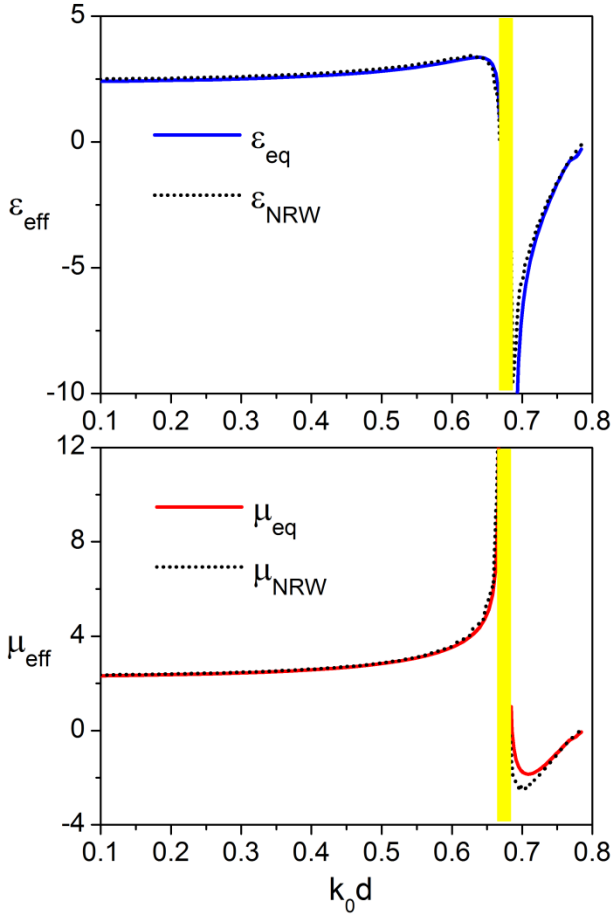

Figure 5.3 Equivalent parameters (solid lines) derived from the effective parameters in Fig. 5.2, and retrieved parameters (dotted-lines) based on NRW retrieval method for a metamaterial slab, which is composed of six layers in the propagating direction.

For example, in Fig. 5.1, we show that the pattern of eigen-modal induced electric currents may circulate in magnetodielectric spheres at higher frequencies (Point B and C). The circulating current may support strong artificial magnetic effects, causing the interaction between electric and magnetic fields. Therefore, in order to characterize metamaterials with exotic properties, we need to consider possible magneto-electric coupling in the structure. In other words, the nonphysical features in the equivalent

parameters and NRW retrieval results are associated with neglecting these aspects in modeling the arrays.

5.3.1.2 Homogenized parameters for wave propagation in oblique directions

After discussing the propagation along the lattice axes, we study two cases of eigenmodal oblique propagation , along $(\theta,\phi)=(45°,90°)$ and $(\theta,\phi)=(30°,30°)$ for the same metamaterial array. Figure 5.4 shows the dispersion of the first three eigen-modes for these two cases in the region of $k_0 d<1.0$. Quite surprisingly, we obtain here split dispersion curves in each branch, despite the strong isotropy of the array. By checking the eigenvectors corresponding to each dispersion curve, we are able to categorize them as TE and TM modes, respectively. In the insets of Fig. 5.4, we show the calculated eigenmodal patterns of magnetic and electric fields in the symmetry plane obtained from the CST numerical eigensolver at $\beta d=1.25$ for each TE and TM modes. In the presented figures, it is obvious that the dispersion curves determined from our homogenization model and full-wave simulations nicely match, and the minor discrepancies are mainly due to the fundamental assumption of dipole approximation in our theory. Like the previous example, we only consider first-order Mie coefficients in the electric and magnetic polarizabilities, and ignore all other higher-order scattering terms in each unit cell.

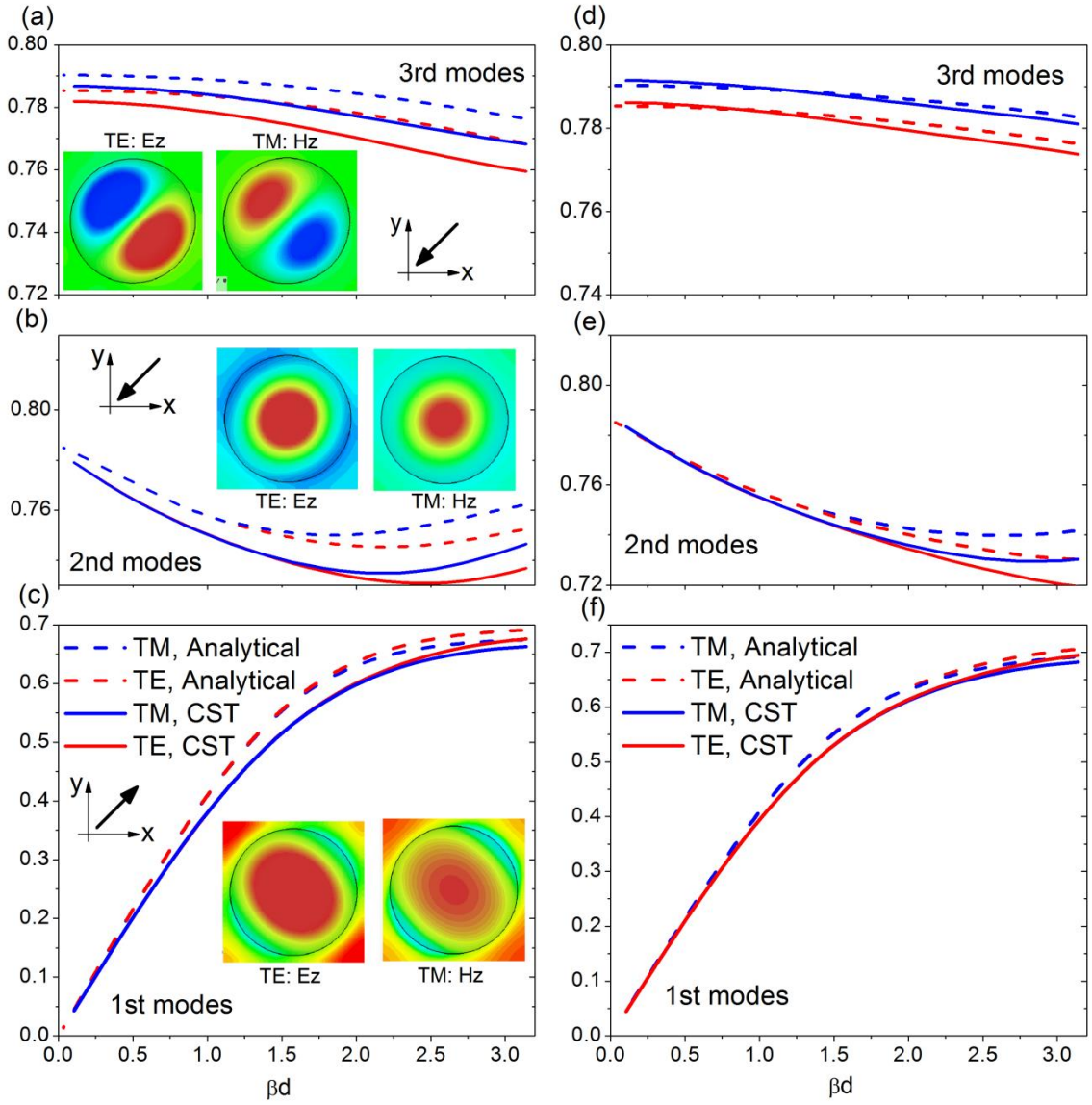

Figure 5.4 Calculated dispersion curves for the magnetodielectric sphere array considered in the previous figures for oblique propagation along (a)-(c) $(\theta,\phi)=(45°,90°)$ and (d)-(f) $(\theta,\phi)=(30°,30°)$. The field contours represent the patterns of TE and TM eigenmodes at $\beta d=1.25$ in each panel, and the bold arrows denote the direction of phase velocity.

By observing the eigenmode patterns, it is evident that the first two modes (Fig. 5.4b and c) are operating in the long-wavelength limit, dominated by dipolar oscillations, but correspond to opposite propagation directions, which are indicated by the bold arrows in the panel. The third group (Fig. 5.4a) is associated with a higher mode and also supports negative phase velocity, as predicted by the negative slope in the dispersion curves. It is also interesting to note that in the second modes (panel b), both TM and TE dispersion curves do not experience monotonic variation versus $|\boldsymbol{\beta}|d$, showing a minimum at $|\boldsymbol{\beta}|d \approx 2.2$ and $|\boldsymbol{\beta}|d \approx 2.5$, respectively. This implies the presence of spatial dispersion, allowing multiple eigenvectors with same polarization at the same eigen-frequency $k_0 d$, a situation that is not admissible in a conventional local continuum. This also implies that simplistic homogenization techniques assuming local parameters are not truly applicable to describe this metamaterial for oblique propagation, as for larger $|\boldsymbol{\beta}|d$. We may obtain two different sets of parameters for the same frequency [29].

In Fig. 5.4d-f we show the dispersion curves for propagation direction $(\theta,\phi)=(30°,30°)$. The results are similar to the previous case, confirming the *quasi-isotropic* properties of this array. Interestingly, the non-monotonic behavior here arises only for the second TM mode, implying that the level of non-locality becomes weaker for this direction of propagation. Based on these results, we can confirm that our homogenization model can accurately predict eigenmodes and dispersion relations of metamaterial arrays, and it can be efficiently applied also to complex values of $\boldsymbol{\beta}d$ arising when materials have losses, gain and frequency dispersion, which are common in realistic metamaterials. This is not true, however, for conventional commercial eigen-solvers. It is interesting to realize how such simple metamaterial array, with quasi-

isotropic properties, may support quite complex wave propagation, not at all captured by conventional homogenization schemes.

To complete the study of homogenization for oblique propagation, we substitute the dispersion results of Fig. 5.4a-c into the generalized interaction dyads in Eqs. (5.19)-(5.22) to determine the effective parameters in Eqs. (5.29)-(5.32). Figure 5.5 presents the four effective parameters in tensor form for the metamaterials under TE propagation towards $(\theta,\phi)=(45°,90°)$. Also in this case, we only show the nonzero entries. As expected, in this oblique case we can obtain also off-diagonal terms in the *xy*- and *yx*-plane of the permittivity and permeability tensors. These two terms are identical to each other due to symmetry and reciprocity. Interestingly, we also find that all the diagonal terms in $\boldsymbol{\varepsilon}_{eff}$ and $\boldsymbol{\mu}_{eff}$ obey Kramers-Kronig relations and their slope is positive for the first mode. At very low frequencies, the lattice is highly isotropic and the off-diagonal or anisotropic terms are very small. Unlike the diagonal entries, these off-diagonal terms may experience negative slopes near the resonances for oblique propagation, indicating that the level of spatial dispersion in this scenario is stronger and cannot be fully taken into account by simply the magnetoelectric coefficient. It is worth noting that in this oblique configuration only the ε_{zz} and μ_{zz} components are truly *transverse* constitutive parameters, since the fields establish a longitudinal component in the *x*- and *y*-direction. Generally, the permittivity and permeability tensors nicely follow the reciprocity conditions $\boldsymbol{\varepsilon}_{eff}=\boldsymbol{\varepsilon}_{eff}^{\dagger}$ and $\boldsymbol{\mu}_{eff}=\boldsymbol{\mu}_{eff}^{\dagger}$ [61], as expected.

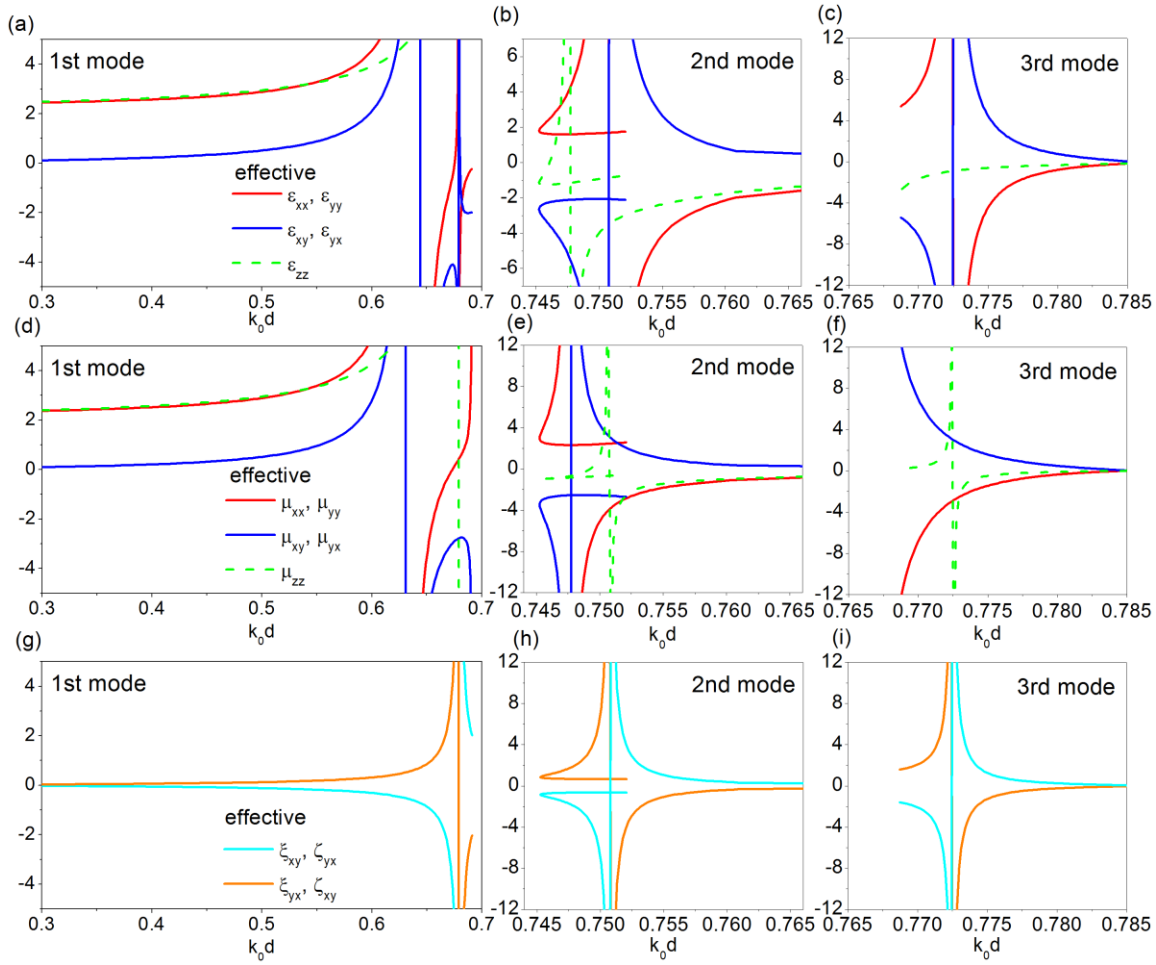

Figure 5.5 Dyadic effective parameters for TE eigen-modes in the same metamaterials as in the previous figures for oblique propagation $(\theta,\phi)=(45°,90°)$.

The results for higher-order TE modes are more complex and spatial dispersion becomes important. For the second mode, the dispersion curves are two-valued around $|\boldsymbol{\beta}|d\approx 2.5$, and this implies that these homogenized parameters lose much of their conventional meaning, since there are two different values of effective parameters corresponding to the same frequency. Additional boundary conditions are required in this regime to properly solve a scattering problem involving these homogenized parameters, as multiple modes with the same polarization may be supported by the array [68].

Importantly, we find that the regime with dispersion with negative slopes presents double negative values of ε_{zz} and μ_{zz}, which corresponds to a negative phase velocity as predicted in full-wave simulations.

The results for the bianisotropic dyads $\underline{\underline{\xi}}_{eff}$ and $\underline{\underline{\zeta}}_{eff}$ governing the magneto-electric interactions are also very interesting. Similar to propagation along the axis, the diagonal terms are all zeros, and the tensors are again not satisfying the reciprocity relations (5.42). It is interesting to note that these bianisotropic dyads are significant at frequencies near the lattice resonance, and can be neglected for small $|\boldsymbol{\beta}|d$. These effective parameters still follow the relations in Eq. (5.43).

Overall our results show that the proposed homogenization model may efficiently characterize the bulk behavior of metamaterials and capture the complex physics hidden in simple metamaterial arrays. It is apparent that the homogenized parameters obtained for normal and oblique propagation are not identical, even after applying appropriate linear transformations of the tensors. This implies that there is an inherent form of anisotropy even in very regular arrays, and spatial dispersion effects may become important even for long wavelengths. These exotic effects are mainly contributed by the inclusion or lattice resonances, and near these frequencies a careful analysis should be conducted to understand up to what degree the metamaterial can be described with quasi-local parameters. It is important to notice that these resonances can be quite sensitive to the wave propagation direction, because slight changes in the field polarization can change the coupling between neighboring, almost touching spheres. This explains why the homogenized parameters for normal and oblique incident cases can be different to some extent, and we predict that less dense arrays would be less problematic.

We can also calculate the *equivalent* parameters of the array by considering the expressions (5.38) and (5.39). Figure 5.6 shows the dispersion of equivalent

permittivity and permeability for the first and third TE modes (second modes are not considered here, due to the strong spatial dispersion highlighted in the previous figure). For long wavelengths, when the inclusions and arrays operate far away from their resonance, the bianisotropic dyads $\boldsymbol{\xi}_{eff}$ and $\boldsymbol{\zeta}_{eff}$ can be neglected, and the parameters $\boldsymbol{\varepsilon}_{eff}$ and $\boldsymbol{\varepsilon}_{eq}$ ($\boldsymbol{\mu}_{eff}$ and $\boldsymbol{\mu}_{eq}$) are consistent to each other. Also anisotropic effects are very weak in this regime, as expected. For larger frequencies, the curves of permittivity ε_{zz} and permeability μ_{xx} (μ_{yy}) experience negative slopes versus $k_0 d$ due to the non-local effects stemming from the inherent magneto-electric interactions.

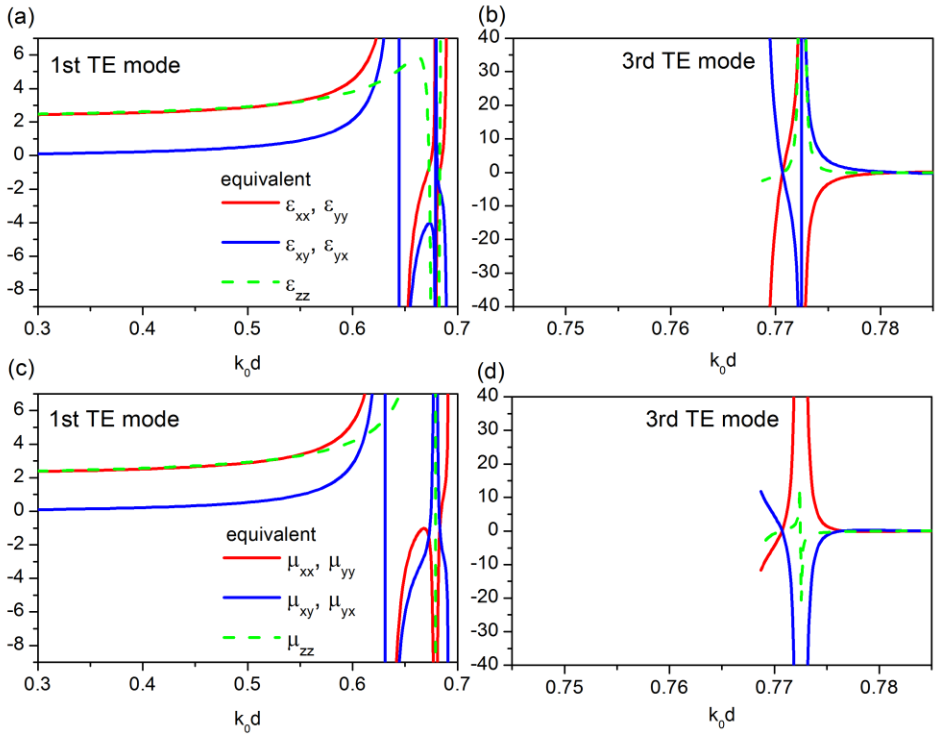

Figure 5.6 Dyadic equivalent parameters for TE modes in a metamaterial composed of magnetodielectric spheres for oblique propagation $(\theta,\phi)=(45°,90°)$.

This is consistent with the previous case for propagation along the axis, in which we were able to compare the equivalent curves with NRW retrieval results and draw a

comparison to highlight the issues associated with weak spatial dispersion captured by the effective magneto-electric dyads.

5.3.2 Homogenization of metamaterials composed of SRR pairs

In this section, we extend our discussion to 3-D metamaterials composed of complex inclusions with strong anisotropic and bianisotropic effects at the unit cell level. Here, we consider SRR inclusions arranged in anti-symmetric and symmetric pairs. We use the same geometry discussed in Chapter 2, and therefore we can directly apply the determined polarizability tensors in Figs. 2.8 and 2.9 in the following results. Based on the retrieved polarizability tensors, we can apply the eigenmodal analysis and homogenization theory described in this chapter to determine the dispersion curves and dyadic effective parameters. It is important to note that, when substituting the polarizability tensors into the eigenmodal analysis, we should carefully identify the arrangement of inclusions and correctly assign proper coordinate systems to the inclusion and array, respectively. In Fig. 5.7, we present the dispersion curves for 3-D arrays of anti-symmetric and symmetric SRR pairs, and we also compare them to the results obtained from CST eigensolver. The inset coordinates shown in Fig 5.7 are the coordinate systems for these arrays, which are different from the coordinates used for isolated inclusions in Chapter 2. In Fig 5.7a and b, the wave propagating direction is set along the *z*-axis and in the oblique direction $(\theta = 30°, \phi = 30°)$, respectively. It is evident that the calculated dispersion curves nicely match our numerical simulations and these results again validate our polarizability retrieval method and generalized eigenmodal analysis.

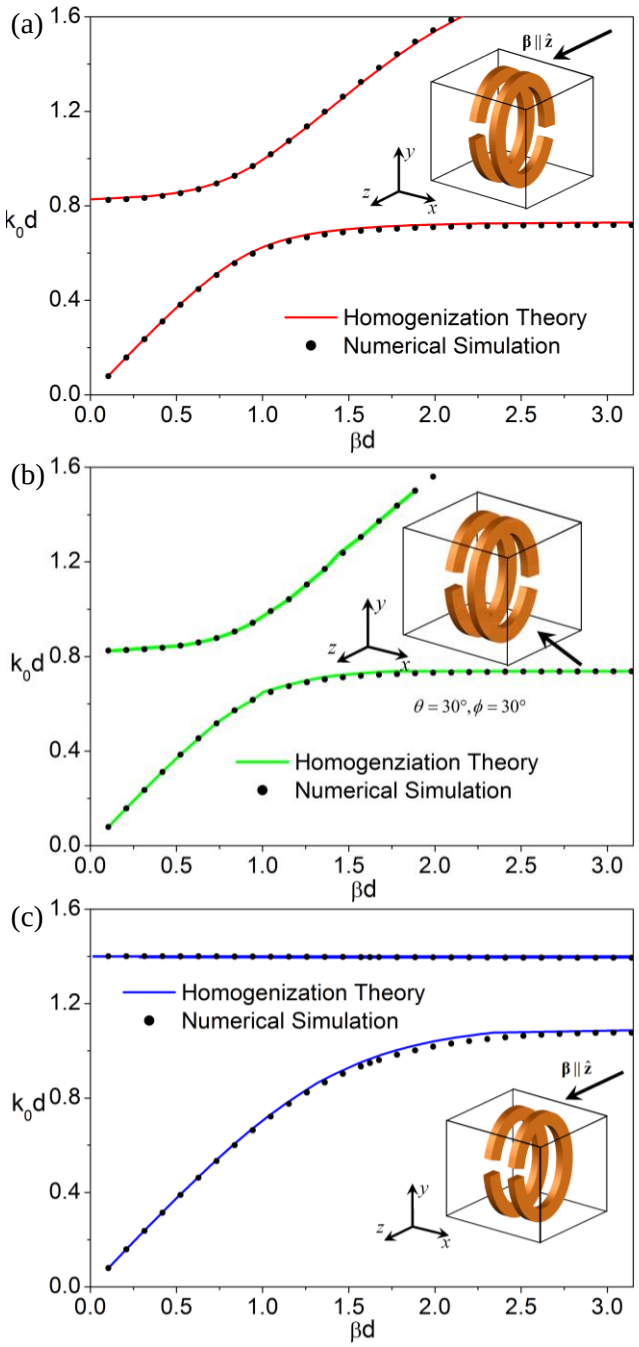

Figure 5.7 Dispersion curves for (a) anti-symmetric and (c) symmetric SRR pairs for propagation along the axis, and (b) anti-symmetric SRR pairs for oblique propagation. We compare our analytical results (solid lines) with full-wave simulation obtained from the CST eigensolver (dots).

For the anti-symmetric pair, only positive slopes are obtained because the bianisotropic effects are cancelled out by the anti-symmetric arrangement [11]. The dispersion behavior is similar to the one of a pair of small conducting rings without chirality. At the resonance, only a simple magnetic response is obtained, producing a bandgap. On the other hand, the symmetric case appears more interesting. For the first mode in Fig. 5.7b, the dispersion curve performs a typical asymptotic variation, suggesting the presence of a slow-wave mode. The second branch shows a slightly negative slope, stemming from the induced magneto-electric coupling in the SRRs. Although the branch with negative slope is narrowband, our analytical model can precisely capture this behavior. Again, it is worth noting that the analytical eigenmodal analysis is much more efficient than the numerical approach, and it can be applied to lossy or active inclusions with strong frequency dispersion.

From the calculated polarizability tensors and dispersion curves, we can further determine the dyadic effective parameters of these two 3-D metamaterials. As shown in Figs. 5.8 and 5.9, we present the non-zero terms in the effective parameters calculated using homogenization theory in Eqs. (5.29)-(5.32). Generally, both schemes of SRR array show bianisotropic effects. However, the effects sustained on two arrangements are very different. Notice that the permeability curves stop at zero and do not continue in the region where negative permeability is expected. This is because we are applying our homogenization technique to only real β , while in this configuration the negative-permeability region falls in a bandgap in which β is purely imaginary. A conventional eigen-solver completely misses this range of frequencies, but our analytical formulas can easily calculate also the rest of this branch.

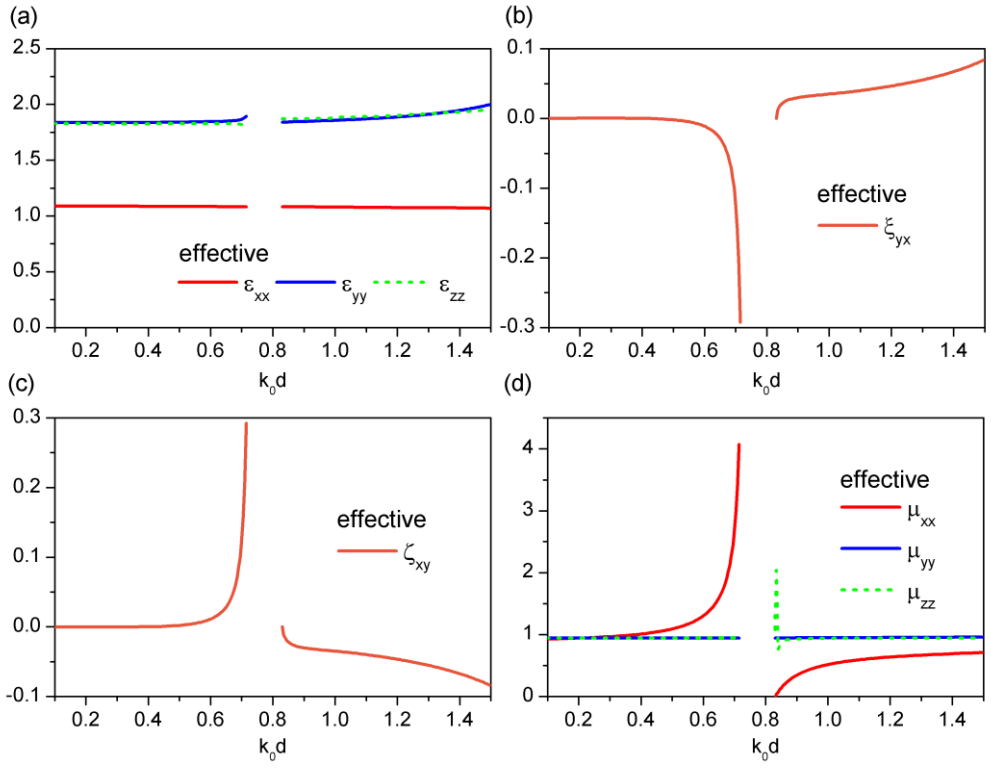

Figure 5.8 Effective parameters for anti-symmetric SRR pairs. Only the significant entries of the tensors are shown.

In Fig. 5.8, the bianisotropic parameters are produced only by the coupling effects in the array because bianisotropic effects of the isolated inclusion are cancelled, consistent with the results in Chapter 2. Due to symmetry, both permittivity and permeability tensors are diagonal and ε_{yy} and ε_{zz} are much larger than ε_{xx} for the geometry of the ring. In contrast, μ_{xx} dominates the permeability tensor as expected, and *xy* and *yx* elements are the only non-zero terms in ξ_{eff} and ζ_{eff} tensors. As expected, the results for ξ_{eff} and ζ_{eff} tensors do not satisfy the reciprocity relations in Eq. (5.42), since they are dominated by the lattice effects.

In contrast, the symmetric SRR pairs show more sophisticated results (Fig. 5.9) due to the existence of bianisotropic effects at the inclusion level. The overall

bianisotropic tensors are affected by both magneto-electric interaction at the lattice level and intrinsic bianisotropic effects at the unit cell level, producing both odd and even contributions to the bianisotropic coefficients. Another striking difference with respect to anti-symmetric SRRs consists in the electric resonance at the gap of the ring, consistent with our results in Chapter 2, which results in a Lorentzian resonance in ε_{yy}. Once again, we miss in these plots the negative branch of the Lorentzian curve because the negative permittivity region falls in a bandgap for eigen-modes.

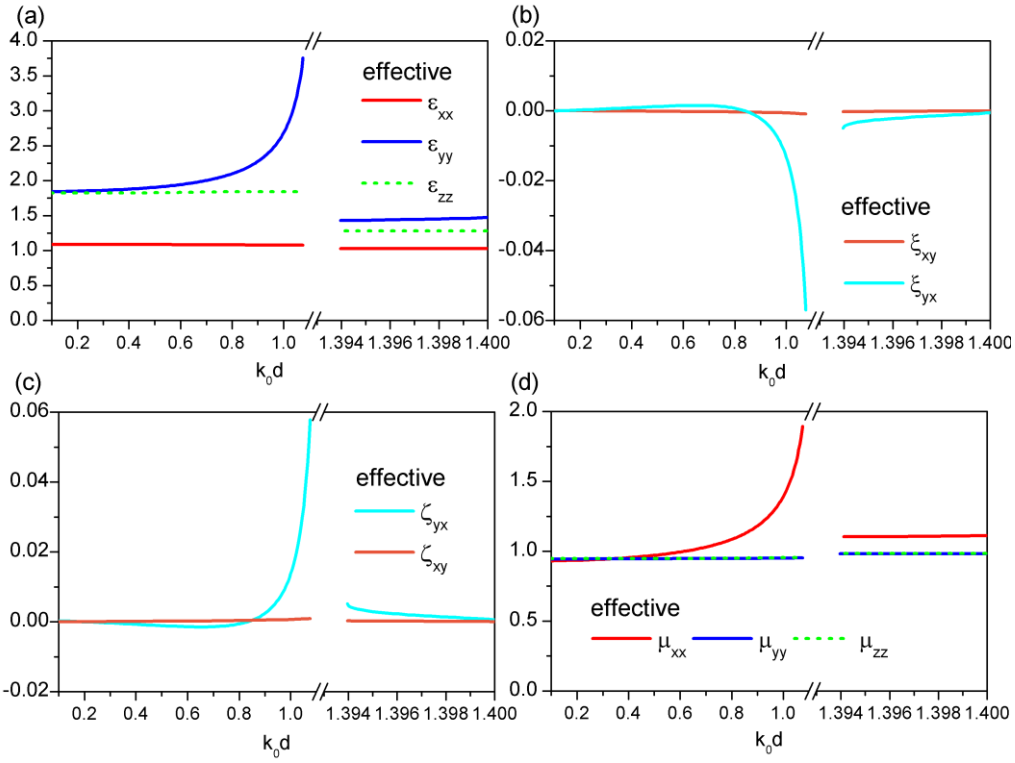

Figure 5.9 Effective parameters for metamaterials composed of symmetric SRR pairs. Only major entries in tensors are shown.

To the best of our knowledge, these are the first complete set of homogenized results for 3-D metamaterials composed of SRR pairs, highlighting the challenges

involved in properly modeling their electromagnetic response. Based on our homogenization theory, we are able to determine the effective full-tensor for these 3-D metamaterials, and we can apply similar procedures to complex metamaterial arrays at microwaves and optical frequencies.

5.4 Generalized Retrieval Method based on Homogenization Theory

In this section, we generalize the conventional Nicolson-Ross-Weir (NRW) retrieval method [17-18,66-67] to take into account the important results derived in the previous section, with the goal of deriving a generalized retrieval method that can provide physically meaningful metamaterial parameters. In conventional retrieval methods, we usually apply different excitations (i.e., plane waves) to examine the macroscopic properties of finite-sized metamaterials by calculating or measuring the transmission and reflection spectra. By manipulating these coefficients, we are able to retrieve the equivalent bulk parameters of the presumed homogeneous object that is macroscopically equal to the given metamaterials sample. This retrieval method is very popular in modern metamaterials because it is based on the scattering coefficients, which can be efficiently obtained from both experimental measurements and full-wave simulations.

However, this approach contains several drawbacks due to its simple assumptions for the metamaterials. Many homogenized parameters obtained from the NRW retrieval method have been reported to violate causality or material passivity [43]. In addition, when the metamaterial samples are thicker than the wavelength of operation, it is ambiguous to determine the correct branches for propagation constant inside the homogeneous bulk [66]. Moreover, the noise in simulations and measurements also lead to unreliable results, especially when metamaterials are operating near the Fabry-Perot resonance frequencies [69]. In the vicinity of these frequencies, the retrieval model is

very vulnerable to numerical or measurement errors. Even a small amount of noise may give rise to significant nonphysical artifacts and cause obviously incorrect retrieved parameters.

In this section, we develop a generalized retrieval method (GRM) based on our homogenization theory to evaluate physically meaningful effective parameters given the scattering properties of a metamaterial sample. The proposed method is divided in two steps: we first employ an improved version of the conventional NRW retrieval to determine *equivalent* constitutive parameters, as defined in Eqs. (5.38) and (5.39), with the same limitations as described above. Secondly, we apply the FPHT results to restore the physical meaning of these parameters and derive the *effective* constitutive parameters of the metamaterial, properly taking into account weak forms of spatial dispersion neglected in conventional NRW retrieval approaches [66]. The proposed GRM not only determines physically meaningful bulk parameters for a broad class of metamaterial geometries, but also returns, as a byproduct, the polarizabilities of each unit cell, which capture the scattering characteristics of the elementary inclusions composing the array.

After formulating the GRM, we apply it to a representative example, a metamaterial composed of subwavelength magnetodielectric spheres, and we compare the conventional NRW approach with this method to discuss physical insights and highlight its advantages. We demonstrate that the GRM returns effective constitutive parameters that satisfy the expected causality relations, in contrast with conventional retrieval approaches, and we also show its inherent robustness to measurement errors, associated with the physical foundations of its formulation. In addition to the physical insights presented in the following, from the engineering point of view this technique becomes a valuable tool to derive meaningful homogenized parameters with local

properties, which can therefore be applied to different metamaterial shapes and forms of excitation.

5.4.1 Formulations of generalized retrieval method

We formulate the GRM for a general periodic metamaterial array composed of subwavelength inclusions in an orthorhombic lattice. Extension to different lattice configurations would be straightforward, but it is not an objective of this paper. Provided that the subwavelength inclusions are not too closely packed, their scattering properties and collective interaction can be described by the dipolar polarizabilities α_{ee} and α_{mm} (magnetic), which are assumed scalar here to keep the formulation simpler. For the sake of simplicity, and to better highlight the merits of the proposed retrieval method compared to conventional techniques, we also assume absence of magneto-electric coupling within the inclusions, i.e., $\alpha_{em} = \alpha_{me} = 0$. We may simplify the bianisotropic Tellegen constitutive relations in Eqs. (5.27) and (5.28) into a *bi-isotropic* version homogenization theory, which are [39]

$$\begin{aligned} \mathbf{D}_{av} &= \varepsilon_0 \mathbf{E}_{av} + \mathbf{P}_{av} = \varepsilon_{eff} \mathbf{E}_{av} - \chi^o_{eff} \hat{\boldsymbol{\beta}} \times \mathbf{H}_{av} \\ \mathbf{B}_{av} &= \mu_0 \mathbf{H}_{av} + \mathbf{M}_{av} = \mu_{eff} \mathbf{H}_{av} + \chi^o_{eff} \hat{\boldsymbol{\beta}} \times \mathbf{E}_{av} \end{aligned}, \tag{5.44}$$

where the subscript *av* denotes the spatially averaged field within a unit cell [73], $\hat{\boldsymbol{\beta}}$ is the propagation unit vector in the metamaterial, and the *local* effective parameters are written as

$$\varepsilon_{eff} = \varepsilon_0 \left[1 + \frac{1}{d^3} \frac{\alpha_m^{-1} - C_{\text{int}}}{\left(\alpha_e^{-1} - C_{\text{int}}\right)\left(\alpha_m^{-1} - C_{\text{int}}\right) - C_{em}'^2} \right], \tag{5.45}$$

$$\mu_{eff} = \mu_0 \left[1 + \frac{1}{d^3} \frac{\alpha_e^{-1} - C_{\text{int}}}{\left(\alpha_e^{-1} - C_{\text{int}}\right)\left(\alpha_m^{-1} - C_{\text{int}}\right) - C_{em}'^2} \right], \tag{5.46}$$

$$\chi_{eff}^{o} = \frac{1}{c_0 d^3} \frac{C'_{em}}{\left(\alpha_e^{-1} - C_{\text{int}}\right)\left(\alpha_m^{-1} - C_{\text{int}}\right) - C'^{2}_{em}} . \tag{5.47}$$

Here we use the scalar interaction coefficients simplied from Eqs. (5.11) and (5.12)

$$C_{\text{int}} = -\frac{1}{d^3} \frac{k_0^2}{\beta^2 - k_0^2} + \sum_{(l,m,n)\neq(0,0,0)} \hat{\mathbf{p}} \cdot \mathbf{G}_{ee}\left(\mathbf{r}_{lmn}\right) e^{i\boldsymbol{\beta}\cdot\mathbf{r}_{lmn}} \cdot \hat{\mathbf{p}} , \tag{5.48}$$

$$C'_{em} = -\left[\frac{1}{d^3} \frac{\beta k_0}{\beta^2 - k_0^2}\right] + \sum_{(l,m,n)\neq(0,0,0)} \hat{\mathbf{p}} \cdot \mathbf{G}_{em}\left(\mathbf{r}_{lmn}\right) e^{i\boldsymbol{\beta}\cdot\mathbf{r}_{lmn}} \cdot \hat{\mathbf{m}} , \tag{5.49}$$

describing the co- and cross-polarization coupling of electric and magnetic dipole moments in each unit cells based on Green's functions $\mathbf{G}_{ee}$ and $\mathbf{G}_{em}$. In order to efficiently calculate the infinite summations involved in these interaction coefficients, fast algorithms are required [20, 70]. It is important to note that the constitutive relations (5.44) are written in the general Tellegen (or bianisotropic) form, which implies a form of magneto-electric coupling relating $\mathbf{D}_{av}$ to $\mathbf{H}_{av}$ and $\mathbf{B}_{av}$ to $\mathbf{E}_{av}$, even in the present case for which the inclusions in the lattice are center-symmetric. This is due to the presence of the bianisotropy parameter χ_{eff}^{o}. As discussed in previous works [71,75], this inherent form of bianisotropy, especially relevant near the inclusion or lattice resonances, is produced by weak nonlocal effects arising even in the long wavelength limit when the granularity of the array is not negligible compared to $1/\beta$. By properly taking into account these effects, it is possible to restore local and physically meaningful effective parameters [71] in the long-wavelength regime.

It should be stressed that the homogenized description in Eq. (5.44) is valid for arbitrary excitation of the structure and not only in its eigen-modal operation, as proven in Ref. 71. This property is very appealing for practical applications, as it allows using

these parameters independent on the form and type of excitation of the metamaterial sample. In the general case, the constitutive parameters (5.45)-(5.47) are functions of the independent variables β and k_0. However, in the special case in which no sources are impressed inside the metamaterial, the values of β and k_0 are inherently related to each other through the eigen-modal dispersion relation, which also forces a relation between the averaged electric and magnetic fields and allows rewriting Eq. (5.44) in the more common form

$$\begin{aligned} \mathbf{D}_{av} &= \varepsilon_{eq}\mathbf{E}_{av} \\ \mathbf{B}_{av} &= \mu_{eq}\mathbf{H}_{av} \end{aligned}, \tag{5.50}$$

with these vectors satisfying the usual macroscopic form of Maxwell's equations. Similarly, there is a direct relationship between the *effective* parameters used in (5.44) and the *equivalent* parameters in Eq. (5.50), which are scalar version of Eqs. (5.40) and (5.41) [39]:

$$\varepsilon_{eq} = \frac{\varepsilon_{eff}}{1-\dfrac{c_0\chi^o_{eff}}{\beta/k_0}}, \tag{5.51}$$

$$\mu_{eq} = \frac{\mu_{eff}}{1-\dfrac{c_0\chi^o_{eff}}{\beta/k_0}}, \tag{5.52}$$

Both constitutive models are valid in the absence of embedded sources if the goal is simply to describe the array propagation and bulk scattering properties of the metamaterial, and this explains the success of the conventional NRW approach, which is essentially based on the *equivalent* description, to describe and tailor the scattering of metamaterials. However, we need to keep in mind that this *equivalent* description is inherently nonlocal even in the long-wavelength limit, and therefore should not be

expected to follow the usual requirements and properties on local permittivity and permeability, nor even share their commonly accepted meaning. In our previous works [71,75], we indeed proved that this is the reason behind the common violation of Kramers-Kronig and causality relations associated with the *equivalent* constitutive parameters, which implicitly hide the weak spatial dispersion effects captured in χ_{eff}^{o} and are valid only for eigen-modal propagation.

As mentioned, since the constitutive model (5.50) is the same as the one conventionally assumed in NRW retrieval procedures, the equivalent parameters in Eqs. (5.51)-(5.52) are consistent with the parameters ε_{NRW} and μ_{NRW} that we would extract by using this standard retrieval method [71,75], and they obviously share the same limitations. Small differences between the analytical formulas in (5.51)-(5.52) and the parameters retrieved from a scattering measurement may be expected, due to the dipolar assumptions used in Eqs (5.45)-(5.47). These differences will be more significant for dense arrays, for which higher-order multipolar scattering plays a more important role.

In the following, we are interested in improving the retrieval procedure to take into account these concepts and propose a way to extract the more physically meaningful effective parameters in Eqs. (5.45)-(5.47). We concentrate on the eigen-modal scenario in which sources are not embedded in the metamaterial sample, which is the more common case and allows a direct comparison with conventional NRW retrieval. In this case, the metamaterial secondary parameters, i.e., the characteristic impedance η and the wave number β, fully characterize the metamaterial bulk response in the limit in which only one eigenmode is supported at the given frequency of excitation. These parameters are related to the three sets of constitutive parameters defined above through the following relations:

$$\eta = \sqrt{\frac{\mu_{NRW}}{\varepsilon_{NRW}}} \approx \sqrt{\frac{\mu_{eq}}{\varepsilon_{eq}}} = \sqrt{\frac{\mu_{eff}}{\varepsilon_{eff}}}\,, \tag{5.53}$$

$$\begin{aligned} \beta &= \sqrt{\mu_{NRW}\varepsilon_{NRW}} \approx \sqrt{\mu_{eq}\varepsilon_{eq}} \\ &= \omega\sqrt{\varepsilon_{eff}\mu_{eff}}\Big/\left(1-\frac{c_0\chi^o_{eff}}{\beta/k_0}\right) \end{aligned}\,. \tag{5.54}$$

where the nearly-equal sign indicates the potential difference between NRW and equivalent parameters due to the influence of higher-order multipoles. A conventional retrieval procedure would first derive η and β from the scattering measurements (usually the reflection R and transmission T from a planar slab) and then obtain the NRW parameters by inverting Eqs. (5.53)-(5.54). It is not possible, however, to determine the *effective* parameters using just Eqs. (5.53)-(5.54), since η and β do not univocally determine them. This is related to the fact, discussed in more details in Ref. 39, that χ^o_{eff} is essentially a measure of the spatial dispersion stemming from the fact that βd is not infinitesimally small, and therefore the wave feels the lattice granularity as it propagates across each unit cell. For this reason, different combinations of *effective* parameters can produce the same values of η and β, as a function of βd. In order to accurately capture these weak spatial dispersion effects, it is not sufficient to just measure R and T, but we also need to know the average array period d of the array under analysis. With the knowledge of this geometry parameter, which is easily obtainable for a given metamaterial, we may invert the system formed by the combination of Eqs. (5.45)-(5.47) and (5.53)-(5.54) to retrieve the effective constitutive parameters of the metamaterial under analysis.

In practice, we have a set of five independent relations that may be solved for the five complex unknowns ε_{eff}, μ_{eff}, χ^o_{eff}, α_e and α_m. This implies that the proposed GRM does not only provide the effective parameters, but it also returns the averaged

polarizability of each unit cell as a byproduct. Although it is not possible to analytically invert the system due to the complex dependence of the coupling parameters C_{int} and C'_{em} on β, we may use an optimized numerical procedure or root-finding method to solve for the unknowns. In the following section, we apply this method to a specific metamaterial sample and outline its advantages compared to the conventional retrieval approach.

5.4.2 Effective parameters extracted from generalized retrieval method

Here, we apply the developed GRM to extract the effective local parameters and draw comparison to the NRW retrieval results to address the inherent spatial dispersion effect in metamaterials. We consider a three-dimensional simple cubic array (with period *d*) composed of magnetodielectric spheres (with radius *a*) in free space. In order to achieve strong induced currents on the inclusions and field couplings in the lattice for weak spatial dispersive, we use the dense permittivity and permeability values $\varepsilon_r = 13.8\varepsilon_0$ and $\mu_r = 11.0\mu_0$ for the inclusions and tight arrangement for the sphere arrays with $a/d = 0.45$.

As discussed in the previous section, we can first apply a conventional NRW retrieval procedure to determine the secondary parameters of the array and the associated *equivalent* constitutive model -(5.52). We use CST Microwave Studio to numerically compute the reflection and transmission coefficients of a finite-thickness slab composed of 6 layers of unit cells in the propagation direction. The impedance and wave numbers may be easily retrieved from R and T using the following equations, as a function of the transverse-electric (TE) or transverse-magnetic (TM) polarization and incidence angle θ_i

$$\text{TE}:\begin{cases}\eta^2=\eta_0^2\dfrac{(1+R)^2-T^2}{(1-R)^2-T^2}\left(\dfrac{\cos\theta_t}{\cos\theta_i}\right)^2\\ \cos(\beta d\cos\theta_t)=\dfrac{1-R^2+T^2}{2T}\end{cases}, \tag{5.55}$$

$$\text{TM}:\begin{cases}\eta^2=\eta_0^2\dfrac{(1-R)^2-T^2}{(1+R)^2-T^2}\left(\dfrac{\cos\theta_t}{\cos\theta_i}\right)^2\\ \cos(\beta d\cos\theta_t)=\dfrac{1-R^2+T^2}{2T}\end{cases}. \tag{5.56}$$

In these formulas, the refraction angle θ_t depends on the incident angle as $\sin\theta_t = k_0 \sin\theta_i/\beta$.

Figure 5.10 shows the conventionally retrieved parameters for normal incidence and for 45-degree TE incidence. In these calculations, we have used an improved procedure, as described in Ref. 69, to suppress numerical artifacts inherently arising near the Fabry-Perot resonances of the slab. It is evident that the retrieved parameters show quite remarkable differences for different incidence angles. These discrepancies become especially important near the bandgap region marked by a yellow shadow in the figure, and are an indication of spatial dispersion in the array. Right past this bandgap region, the metamaterial supports a double-negative operation, in which both equivalent permittivity and permeability are negative, and in this region the relevant differences between the retrieved parameters are also evident for different incidence angles.

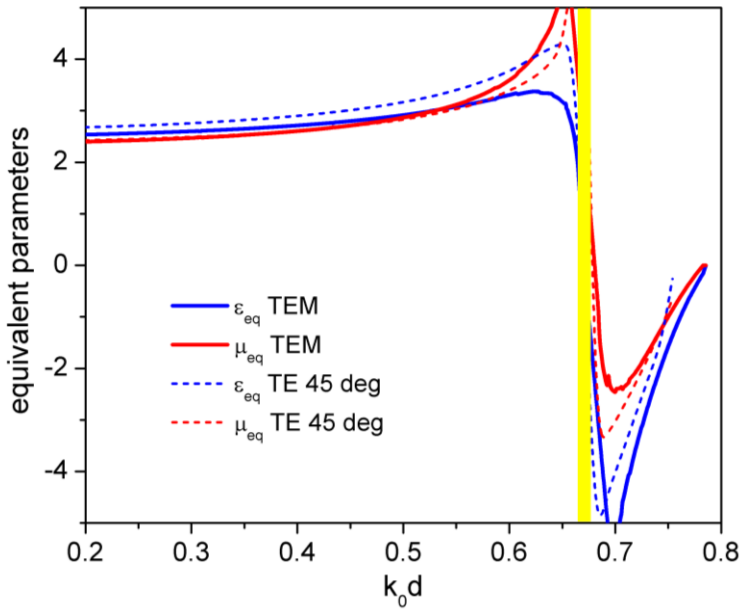

Figure 5.10 Equivalent parameters obtained from an improved NRW retrieval consistent with Ref. 69 for normal incidence (solid lines) and 45-degree TE incidence (dashed lines).

The retrieved parameters, as expected, are purely real within the propagation region due to the absence of losses, but they have a negative slope versus frequency around the bandgap region that violates the dispersion expected from Kramers-Kronig relations. This is consistent with the common violation of Kramers-Kronig relations of the retrieved metamaterial parameters, and it is also another indication of the spatial dispersion and nonlocality effects outlined in the previous section. When the metamaterial operates near the inclusion resonance, especially in the negative-index regime, the magneto-electric coupling associated with the finite granularity of the array and taken into account by χ_{eff}^{o} cannot be captured by the simple constitutive model assumed in this conventional NRW approach. The phase variation across each unit cell cannot be ignored, as implicitly assumed in a simple retrieval procedure, and this is the root of the reason why the extracted parameters do not retain the conventional meaning of

local permittivity and permeability. These retrieved parameters, not considering the finite phase velocity within each unit cell, can strongly vary for different incidence angles and violate basic causality conditions.

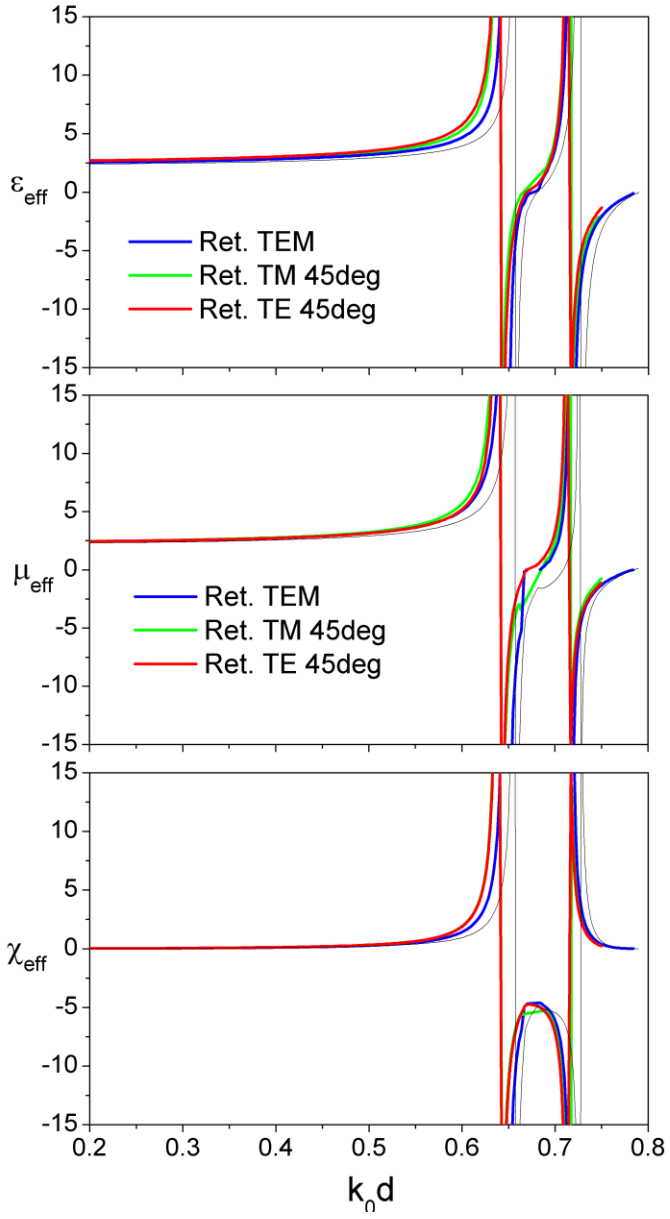

Figure 5.11 Effective parameters calculated using the analytical homogenization theory (thin-black line) and the proposed GRM for different incidence angles and polarizations.

We then apply the inversion procedure discussed in the previous section, solving the set of equations (5.45)-(5.47) and (5.53)-(5.54), with input R, T and the additional information on the array period d, which we assume to know. Figure 5.11 shows the retrieved effective parameters ε_{eff}, μ_{eff}, χ^{o}_{eff}, with blue, green and red lines, referring to the results for normal incidence, 45-degree TE and TM incidence, respectively. The thin-black lines, reported for comparison, are the analytical results calculated using (5.45)-(5.47) and the Mie polarizability expressions for the isolated spheres, as reported in Ref. 75.

Interestingly, all the curves in Figs. 5.11a and b possess Lorentzian frequency dispersion, and they do not show negative slopes within the propagation region. The differences between retrieved results for different excitation angles become much smaller, and the residual discrepancy is simply associated with the large array density, which makes the coupling between neighboring spheres dependent on the field polarization, introducing some small form of anisotropy.

The retrieved curves of permittivity and permeability, consistent with the analytical ones, are remarkably different from the NRW retrieval. Each of them shows two distinct Lorentzian resonances, associated with the electric and magnetic resonance of the spheres, which affect both the electric and magnetic bulk response of the array, due to the properly captured magneto-electric coupling in the lattice. These effects are completely overlooked in the conventional retrieval results shown in Fig. 5.10.

It is possible to see a small frequency shift between retrieved curves and the analytical results. The obvious reason behind this shift lies in the dipolar approximations used in the direct homogenization model, in which we only take into account the dipolar coupling among neighboring inclusions. It is obvious that a full retrieval approach is able to capture the correct coupling among inclusions with much better accuracy, including

higher-order multipolar interactions, and essentially provides a corrected polarizability response that includes near-field effects. These differences would be less important for arrays with smaller filling ratios and with weaker near-field coupling among neighboring inclusions, for which the retrieved parameters would converge more closely to the analytical curves. It is quite remarkable how the proposed GRM may essentially provide even more accurate results than our analytical derivation, going beyond the dipolar approximation used in Ref. 39.

Figure 5.11c shows the retrieved χ^{o}_{eff}, which highlights the relevance of the magneto-electric coupling near the bandgap and in the negative-index region. This quantity is completely neglected in conventional retrieval procedures, but is evidently responsible for the deviations from a Lorentzian, causal dispersion of the *equivalent* permittivity and permeability in Fig. 5.10. Away from the inclusion resonance frequency where the array performs more as a mixture, these effects are negligible, i.e. $\chi^{o}_{eff} \approx 0$, and the results converge to a conventional retrieval.

As outlined above, the GRM also returns, as a byproduct of the inversion procedure, the electric and magnetic polarizabilities of the inclusions. Figure 5.12 shows the retrieved values, compared with the analytically calculated Mie polarizability coefficients for the spheres considered in this example. It is seen how all the retrieved curves are perfectly Lorentzian in shape, satisfy causality, passivity and the radiation condition [76]. Consistent with the previous results, the resonance frequency of our retrieved polarizabilities is slightly red shifted compared to the analytical Mie polarizability, due to the near-field coupling between neighboring spheres. It is interesting that even in the retrieved curves different field polarizations predict slightly shifted inclusion resonances, due to the modification of near-field coupling. These effects disappear for less close spheres.

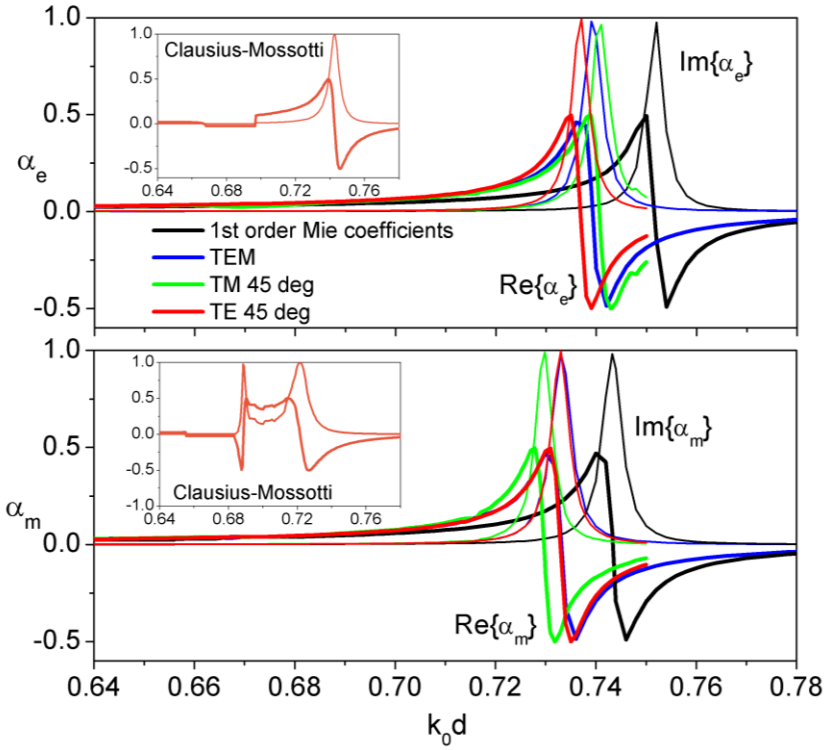

Figure 5.12 Electric and magnetic polarizability obtained from analytical Mie coefficient, generalized retrieval method, and Clausius-Mossotti model.

It is striking to compare these retrieved polarizability curves not only with the expected analytical results for the sphere polarizability as in Fig. 5.12, but also with the values we would get using a more conventional Clausius-Mossotti model [76] that neglects the magneto-electric coupling. We obtain these *equivalent* polarizabilities of the array by assuming again to know d and inverting the equations

$$\varepsilon_{eq} = \varepsilon_0 \left(1 + \frac{d^{-3}}{\alpha_e^{-1} - C_{\text{int}}} \right), \tag{57}$$

$$\mu_{eq} = \mu_0 \left(1 + \frac{d^{-3}}{\alpha_m^{-1} - C_{\text{int}}} \right), \tag{58}$$

obtained from Eqs. (5.45)-(5.46) after neglecting the magneto-electric interaction C'_{em}. These are shown in the insets of Fig. 5.12, highlighting the nonphysical, non-Lorentzian frequency dispersion that is implicitly assumed in the inclusions when we adopt a more conventional retrieval approach. As we get closer to the metamaterial resonance, and over a quite broad range of frequencies, it is obvious that a simplistic constitutive model that neglects the magneto-electric coupling stemming from the lattice granularity would completely fail to describe the inclusions as causal and passive particles and cannot be considered a physically meaningful description of the array. Our retrieval procedure, on the contrary, returns physically meaningful bulk material parameters and the polarizability of the inclusions composing the array under analysis, correctly capturing these hidden magneto-electric effects.

Finally, it is important to test how sensitive our method is to the knowledge of the array period. In practical configurations, in fact, the array may not be ideally periodic, and/or the information on the average distance among the inclusions may not be known in precise terms. For this reason, in Fig. 5.13, we show the retrieved parameters obtained after running our retrieval algorithm for different period values d_r within a $\pm 5\%$ variation from the correct value. We stress that in calculating these results we are keeping the scattering parameters R and T fixed, based on the numerical results used in the previous calculations, and we assume the same total thickness of the sample to extract the secondary parameters. As evident in the figure, our results are very stable after changing this input parameter. The Lorentzian nature of the curves is nicely preserved, as it is fundamentally at the basis of the physical mechanisms considered in the homogenization theory. Slight differences are noticed, as expected, only near the bandgap, where χ^o_{eff} is more relevant. For larger values of d_r the effective parameters get slightly smaller in this region and the Lorentzian resonance shifts to slightly larger frequencies.

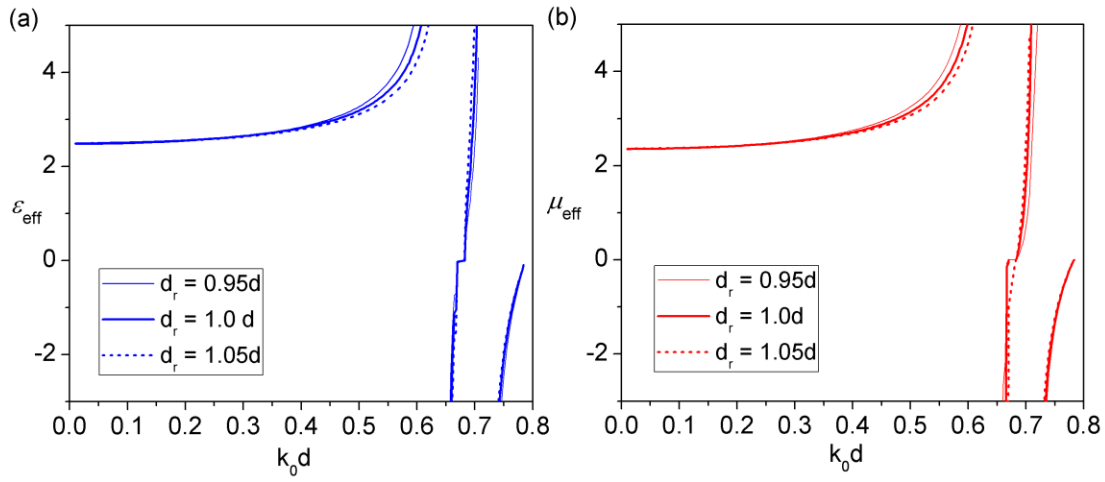

Figure 5.13 Effective parameters obtained by the GRM with different values of lattice period based on the same set of scattering coefficients.

5.5 Applications of 3-D Metamaterial Homogenization to Realistic Devices

5.5.1 Double-negative metamaterial prisms and slabs

Based on the effective and equivalent parameters determined in the previous section, we focus on two specific frequencies of interest: $k_0 d = 0.524$ and $k_0 d = 0.733$. From the results in Fig. 5.3, the first frequency corresponds to a region with a positive index of refraction and equivalent permittivity and permeability $\varepsilon = 3.202\varepsilon_0$ and $\mu = 3.184\mu_0$, respectively. At the second frequency, negative index of refraction is expected and the equivalent parameters are simultaneously negative: $\varepsilon = -2.366\varepsilon_0$ and $\mu = -1.471\mu_0$.

We show in Fig. 5.14 the full-wave simulations of two large 2-D metamaterial prisms (infinite numbers of period in *y*-direction), with total width $k_0 W = 41.050$, maximum thickness $k_0 T = 11$ and angle at the basis of 15°, realized using the metamaterial geometry of Fig. 5.1, at the two frequencies of interest here. We excite the prism with a TE^z polarized Gaussian beam with large waist (exciting most part of the prism) and we verify that indeed the beam refraction is oppositely oriented in the two

cases (Fig. 5.14a and c). In the figure, we compare the full-wave simulations of the nanosphere array with its homogenized model (Fig. 5.14b and d), using the equivalent parameters specified above, extracted from Fig. 5.3. It is seen that the near-field distributions and the refraction angles are accurately reproduced by the homogenized model in both circumstances, despite some minor truncation differences due to the granularity of the metamaterial array. The negative-index simulations show a slightly less accurate prediction of the refraction angle, as expected due to the higher frequency (or shorter wavelength) of operation, which makes these truncation effects slightly more relevant. The overall homogenization results are remarkably close to the full-wave simulations of the complex array, despite the complexity of its wave interaction. In particular, the homogenized model not only correctly predicts a negative refraction angle, but also the backward propagation inside the finite metamaterial prism at this higher-frequency band, despite the fact that multiple reflections between the prism interfaces induce a spectrum of propagation directions in the metamaterial.

Figures 5.15 show the simulations of a planar metamaterial slab with width $k_0 W = 30.055$ and thickness $k_0 T = 11.729$ and its homogenized model, excited at the negative-index frequency $k_0 d = 0.733$ by a Gaussian beam with small waist. This excitation is effectively composed by a wide angular spectrum, hitting the slab at an oblique angle, as shown in the figures. Indeed, both simulations agree in predicting a negative shift of the impinging beam and a backward propagation inside the slab. The same geometry and form of excitation are used in Fig. 5.15c and d for the frequency $k_0 d = 0.796$, which corresponds to the equivalent parameters $\varepsilon = 0.0014\varepsilon_0$ and $\mu = 0.187\mu_0$. In this scenario, the metamaterial operates in another exotic frequency region, at its zero-index operation, of interest in a variety of radiation applications [76,

77]. At this frequency, the effective metamaterial impedance $\eta_{eff} = 11.55\eta_0$ is very large, and most of the impinging energy is reflected at the first slab interface, as expected. Nevertheless, the portion of wave that gets transmitted propagates, as expected, with near-infinite phase velocity within the slab, producing uniform radiated beams at the slab output.

5.5.2 Superlens metamaterials

In Fig. 5.16a, we show the electric field distribution (snapshot in time) of a finite superlens planar slab based on metamaterial structures studied in Fig. 5.1 with thickness $h_0 = 0.834\lambda_0$ and transverse width $w_0 = 3.1\lambda_0$ at the normalized frequency $k_0 d = 0.749$. We excite the array with an electric line source (which is denoted by • in the figure), orthogonal to the plane of the figure and placed at distance $h_0/2$ underneath the slab.

Our numerical simulations clearly confirm the focusing properties of the array, also in this finite configuration. The electric field distribution, snapshot in time, is nicely symmetric below and above the metamaterial array, as expected from the focusing properties of a planar metamaterial with $n_{eq} \approx -1$. In Fig. 5.16b we compare these results with the electric field distribution obtained with an ideal homogeneous metamaterial slab with equivalent permittivity $\varepsilon = -1.116\varepsilon_0$ and permeability $\mu = -0.902\mu_0$, as obtained in Fig. 5.3 by our homogenization model, confirming a similar field distribution, not only around the slab, but even inside the array with a localized focus in the center of the lens. Small differences arise due to the granularity and slight anisotropy of the metamaterial, in particular at the lens edges.

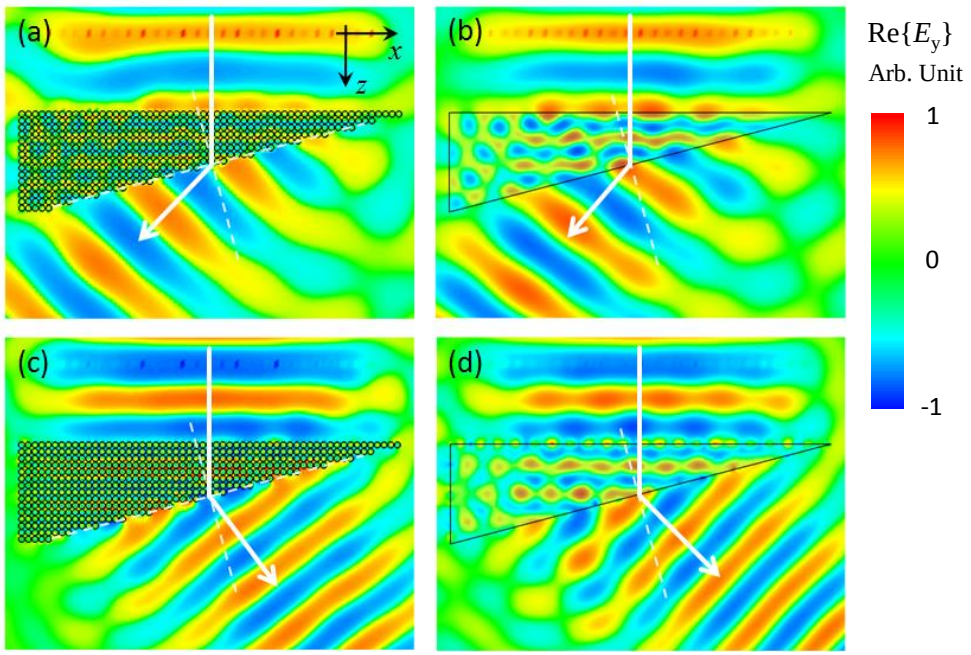

Figure 5.14 Near-field electric field distribution (time snapshot) for a 2-D metamaterial prism excited by a Gaussian beam at the two frequencies $k_0 d = 0.524$ (a, b), with positive index of refraction, and $k_0 d = 0.733$ (c, d), with negative index. Comparison between: (a, c) the nanosphere array, consistent with the design of Fig. 5.1, and (b, d) its homogenized model, using the equivalent parameters shown in Fig. 5.3.

Figure 5.16c shows the normalized distribution of $|\mathbf{E}|^2$ on the image plane, placed at distance $h/2$ above the lens, for both scenarios, compared with the one at the source plane and with the one obtained if the lens is removed. There is no doubt that the metamaterial array produces significant focusing in the image plane, but the resolution is only slightly below the diffraction limit. Even in the homogeneous model the focus is not perfect due to the finite size of the lens, but the array granularity in metamaterials additionally affects the final resolution properties. Wider lenses would in both scenarios improve the resolution, but an inherent limit in the ultimate achievable resolution is dictated by the metamaterial granularity and its isotropy properties.

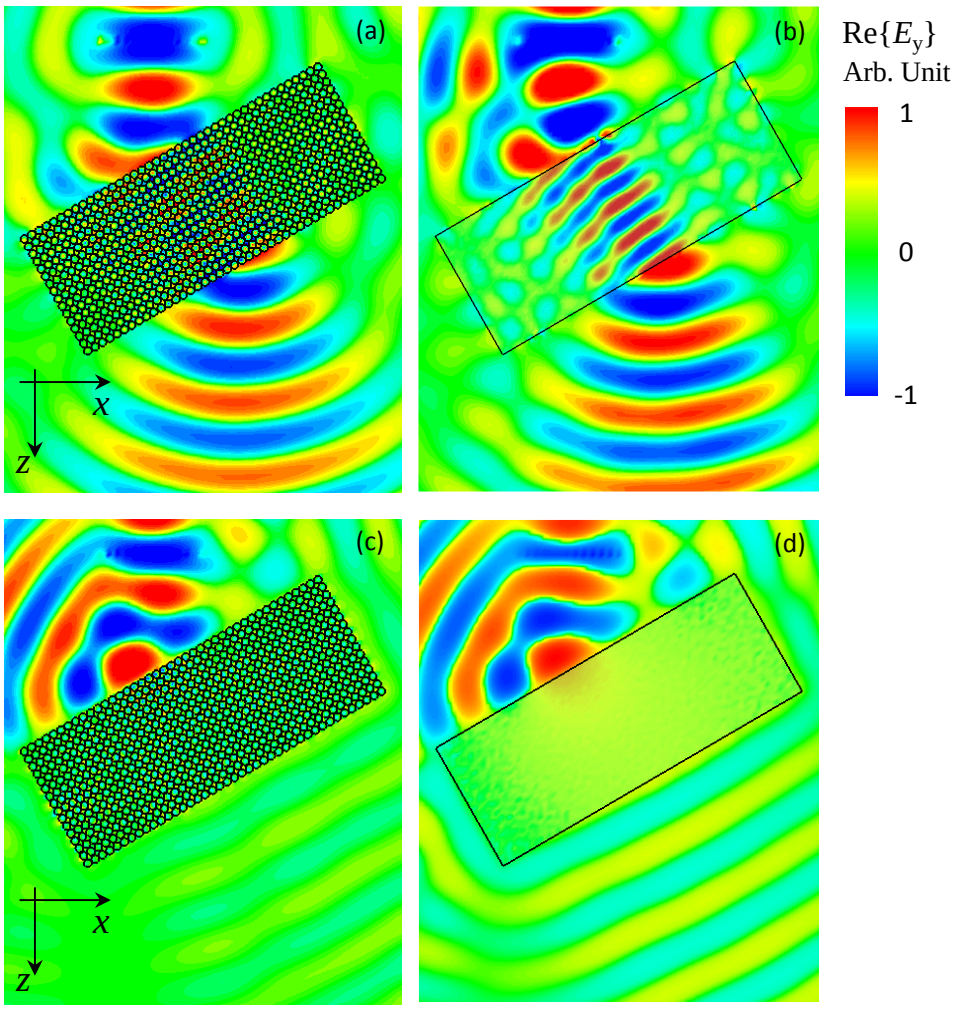

Figure 5.15 A planar slab with (a, b) negative-index and (c, d) near-zero-index properties, excited at oblique incidence by a small-waist Gaussian beam. The simulations refer to the electric field distribution (snapshot in time), and panels (a, c) compare the finite metamaterial array with its homogenized model (b, d).

5.5.2 Metamaterials as concave lens metamaterials

In Fig. 5.17 we show the field distribution generated by a line source placed at the focus of a parabolic plano-concave lens, which has focal length 175 mm or 5d [79]. In Fig. 5.17a the lens is made of a positive index of refraction $n = 2.250$ and, as expected, the radiated beam diffracts in the outward direction. If we choose a negative index of refraction $n = -2.522$ for the metamaterial lens, however, we can reverse the diffraction

and produce a highly directive beam in the far field, as shown in Fig. 5.15b, consistent with simple ray optics. In Fig. 5.17c we have moved the excitation line source by a distance $0.3\lambda_0$ and, as expected from the inverted Snell's law, the radiated beam is considerably tilted in the far-field. This implies that small distances around the focal point of the parabolic inner surface of the lens may be magnified in its far field, which may possibly represent a viable way to far-field sub-resolution imaging using negative-index metamaterials.

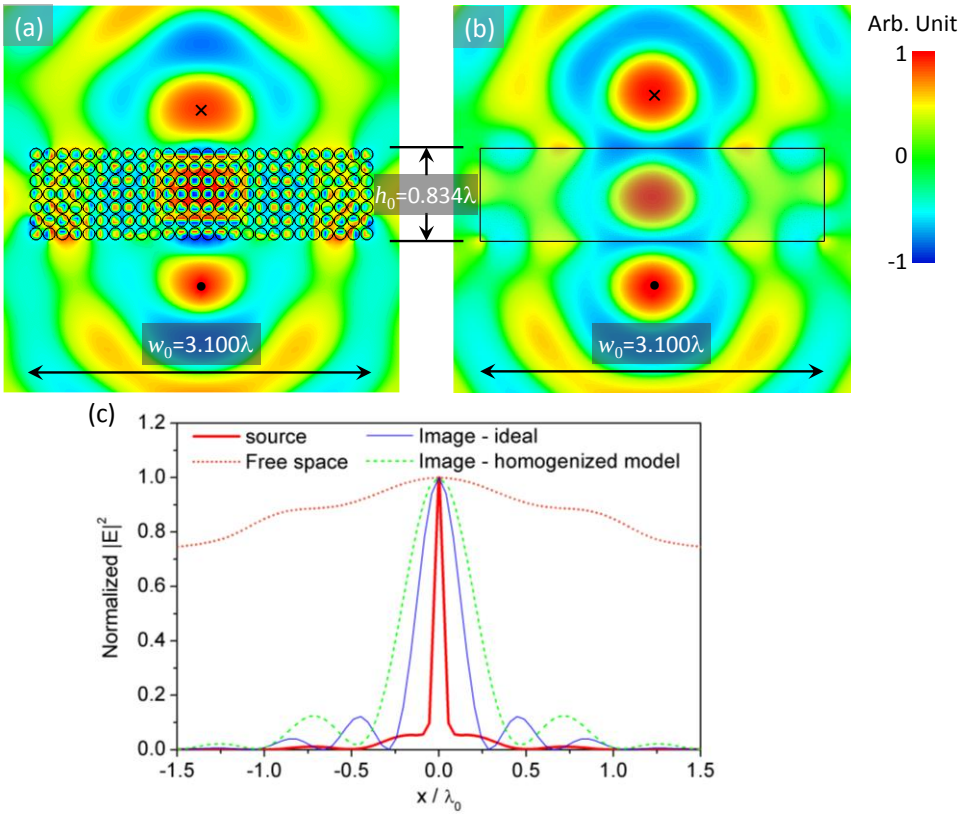

Figure 5.16 (a) Electric field distribution (snapshot in time) for a finite planar lens made of the metamaterial array, excited by a line source at $k_0 d = 0.749$, (b) Analogous distribution for the homogenized model, as from Fig. 1, using $\varepsilon = -1.116\varepsilon_0$, $\mu = -0.902\mu_0$. The source and image are indicated by • and × in figures, respectively, (c) Normalized distribution of $|\mathbf{E}|^2$ at the source and image planes with and without the metamaterial lens.

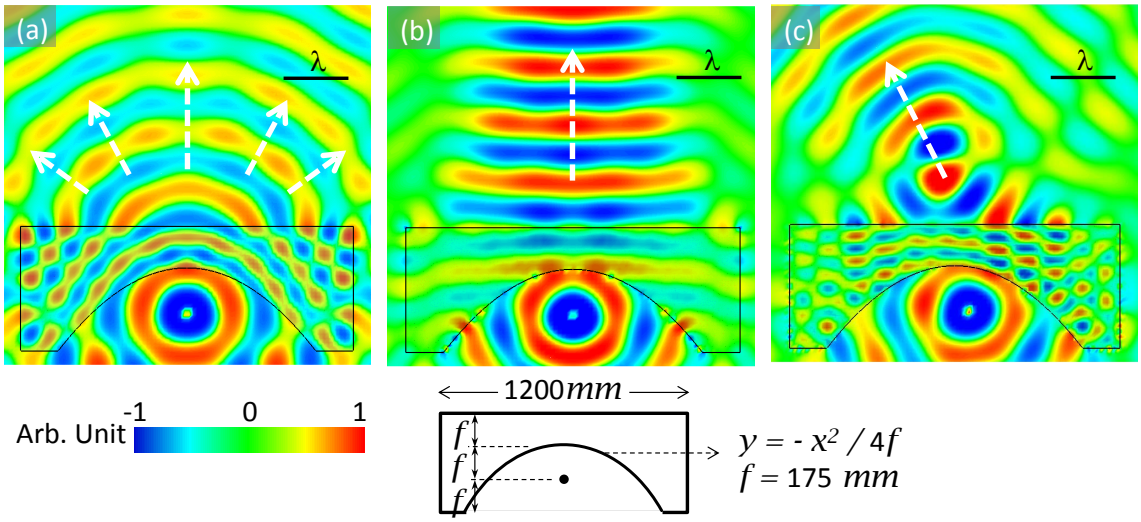

Figure 5.17 Electric field distribution (snapshot in time) produced by a line source in the focus of a homogeneous plano-concave lens with: (a) positive and (b) negative index of refraction. In (c) we have moved the source by $0.3\lambda_0$ in the negative index scenario.

In Figure 5.18, we apply this concept to the metamaterial array designed in the previous example, realizing a plano-concave metamaterial lens analogous to Fig. 5.17, but with $k_0 d = 0.723$ and $n = -2.522$. Fig. 5.18a considers the excitation with a single source at the focal plane, confirming the result in Fig. 5.17b for the case of a realistic metamaterial array. Indeed, directive far-field radiation towards the normal is obtained, due to the negative-index properties of the array, consistent with the homogenized model in Fig. 5.17 and the inverted Snell's law. In Fig. 5.18d (green dashed line), we show the normalized amplitude of $|\mathbf{E}|^2$ at distance $3.2\lambda_0$ from the lens exit, which is indeed concentrated around the region $x = 0$. In Fig. 5.18b, we horizontally shift the line source by a distance $\delta = 0.334\lambda_0$ away from the focal point and obtain beam tilting in the far-field. The new field distribution at distance $3.2\lambda_0$ from the lens exit has shifted by about one wavelength (red dot-dashed line in Fig. 5.18d), which may be clearly resolved in the far field. Finally, by placing two sources near the focal point at distance $2\delta = 0.668\lambda_0$, as in Fig. 5.18c, we obtain split beams which are resolving these details in

the far field, as indicated by the blue dotted line in Fig. 5.18d. Figure 5.18e for comparison shows the original distribution of fields at the source plane and the far-field distribution at the plane of Fig. 5.18d in the absence of the plano-concave lens. This result shows that, by combining negative-index of refraction with an optimized lens shape, it may be possible to transfer sub-wavelength details of an image to the far field. Moreover, by comparing Figs. 5.17 and 5.18, it is noticed how the homogenization model proposed here may accurately describe the bulk response of the metamaterial array, despite its large density, for arbitrary metamaterial shape and excitation form.

5.6 Inverse Design Procedure For Periodic Metamaterials

In the final section of this chapter, we propose an inverse design procedure for 3-D metamaterials based on the previous findings, which may be applied to search for the required inclusion geometry and constituent material parameters to achieve exotic phenomena, such as double-negative parameters, in the assigned frequency regime. The concepts of this procedure and homogenization theory are schematically shown in Fig. 5.19.

For a given metamaterial sample, we are able to apply the NRW retrieval to extract the homogenized (or equivalent) parameters (procedure A) based on the computed or measured transmission and reflection coefficients under plane wave excitations. We can also decompose the metamaterials into isolated elements (procedure B), and determine their polarizability tensors by the system presented in Chapter 2 (procedure C) to model the metamaterials as dipole arrays (procedure D). The wave propagation and field interaction among these dipole arrays can be related to the analytical effective and equivalent parameters based on our homogenization theory

(procedures F and G). This route allows us to characterize metamaterials by considering the wave propagation and scattering from a microscopic point of view.

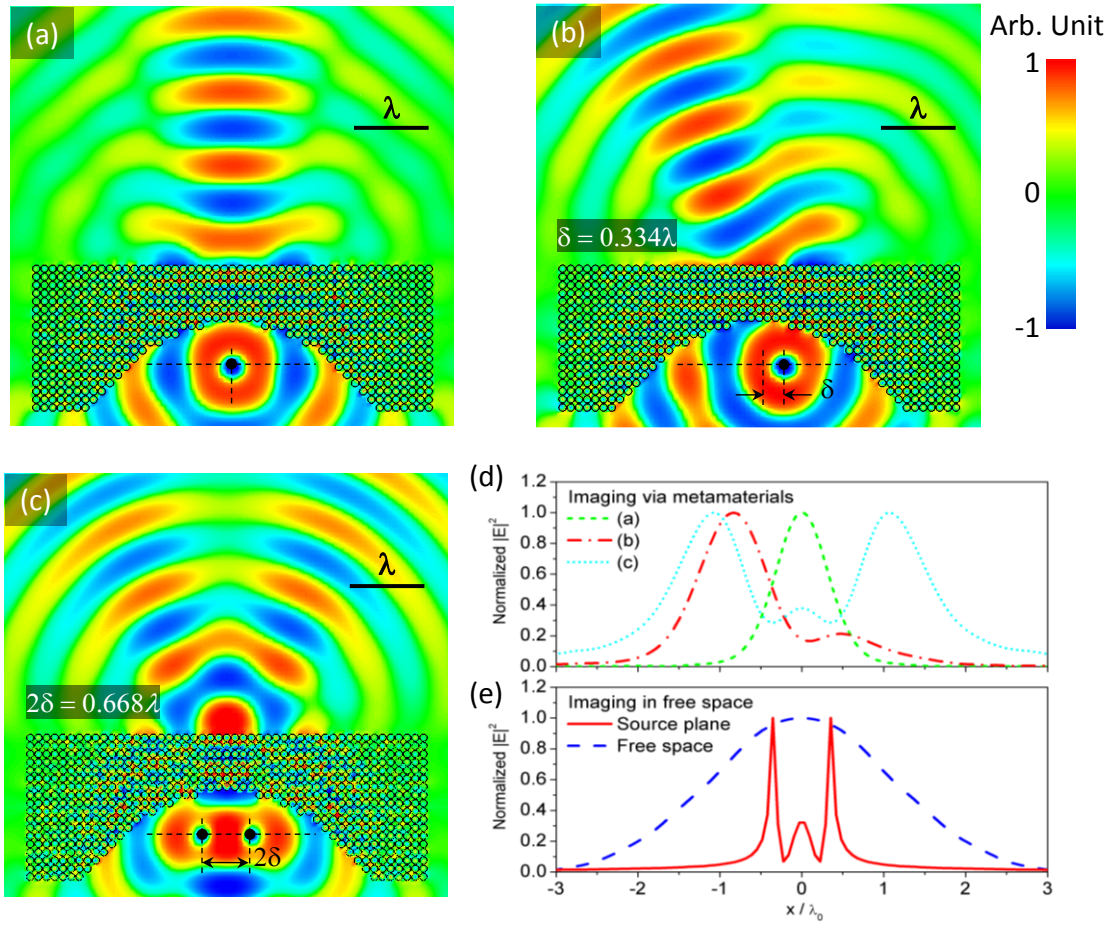

Figure 5.18 Plano-concave planar metamaterial lenses, with similar parameters as in Fig. 5.15, but based on the metamaterial design of array (A) operating at $k_0 d = 0.723$. (a) Electric field distribution (snapshot in time) generated by a single line source at the focal point of the lens; (b) The source location is shifted by $0.3\lambda_0$; (c) The lens is excited by two line sources with relative distance $2\delta = 0.668\lambda_0$. (d) Normalized $|\mathbf{E}|^2$ for the different panels at a distance $3.2\lambda_0$ from the lens exit; (e) Distribution of normalized $|\mathbf{E}|^2$ at the source plane and distribution on the plane at $3.2\lambda_0$ from the lens exit in absence of the lens for the excitation in (c).

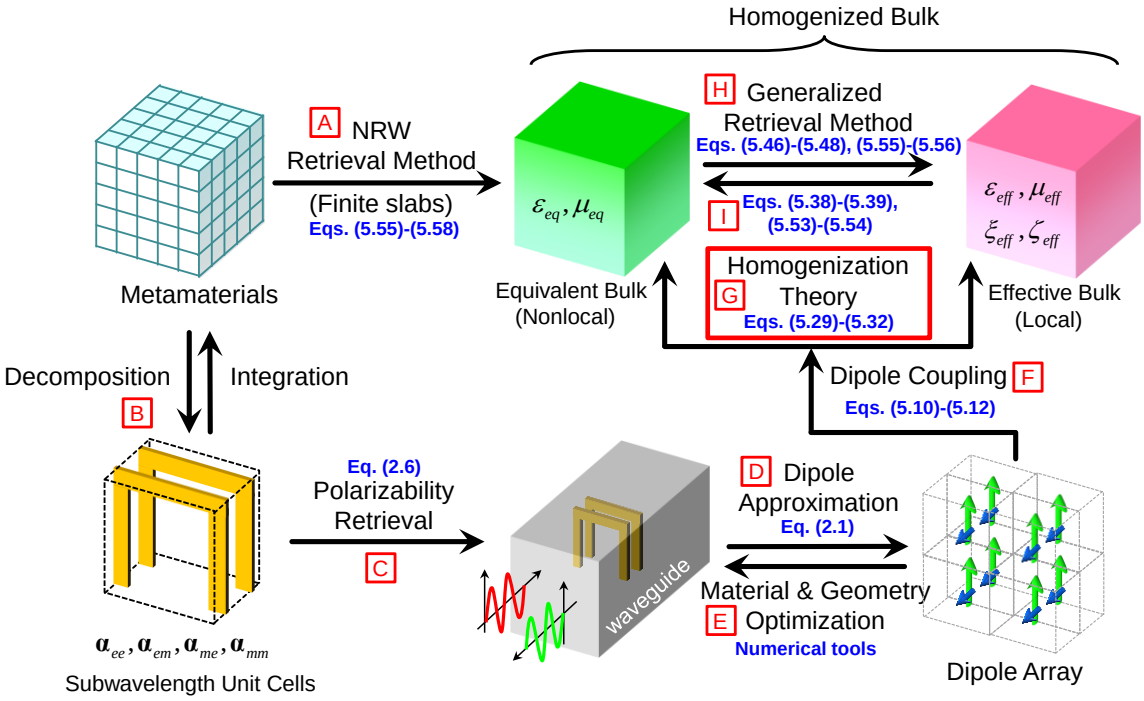

Figure 5.19 - The concept of homogenization theory and inverse design procedure

On the other hand, given a certain set of effective (or equivalent) parameters at some frequencies, we are able to inversely find the required dipole moments in a 3-D array to support the corresponding phase variations within the periodic structure (inverse procedures of F and G). Then, we can look for the geometry and materials of subwavelength inclusions (procedure E), which effectively achieve the required dipole moments among the array under assigned propagation and polarization directions. We call this process an *inverse* metamaterial design procedure.

In the past, the most common method for researchers to look for specific metamaterial designs with desired exotic properties has been to build a sample of finite thickness slab with candidate inclusions in simulation and/or measurement setups, and compute and/or measure the transmission and reflection coefficients to determine the retrieval parameters by NRW methods. Although this method is straightforward and

simple, it usually requires a large computational or experimental cost to simulate or fabricate arrays for each trial and it also fails to characterize physically meaningful parameters. In our inverse design procedure, we are able to relate the desired effective parameters to the polarizability of the inclusions, which can be efficiently determined as described in Chapter 2. In other words, by using this novel concept, we may reduce the computational complexity of metamaterial design from 3-D to 2-D or 0-D (a single inclusion).

Ideally, we can begin the inverse design procedure by using any inclusion shape and use some numerical techniques, such as genetic algorithms, to look for geometry and material properties that can match our desired properties. In reality, it is always helpful to start with some well-studied inclusions, like core-shell or SRR elements, and search for the optimal design within a smaller design space.

In this section, we give a simple example to show that we may use this inverse design procedure to look for metamaterial inclusions that support double-positive (DPS) and double-negative (DNG) parameters at the frequency of interest. We consider a core-shell subwavelength particle composed of a metallic core and a dielectric shell (as shown in Fig. 5.20), whose materials are described by the free electron Drude model $\varepsilon_1 = 1 - \omega_p^2 / \omega^2$ and a non-dispersive dielectric constant ε_2, respectively. The goal of this example is to find the geometry parameter a_1/a_2 and the required ω_p and ε_2 to achieve DPS and DNG parameters at frequencies $k_0 dx \approx 0.8$ and $k_0 dx \approx 1.3$.

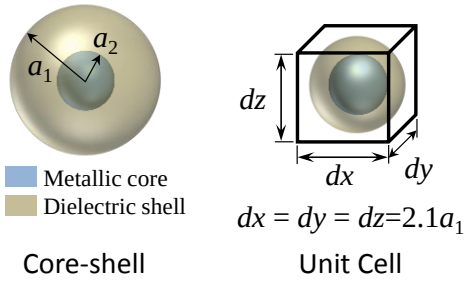

Figure 5.20 Core-shell inclusion used in the example of inverse design procedure

By manipulating the core-shell structures and their constituent materials, we are able to obtain different induced electric and magnetic dipoles. In other words, we can play with these parameters to find the required polarizabilities α^{ee} and α^{mm} to achieve DPS and DNG operation at assigned frequency. Based on the results in the previous sections, we know that the arrangement of isotropic inclusions must be quite dense in order to obtain strong magneto-electric coupling for supporting exotic properties. Therefore, in this example, we begin by considering a dense array with $dx/a_1 = 2.1$ and focus on the frequency $k_0 dx = 1.3$ to find out the required polarizability α^{ee} and α^{mm} to support a pair of negative parameters $\varepsilon_{eq} \approx -1.5$ and $\mu_{eq} \approx -1.5$ in Eqs. (5.51) and (5.52). Here, we use the built-in FindRoot function in Mathematica to search for the value of ω_p and ε_2, and we found as $k_p dx = 7.59$ ($k_d = \omega_p / c$), $\varepsilon_2 = 29.23$ and $a_2/a_1 = 0.24$, we can achieve the desired DNG parameters. In the meanwhile, these material and geometry parameters also support DPS at the smaller values of $k_0 dx$. We show in Fig. 5.21 full-wave simulation results for the metamaterial prisms composed of the above inclusions. In this Figure, we can see that a 25° prism composed of the core-shell particles can perform homogenized DPS and DNG parameters at $k_0 dx = 0.81$ and $k_0 dx = 1.29$, respectively. This same concept may be extended to the geometry parameters of an SRR pair or any other inclusion considered in this dissertation. The

power of this method is to efficiently connect the geometry parameters to the polarizability retrieval, and include the lattice information at a later stage in the inverse design process, allowing for an efficient search in the complete parameter space to achieve optimal performance in terms of the desired figure of merit (which may be loss robustness, bandwidth or reduced sensitivity to disorder).

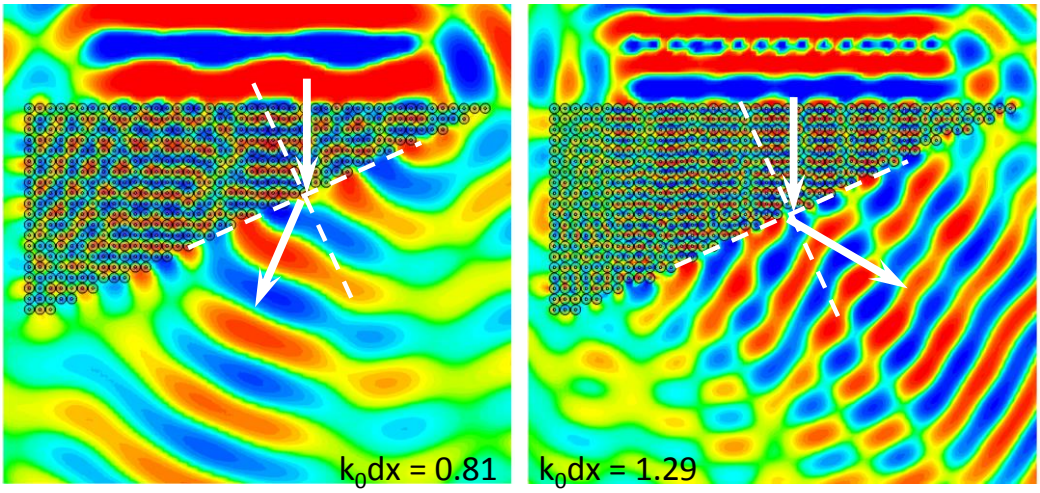

Figure 5.21 - Metamaterial prism with DPS and DNG parameters realized using optimized core-shell inclusions as shown in Fig. 5.20. Notice that in this design we do not use magnetic materials to realize a DNG response.

5.7 Conclusions

In this chapter we have proposed an analytical homogenization model for calculating the complete dyadic effective parameters of 3-D periodic metamaterials composed of discrete subwavelength inclusions and unit cells with arbitrary geometry. The model is based on the long-wavelength approximation assuming that the scattering response of nonconnected inclusions can be treated as electric/magnetic dipole radiation. Taking into account the interaction of these dipoles in the array and applying the dyadic Green's

functions, we are able to derive the dyadic dispersion relations for these arrays. We demonstrated and verified that the homogenization theory can correctly capture the physics in complex 3D metamaterials by presenting the complete dyadic effective parameters for metamaterials composed of magnetodielectric spheres and conducting SRR pairs. Based on this homogenization theory, we also revisited the NRW retrieval method and proposed a modified approach to extract physically meaningful effective parameters of given metamaterial samples. This novel method not only provides homogenized bulk properties, but also returns the polarizabilities of constituent inclusions without knowing their geometry and material parameters. In order to show that our homogenization theory indeed correctly predicts the macroscopic behavior of metamaterials, we reported full-wave simulations of metamaterials applied to practical devices, including metamaterial prisms, slabs and superlens. Finally, we presented the vision for an inverse design procedure to efficiently determine the required inclusion geometry and materials to achieve effective DPS and DNG parameters in the desired frequency regime.

5.7 REFERENCES

1. J. D. Jackson, *Classical Electrodynamics* (Wiley, New-York, 1975).
2. Bohren, C. F. and D. R. Huffman, *Absorption and Scattering of Light by Small Particles* (Wiley, New-York, 1983).
3. J. C. Maxwell-Garnett, "Colours in metal glasses and in metallic films," *Phios. Trans. Roy. Soc. Lond. A* **203**, 385-420 (1904).
4. D. A. G. Bruggeman, "Berechnung verschiedener physikalischer Konstanten von heterogenen Substanzen. I. Dielektrizitatskonstanten und Leitfahigkeiten der Misch- korper aus isotropen Substanzen," *Ann. Phys*. **24** 636–664, (1935).
5. R. El-Mallawany, "The optical properties of tellurite glasses," *J. Appl. Phys*. **72**, 1774-1777 (1992).
6. G. L. Hornyak, C. J. Patrissi, E. B. Oberhauser, C. R. Martin, J-C Valmalette, L.

Lemaire, J. Dutta, H. Hofmann, "Effective medium theory characterization of Au/Ag nanoalloy-porous alumina composites," *Nanostruct. Mater*. **9** 571-574 (1998).
7. C. R. Simovski and S. A. Tretyakov, "Local constitutive parameters of metamaterials from an effective-medium perspective," *Phys. Rev. B* **75**, 195111 (2007).
8. D. R. Smith, J. B. Pendry and M. C. K. Wiltshire, "Metamaterials and Negative Refractive Index," *Science* **305**, 788792 (2004).
9. R. A. Shelby, D. R. Smith and S. Schultz, "Experimental Verification of a Negative Index of Refraction," *Science* **292**, 77-79 (2001).
10. J. B. Pendry, A. J. Holden, D. J. Robbins, and W. J. Stewart, "Magnetism from conductors and enhanced nonlinear phenomena," *IEEE Trans. Microwave Theory Tech* **47**, 2075-2084 (1999).
11. R. Marqués, F. Medina, and R. Rafii-El-Idrissi, "Role of bianisotropy in negative permeability and left-handed metamaterials," *Phys. Rev. B* **65**, 144440 (2002).
12. E. Plum, X.-X. Liu, V. A. Fedotov, Y. Chen, D. P. Tsai, and N. I. Zheludev, "Metamaterials: Optical Activity without Chirality," *Phys. Rev. Lett.* **102**, 113902 (2009).
13. Y. Zhao, M. A. Belkin, and A. Alù, "Twisted Optical Metamaterials for Planarized, Ultrathin, Broadband Circular Polarizers," *Nat. Commun.*, **3** 870 (2012).
14. C. R. Simovski and S. He, "Frequency range and explicit expressions for negative permittivity and permeability for an isotropic medium formed by a lattice of perfectly Ω conducting particles," *Phys. Lett. A* **311**, 254 (2003).
15. K. Aydin, Z. Li, M. Hudlicka, S. A. Tretyakov, and E. Ozbay, "Transmission characteristics of bianisotropic metamaterials based on omega shaped metallic inclusions," *New J. Phys.* **9** 326 (2007).
16. J. K. Gansel, M. Thiel, M. S. Rill, M. Decker, K. Bade, V. Saile, G. von Freymann, S. Linden and M. Wegener, "Gold Helix Photonic Metamaterial as Broadband Circular Polarizer," *Science* **325**, 1513-1515 (2009).
17. D. R. Smith, S. Schultz, P. Markos, and C. M. Soukoulis, "Determination of effective permittivity and permeability of metamaterials from reflection and transmission coefficients," *Phys. Rev. B* **65**, 195104 (2002).
18. X. Chen, B.-I. Wu, J. A. Kong, and T. M. Grzegorczyk, "Retrieval of the effective constitutive parameters of bianisotropic metamaterials," *Phys. Rev. E* **71**, 046610 (2005).
19. C. R. Simovski, P. A. Belov, and S. He, "Backward wave region and negative material parameters of a structure formed by lattices of wires and split-ring resonators," *IEEE Trans. Antennas Propag*. **51**, 2582-2591 (2003).
20. P. A. Belov and C. R. Simovski, "Homogenization of electromagnetic crystals formed by uniaxial resonant scatterers," *Phys. Rev. E* **72**, 026615 (2005).
21. D. R. Smith and J. B. Pendry, "Homogenization of metamaterials by field

averaging (invited paper)," *JOSA B* **23** 391-403 (2006).
22. M. G. Silveirinha and C. A. Fernandes, "Homogenization of 3-D-connected and nonconnected wire metamaterials," *IEEE Trans. Microwave Theory Tech*. **53**, 1418-1430 (2005).
23. M. G. Silveirinha, "Metamaterial homogenization approach with application to the characterization of microstructured composites with negative parameters," *Phys. Rev. B* **75**, 115104 (2007).
24. M. G. Silveirinha, "Nonlocal homogenization model for a periodic array of ϵ-negative rods," *Phys. Rev. E* **73**, 046612 (2006).
25. J. D. Baena, L. Jelinek, R. Marqués, and M. Silveirinha, "Unified homogenization theory for magnetoinductive and electromagnetic waves in split-ring metamaterials," *Phys. Rev. A* **78**, 013842 (2008).
26. C. Fietz and G. Shvets, "Current-driven metamaterial homogenization," *Physica B* **405,** 2930–2934 (2010).
27. C. Fietz and G. Shvets, "Homogenization theory for simple metamaterials modeled as one-dimensional arrays of thin polarizable sheets," *Phys. Rev. B* **82**, 205128 (2011).
28. C. Fietz, Y. Urzhumov, and G. Shvets, "Complex k band diagrams of 3D metamaterial/photonic crystals," *Opt. Express* **19**, 19027-19041 (2011).
29. R. A. Shore and A. D. Yaghjian, "Traveling waves on two- and three-dimensional periodic arrays of lossless scatterers," *Radio Sci.* **42**, RS6S21 (2007).
30. R. A. Shore and A. D. Yaghjian, "Traveling Waves on Three-Dimensional Periodic Arrays of Two Different Alternating Magnetodielectric Spheres," *IEEE Trans. Antennas Propag.***57,** 3077- 3091 (2009).
31. A. Pors, I. Tsukerman, and S. I. Bozhevolnyi, "Effective constitutive parameters of plasmonic metamaterials: Homogenization by dual field interpolation," *Phys. Rev. E* **84**, 016609 (2011).
32. I. Tsukerman, "Nonlocal homogenization of metamaterials by dual interpolation of field," *JOSA B* **28**, 2956-2965 (2011).
33. O. Ouchetto, C.-W. Qiu, S. Zouhdi, L.-W. Li, and A. Razek, "Homogenization of 3-D Periodic Bianisotropic Metamaterials," *IEEE Trans. Microwave Theory Tech.* **54**, 3893-3898 (2006).
34. J. Jin, S. Liu, Z. Lin, and S. T. Chui, "Effective-medium theory for anisotropic magnetic metamaterials," *Phys. Rev. B* **80**, 115101 (2009).
35. S. Zhou, W. Li, and Q. Li, "Design of 3-D Periodic Metamaterials for Electromagnetic Properties," *IEEE Trans. Microwave Theory Tech.* **58**, 910-916 (2010).
36. M. H. Belyamoun and S. Zouhdi, "On the modeling of effective constitutive parameters of bianisotropic media by a periodic unfolding method in time and frequency domains," *Appl. Phys. A* **103**, 881-887 (2011).
37. V. Boucher and D. Ménard, "Effective magnetic properties of arrays of interacting ferromagnetic wires exhibiting gyromagnetic anisotropy and retardation effects," *Phys. Rev. B* **81**, 174404 (2010).

38. S. B. Raghunathan and N. V. Budko, "Effective permittivity of finite inhomogeneous objects," *Phys. Rev. B* **81**, 054206 (2010).
39. A. Alù, "First-principles homogenization theory for periodic metamaterials," *Phys. Rev. B* **84**, 075153 (2011).
40. A. D. Yaghjian, R. A. Shore, and A. Alù, "A General Macroscopic Anisotropic Representation for Spatially Dispersive Media," General Assembly and Scientific Symposium, 2011 XXXth URSI.
41. A. M. Nicolson and G. F. Ross, "Measurement of the intrinsic properties of materials by time-domain techniques," *IEEE Trans. Instrum. Meas.* **IM-19**, 377–382 (1970).
42. W. B. Weir, "Automatic measurement of complex dielectric constant and permeability at microwave frequencies," *Proc. IEEE* **62**, 33–36 (1974).
43. C. R. Simovski, "On electromagnetic characterization and homogenization of nanostructured metamaterials," *J. Opt.* **13**, 013001 (2011).
44. L. D. Landau, E. M. Lifshitz, and L. P. Pitaevskii, *Electrodynamics of ContinuousMedia*, (B-H, Oxford, 1984).
45. J. Costa, S. Mário, and A. Alù, "Poynting vector in negative-index metamaterials," *Phys. Rev. B* **83**, 165120 (2011).
46. S. A. Tretyakov, F. Mariotte, C. R. Simovski, T. G. Kharina, and J.-P. Heliot, "Analytical antenna model for chiral scatterers: comparison with numerical and experimental data," *IEEE Trans. Antennas Propag*. **44**, 1006-1014 (1996).
47. R. Marqués, F. Mesa, J. Martel, and F. Medina, "Comparative Analysis of Edge- and Broadside-Coupled Split Ring Resonators for Metamaterial Design—Theory and Experiments," *IEEE Trans. Antennas Propag.* **51**, 2572-2581 (2003).
48. N. Liu, H. Liu, S. Zhu, and H. Giessen, "Stereometamaterials," *Nat. Photonics* **3**, 157-162 (2009).
49. S. Tretyakov, *Analytical Modeling in Applied Electromagnetics*, Artech House (2003).
50. A. Ishimaru, S.-W. Lee, Y. Kuga, and V. Jandhyala, "Generalized constitutive relations for metamaterials based on the quasi-static Lorentz theory," *IEEE Trans. Antennas Propag.* **51**, 2550-2557 (2003).
51. X. Cheng, H. Chen, L. Ran, B.-I. Wu, T. M. Grzegorczyk, and J. A. Kong, "Negative refraction and cross polarization effects in metamaterial realized with bianisotropic S-ring resonator," *Phys. Rev. B* **76**, 024402 (2007).
52. A. D. Scher and E. F. Kuester, "Extracting the bulk effective parameters of a metamaterial via the scattering from a single planar array of particles," *Metamaterials* **3**, 44-55 (2009).
53. L. Jelinek and J. Machac, "Free space polarizability measurement method," in *Proceedings of Metamaterials '2011: The Fifth International Congress on Advanced Electromagnetic Materials in Microwaves and Optics*, Barcelona, 967-969 (2011).
54. J. A. Kong, "Optics of bianisotropic media," *JOSA* **64**, 1304-1308 (1974).

55. S. Kim, E. F. Kuester, C. L. Holloway, A. D. Scher, and J. Baker-Jarvis, "Boundary Effects on the Determination of Metamaterial Parameters From Normal Incidence Reflection and Transmission Measurements." *IEEE Trans. Antennas Propag.* **59**, 2226-2240 (2011).
56. A. P. Vinogradov, A. I. Ignatov, A. M. Merzlikin, S. A. Tretyakov, and C. R. Simovski, "Additional effective medium parameters for composite materials (excess surface currents)," *Opt. Express* **19**, 6699-6704 (2011).
57. I. Sersic, C. Tuambilangana, T. Kampfrath, and A. F. Koenderink, "Magneto-electric point scattering theory for metamaterial scatterers," *Phys. Rev. B* **83**, 245102 (2011).
58. M. G. Silveirinha and C. A. Fernandes, "A New Acceleration TechniqueWith Exponential Convergence Rate to Evaluate Periodic Green Functions," *IEEE Trans. Antennas Propag*. **53**, 347-355 (2005).
59. T. G. Mackay, "Linear and Nonlinear Homogenized Composite Mediums as Metamaterials," *Electromagnetics* **25**, 461–481 (2005).
60. X.-X. Liu and A. Alù, "Homogenization of quasi-isotropic metamaterials composed by dense arrays of magnetodielectric spheres," *Metamaterials* **5**, 56-63 (2011).
61. J. A. Kong, "Reciprocity relationships for bianisotropic media," *Proc. IEEE (Lett.)* **58**, 1966-1967 (1970).
62. J. A. Kong and D. K. Cheng, "Modified reciprocity theorem for bianisotropic meida," *Proc. Inst. Elec. Eng.* **117**, 349-350 (1970).
63. M. Dressel and G. Grüner, *Electrodynamics of Solids* (Cambridge University Press, Cambridge, 2002).
64. D. R. Smith, J. B. Pendry and M. C. K. Wiltshire, "Metamaterials and Negative Refractive Index," *Science* **305**, 788792 (2004).
65. J. Huangfu, L. Ran, H. Chen, X. Zhang, K. Chen, T. M. Grzegorczyk, and J. A. Kong, "Experimental confirmation of negative refractive index of a metamaterial composed of Ω-like metallic patterns," *Appl. Phys. Lett*. **84**, 1537 (2004).
66. X. Chen, T. M. Grzegorczyk, B.-I. Wu, J. P., Jr., and J. A. Kong, "Robust method to retrieve the constitutive effective parameters of metamaterials," *Phys. Rev. E* **70**, 016608 (2004).
67. J. Baker-Jarvis, E.J. Vanzura, and W.A. Kissick, "Improved technique for determining complex permittivity with the transmission/reflection method," *IEEE Trans. Microwave Theory Tech.* **38**, 1096-1103 (1990).
68. M. G. Silveirinha, "Additional boundary conditions for nonconnected wire media," New J. Phys. **11**, 113016 (2009).
69. X.-X. Liu, D. A. Powell, and A. Alù, "Correcting the Fabry-Perot artifacts in metamaterial retrieval procedures," *Phys. Rev. B* **84**, 235106 (2011).
70. M. G. Silveirinha and C. A. Fernandes, "A new acceleration technique with exponential convergence rate to evaluate periodic Green functions," *IEEE Trans. Antennas Propag*. **53**, 347-335 (2005).
71. A. Alù, "Restoring the physical meaning of metamaterial constitutive parameters,"

Phys. Rev. B **83**, 081102(R) (2011).
72. H. Wallén, H. Kettunen, J. Qi, and A. Sihvola, "Anti-resonant response of resonant inclusions?" General Assembly and Scientific Symposium, 2011 XXXth URSI.
73. M. G. Silveirinha, "Generalized Lorentz-Lorenz formulas for microstructured materials," *Phys. Rev. B* **76**, 245117 (2007).
74. A.H. Sihvola, A.J. Viitanen, I.V. Lindell and S.A. Tretyakov, *Electromagnetic Waves in Chiral and Bi-Isotropic Media* (Artech House Antenna Library, 1994).
75. X.-X. Liu, A. Alù, "Homogenization of quasi-isotropic metamaterials composed by dense arrays of magnetodielectric spheres," *Metamaterials* **5**, 56-63 (2011).
76. S. A. Tretyakov, *Analytical Modeling in Applied Electromagnetics* (Artech House, London, 2002).
77. A. Alù, M. G. Silveirinha, A. Salandrino, and N. Engheta, "Epsilon-near-zero metamaterials and electromagnetic sources: Tailoring the radiation phase pattern," *Phys. Rev. B* 75, 155410 (2007).
78. R. W. Ziolkowski, "Propagation in and scattering from a matched metamaterial having a zero index of refraction," *Phys. Rev. E* 70, 046608 (2004).
79. E. Hecht, *Optics*, 4th ed., (Addison Wesley, 2001).

Chapter 6 Conclusions and Future Work

6.1 Conclusions

In this dissertation, we have presented a complete analytical homogenization theory for 1-D, 2-D and 3-D periodic metamaterials composed of nonconnected inclusions to conceptually treat these metamaterials as waveguides, leaky-wave antennas, uniform surfaces and homogeneous bulk materials and to determine their corresponding effective parameters, including wavenumber, surface susceptibility, permittivity and permeability. Due to the subwavelength scale of inclusions and unit cells, the derived theory is based on the dipole approximation and it can generally be divided into two parts. First, we characterize the elementary inclusions as dipole moments at the unit cell level. In chapter 2, we proposed a retrieval procedure to extract the general polarizability tensor for subwavelength scatterers with arbitrary geometry and made of arbitrary constituent materials. By applying this technique, the inclusions can be described as a combination of electric and magnetic induced dipole moments. In other words, the complex metamaterial structures are simplified as arrays of dipoles. This retrieval method may capture complete scattering properties of complex inclusions, including magneto-electric coupling and higher-order interaction among the array, and it provides an important advance for characterizing elements of metamaterials.

The second part of homogenization theory consists in capturing the complicated coupling in the array in analytical form. From Chapter 3 to 5, we discussed metamaterials composed of 1-D, 2-D and 3-D arrays and homogenize them to form uniform waveguides, metasurfaces and bulk materials characterized by physically meaningful, yet exotic, effective parameters.

In Chapter 3, we studied 1-D linear chains made of dielectric and plasmonic nanoparticles as waveguides and leaky-wave antennas in the optical regime. By analyzing

their dispersion relations, we are able to define possible regimes for guided- and leaky-wave operation of single and parallel linear chains. We generally mapped all the possible modes in terms of dimensionless parameters to predict the functions of particle chains with various elements, interparticle distances and operation frequecies. We also considered the performance of leaky-wave longitudinal and transverse eigenmodes on the 1-D arrays, and confirmed that the longitudinal polarization always provides more promising performance for wave propagation and radiation than transverse polarization on particle chains. We showed that the leaky-waves traveling along a single chain can perform frequency scanning, and therefore they may be applied as an optical leaky-wave antenna for nano-scale optical communications.

In Chapter 4, we discussed the homogenization theory for 2-D metasurfaces formed by arbitrary subwavelength inclusions. We defined and derived a generalized effective surface susceptibility to characterize the wave interaction with the metasurfaces. Based on this effective quantity, we can analytically formulate transmission and reflection coefficients of a 2-D array under plane wave excitations with arbitrary incidence and polarization angles. We have also compared our analytical results with numerical simulations to verify accuracy of the analytical model. We considered general metasurfaces composed of PEC spheres, conducting SRRs and plasmonic U-shaped SRRs as examples and showed that the proposed homogenization theory successfully determines the correct transmission and reflection coefficients for these 2-D arrays. Our model generalizes the studies of single-layer metasurfaces in the past decade, and provides promising potential to enhance the applications of optical metamaterials.

In Chapter 5, we presented a generalized homogenization model for metamaterials composed of 3-D arrays. We considered the complete field interaction in the array and formulated Tellegen constitutive relations for general metamaterials to

determine the effective parameters, including permittivity, permeability and magneto-electric coefficients, in tensorial form. Based on the proposed model, we also revisited and modified the conventional NRW retrieval method to calculate physically meaningful effective parameters with *local* properties in the long-wavelength limit. This novel retrieval method not only provides homogenized parameters for given periodic metamaterials, but it also returns the polarizabilities of the inclusions without knowing their geometry and constituent materials. Moreover, we reported several full-wave simulations to demonstrate exotic electromagnetic properties for metamaterial devices, including super-resolution and negative refraction, as predicted by our homogenization model. Finally, we proposed the vision of an inverse design procedure for metamaterials based on the formulation presented in our homogenization theory. This systematic design procedure may seek for the required geometry and materials of the inclusions to achieve double-negative parameters for 3-D array metamaterials based on 2-D array complexity.

6.2 FUTURE WORK

While this dissertation work has presented several advances in the modeling and homogenization of metamaterials, it has also highlighted many new challenging questions and interesting applications that require further work. Here, we envision some important issues that may be important to explore in the context of the theory and modeling of modern metamaterials.

Issue 1. Edge-effects due to finite arrays

In the modeling portion of our work, we only considered infinite arrays and neglected the end-effects always present in practical metamaterial devices. This end-effect issue can be further divided into two important questions:

Q1.1: How many periods in an array are sufficient to use our results based on the assumption of an infinite array?

Q1.2: How the finite boundaries of a metamaterial array influence the predicted homogenization properties?

Some fundamental works [1-3] have been initially discussing these questions by considering Drude transition layers and equivalent surface currents at the array boundaries. However, a general model to estimate the required period number and to formulate the end-effects for finite arrays is still absent.

Issue 2. Imperfect periodicity and disorder in metamaterials

In this work, we have assumed the array and unit cells to be perfectly periodic, but in practical manufacturing processes, there is always a degree of imperfection and disorder. From an engineering point of view, a useful model to estimate deviations of homogenized parameters due to structure or metamaterial defects is required. Some relevant works [4-5] using perturbation methods and numerical simulations to analyze disordered and misaligned arrays have been reported. These results, however, are not general enough to be applied to 2-D and 3-D metamaterials.

Issue 3. Full-wave numerical solvers for anisotropic, bianisotropic and dispersive media

As presented in the 2-D and 3-D metamaterial works, we showed that metamaterials may generally have anisotropic and bianisotropic effects due to magneto-electric coupling at the unit-cell and lattice levels. Therefore, in order to efficiently verify our homogenization theory, a numerical solver that supports wave propagation in bianisotropic or chiral media is required. However, most commercial software does not provide such material model for users. Therefore, an available module or tool for this purpose becomes very important for metamaterial design and applications. Eigen-solvers in commercial modules are also limited to lossless and dispersion-less materials.

Issue 4. Optimization tools for inverse design of metamaterials

The inverse design model proposed in this dissertation heavily relies on optimization tools to efficiently search for the required geometry and constituent materials of subwavelength inclusions. Some optimization moduli combined with available commercial software may be able to automate the design process. An ideal optimization tool for this purpose should be able to efficiently compute the scattering parameters of a periodic 2-D array and to relate it to the design parameters of interest.

6.3 REFERENCES

1. S. Kim, E. F. Kuester, C. L. Holloway, A. D. Scher, and J. Baker-Jarvis, "Boundary Effects on the Determination of Metamaterial Parameters From Normal Incidence Reflection and Transmission Measurements." *IEEE Trans. Antennas Propag.* **59**, 2226-2240 (2011).
2. C. R. Simovski, "On electromagnetic characterization and homogenization of nanostructured metamaterials," *J. Opt.* **13**, 013001 (2011).
3. A. P. Vinogradov, A. I. Ignatov, A. M. Merzlikin, S. A. Tretyakov and C. R. Simovski, "Additional effective medium parameters for composite materials (excess surface currents)," *Opt. express* **19**, 6699-6704 (2011).
4. A. Alu, and N. Engheta, "Effect of small random disorders and imperfections on the performance of arrays of plasmonic nanoparticles," *New J. Phys.* **12** 013015.
5. K. Aydin, K. Guven, N. Katsarakis, C. M. Soukoulis and E. Ozbay, "Effect of disorder on magnetic resonance band gap of split-ring resonator structures," *Opt. Express* **12**, 5896-5901 (2004).
6. M. J. Weber, Handbook of Optical Materials (CRC Press, 2002).

Appendix A

In this appendix, we present the point-dipole radiation method in free-space (FS), used in Fig. 2.4 and 2.5 to find the polarizabilities of simple spherical scatterers. For a given subwavelength object placed in free-space, we may express the induced electric dipole moments by

$$\mathbf{p} = \alpha^{ee}\mathbf{E}_{loc}, \tag{A.1}$$

where we assume the subwavelength scatterer to be highly symmetric and linearly excited, such that the scalar electric polarizability α^{ee} is sufficient to describe the dipolar radiation. This equation shows that the scattering of the subwavelength scatterer can be interpreted as an infinitesimal dipole which has magnitude proportional to the local fields. On the other hand, the radiation field of an ideal point dipole can be written as

$$\mathbf{E}(r) = -\frac{\mathbf{p}}{\varepsilon_0}\left(-\frac{ik_0}{r} - \frac{1}{r^2} + k^2\right)G(r), \tag{A.2}$$

in which the three-dimensional free space Green's function $G(r) = e^{-ik_0 r}/4\pi r$ is used. Based on Eqs. (A.1) and (A.2), the electric polarizability is related to the field extracted at one point around the scatterer through the formula

$$\alpha^{ee} = -\varepsilon_0 \frac{E(r)}{E_{loc}}\left[\left(-\frac{ik_0}{r} - \frac{1}{r^2} + k_0^2\right)G(r)\right]^{-1}, \tag{A.3}$$

where we simplify the vector electric fields into scalar form by assuming we probe $E(r)$ in the E-plane of the dipole radiation pattern. Similarly, the magnetic polarizability can be expressed as

$$\alpha^{mm} = -\mu_0 \frac{H(r)}{H_{loc}} \left[\left(-\frac{ik_0}{r} - \frac{1}{r^2} + k_0^2 \right) G(r) \right]^{-1} \tag{A.4}$$

According to the above derivation, we may easily calculate the electric and magnetic polarizabilities by probing the local and radiation fields of a given subwavelength scatterer. The polarizability curves shown in Fig. 2.4 and 2.5 are normalized by $k_0^3/6\pi\varepsilon_0$ and $k_0^3/6\pi\mu_0$ for α^{ee} and α^{mm}, respectively.

In this portion of the polarizability retrieval, we apply the time-domain solver and plane-wave sources in CST Microwave Studio to determine local and far-field quantities. In order to reach high numerical accuracy and avoid higher-order scattering in the near-fields, we choose the built-in far-field probes in the software to determine $E(r)$ and $H(r)$.

This simple method to retrieve the polarizability may have several drawbacks that make it challenging to find accurate polarizability values for complex inclusions. The first issue is the numerical convergence of the solver. We find that the numerical solver used in Fig. 2.4 and 2.5 shows poor numerical convergence efficiency for complex inclusions, and this computational issue causes less precise retrieved polarizability, especially in terms of phase. Second, it is not possible to determine the completed polarizability tensor of the complex inclusion with sophisticated magneto-electric coupling. For some complicated inclusions, such as the SRRs, the far-field quantities may be simultaneously produced by co- and cross-polarization contributions of the induced currents. Therefore, we are not able to identify every entry of the full polarizability tensor for inclusions with arbitrary geometry. In other words, this method is only useful for simple inclusions for which the induced electric and magnetic dipole moments are independent of each other. Nevertheless, this approach can nicely predict the resonance frequencies of the scatterers due to the strong variation of induced currents on the

inclusion around the resonance frequency. Based on these considerations, we only use this method to draw comparisons with the retrieval results for simple objects, such as the spherical sphere considered in the first examples of Chapter 2.

Appendix B

In this dissertation, we use plasmonic inclusion in some of the examples as metamaterial inclusions to apply our results to the optical regime. For this purpose, the most popular plasmonic material, silver (Ag), is selected in our analyses, and we use the complex values of permittivity obtained from experimental results [B1] and the corresponding fitting Drude model

$$\varepsilon_{Drude} = \varepsilon_{\infty} - \frac{\omega_p^2}{\omega(\omega - i\nu)} \tag{B.1}$$

to describe the material. In the fitting model, the asymptotic dielectric constant is $\varepsilon_{\infty} = 5$, the plasma frequency is $\omega_p = 2175.12\,THz$ and the collision frequency is $\nu = 4.35\,THz$, respectively. The material dispersion curves retrieved from the experimental measurements and fitting model are shown below in Fig. B.1.

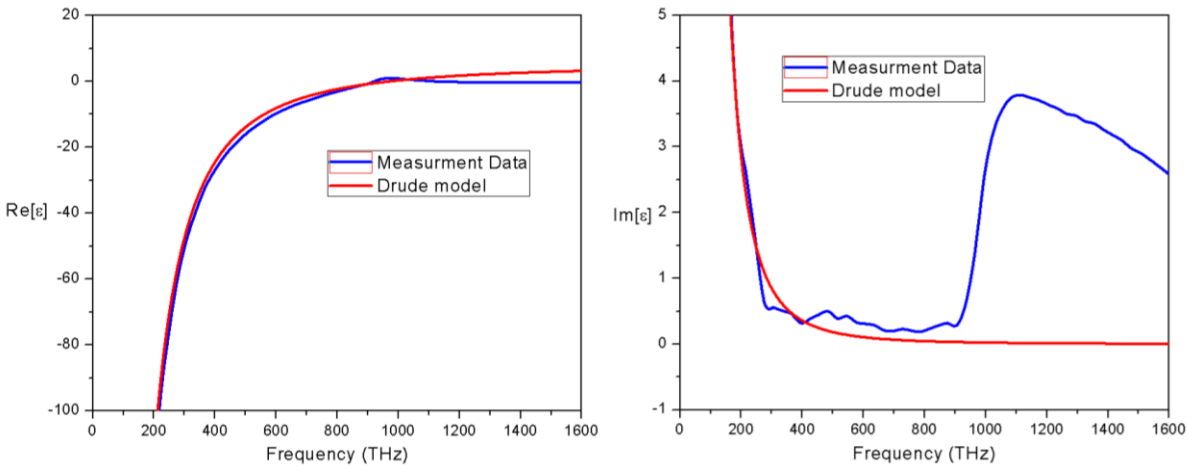

Figure B.1 Dispersion curves of silver permittivity obtained from experimental measurement and the corresponding fitted Drude model

REFERENCES

B1. P. B. Johnson and R. W. Christy, "Optical Constants of the Noble Metals," *Phys. Rev. B* **6**, 4370–4379 (1972).

Appendix C

In Chapter 4, we define the interaction matrix $\mathbf{C}^{2D}$ (see Eq. (4.3)) to describe electric and magnetic dipole interactions on a 2-D metasurface based on the free-space Green's function [C1, C2]

$$g(x,z)=\sum_{(m,n)\neq(0,0)}\frac{e^{-jk_0R_{mn}}}{4\pi R_{mn}}e^{-jk_y nb}, \tag{C.1}$$

where $R_{mn}=\sqrt{(x-ma)^2+(nb)^2+z^2}$ with m and n being the indices of unit cells. The simplified coefficients have been studied in Refs. [C1, C2], and they can be given in the generalized form [C3]:

$$\mathbf{C}=\begin{bmatrix} C_{ee}^{xx} & C_{ee}^{xy} & 0 & 0 & 0 & C_{em}^{xz} \\ C_{ee}^{yx} & C_{ee}^{yy} & 0 & 0 & 0 & C_{em}^{yz} \\ 0 & 0 & C_{ee}^{zz} & C_{em}^{zx} & C_{em}^{zy} & 0 \\ 0 & 0 & C_{me}^{xz} & C_{mm}^{xx} & C_{mm}^{xy} & 0 \\ 0 & 0 & C_{me}^{xy} & C_{mm}^{yx} & C_{mm}^{yy} & 0 \\ C_{me}^{zx} & C_{me}^{zy} & 0 & 0 & 0 & C_{mm}^{zz} \end{bmatrix}. \tag{C.2}$$

The closed-form and fast-convergent formulation (derived based on Poisson's summation [C4]) for the elements in the above matrix is given as follows [C1-C3]:

$$
\begin{aligned}
C_{ee}^{xx} &= \lim_{x\to 0}\left(k_0^2+\frac{\partial^2}{\partial x^2}\right)g\left(x,0\right)\\
&= -\frac{1}{\pi a}\sum_{n=1}^{\infty}\sum_{\mathrm{Re}(p_m)\neq 0} p_m^2 K_0\left(p_m\left|nb\right|\right)\cos\left(k_y nb\right)\\
&\quad -\frac{1}{2ab}\sum_{\mathrm{Re}(p_m)=0} p_m^2\left[\frac{1}{jk_z^{m0}}+\sum_{n=1}^{\infty}\left(\frac{1}{jk_z^{mn}}+\frac{1}{jk_z^{m,-n}}-\frac{b}{\pi n}-\frac{l_m b^3}{8\pi^3 n^3}\right)\right.\\
&\qquad\qquad \left.+1.202\frac{l_m b^3}{8\pi^3}+\frac{b}{\pi}\left(\ln\frac{\left|p_m\right|b}{4\pi}+\gamma+j\frac{\pi}{2}\right)\right] \qquad \text{(C.3)}\\
&\quad +\frac{1}{4\pi a^3}\left\{4\sum_{m=1}^{\infty}\frac{\left(2jk_0a+3\right)m+2}{m^3\left(m+1\right)\left(m+2\right)}e^{-jk_0am}\cos\left(k_x am\right)\right.\\
&\qquad -\left(jk_0a+1\right)\left[t_+^2\ln t_+ + t_-^2\ln t_- + 2e^{jk_0a}\cos\left(k_x a\right)\right]\\
&\qquad \left.-2jk_0a\left(t_+\ln t_+ + t_-\ln t_-\right)+\left(7jk_0a+3\right)\right\}
\end{aligned}
$$

$$
C_{ee}^{yy}\left(a,b,k_x,k_y\right)=C_{ee}^{yy}\left(b,a,-k_y,k_x\right) \qquad \text{(C.4)}
$$

$$
\begin{aligned}
C_{ee}^{zz} &= \lim_{z\to 0}\left(k_0^2+\frac{\partial^2}{\partial z^2}\right)g(0,z)\\
&= \frac{1}{\pi a}\sum_{n=1}^{\infty}\sum_{\mathrm{Re}(p_m)\neq 0}\left[k_0^2K_0(p_m nb)-\frac{p_m}{nb}K_1(p_m nb)\right]\cos(k_y nb)\\
&\quad+\frac{k_0^2}{2ab}\sum_{\mathrm{Re}(p_m)=0}\left[\frac{1}{jk_z^{m0}}+\sum_{n=1}^{\infty}\left(\frac{1}{jk_z^{mn}}+\frac{1}{jk_z^{m,-n}}-\frac{b}{\pi n}-\frac{l_m b^3}{8\pi^3 n^3}\right)\right.\\
&\qquad\left.+1.202\frac{l_m b^3}{8\pi^3}+\frac{b}{\pi}\left(\ln\frac{|p_m|b}{4\pi}+\gamma+j\frac{\pi}{2}\right)\right]\\
&\quad+\frac{1}{2ab}\sum_{\mathrm{Re}(p_m)=0}\left[jk_z^{m0}+\sum_{n=1}^{\infty}\left(jk_z^{mn}+jk_z^{m,-n}-\frac{4\pi n}{b}-\frac{bp_m^2}{2\pi n}-\frac{p_m^2t_m b^3}{32\pi^3n^3}\right)+1.202\frac{p_m^2t_m b^3}{32\pi^3}\right.\\
&\qquad\left.+\frac{bp_m^2}{2\pi}\left(\ln\frac{|p_m|b}{4\pi}+\frac{2\gamma+1}{2}+j\frac{\pi}{2}\right)-\frac{\pi}{3b}\right]\\
&\quad-\frac{k_0^2}{4\pi a}\left(\ln t^+ +\ln t^-\right)-\frac{1}{8\pi a^3}\left\{4\sum_{m=1}^{\infty}\frac{(2jk_0a+3)m+2}{m^3(m+1)(m+2)}e^{-jk_0am}\cos(k_x am)\right.\\
&\qquad-(jk_0a+1)\left[t_+^2\ln t_+ + t_-^2\ln t_- + 2e^{jk_0a}\cos(k_x a)\right]\\
&\qquad\left.-2jk_0a\left(t_+\ln t_+ + t_-\ln t_-\right)+(7jk_0a+3)\right\}
\end{aligned}
\tag{C.5}
$$

$$
\begin{aligned}
\bar{C}_d^{xy} &= \lim_{z\to 0}\left(k_0^2+\frac{\partial^2}{\partial x\partial y}\right)g(0,z)\\
&= \frac{-k_0}{\pi a}\sum_{n=1}^{\infty}\sum_{\mathrm{Re}(p_m)\neq 0}k_x^{(m)}p_m K_1(p_m n\bar{b})\sin(k_y nb)\\
&\quad-\frac{k_0}{2ab}\sum_{\mathrm{Re}(p_m)=0}k_x^{(m)}\sum_{n=1}^{+\infty}\left(\frac{k_y^{(n)}}{\sqrt{p_m^2+k_y^{(n)2}}}+\frac{k_y^{(-n)}}{\sqrt{p_m^2+k_y^{(-n)2}}}-\frac{\bar{b}^3p_m^2k_y}{4\pi^3n^3}\right)\\
&\quad-\frac{k_0}{2ab}\sum_{\mathrm{Re}(p_m)=0}k_x^{(m)}\left(\frac{1.20206}{4\pi^3}\bar{b}^3p_m^2k_y+\frac{k_y}{\sqrt{p_m^2+k_y^2}}\right)
\end{aligned}
\tag{C.6}
$$

$$
C_{xx}^{mm}=C_{xx}^{ee},\ C_{yy}^{mm}=C_{yy}^{ee},\ C_{zz}^{mm}=C_{zz}^{ee} \tag{C.7}
$$

$$
\begin{aligned}
C_{em}^{yz} &= jk_0 \lim_{x\to 0} \frac{\partial}{\partial x} g\left(x,0\right) \\
&= \frac{k_0}{\pi a} \sum_{n=1}^{\infty} \sum_{\mathrm{Re}\left(p_m\right)\neq 0} k_x^m K_0\left(p_m \left|nb\right|\right) \cos\left(k_y nb\right) \\
&\quad + \frac{k_0}{2ab} \sum_{\mathrm{Re}\left(p_m\right)=0} k_x^m \left[\frac{1}{jk_z^{m0}} + \sum_{n=1}^{\infty} \left(\frac{1}{jk_z^{mn}} + \frac{1}{jk_z^{m,-n}} - \frac{b}{\pi n} - \frac{l_m b^3}{8\pi^3 n^3} \right) \right. \\
&\qquad \left. +1.202 \frac{l_m b^3}{8\pi^3} + \frac{b}{\pi} \left(\ln \frac{\left|p_m\right| b}{4\pi} + \gamma + j\frac{\pi}{2} \right) \right] \\
&\quad + \frac{k_0^2}{4\pi a} \left(\ln t_+ - \ln t_- \right) \\
&\quad + \frac{jk_0}{4\pi a^2} \left\{ -4j \sum_{m=1}^{\infty} \frac{1}{m^2\left(m+1\right)\left(m+2\right)} e^{-jk_0 bn} \sin\left(k_x am\right) \right. \\
&\qquad -\left(t_+ \ln t_+ - t_- \ln t_- \right) \\
&\qquad \left. -\frac{1}{2}\left[t_+^2 \ln t_+ - t_-^2 \ln t_- + 2je^{jk_0 a} \sin\left(k_x a\right) \right] \right\}
\end{aligned}
\tag{C.8}
$$

The expressions of p_m, $l_m, t_m, k_y^{(n)}$, $k_y^{(-n)}$, t_+, t_-, t^+, t^-, $k_z^{m,n}$ and $k_z^{m,-n}$ in the above formulations can be found in Ref. C1 and C2.

REFERENCES

C1. P. A. Belov and C. R. Simovski, "Homogenization of electromagnetic crystals formed by uniaxial resonant scatterers," *Phys. Rev. E* **72**, 026615 (2005).

C2. A. I. Dimitriadis, N. V. Kantartzis, I. T. Rekanos and T. D. Tsiboukis, "Efficient Metafilm/Metasurface Characterization for Obliquely Incident TE Waves via Surface Susceptibility Models," *IEEE Trans. Magn*. **48**, 367-370 (2012).

C3. A. N. Askarpour, X. X. Liu, and A. Alù, **"**Interaction Constant for Arbitrary Propagation Constant and Dipole Orientation in a 2D Plane**,"** in preparation.

C4. R. E. Collin, *Field Theory of Guided Waves* (Wiley-IEEE Press, 1990).

Bibliography

Aden, A. L., and M. Kerker, "Scattering of Electromagnetic Waves from Two Concentric Spheres," *J. Appl. Phys*. **22**, 1242 (1951).

Ahmadi, A., S. Ghadarghadr, and H. Mosallaei, "An optical reflectarray nanoantenna: The concept and design," *Opt. Express* **18**, 123 (2010)

Albooyeh, M., D. Morits, and C.R. Simovski, "Electromagnetic characterization of substrated metasurfaces," *Metamaterials* **5**, 178-205 (2011).

Alicia, K. B. and E. Ozbay, "A planar metamaterial: Polarization independent fishnet structure," *Photonics Nanostruct. Fundam. Appl.* **6**, 102-107 (2008).

Alù, A. and N. Engheta, "Achieving transparency with plasmonic and metamaterial coatings," *Phys. Rev. E* **72**, 016623 (2005).

Alù, A. and N. Engheta, "Input Impedance, Nanocircuit Loading, and Radiation Tuning of Optical Nanoantennas," *Phys. Rev. Lett*. **101**, 043901 (2008).

Alù, A. and N. Engheta, "Theory of linear chains of metamaterial/plasmonic particles as subdiffraction optical nanotransmission lines," *Phys. Rev. B* **74**, 205436 (2006).

Alù, A. and N. Engheta, "Tuning the scattering response of optical nanoantennas with nanocircuit loads," *Nat. Photonics* **2**, 307 (2008).

Alù, A. and Nader Engheta, "Achieving transparency with plasmonic and metamaterial coatings," *Phys. Rev. E* **72**, 016623 (2005).

Alù, A., "First-principles homogenization theory for periodic metamaterials," *Phys. Rev. B* **84**, 075153 (2011).

Alù, A., and N. Engheta, "Effect of small random disorders and imperfections on the performance of arrays of plasmonic nanoparticles," *New J. Phys*. **12** 013015.

Alù, A., and N. Engheta, "Three-dimensional nanotransmission lines at optical frequencies: A recipe for broadband negative-refraction optical metamaterials," *Phys. Rev. B* **75**, 024304 (2007).

Alù, A., and N. Engheta, "Wireless at the Nanoscale: Optical Interconnects using Matched Nanoantennas," *Phys. Rev. Lett*. **104**, 213902 (2010).

Alù, A., M. G. Silveirinha, A. Salandrino, and N. Engheta, "Epsilon-near-zero metamaterials and electromagnetic sources: Tailoring the radiation phase pattern," *Phys. Rev. B* **75**, 155410 (2007).

Alù, A., P. A. Belov, and N. Engheta, "Coupling and guided propagation along parallel chains of plasmonic nanoparticles," *New J. Phys.* **13**, 033026 (2011).

Alù, A., P. A. Belov, and N. Engheta, "Parallel-chain optical transmission line for a low-loss ultraconfined light beam," *Phys. Rev. B* **80**, 113101 (2009).

Alù, A., "Restoring the physical meaning of metamaterial constitutive parameters," *Phys. Rev. B* **83**, 081102(R) (2011).

Antoniades, M. A. and G. V. Eleftheriades, "A compact and low-profile metamaterial ring antenna with vertical polarization," *IEEE Antennas Wirel. Propag. Lett.* **4**, 333-336 (2005).

Atwater, H. A., "The Promise of Plasmonics," *Sci. Am*. **296**, 56-62 (2010).

Aubry, A., D. Y. Lei, A. I. Fernández-Domínguez, Y. Sonnefraud, S. A. Maier, and J. B. Pendry, "Plasmonic Light-Harvesting Devices over the Whole Visible Spectrum," *Nano Lett*. **10**, 2574-2579 (2010).

Aydin, K., I. M. Pryce, and H. A. Atwater, "Symmetry breaking and strong coupling in planar optical metamaterials," *Opt. Express* **18**, 13407-13417 (2010).

Aydin, K., K. Guven, N. Katsarakis, C. M. Soukoulis and E. Ozbay, "Effect of disorder on magnetic resonance band gap of split-ring resonator structures," *Opt. Express* **12**, 5896-5901 (2004).

Aydin, K., Z. Li, M. Hudlicka, S. A. Tretyakov, and E. Ozbay, "Transmission characteristics of bianisotropic metamaterials based on omega shaped metallic inclusions," *New J. Phys.* **9,** 326 (2007).

Baena, J. D., J. Bonache, F. Martín, R. M. Sillero, F. Falcone, T. Lopetegi, M. A. G. Laso, J. García–García, I. Gil, M. F. Portillo, and M. Sorolla, "Equivalent-Circuit Models for Split-Ring Resonators and Complementary Split-Ring Resonators Coupled to Planar Transmission Lines," *IEEE Trans. Microwave Theory Tech.* **53**, 1451-1461 (2005).

Baena, J. D., L. Jelinek, R. Marqués, and M. Silveirinha, "Unified homogenization theory for magnetoinductive and electromagnetic waves in split-ring metamaterials," *Phys. Rev. A* **78**, 013842 (2008).

Bahr, A. J. and K. R. Clausing, "An Approximate Model for Artificial Chiral Material," *IEEE Trans. Antennas Propag*. **42**, 1592-1599 (1994).

Baker-Jarvis, J., E.J. Vanzura, and W.A. Kissick, "Improved technique for determining complex permittivity with the transmission/reflection method," *IEEE Trans. Microwave Theory Tech.* **38**, 1096-1103 (1990).

Banzer, P., U. Peschel, S. Quabis, and G. Leuchs, "On the experimental investigation of the electric and magnetic response of a single nano-structure," *Opt. Express* **18**, 10905 (2010).

Belov, P. A. and C. R. Simovski, "Homogenization of electromagnetic crystals formed by uniaxial resonant scatterers," *Phys. Rev. E* **72**, 026615 (2005).

Belov, P. A., R. Marqués, S. I. Maslovski, I. S. Nefedov, M. Silveirinha, C. R. Simovski, and S. A. Tretyakov, "Strong spatial dispersion in wire media in the very large wavelength limit," *Phys. Rev. B* **67**, 113103 (2003).

Belyamoun, M. H. and S. Zouhdi, "On the modeling of effective constitutive parameters of bianisotropic media by a periodic unfolding method in time and frequency domains," *Appl. Phys. A* **103**, 881-887 (2011).

Beruete, M., M. Sorolla, R. Marqués, J. D. Baena and M. Freire, "Resonance and Cross-Polarization Effects in Conventional and Complementary Split Ring Resonator Periodic Screens," *Electromagnetics* **26**, 247-260 (2006).

Bohren, C. F. and D. R. Huffman, *Absorption and Scattering of Light by Small Particles* (Wiley, New-York, 1983).

Boucher, V. and D. Ménard, "Effective magnetic properties of arrays of interacting ferromagnetic wires exhibiting gyromagnetic anisotropy and retardation effects," *Phys. Rev. B* **81**, 174404 (2010).

Bouhelier, A., Th. Huser, H. Tamaru, H.-J. Guntherodt, and D. W. Pohl, "Plasmon optics of structured silver films," *Phys. Rev. B* **63**, 155404 (2001).

Brongersma, M. L., J.W. Hartman, and H.A. Atwater, "Electromagnetic energy transfer and switching in nanoparticle chain arrays below the diffraction limit," *Phys. Rev. B* **62**, R16356 (2000).

Bruggeman, D. A. G., "Berechnung verschiedener physikalischer Konstanten von heterogenen Substanzen. I. Dielektrizitätskonstanten und Leitfähigkeiten der Misch- körper aus isotropen Substanzen," *Ann. Phys*. **24** 636–664, (1935).

Burke, J. J., G. I. Stegeman, and T. Tamir, "Surface-polariton-like waves guided by thin, lossy metal films," *Phys. Rev. B* **33,** 5186 (1986).

Cai, W. and V. Shalaev, *Optical Metamaterials: Fundamentals and Applications* (Springer, 2010).

Cai, W., U. K. Chettiar, A. V. Kildishev, and V. M. Shalaev, "Optical cloaking with metamaterials," *Nat. Photonics* **1**, 224 - 227 (2007).

Caloz, C. and T. Itoh, "Metamaterial-based electronically controlled transmission-line structure as a novel leaky-wave antenna with tunable radiation angle and beamwidth," *IEEE Trans. Microwave Theory Tech*. **52**, 2678-2690 (2004).

Caloz, C. and T. Itoh, *Electromagnetic Metamaterials: Transmission Line Theory and Microwave Applications* (Wiley-IEEE Press, 2005).

Casse, B. D. F., W. T. Lu, Y. J. Huang, E. Gultepe, L. Menon, and S. Sridhar, "Super-resolution imaging using a three-dimensional metamaterials nanolens," *Appl. Phys. Lett*. **96**, 023114 (2010).

Chen, P.-W., C. S. Lee, and V. Nalbandian, "Planar double-layer leaky-wave microstrip antenna," *IEEE Trans. Antennas Propag.* **50**, 832 (2002).

Chen, X., B.-I. Wu, J. A. Kong, and T. M. Grzegorczyk, "Retrieval of the effective constitutive parameters of bianisotropic metamaterials," *Phys. Rev. E* **71**, 046610 (2005).

Chen, X., T. M. Grzegorczyk, B.-I. Wu, J. Pacheco, Jr., and J. A. Kong, "Robust method to retrieve the constitutive effective parameters of metamaterials," *Phys. Rev. E* **70**, 016608 (2004).

Cheng, X., H. Chen, L. Ran, B.-I. Wu, T. M. Grzegorczyk, and J. A. Kong, "Negative refraction and cross polarization effects in metamaterial realized with bianisotropicS-ring resonator,"*Phys. Rev. B* **76**, 024402 (2007).

Chuang, S. L., *Physics of Photonic Devices* (Wiley & Sons, 2009).

Collin, R. E. and F. J. Zucker, *Antenna Theory* (McGraw-Hill, New York, 1969).

Collin, R. E., *Field Theory of Guided Waves* (Wiley-IEEE Press, 1990).

Costa, J., S. Mário, and A. Alù, "Poynting vector in negative-index metamaterials," *Phys. Rev. B* **83**, 165120 (2011).

Craster, R. V. and S. Guenneau, *Acoustic Metamaterials: Negative Refraction, Imaging, Lensing and Cloaking* (Springer, 2013).

Crozier, K. B., A. Sundaramurthy, G. S. Kino, and C. F. Quate, "Optical antennas: Resonators for local field enhancement,"*J. Appl. Phys.* **94**, 4632 (2003).

Curto, A. G., G. Volpe, T. H. Taminiau, M. P. Kreuzer, R. Quidant, and N. F. van Hulst, "Unidirectional Emission of a Quantum Dot Coupled to a Nanoantenna," *Science* **329**, 930 (2010).

Dimitriadis, A. I., D. L. Sounas, N. V. Kantartzis, C. Caloz, and T. D. Tsiboukis, "Surface Susceptibility Bianisotropic Matrix Model for Periodic Metasurfaces of Uniaxially Mono-Anisotropic Scatterers Under Oblique TE-Wave Incidence," *IEEE Trans. Antennas Propag.* **60**, 5753-5767 (2012).

Dimitriadis, A. I., N. V. Kantartzis, I. T. Rekanos and T. D. Tsiboukis, "Efficient Metafilm/Metasurface Characterization for Obliquely Incident TE Waves via Surface Susceptibility Models," *IEEE Trans. Magn*. **48**, 367-370 (2012).

Dong, Z. G., M.-X. Xu, S.-Y. Lei, Shuang-Ying, H. Liu, T. Li, F.-W. Wang, and S.-N. Zhu, "Negative refraction with magnetic resonance in a metallic double-ring metamaterial," *Appl. Phys. Lett.* **92**, 064101 (2008).

Dressel, M. and G. Grüner, *Electrodynamics of Solids* (Cambridge University Press, Cambridge, 2002).

Drezet, A., A. Hohenau, A. L. Stepanov, H. Ditlbacher, B. Steinberger, N. Galler, F. R. Aussenegg, "How to erase surface plasmon fringes," *Appl. Phys. Lett*. **89**, 091117 (2006)

Edwards, B., A. Alù, M. G. Silveirinha, and N. Engheta, "Experimental verification of plasmonic cloaking at microwave frequencies with metamaterials," *Phys. Rev. Lett.* **103**, 153901 (2009).

El-Mallawany, R., "The optical properties of tellurite glasses," *J. Appl. Phys.* **72**, 1774-1777 (1992).

Engheta, N. and R. W. Ziolkowski, *Metamaterials: Physics and Engineering Explorations* (Wiley-IEEE Press, Denver, 2006).

Fang, A., T. Koschny, and C. M. Soukoulis, "Optical anisotropic metamaterials: Negative refraction and focusing," *Phys. Rev. B* **79**, 245127 (2009).

Fang, N., D. Xi, J. Xu, M. Ambati, W. Srituravanich, C. Sun, and X. Zhang, "Ultrasonic metamaterials with negative modulus," *Nat. Mater*. **5**, 452 - 456 (2006).

Fang, N., H. Lee, C. Sun and X, Zhang, "Sub–Diffraction-Limited Optical Imaging with a Silver Superlens," *Science* **308**, 534-537 (2005).

Fietz, C. and G. Shvets, "Current-driven metamaterial homogenization," *Physica B* **405,** 2930-2934 (2010).

Fietz C. and G. Shvets, "Homogenization theory for simple metamaterials modeled as one-dimensional arrays of thin polarizable sheets," *Phys. Rev. B* **82**, 205128 (2011).

Fietz, C., Y. Urzhumov, and G. Shvets, "Complex k band diagrams of 3D metamaterial/photonic crystals," *Opt. Express* **19**, 19027-19041 (2011).

Gansel, J. K., M. Thiel, M. S. Rill, M. Decker, K. Bade, V. Saile, G. von Freymann, S. Linden and M. Wegener, "Gold Helix Photonic Metamaterial as Broadband Circular Polarizer," *Science* **325**, 1513-1515 (2009).

García-Meca, C., R. Ortuño, F. J. Rodríguez-Fortuño, J. Martí, and A. Martínez, "Double-negative polarization-independent fishnet metamaterial in the visible spectrum," *Opt. Lett*. **34**, 1603-1605 (2009).

Ghadarghadr, S., Z. Hao, and H. Mosallaei, "Plasmonic array nanoantennas on layered substrates: modeling and radiation characteristics," *Opt. Express* **17**, 18556 (2009).

Han, J., A. Lakhtakia and C.-W. Qiu, "Terahertz metamaterials with semiconductor split-ring resonators for magnetostatic tunability," *Opt. Express* **16**, 14390-14396 (2008).

Hecht, E., *Optics*, 4th ed., (Addison Wesley, 2001).

Highstrete, C., M. Lee, and W. Padilla, "Complementary Planar Terahertz Metamaterials," *Opt. Express* **15**, 1084-1095 (2007).

Holloway, C. L., E. F. Kuester, and A. Dienstfrey, "Characterizing Metasurfaces/Metafilms: The Connection Between Surface Susceptibilities and Effective Material Properties," *IEEE Antennas Wirel. Propag. Lett*. **10**, 1507-1511 (2011).

Holloway, C. L., E. F. Kuester, J. A. Gordon, J. O'Hara, J. Booth, D. R. Smith, "An Overview of the Theory and Applications of Metasurfaces: The Two-Dimensional Equivalents of Metamaterials," *IEEE Antennas Propag. Mag*. **54**, 10-35 (2012).

Holloway, C. L., E. F. Kuester, J. Baker-Jarvis, and P. Kabos, "A double negative (DNG) composite medium composed of magnetodielectric spherical particles embedded in a matrix," *IEEE Trans. Antennas Propag*. **51**, 2596-2603 (2003).

Holloway, C. L., M. A. Mohamed, E. F. Kuester and A. Dienstfrey, "Reflection and Transmission Properties of a Metafilm: With an Application to a Controllable Surface Composed of Resonant Particles," *IEEE Trans. Electromag. Compat.* **47**, 853-865 (2005).

Holloway, C. L., P. Kabos, M. A. Mohamed, E. F. Kuester, J. Gordon, M. D. Janezic, and J. Baker-Jarvis, "Realization of a Controllable Metafi lm/Metasurface Composed of Resonant Magnetodielectric Particles: Measurements and Theory," *IET Microwaves Antennas Propag.* **4**, 1111-1122 (2010).

Holloway. C. L., A. Dienstfrey, E. F. Kuester, J. F. O'Hara, A. K. Azad, and A. J. Taylor, "A discussion on the interpretation and characterization of metafilms/metasurfaces: The two-dimensional equivalent of metamaterials," *Metamaterials* **3**, 100-112 (2009).

Hong, W., T.-L. Chen, C.-Y. Chang, J.-W. Sheen, Y.-D. Lin, "Broadband tapered microstrip leaky-wave antenna," *IEEE Trans. Antennas Propag*. **51,** 1922 (2003).

Hornyak, G. L., C. J. Patrissi, E. B. Oberhauser, C. R. Martin, J-C Valmalette, L. Lemaire, J. Dutta, and H. Hofmann, "Effective medium theory characterization of Au/Ag nanoalloy-porous alumina composites," *Nanostruct. Mater*. **9** 571-574 (1998).

Hu, J. and C. R. Menyuk, "Understanding leaky modes: slab waveguide revisited," *Adv. Opt. Photon*. **1**, 58 (2009).

Huang, L., J.-C. Chiao, and M. P. De Lisio, "An electronically switchable leaky wave antenna," *IEEE Trans. Antennas Propag*. **48**, 1769 (2000).
Huangfu, J., L. Ran, H. Chen, X. Zhang, K. Chen, T. M. Grzegorczyk, and J. A. Kong, "Experimental confirmation of negative refractive index of a metamaterial composed of Ω-like metallic patterns," *Appl. Phys. Lett*. **84**, 1537 (2004).
Husnik, M., M. W. Klein, N. Feth, M. König, J. Niegemann, K. Busch, S. Linden, and M. Wegener, "Absolute extinction cross-section of individual magnetic split-ring resonators," *Nat. Photonics* **2**, 614 (2008).
Idemen, M., "Straightforward Derivation of Boundary Conditions on Sheet Simulating an Anisotropic Thin Layer," *Electron. Lett.* **24**, 663-665 (1988).
Ishimaru, A., S.-W. Lee, Y. Kuga, and V. Jandhyala, "Generalized constitutive relations for metamaterials based on the quasi-static Lorentz theory," *IEEE Trans. Antennas Propag.* **51**, 2550-2557 (2003).
Jackson, D. R., A. A. Oliner, "Leaky-Wave Antennas," in *Modern Antenna Handbook*, C. A. Balanis ed. (Wiley, 2008).
Jackson, J. D., *Classical Electrodynamics* (Wiley, New-York, 1975).
Jelinek, L. and J. Machac, "Free space polarizability measurement method," in *Proceedings of Metamaterials '2011: The Fifth International Congress on Advanced Electromagnetic Materials in Microwaves and Optics*, Barcelona, 967-969 (2011).
Jin, J., S. Liu, Z. Lin, and S. T. Chui, "Effective-medium theory for anisotropic magnetic metamaterials," *Phys. Rev. B* **80**, 115101 (2009).
Johnson, P. B. and R. W. Christy, "Optical Constants of the Noble Metals," *Phys. Rev. B* **6**, 4370-4379 (1972).
Kafesaki, M., I. Tsiapa, N. Katsarakis, Th. Koschny, C. M. Soukoulis, and E. N. Economou, "Left-handed metamaterials: The fishnet structure and its variations," *Phys. Rev. B* **75**, 235114 (2007).
Kim, S., E. F. Kuester, C. L. Holloway, A. D. Scher, and J. Baker-Jarvis, "Boundary Effects on the Determination of Metamaterial Parameters From Normal Incidence Reflection and Transmission Measurements." *IEEE Trans. Antennas Propag.* **59**, 2226-2240 (2011).
Kim, S.-H, "Seismic wave attenuator made of acoustic metamaterials," *J. Acoust. Soc. Am*. **131**, 3292-3292 (2012).
Kock, W. E., "Path-length microwave lenses," *Proc. IRE* **37**, 852-855 (1948).
Kock, W. E., Metallic delay lenses, *Bell Syst. Tech. J*. **27**, 58-82 (1948).
Kong, J. A. and D. K. Cheng, "Modified reciprocity theorem for bianisotropic meida," *Proc. Inst. Elec. Eng.* **117**, 349-350 (1970).
Kong, J. A., "Optics of bianisotropic media," *JOSA* **64**, 1304-1308 (1974).
Kong, J. A., "Reciprocity relationships for bianisotropic media," *Proc. IEEE (Lett.)* **58**, 1966-1967 (1970).
Krenn, J. R., M. Salerno, N. Felidj, B. Lamprecht, G. Schider, A. Leitner, F. R. Aussenegg, J. C. Weeber, A. Dereux and J. P. Goudonnet, "Light field propagation by metal micro- and nanostructures," *J. Microscopy* **202**, 122 (2001)

Kuester, E. F., M.A. Mohamed, M. Piket-May, and C. L. Holloway, "Averaged transition conditions for electromagnetic fields at a metafilm," *IEEE Trans. Antennas Propag.* **51**, 2641-2651 (2003).
Lai, A., T. Itoh, and C. Caloz, "Composite right/left-handed transmission line metamaterials," *IEEE Microw. Mag*. **5,** 34 (2009).
Lai, Y., Y. Wu, P. Sheng and Z.-Q. Zhang, "Hybrid elastic solids," *Nat. Mater*. **10**, 620-624 (2011).
Lakhtakia, A., "On the genesis of Postconstraint in modernelectromagnetism," *Optik* **115**, 151-158 (2004).
Lampariello, P., F. Frezza, and A. A. Oliner, "The transition region between bound-wave and leaky-wave ranges for a partially dielectric-loaded open guiding structure," *IEEE Trans. Microwave Theory Tech*. **38**, 1831 (1990).
Landau, L. D., E. M. Lifshitz, and L. P. Pitaevskii, *Electrodynamics of Continuous Media* (Butterworth-Heinemann, Oxford, 1982).
Lassiter, J. B., J. Aizpurua, L. I. Hernandez, D. W. Brandl, I. Romero, S. Lal, J. H. Hafner, P. Nordlander, and N. J. Halas, "Close Encounters between Two Nanoshells," *Nano Lett.* **8**, 1212 (2008).
Lewin, L., *Polylogarithms and Associated Functions*, (Elsevier, New York, 1981).
Li, J., L. Fok, X. Yin, G. Bartal, and X. Zhang, "Experimental demonstration of an acoustic magnifying hyperlens," *Nat. Mater*. **8**, 931-934 (2009).
Lin, D.-H. and P.G. Luan, "Cloaking of matter waves under the global Aharonov–Bohm effect," *Phys. Rev. A* **79**, 051605 (2009).
Lin, S.-C. S., *Acoustic Metamaterials: Tunable Gradient-Index Phononic Crystals for Acoustic Wave Manipulation* (Academic Publishing, 2012).
Lindell, I. V., A. H. Sihvola, and J. Kurkijarvi, "Karl F. Lindman: The last Hertzian, and a harbinger of electromagnetic chirality," *IEEE Antennas Propag. Mag.* **34**, 24-30 (1992).
Lindell, I. V., *Electromagnetic waves in chiral and Bi-isotropic media* (Artech House, Boston, 1994).
Linden, S., C. Enkrich, M. Wegener, J. Zhou, T. Koschny, and C. M. Soukoulis, "Magnetic Response of Metamaterials at 100 Terahertz," *Science* **306**, 1351-1353 (2004).
Lindmann, K. F., "Rotation polarisation of electromagnetic waves generated by the isotropic system of spiral resonators," *Annalen der Physik* **63**, 621-644 (1920).
Liu, H., D. A. Genov, D. M. Wu, Y. M. Liu, Z. W. Liu, C. Sun, S. N. Zhu, and X. Zhang, "Magnetic plasmon hybridization and optical activity at optical frequencies in metallic nanostructures," *Phys. Rev. B* **76**, 073101 (2007).
Liu, L., C. Caloz, and T. Itoh, "Dominant mode leaky-wave antenna with backfire-to-endfire scanning capability," *Electr. Lett*. **38**, 1414-1416 (2002).
Liu, N., H. Guo, L. Fu, S. Kaiser, H. Schweizer, and H. Giessen, "Three-dimensional photonic metamaterials at optical frequencies," *Nat. Mater*. **7**, 31-37 (2008).
Liu, N., H. Liu, S. Zhu, and H. Giessen, "Stereometamaterials," *Nat. Photonics* **3**, 157-162 (2009).

Liu, X.-X. and A. Alù, "Homogenization of quasi-isotropic metamaterials composed by dense arrays of magnetodielectric spheres," *Metamaterials* **5**, 56-63 (2011).
Liu, X.-X. and A. Alu, "Limitations and potentials of metamaterial lenses," *J. Nanophoton*. 5, 053509 (2011).
Liu, X.-X., D. A. Powell, and A. Alù, "Correcting the Fabry-Perot artifacts in metamaterial retrieval procedures," *Phys. Rev. B* **84**, 235106 (2011).
Liu, Z., H. Lee, Y. Xiong, C. Sun, and X. Zhang, "Far-Field Optical Hyperlens Magnifying Sub-Diffraction-Limited Objects," *Science* **315**, 1686 (2007).
Mackay, T. G., "Linear and Nonlinear Homogenized Composite Mediums as Metamaterials," *Electromagnetics* **25**, 461–481 (2005).
Mahmoud, S. F., "A new miniaturized annular ring patch resonator partially loaded by a metamaterial ring with negative permeability and permittivity," *IEEE Antennas Wirel. Propag. Lett.* **3**, 19-22 (2004).
Maier, S. A., M. L. Brongersma, P. G. Kik, S. Meltzer, A. A. G. Requicha, and H. A. Atwater, "Plasmonics—A Route to Nanoscale Optical Devices," *Adv. Mater*. **13**, 1501 (2001).
Maier, S. A., P. G. Kik, and H. A. Atwater, "Observation of coupled plasmon-polariton modes in Au nanoparticle chain waveguides of different lengths: Estimation of waveguide loss," *Appl. Phys. Lett*. **81**, 1714 (2002).
Maier, S. A., P. G. Kik, H. A. Atwater, S. Meltzer, E. Harel, B. E. Koel and A. A. G. Requicha, "Local detection of electromagnetic energy transport below the diffraction limit in metal nanoparticle plasmon waveguides," *Nat. Mater*. **2**, 229 (2003).
Maier, S. A., P. E. Barclay, T. J. Johnson, M. D. Friedman, and O. Painter, "Low-loss fiber accessible plasmon waveguide for planar energy guiding and sensing," *Appl. Phys. Lett.* **84**, 3990 (2004).
Maier. S. A., P. G. Kik, and H. A. Atwater, "Optical pulse propagation in metal nanoparticle chain waveguides," *Phys. Rev. B* **67**, 205402 (2003).
Marqués, R., F. Martín, and M. Sorolla, *Metamaterials with Negative Parameters* (John Wiley & Son, Hoboken, 2008).
Marqués, R., F. Medina, and R. Rafii-El-Idrissi, "Role of bianisotropy in negative permeability and left-handed metamaterials," *Phys. Rev. B* **65**, 144440 (2002).
Marqués, R., F. Mesa, J. Martel, and F. Medina, "Comparative Analysis of Edge- and Broadside-Coupled Split Ring Resonators for Metamaterial Design—Theory and Experiments,"*IEEE Trans. Antennas Propag.* **51**, 2572-2581 (2003).
Marqués, R., J. Martel, F. Mesa, and F. Medina, "Left-Handed-Media Simulation and Transmission of EM Waves in Subwavelength Split-Ring-Resonator-Loaded Metallic Waveguides," *Phys. Rev. Lett*. **89**, 183901 (2002).
Maxwell-Garnett, J. C., "Colours in metal glasses and in metallic films," *Phios. Trans. Roy. Soc. Lond. A* **203**, 385-420 (1904).
Melville, D. O. S. and R. J. Blaikie, "Super-resolution imaging through a planar silver layer*," Opt. Express* **13**, 2127-2134 (2005).

Menzel, C., T. Paul, C. Rockstuhl, T. Pertsch, S. Tretyakov, and F. Lederer, "Validity of effective material parameters for optical fishnet metamaterials," *Phys. Rev. B* **81**, 035320 (2010).

Morits, D. and C. Simovski, "Electromagnetic characterization of planar and bulk metamaterials: A theoretical study," *Phys. Rev. B* **82**, 165114 (2010).

Mousavi, S. H., A. B. Khanikaev, and G. Shvets, "Optical properties of Fano-resonant metallic metasurfaces on a substrate," *Phys. Rev. B* **85**, 155429 (2012).

Mühlschlegel, P., H.-J. Eisler, O. J. F. Martin, B. Hecht, and D. W. Pohl, "Resonant Optical Antennas," *Science* **308**, 1607 (2005).

Munk, B. A., *Frequency Selective Surfaces: Theory and Design*, (Wiley-Interscience, 2000).

Nicolson, A. M. and G. F. Ross, "Measurement of the intrinsic properties of materials by time-domain techniques," *IEEE Trans. Instrum. Meas.* **IM-19**, 377–382 (1970).

Noginov, M. A. and V. A. Podolskiy, *Tutorials in Metamaterials* (CRC Press, 2011).

Novotny, L., "Effective Wavelength Scaling for Optical Antennas," *Phys. Rev. Lett*. **98**, 266802 (2007).

O'Hara, J. F., E. Smirnova, A. K. Azad, H.-T. Chen, and A. J. Taylor, "Effects of Microstructure Variations on Macroscopic Terahertz Metafilm Properties," *Act. Passive Electron. Compon*. art. 49691 (2007).

Ouchetto, O., C.-W. Qiu, S. Zouhdi, L.-W. Li, and A. Razek, "Homogenization of 3-D Periodic Bianisotropic Metamaterials," *IEEE Trans. Microwave Theory Tech.* **54**, 3893-3898 (2006).

Ozbay, E., K. Aydin, E. Cubukcu, and M. Bayindir, "Transmission and reflection properties of composite double negative metamaterials in free space," *IEEE Trans. Antennas Propag.* **51**, 2529-2595 (2003).

Padilla, W. J., A. J. Taylor, C. Highstrete, M. Lee, and R. D. Averitt, "Dynamical Electric and Magnetic Metamaterial Response at Terahertz Frequencies," *Phys. Rev. Lett.* **96**, 107401 (2006).

Padilla, W. J., D. N. Basov, and D. R. Smith, "Negative Refractive Index Metamaterials," *Mater. Today* **9**, 28-35 (2006).

Palik, E., *Handbook of Optical Constants of Solids*. (New York: Academic Press, 1985).

Paniagua-Domínguez, R., F. López-Tejeira, R. Marqués, and J. A. Sánchez-Gil, "Metallo-dielectric core–shell nanospheres as building blocks for optical three-dimensional isotropic negative-index metamaterials," *New J. Phys*. **13**, 123017 (2011).

Papasimakis, N., V. A. Fedotov, N. I. Zheludev and S. L. Prosvirnin, "Metamaterial Analog of Electromagnetically Induced Transparency," *Phys. Rev. Lett*. **101**, 253903 (2008).

Papasimakis, N., Y. H. Fu, V. A. Fedotov, S. L. Prosvirnin, D. P. Tsai, and N. I. Zheludev, "Metamaterial with polarization and direction insensitive resonant transmission response mimicking electromagnetically induced transparency," *Appl. Phys. Lett*. **94**, 211902 (2009).

Pendry, J. B., A. J. Holden, D. J. Robbins, and W. J. Stewart, "Magnetism from conductors and enhanced nonlinear phenomena," *IEEE Trans. Microwave Theory Tech*. **47**, 2075-2084 (1999).

Pendry, J. P., "Negative Refraction Makes a Perfect Lens," *Phys. Rev. Lett.* **85**, 3966-3969 (2000).

Pimenov, A., A. Loidl, K. Gehrke, V. Moshnyaga, and K. Samwer, "Negative Refraction Observed in a Metallic Ferromagnet in the Gigahertz Frequency Range," *Phys. Rev. Lett*. **98**, 197401 (2007).

Plum, E., X.-X. Liu, V. A. Fedotov, Y. Chen, D. P. Tsai, and N. I. Zheludev, "Metamaterials: Optical Activity without Chirality," *Phys. Rev. Lett.***102**, 113902 (2009).

Pors, A., I. Tsukerman, and S. I. Bozhevolnyi, "Effective constitutive parameters of plasmonic metamaterials: Homogenization by dual field interpolation," *Phys. Rev. E* **84**, 016609 (2011).

Post, E. J., *Formal Structure of Electromagnetics* (North-Holland, Amsterdam, 1962).

Pozar, D. M., *Microwave Engineering* 3rd ed., (Wiley & Sons, 2005).

Quinten, M., A. Leitner, J. R. Krenn, and F. R. Aussenegg, "Electromagnetic energy transport via linear chains of silver nanoparticles," *Opt. Lett*., **23**, 1331 (1998).

Raghunathan, S. B. and N. V. Budko, "Effective permittivity of finite inhomogeneous objects," *Phys. Rev. B* **81**, 054206 (2010).

Reithmaier, J., P. Petkov, W. Kulisch, and C. Popov, *Nanostructured Materials for Advanced Technological Applications* (Springer, Bulgaria, 2008).

Rockstuhl, C., C. Menzel, T. Paul, T. Pertsch, and F. Lederer, "Light propagation in a fishnet metamaterial," *Phys. Rev. B* **78**, 155102 (2008).

Salandrino, A. and N. Engheta, "Far-field subdiffraction optical microscopy using metamaterial crystals: Theory and simulations," *Phys. Rev. B* **74**, 075103 (2006).

Scher, A. D. and E. F. Kuester, "Extracting the bulk effective parameters of a metamaterial via the scattering from a single planar array of particles,"*Metamaterials* **3**, 44-55 (2009).

Schnell, M., A. García-Etxarri, A. J. Huber, K. Crozier, J. Aizpurua and R. Hillenbrand, "Controlling the near-field oscillations of loaded plasmonic nanoantennas," *Nat. Photonics* **3**, 287 (2009).

Schuck, P. J., D. P. Fromm, A. Sundaramurthy, G. S. Kino, and W. E. Moerner, "Improving the Mismatch between Light and Nanoscale Objects with Gold Bowtie Nanoantennas," *Phys. Rev. Lett.* **94**, 017402 (2005).

Schuller, J. A., R. Zia, T. Taubner, and M. L. Brongersma, "Dielectric Metamaterials Based on Electric and Magnetic Resonances of Silicon Carbide Particles," *Phys. Rev. Lett*. **99**, 107401 (2007).

Schurig, D., J. J. Mock, B. J. Justice, S. A. Cummer, J. B. Pendry, A. F. Starr, and D. R. Smith, "Metamaterial Electromagnetic Cloak at Microwave Frequencies," *Science* **314**, 977-980 (2006).

Sersic, I., C. Tuambilangana, T. Kampfrath, and A. F. Koenderink, "Magneto-electric point scattering theory for metamaterial scatterers," *Phys. Rev. B* **83**, 245102 (2011).
Sersic, I., M. Frimmer, and A. F. Koenderink, "Electric and Magnetic Dipole Coupling in Near-Infrared Split-Ring Metamaterial Arrays," *Phys. Rev. Lett*. **103**, 213902 (2009).
Shalaev, V. M., "Optical negative-index metamaterials," *Nat. Photon*ics **1**, 41-48 (2007).
Shelby, R. A., D. R. Smith and S. Schultz, "Experimental Verification of a Negative Index of Refraction," *Science* **292**, 77-79 (2001).
Shore, R. A. and A. D. Yaghjian, "Traveling Waves on Three-Dimensional Periodic Arrays of Two Different Alternating Magnetodielectric Spheres," *IEEE Trans. Antennas Propag.***57,** 3077-3091 (2009).
Shore, R. A. and A. D. Yaghjian, "Traveling waves on two- and three-dimensional periodic arrays of lossless scatterers," *Radio Sci.* **42**, RS6S21 (2007).
Shore, R. A. and A.D. Yaghjian, "Travelling electromagnetic waves on linear periodic arrays of lossless spheres," *Electr. Lett*. **41**, 578 (2005).
Shore, R. A., and A. D. Yaghjian, "Traveling Electromagnetic Waves on Linear Periodic Arrays of Lossless Penetrable Spheres," *IEICE Trans. Commun*. **E88-B**, 2346 (2005).
Sihvola, A.H., A.J. Viitanen, I.V. Lindell and S.A. Tretyakov, *Electromagnetic Waves in Chiral and Bi-Isotropic Media* (Artech House Antenna Library, 1994).
Silveirinha, M. and N. Engheta, "Design of matched zero-index metamaterials using nonmagnetic inclusions in epsilon-near-zero media," *Phys. Rev. B* **75**, 075119 (2007).
Silveirinha, M. G. and C. A. Fernandes, "A New Acceleration TechniqueWith Exponential Convergence Rate to Evaluate Periodic Green Functions," *IEEE Trans. Antennas Propag*. **53**, 347-355 (2005).
Silveirinha, M. G. and C. A. Fernandes, "Homogenization of 3-D-connected and nonconnected wire metamaterials," *IEEE Trans. Microwave Theory Tech*. **53**, 1418-1430 (2005).
Silveirinha, M. G., "Generalized Lorentz-Lorenz formulas for microstructured materials," *Phys. Rev. B* **76**, 245117 (2007).
Silveirinha, M. G., "Metamaterial homogenization approach with application to the characterization of microstructured composites with negative parameters," *Phys. Rev. B* **75**, 115104 (2007).
Silveirinha, M. G., "Nonlocal homogenization model for a periodic array of ϵ-negative rods," *Phys. Rev. E* **73**, 046612 (2006).
Silveirinha, M. G. and C. A. Fernandes, "A new acceleration technique with exponential convergence rate to evaluate periodic Green functions," *IEEE Trans. Antennas Propag*. **53**, 347-335 (2005).
Simovski, C. R. and S. A. Tretyakov, "Local constitutive parameters of metamaterials from an effective-medium perspective," *Phys. Rev. B* **75**, 195111 (2007).

Simovski, C. R. and S. A. Tretyakov, "Model of isotropic resonant magnetism in the visible range based on core-shell clusters," *Phys. Rev. B* **79**, 045111 (2009).
Simovski, C. R., "On electromagnetic characterization and homogenization of nanostructured metamaterials," *J. Opt*. **13**, 013001 (2011).
Simovski, C. R., P. A. Belov, and S. He, "Backward wave region and negative material parameters of a structure formed by lattices of wires and split-ring resonators," *IEEE Trans. Antennas Propag*. **51**, 2582-2591 (2003).
Simovski, C. R., S. He, "Frequency range and explicit expressions for negative permittivity and permeability for an isotropic medium formed by a lattice of perfectly Ω conducting particles," *Phys. Lett. A* **311**, 254 (2003).
Sipe, J. E., and J. V. Kranendonk, "Macroscopic electromagnetic theory of resonant dielectrics," *Phys. Rev. A* **9**, 1806 (1974).
Smith, D. R. and J. B. Pendry, "Homogenization of metamaterials by field averaging (invited paper)," *JOSA B* **23**, 391-403 (2006).
Smith, D. R., D. C. Vier, Th. Koschny, and C. M. Soukoulis, "Electromagnetic parameter retrieval from inhomogeneous metamaterials," *Phys. Rev. E* **71**, 036617 (2005).
Smith, D. R., D. Schurig, and J. J. Mock, "Characterization of a Planar Artifi cial Magnetic Metamaterial Surface," *Phys. Rev. E* **74**, 036604 (2006).
Smith, D. R., J. B. Pendry, and M. C. K. Wiltshire, "Metamaterials and Negative Refractive Index," *Science* **305**, 788792 (2004).
Smith, D. R., S. Schultz, P. Markos, and C. M. Soukoulis, "Determination of effective permittivity and permeability of metamaterials from reflection and transmission coefficients," *Phys. Rev. B* **65**, 195104 (2002).
Sounas, D. L. and N. V. Kantartzis, "Systematic surface waves analysis at the interfaces of composite DNG/SNG media," *Opt. Express* **17**, 8513-8524 (2009).
Sungjoon, L., C. Caloz, and T. Itoh, "A reflectodirective system using a composite right/left-handed (CRLH) leaky-wave antenna and heterodyne mixing," *IEEE Microw. Wireless Compon. Lett*. **14,** 183 (2004).
Talley, C. E., J. B. Jackson, C. Oubre, N. K. Grady, C. W. Hollars, S. M. Lane, T. R. Huser, P. Nordlander, and N. J. Halas, "Surface-Enhanced Raman Scattering from Individual Au Nanoparticles and Nanoparticle Dimer Substrates," *Nano Lett.* **5**, 1569 (2005).
Tao, H., A. C. Strikwerda, K. Fan, W. J. Padilla, X. Zhang, and R. D. Averitt, "Reconfigurable Terahertz Metamaterials," *Phys. Rev. Lett.* **103**, 147401 (2009).
Tretyakov, S. A., A. H. Sihvola, A. A. Sochava, and C. R. Simovski, "Magneto-electric Interactions in Bi-Anisotropic Media," *J. Electromagn. Waves Appl*. **12**, 481 (1998).
Tretyakov, S. A., *Analytical Modeling in Applied Electromagnetics* (Artech House, London, 2002).
Tretyakov, S. A. and A. J. Viitanen, "Line of periodically arranged passive dipole scatterers," *Electr. Eng*. **82**, 35 (2000).

Tretyakov, S. A., F. Mariotte, C. R. Simovski, T. G. Kharina, and J.-P. Heliot, "Analytical antenna model for chiral scatterers: comparison with numerical and experimental data," *IEEE Trans. Antennas Propag*. **44**, 1006-1014 (1996).

Tretyakov, S. A., S. I. Maslovski, I. S. Nefedov, A. J. Viitanen, P. A. Belovand and A. Sanmartin, "Artificial Tellegen Particle," *Electromagnetics* **23**, 665-680 (2003).

Tretyakov, S.A., F.Mariotte, C.R. Simovski, T. G. Kharina, J.-P. Heliot, "Analytical antenna model for chiral scatterers: comparison with numerical and experimental data," *IEEE Trans. Antennas Propag.* **44**, 1006-1014 (1996).

Tsukerman, I., "Nonlocal homogenization of metamaterials by dual interpolation of field," *JOSA B* **28**, 2956-2965 (2011).

Valentine, J., S. Zhang, T. Zentgraf, E. Ulin-Avila, D. A. Genov, G. Bartal, and X. Zhang, "Three-dimensional optical metamaterial with a negative refractive index," *Nature* **455**, 376-379 (2008).

Verhagen, E., R. de Waele, L. Kuipers, and A. Polman, "Three-Dimensional Negative Index of Refraction at Optical Frequencies by Coupling Plasmonic Waveguides," *Phys. Rev. Lett.* **105**, 223901 (2010).

Vinogradov, A. P., A. I. Ignatov, A. M. Merzlikin, S. A. Tretyakov, and C. R. Simovski, "Additional effective medium parameters for composite materials (excess surface currents)," *Opt. Express* **19**, 6699-6704 (2011).

Vynck, K., D. Felbacq, E. Centeno, A. I. Căbuz, D. Cassagne, and B. Guizal, "All-Dielectric Rod-Type Metamaterials at Optical Frequencies," *Phys. Rev. Lett*. **102**, 133901 (2009).

Wallén, H., H. Kettunen, J. Qi, and A. Sihvola, "Anti-resonant response of resonant inclusions?" in *proceedings of General Assembly and Scientific Symposium*, 2011 XXXth URSI.

Weber, W. H. and G. W. Ford, "Propagation of optical excitations by dipolar interactions in metal nanoparticle chains," *Phys. Rev. B* **70**, 125429 (2004).

Weir, W. B., "Automatic measurement of complex dielectric constant and permeability at microwave frequencies," *Proc. IEEE* **62**, 33-36 (1974).

Wood, B, J. B. Pendry, and D. P. Tsai, "Directed subwavelength imaging using a layered metal-dielectric system," *Phys. Rev. B* **74**, 115116 (2006).

Wu, B.-I., W. Wang, J. Pacheco, X. Chen, T. M. Grzegorczyk, and J. A. Kong, "a study of using metamaterials as antenna substrate to enhance gain," *Prog. Electromagn. Res.* **51**, 295-328 (2005).

Yaghjian, A. D., R. A. Shore, and A. Alu, "A General Macroscopic Anisotropic Representation for Spatially Dispersive Media," in *proceedings of General Assembly and Scientific Symposium*, 2011 XXXth URSI.

Yang, F. and Y. Rahmat-Samii, "Reflection phase characterizations of the EBG ground plane for low profile wire antenna applications," *IEEE Antennas Propag. Mag*. **51**, 2691- 2703 (2003).

Yao, J., Z. Liu, Y. Liu, Y. Wang, C. Sun, G. Bartal, A. M. Stacy, and X. Zhang, "Optical Negative Refraction in Bulk Metamaterials of Nanowires," *Science* **321**, 930 (2008).

Yariv, A. and P. Yeh, Photonics: *Optical Electronics in Modern Communications* 6th ed. (Oxford University Press, 2007).
Ye, H.-X. and Y.-Q. Jina, "Polarimetric scattering from a layer of spatially oriented metamaterial small spheroids," *Eur. Phys. J. Appl. Phys.* **31**, 3-9 (2005).
Zhang, S., D. A. Genov, C. Sun, X. Zhang, "Cloaking of matter waves," *Phys. Rev. Lett*. **100**, 123002 (2008).
Zhang, S., Y.-S. Park, J. Li, X. Lu, W. Zhang, and X. Zhang, "Negative Refractive Index in Chiral Metamaterials," *Phys. Rev. Lett.***102**, 023901 (2009).
Zhao, Y., M.A. Belkin, and A. Alù, "Twisted optical metamaterials for planarized ultrathin broadband circular polarizers," *Nat. Commun.* **3**, 870 (2012).
Zheludev, N. I., "The Road Ahead for Metamaterials," *Science* **328**, 582-583 (2010).
Zhou, L. and C. T. Chan, "High-impedance reflectivity and surface-wave band gaps in metamaterials," *Appl. Phys. Lett.* **84**, 1444-1446 (2004).
Zhou, S., W. Li, and Q. Li, "Design of 3-D Periodic Metamaterials for Electromagnetic Properties," *IEEE Trans. Microwave Theory Tech.* **58**, 910-916 (2010).
Zhuromskyy, O., O. Sydoruk, E. Shamonina, and L. Solymar, "Slow waves on magnetic metamaterials and on chains of plasmonic nanoparticles: Driven solutions in the presence of retardation," *J. Appl. Phys*. **106**, 104908 (2009).
Ziolkowski, R. W., "Design, fabrication, and testing of double negative metamaterials," *IEEE Trans. Antennas Propag*. **51**, 1516-1529 (2003).
Ziolkowski, R. W., "Propagation in and scattering from a matched metamaterial having a zero index of refraction," *Phys. Rev. E* **70**, 046608 (2004).